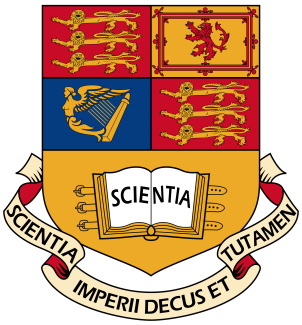
Dual Velocity-Component Investigation of Transient Growth in the Blasius Boundary Layer

by

Ivan H. Roldan Becerra



Department of Aeronautics
Imperial College London
London SW7 2AZ

This thesis is submitted for the
degree of Doctor of Philosophy
of Imperial College London

June 2013

to Rosetta

If there is something that may go bad, be sure it will.
Try to foresee it and adopt the necessary measures
to minimise setbacks.

And never give up.

Acknowledgements

First and foremost I offer my sincerest gratitude to my supervisor and friend, Professor Jonathan F. Morrison. First, for accepting me as his pupil and enabling me to conduct this research. And then, for his numberless words of wisdom and advice, his ceaseless encouragement, and his unconditional support at every single setback that I came across.

I would like to thank very much Dr. Martin Hyde, from TSI Instruments, for his virtually instantaneous assistance and support regarding the Laser Doppler Anemometry apparatus. Also many thanks to Dr. David M. Birch for his invaluable comments and suggestions on how to carry out careful and rigourous wind-tunnel experiments. I would also like to thanks Professor Sergei Chernyshenko and Dr. Luis Parras for their tremendous help on the numerical simulation side of the present study.

I would like to thank Roland Hutchins, manager of the Department of Aeronautics' workshop, and all his colleagues, in particular Ian James, for their help and availability.

A great thanks goes to my colleagues Anthony Oxlade, Dr. Kevin Gouder, Edo Abraham, Dr. Marcos Garcia de la Cruz, Dr. Errikos Levis, Dr. Omar Katamish and Dr. Dhruve Patel for helping me and sharing a great time at Imperial from beginning to end.

I am hugely grateful to both TALENTIA Fellowship Programme (Spain) and EPSRC (U.K.) for their financial support.

Many thanks to my family and friends for their moral support. Also many thanks to Kate Yeo for her valuable proofreading.

Standing on the shoulders of giants

Declaration

This is to certify that the work presented in this thesis has been carried out at Imperial College London and has not been previously submitted to any other university or technical institution for a degree or award. The thesis comprises only the original work of the author. Due acknowledgment is specifically made where appropriate.

Ivan Roldan

Abstract

Transient growth of finite three-dimensional perturbations in wall-bounded laminar shear flows has been extensively studied theoretical, numerical and experimentally. With regard to the experimental work, the vast majority of the investigations have been focused only on the behaviour of the streamwise velocity component, u', despite the importance of the spanwise gradient of the wall-normal velocity component, $\partial v'/\partial z$, as the forcing agent. The present study provides a step forward in the experimental characterisation of transient growth providing, by Laser Doppler Anemometry, simultaneous and highly spatially resolved measurements of both streamwise and wall-normal velocity components of three-dimensional disturbances embedded in a two-dimensional laminar boundary layer. The disturbances are deterministic, as they are generated by a spanwise array of cylindrical roughness elements. The readings are concentrated in both the wake and u'-energy growth regions. Contrary to non-normal operator theory, which describes transient growth as a linear mechanism, a spectral analysis in the present study demonstrates that there exists an underlying non-linear mechanism. This non-linear behaviour is attributed to the influence of the wake in the u'-energy growth region. Numerical simulations considering non-linear terms confirm this conclusion. Both spectral and wavelet analyses have been conducted, providing information regarding the spatial location of the components of the perturbation as well as the relationship between the scales of motion. The numerical simulations are also employed as a workbench to design actuators for open-loop control of transient growth.

Contents

Table of Contents **I**

Nomenclature **V**

1 Fundamentals of the Study **1**

1.1 Boundary Layers . . . 2

1.2 Importance of Transition to Turbulence . . . 3

1.2.1 Boundary Layer Growth and Skin Friction . . . 3

1.2.2 Transition from the Linear Stability Analysis Point of View . . . 6

1.2.3 Discrepancy between Linear Theory and Experiments . . . 8

1.2.4 Receptivity . . . 10

1.3 Non-Normality . . . 12

1.3.1 The Linearised Navier-Stokes Operator . . . 12

1.3.2 Implications of the Coupling Term . . . 16

1.4 Transient Growth . . . 18

1.4.1 Condition for Growth . . . 19

1.4.2 Nature of Growth . . . 20

1.4.3 Optimal Perturbation . . . 24

1.4.4 Experimental Generation of Steady Streaks . . . 28

1.5 Contribution of the Present Study . . . 29

2 Experiments **31**

2.1 Experimental Setup and Techniques . . . 32

2.1.1 Wind Tunnel . . . 32

2.1.2 Flat-Plate and Roughness Element Array . . . 33

2.1.3 Hot-Wire Anemometry . . . 36

2.1.4 Laser Doppler Anemometry . . . 39
2.1.5 Post-Flow Visualisation . . . 55
2.2 Design of Experiments . . . 55
2.2.1 Base Flow Characterisation . . . 55
2.2.2 Perturbed Boundary Layer . . . 60
2.3 Determination of Wall Position . . . 63

3 Results **69**
3.1 Unperturbed Boundary Layer . . . 70
3.1.1 Wall-Normal Velocity Profiles . . . 70
3.1.2 Streamwise Variation of δ_{99}, δ_1, δ_2 and H . . . 71
3.2 Perturbed Boundary Layer . . . 74
3.2.1 Free Stream Characterisation . . . 75
3.2.2 Overview of the Perturbation . . . 78
3.2.3 Mean Boundary Layer Profiles . . . 89
3.2.4 Ensemble Averages . . . 91
3.2.5 Energy . . . 99
3.2.6 Spectral Analysis . . . 100
3.2.7 Wavelet Analysis . . . 108

4 Discussion and Conclusions **119**
4.1 Discussion . . . 119
4.2 Conclusions . . . 123
4.2.1 LDA Experiments . . . 123
4.2.2 Numerical Simulations . . . 124
4.3 Future Work . . . 125

Bibliography **127**

Appendices **135**

A Brief Description of the Laser Doppler Anemometry Technique **137**
A.1 Introduction . . . 138
A.2 Doppler Shift . . . 138
A.3 Interference Phenomenon . . . 139

A.4 Coincidence 141

B Determination of Non-Linear Processes by Spectral Analysis 145

C Skewness and Kurtosis Analysis of the Roughness-Induced Perturbation 151

C.1 Definitions 151

C.1.1 Skewness 151

C.1.2 Kurtosis 151

C.2 Results 152

D Finite Difference Simulations 159

D.1 Purpose 160

D.2 Characterisation of the Active Surface 160

D.2.1 Types of Actuator 160

D.3 Formulation 168

D.4 Time-Marching Method 170

D.5 Discretisation 171

D.5.1 Derivative Approximations - Finite Differences 171

D.5.2 Boundary Conditions 178

D.5.3 Mesh 178

D.6 Stability Analysis 181

D.7 Code Validation 182

D.7.1 Stokes' 2nd Problem 182

D.7.2 Lid-Driven Cavity 184

D.7.3 Case Set 186

D.7.4 Results 187

E Finite Volume Simulations 195

E.1 Purpose 196

E.2 Problem Statement 196

E.3 Boundary Conditions 196

E.4 Computational Domain Dimensions 197

E.5 Spatial Grid 198

E.6 Physical Model 199

E.7 Method 199
E.8 Convergence 200
E.9 Validation 200

Nomenclature

Abbreviations

CWT	Continuous Wavelet Transform, page 120.
EAP	Electroactive Polymer, page 158.
FST	Free-Stream Turbulence, page 10.
FVS	Finite Volume Simulations, page 30.
HWA	Hot-Wire Anemometry, page 36.
LDA	Laser Doppler Anemometry, page 30.
SFV	Stream Function - Vorticity, page 166.

Greek Symbols

α	streamwise Fourier wavenumber, page 15.
β	spanwise Fourier wavenumber, page 15.
δ	general notation for the boundary layer thickness, page 4.
$\delta_1(x)$	displacement thickness, equation (1.3), page 4.
$\delta_2(x)$	momentum thickness, equation (3.6), page 71.
$\delta_{99}(x)$	boundary layer thickness as the wall-normal location where the velocity reaches a 99% of U_∞, page 4.

$\eta = y\sqrt{U_\infty/\nu x}$	self-similiarity variable in the Blasius flow for the wall-normal direction, page 4.
μ	dynamic viscosity, page 4.
ν	kinematic viscosity, page 8.
ω	angular frequency, page 9.
ϖ	angular frequency, page 15.
ρ	density, page 4.
$\tau_w = \mu \frac{\partial u}{\partial y}\big\vert_{y=0}$	wall shear stress, page 4.

Roman Symbols

$H = \frac{\delta_1}{\delta_2}$	boundary-layer shape factor, page 72.
k	roughness element height, page 36.
p	full static pressure, page 13.
p'	perturbation static pressure, page 13.
P	steady static pressure, page 13.
$R = Re_x^{1/2}$	alternative notation for Re_x, page 9.
$Re_{\delta_1} = \frac{U_\infty \delta_1(x)}{\nu}$	Reynolds number based on local δ_1, page 8.
$Re_{\delta_1}\vert_c$	critical value of Re_{δ_1} at which transition to turbulence is considered to begin, page 7.
$Re_{\delta_1}\vert_t$	Re_{δ_1} for which the boundary layer is fully turbulent, page 8.
$Re_k = \frac{u_k k}{\nu}$	roughness-based Reynolds number, page 75.
$Re_x = \frac{U_\infty x}{\nu}$	Reynolds number based on distance from the boundary layer origin, page 3.

Re_c	critical value of Re_x, page 12.
u	full streamwise velocity component, page 8.
$\vec{u'}$	perturbation velocity, page 13.
$\vec{U}$	steady velocity, page 13.
$\vec{u}$	full velocity, page 13.
U_∞	free-stream velocity, page 8.
$\langle U_\infty \rangle_z$	spanwise-averaged free-stream velocity at fixed x and y locations, page 75.
u_k	velocity at $x = x_k$ and $y = k$ in the absence of roughness element array, page 75.
v	full wall-normal velocity component, page 13.
w	full spanwise velocity component, page 13.
x	streamwise direction, page 8.
x_k	streamwise location of roughness element array, page 36.
y	wall-normal direction, page 8.
z	spanwise direction, page 13.

Chapter 1

Fundamentals of the Study

$$\frac{\partial v}{\partial z}$$

Figure 1.1: Nomenclature for the spatial variation of the wall-normal component of a velocity field with respect to its spanwise direction.

1.1 Boundary Layers

The concept of a boundary layer was introduced for the first time by Ludwig Prandtl at the third International Congress of Mathematicians at Heidelberg (Germany) in 1904, and it is commonly acknowledged that such an advancement in fluid mechanics would well deserve a Nobel prize if there was one for this scientific field. Boundary layers are regions always present when fluid flows adjacent to solid surfaces and hence they are omnipresent in the every-day world.

In boundary layers, molecular transport phenomena (mass diffusion, viscosity and thermal conduction) are as important as convective phenomena, regardless of how the "external" flow field is applied. Beyond the boundary layer, the "free-stream" region is closer in behaviour to an inviscid flow (in which molecular transport effects can be considered negligible). As pointed out by Prandtl in 1904, the importance of viscous effects arises, not because viscosity is larger in the boundary layers compared to the free-stream, but from the fact that significant changes of velocity occur in the direction normal to the surface, from being zero at the wall up to that of the free-stream at the edge of the layer. The zero relative velocity between particles of a solid surface and those fluid particles nearest to the surface is called the "no-slip" condition.

The Navier-Stokes equations are presently considered to be the best mathematical description of fluid flows and was well known by 1904. However, until the appearance of the concept of boundary layer, fluid dynamicists were unsuccessful in solving practical engineering problems by means of these equations, as mentioned by Anderson (2001) among many others. For instance, the skin friction drag around solid bodies moving in a fluid could not have been explained without employing the concept of a boundary layer. Owing to the fact that boundary layers are a key factor in a very wide range of fluid mechanics phenomena, a vast number of authors ever since 1904 have been, and are still, studying boundary layers as well as the processes that take place in them. Primarily this includes turbulence generation when the Reynolds number is sufficiently high.

1.2 Importance of Transition to Turbulence

In fluid mechanics, walls are commonly known as "turbulence generators". The reason for this is that, regardless of how smooth a wall surface is, the boundary layer always ends up becoming turbulent after a sufficient streamwise length.

1.2.1 Boundary Layer Growth and Skin Friction

When a laminar boundary layer becomes turbulent, its thickness becomes considerably larger and its "skin friction" (i.e. shear stress on the wall) is significantly greater than when laminar. Figure 1.2, adapted from Schlichting (2000), who originally adapted it from Hansen (1928), shows the dependence of the boundary layer thickness growth on Re_x for both laminar and turbulent cases, with a fictitious origin at $Re_x = 1.5 \times 10^5$ for the turbulent case. It can be clearly seen that the laminar boundary layer growth is small compared to that when turbulent. In other words, when a laminar boundary layer becomes turbulent, it rapidly expands into the free stream, through a process of entrainment.

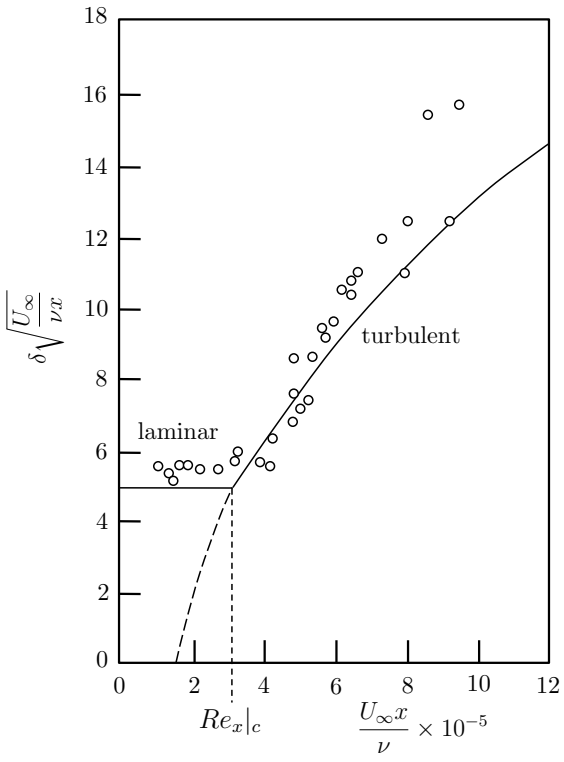


Figure 1.2: Bondary layer thickness evolution from Blasius to turbulent. Figure adapted from Schlichting (2000).

The lines represented in figure 1.2 are given, in the laminar case, by

$$\delta_{99}(x) \simeq 4.95\sqrt{\frac{\nu x}{U_\infty}}, \tag{1.1}$$

as a numerical solution of the incompressible zero streamwise-pressure-gradient boundary layer equations (also called "Blasius flow"), and in the turbulent case by

$$\frac{\delta U_\infty}{\nu} = 0.14\frac{Re_x}{\ln(Re_x)}G\left(\ln(Re_x)\right), \tag{1.2}$$

which was obtained empirically and where G is a function that weakly depends on $\ln(Re_x)$ only, as stated by Schlichting (2000). The data points in the figure are experimental data from Hansen (1928).

This analysis also shows that a relationship between a streamwise location and a boundary layer thickness value can be inferred. The displacement thickness, δ_1, defined as

$$\delta_1(x) = \int_0^\infty \left[1 - \frac{u(x,y)}{U_\infty}\right] dy, \tag{1.3}$$

is commonly used, instead of δ_{99}, since it is an integral magnitude. Regarding skin friction, figure 1.3, adapted from Dhawan (1953), shows that the skin friction coefficient, c_f, is significantly larger in the turbulent case and that this difference increases with Re_x.

The lines in figure 1.3 are given, for the laminar case, by

$$c_{f,lam} = \frac{\tau_w(x)}{\frac{\rho}{2}U_\infty^2} \tag{1.4}$$

and

$$c_{f,turb} = 2\left[\frac{\kappa}{\ln(Re_x)}G\left(\ln(Re_x)\right)\right]^2, \tag{1.5}$$

is an empirical correlation for that turbulent, where $\kappa = 0.41$ is the von Kármán constant. The symbols correspond to directly and indirectly measured data of wall shear stress.

The reason for this increase in friction is that, for a given value of Re_x, the gradient at the wall of the turbulent velocity profile is steeper than that in the laminar profile. This is shown in figure 1.4, also adapted from Dhawan (1953), using self-similiarity variables of the laminar case, that is, U_∞ and η.

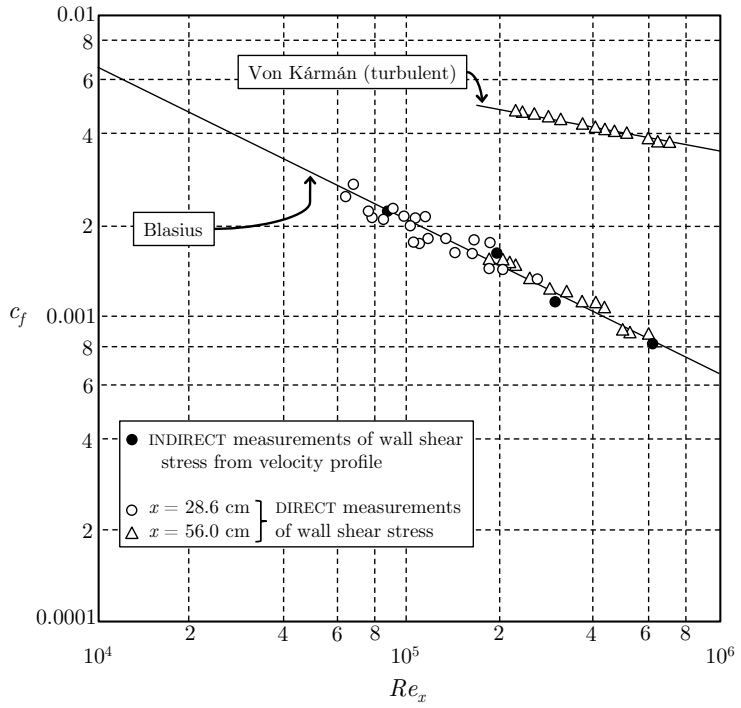


Figure 1.3: Comparison of local skin friction coefficient of both incompressible laminar and turbulent boundary layers over a flat plate at zero incidence. Figure adapted from Dhawan (1953).

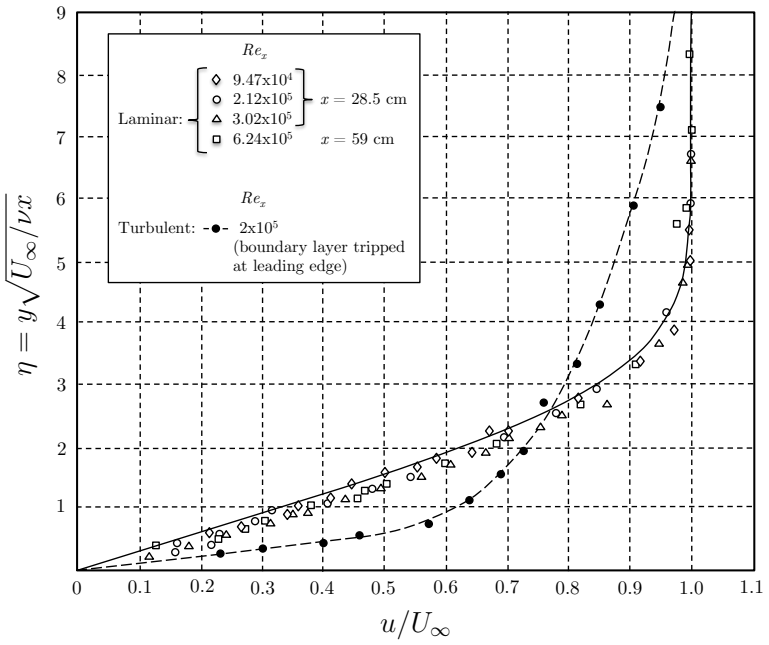


Figure 1.4: Comparison wall-normal velocity profiles of both incompressible laminar and turbulent boundary layers over a flat plate at zero incidence. Figure adapted from Dhawan (1953).

Given these facts, it is clear that determining accurately where transition to turbulence takes place, as well as understanding the mechanisms and conditions that lead to it, is of paramount importance for a very wide range of engineering applications, especially for those in which skin-friction drag reduction is desirable.

In the instance of aircraft or turbine manufacturing industries, knowing in advance where, and under what conditions, transition occurs may play an essential role in the design of both wings and blades. They can be designed, when possible, so that the trailing edge is upstream of where transition begins and therefore the boundary layer remains laminar for the entire chord. When, owing to external conditions, these ideal circumstances cannot be satisfied, control becomes very important. In this respect, flow control is a multidisciplinary field, which has been gaining importance as technology advances, focused on altering the flow in a desired way by measuring it, processing it and consequently acting on it by means of either open- or closed-loop control strategies. This is achieved by the implementation of MEMS[1] in the form of sets of sensors and actuators. As mentioned by Joslin (1998), boundary layer transition control studies have been attempted ever since the 1930s. Some examples of actuation to delay laminar-turbulent transition are suction by slots, as shown by Loftin Jr. & Burrows (1949), who tested hole slots, screen slots and wall-parallel slots on boundary layers with both favourable and unfavourable pressure gradients; or porous-surface suction, as shown for instance by Braslow & Visconti (1950) or more recently by Fransson & Alfredsson (2003); or streamwise-local, spanwise-periodic suction and blowing, as in the numerical study by Laurien & Kleiser (1988). Another approach has been the use of wall-cooling, as shown for instance by Malik (1989) in supersonic and hypersonic boundary layers. Also, by employing compliant surfaces, in the form of a flexible wall with an appropriate damping factor, transition can be delayed, as shown by Benjamin (1960) in hydrodynamic boundary layers.

1.2.2 Transition from the Linear Stability Analysis Point of View

The scenario of transition to turbulence by the appearance and growth of Tollmien-Schlichting (TS) waves has been studied for many years and is well understood. Figure 1.5, extracted and adapted from White (2003), shows a qualitative schematic of

[1] MEMS stands for Micro Electro-Mechanical Systems.

what has been experimentally observed regarding transition due to TS waves, and is described as follows:

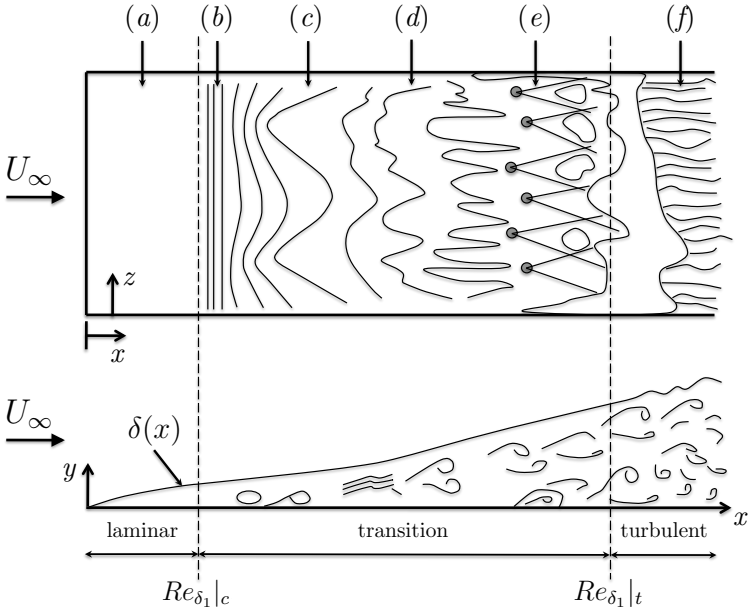


Figure 1.5: Conceptual view of the laminar-to-turbulent boundary layer transition through TS waves; figure adapted from White (2003).

(a) Upstream laminar flow;

(b) TS waves start appearing for $Re_{\delta_1} > Re_{\delta_1}|_c$;

(c) the TS waves start becoming unstable to three-dimensional perturbations leading to three-dimensional TS waves (modulated in the spanwise direction). As mentioned by Fransson & Alfredsson (2003), this occurs when the amplitude of the two-dimensional TS waves exceed approximately 1% of U_∞. In this scenario, the perturbations have grown up to a level above which linear theory is no longer valid;

(d) moving downstream, the three-dimensional TS waves increase their modulation in the spanwise direction, forming periodic vortices with shape of Λ (Klebanoff's modes) which yield to an intensification of the vorticity at the peaks of the waves, leading at those locations to intermittent turbulent bursts;

(e) these turbulent flow bursts yield downstream to turbulent spots of high velocity fluctuations;

(f) then, these spots eventually merge, and beyond the location $Re_{\delta_1}|_t \simeq 3000$ the boundary layer is fully turbulent.

With the aid of a linear stability analysis (Schlichting, 2000), it can be shown that small perturbations in the form of TS waves appear and grow up to a level, at which turbulent spots are formed and eventually coalesce to lead to a fully turbulent flow. TS waves are described, for instance by Luchini (1996), as short longitudinal-wavelength two-dimensional perturbations. The process just described is known as *transition* from a laminar to a turbulent boundary layer.

From this linear stability analysis a location for the appearance of the instabilities can be inferred in terms of Re_{δ_1}. It predicts that the Blasius flow becomes unstable and TS waves appear when $Re_{\delta_1}|_c \simeq 520$, or, in other words, when $x > \left(Re_{\delta_1}|_c/1.72\right)^2 \nu/U_\infty$.

1.2.3 Discrepancy between Linear Theory and Experiments

The estimation of $Re_{\delta_1}|_c$ by linear stability theory is, in many cases, at odds with experimental data. Over many years this discrepancy was believed to arise from the assumption of parallel flow in the linear stability theory when, in fact, the Blasius boundary layer thickness grows with x. However, a number of studies, for instance Gaster (1974) or Bertolotti *et al.* (1992), have shown this effect to be weak. As mentioned by Luchini (1996), the linear growth of TS waves can be experimentally observed only at low levels of environmental disturbance. In order to overcome the latter, a ribbon embedded in the wall and vibrating at an appropriate frequency is commonly used to artificially excite TS waves, which may grow at a different rate (Bertolotti *et al.*, 1992). Other mechanisms also exist, such as controlled free-stream sound, free-stream vorticity or distributed wall-roughness, and their interaction with the leading edge excites TS waves, as reviewed by Saric *et al.* (2002). These, alongside other experimental uncertainties, were considered as possible reasons that explain the discrepancy between theory and experiments. Another aspect that could explain this discrepancy, as pointed out by Bertolotti *et al.* (1992), could be the way in which the growth rate of TS waves is defined.

Figure 1.6, reproduced from Bertolotti *et al.* (1992), shows a comparison between numerical and experimental data of the neutral stability curve obtained from the linear stability analysis. $F = 10^6\omega\nu/U_\infty^2$, where ω is the angular frequency, and $R = Re_x^{1/2}$.

It can be seen that the experimental data imply values of $Re_{\delta_1}|_c$ which are considerably smaller than those predicted by the theory.

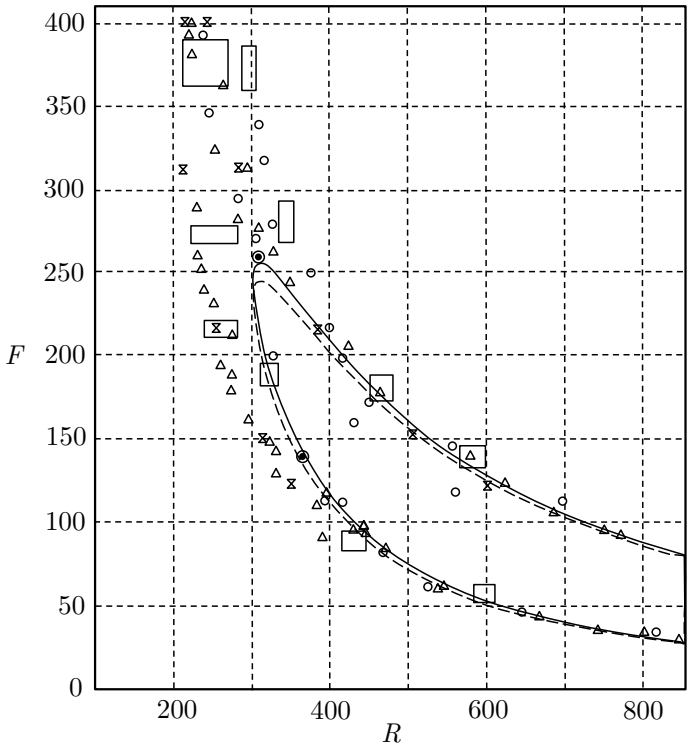


Figure 1.6: Neutral stability curve on the plane $F - R$. Comparison between numerical (lines) and experimental (symbols) data. Figure reproduced from Bertolotti *et al.* (1992).

The transition scenario described by the linear stability theory is no longer valid when boundary layers develop subject to sufficiently strong external conditions, which can play a major role in how transition occurs.

When linking the linear theory to real situations, at the very beginning it was believed that the generation of the small perturbations which lead to TS waves was simply a result of the Brownian motion of the molecules of the fluid, as mentioned by Ruban (2010). However, after many years of study, it is known that the creation of perturbations in the boundary layer actually arises as the result of the process of "receptivity", understood as the interaction between the generation of the boundary layer and the surroundings and flow singularities, like that at the flat-plate leading edge.

1.2.4 Receptivity

Morkovin (1969*a*) was the first to describe the receptivity process through which free-stream turbulence (FST) induces instabilities in laminar boundary layers (Hammerton & Kerschen, 1996). As mentioned by Saric *et al.* (2002), receptivity can be seen as the establishment of the set of initial conditions of amplitude, frequency and phase of disturbances fed by FST into the boundary layer for its subsequent breakdown to turbulence, providing the link between FST and the response of the boundary layer. In essence, receptivity focuses on the generation of instability waves, instead of their development. A key contribution to the field, seminal for the further progress in receptivity over the years, is that of Goldstein (1985). In that study, the author showed that TS waves are formed in the vicinity of the leading edge of a flat-plate due to the "impingement" of free-stream disturbances, which is something that the linear stability theory cannot predict.

When FST is not negligible, the description of transition based purely on the development of TS waves is no longer valid. In fact, apart from FST, factors such non-zero streamwise pressure gradient, Reynolds number, Mach number, acoustic radiation, surface roughness, surface temperature, surface curvature, or the history of these, can prevent linear stability theory from accurately describing the process of transition (Abu-Ghannan & Shaw, 1980). Figure 1.7 shows a conceptual view of the generally accepted paths to turbulence due to FST.

This figure is described by Saric *et al.* (2002) as follows:

- **Path *A* (classical view):**

  When weak disturbances enter the boundary layer, primary modes (TS waves) are formed according to the linear stability theory and weakly grow over a long streamwise length scale. Then, for a sufficiently large disturbance amplitude, secondary instabilities (non-linear interactions) take place and rapidly lead to a breakdown to turbulence. This path corresponds to the description illustrated in figure 1.5.

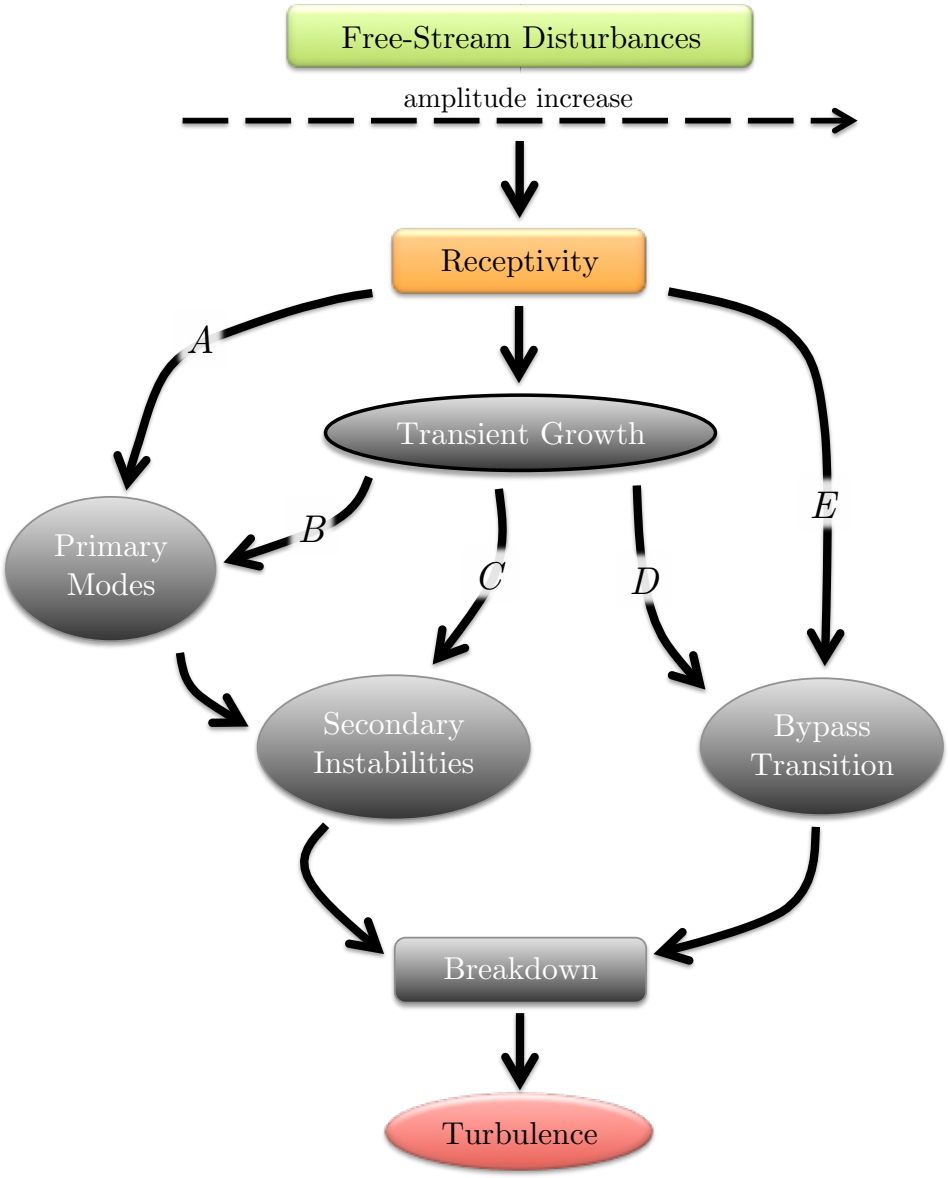


Figure 1.7: Paths from receptivity to turbulence. Figure adapted from Saric *et al.* (1999).

- **Path *B*, *C* and *D* (transient growth):**

  Historically, only either paths *A* or *E* were considered to describe the transition to turbulence. However, over the years it has been shown that intermediate paths can be found. The spectrum of transition processes between the two end paths A and E are labelled as transient growth. Bearing in mind that the linear stability theory is based on orthogonal modes of 2-D disturbances, the fundamentals of transient growth are understood as the interaction of two non-orthogonal eigenvectors of 3-D disturbances

which leads to an algebraic growth of energy and then an exponential decay, if FST is small, or if sufficiently large, to breakdown to turbulence. Depending on the initial disturbance amplitude, transient growth may either lead to spanwise modulations of 2-D disturbances (path B), or create an environment in which secondary instabilities take place (path C), or trigger "bypass" transition (path D).

- **Path *E* (transition bypass):**

  When external disturbances are very strong, transition to turbulence occurs abruptly as turbulent spots appear. Linear stability theory fails when trying to predict this process.

1.3 Non-Normality

Linear mechanisms derived from the existence of non-normal eigenmodes of the linearised Navier-Stokes equations have received much attention over the past decades. Non-normality (NN) has been postulated to be responsible not only for transition to turbulence at subcritical Reynolds numbers, as seen in experiments, but also for the existence of near-wall streaky structures in turbulent boundary layers (Kim & Lim, 2000).

Table 1.1, adapted from Henningson & Reddy (1994), shows discrepancies between critical parameters found in experiments and those predicted by the classical linear stability theory for a number of flows. It also indicates if the linearised Navier-Stokes equations applied to the evolution of a small disturbance present non-normality. For instance, in the case of a Hagen-Poiseuille flow, the classical stability theory predicts no transition whereas it can readily be found from experiments that transition occurs for $Re_c \simeq 2000$. On the other hand, the prediction for a Bénard flow (stationary flow heated from below) is remarkably accurate, as in this case the linearised Navier-Stokes operator is normal. For those flows with instabilities driven by thermal or centrifugal forces the classical stability theory matches the experiments (Trefethen *et al.*, 1993).

1.3.1 The Linearised Navier-Stokes Operator

Considering a non-dimensional velocity field $\vec{u}(\vec{x},t) = (u,v,w)$ and pressure field $p(\vec{x},t)$, with $\vec{x} = (x,y,z)$ a location in a 3-D domain Ω, the non-dimensional Navier-Stokes

Flow	$Re_c\|_{exp}$	$Re_c\|_{class}$	NN
Hagen-Poiseuille	$\simeq 2000$	∞	yes
Plane Poiseuille	$\simeq 1000$	5772	yes
Plane Couette	$\simeq 360$	∞	yes
Bénard	$Ra \simeq 1700$	Ra=1708	no

Table 1.1: Critical Reynolds (and Rayleigh for the case of Bénard flow) numbers found in experiments ($Re_c|_{exp}$) and predicted by the classical linear stability theory ($Re_c|_{class}$). The final column points out if the corresponding flow presents non-normal eigenmodes (NN). Adapted from Henningson & Reddy (1994)

equations in vector form for an incompressible flow are

$$\frac{\partial \vec{u}}{\partial t} + \vec{u} \cdot \nabla \vec{u} = -\nabla p + \frac{1}{Re} \nabla^2 \vec{u} + \vec{f}, \tag{1.6}$$

with $\nabla \cdot \vec{u} = 0$ (continuity), $\vec{u}(t=0) = \vec{u}_0$ the initial condition, $\vec{u} = \vec{u}_s$ on the boundaries $\partial\Omega$ (if Ω is unbounded, periodicity in those directions is assumed) and $\vec{f}$ the body force field per unit mass. It is also assumed that $\vec{u}_s$ does not alter Ω.

Considering perturbations $\vec{u'}(\vec{x}, t)$ and $p'(\vec{x}, t)$ around an assumed time-independent field $(\vec{U}, P)$ which may or may not be stable, such that

$$\vec{u} = \vec{U} + \vec{u'}, \tag{1.7}$$

$$p = P + p', \tag{1.8}$$

expression (1.6) can be rewritten as

$$\frac{\partial \vec{u'}}{\partial t} + \vec{u'} \cdot \nabla \vec{u'} + \vec{U} \cdot \nabla \vec{u'} + \vec{u'} \cdot \nabla \vec{U} = -\nabla p' + \frac{1}{Re} \nabla^2 \vec{u'}, \tag{1.9}$$

with $\nabla \cdot \vec{u'} = 0$, $\vec{u'}(t=0) = \vec{u'}_0$ and homogeneous boundary conditions (no-slip condition in walls).

By retaining first-order terms only, the term $\vec{u'} \cdot \nabla \vec{u'}$ can be neglected and the linearised Navier-Stokes equations for the evolution of small perturbations are obtained:

$$\boxed{\frac{\partial \vec{u'}}{\partial t} + \vec{U} \cdot \nabla \vec{u'} + \vec{u'} \cdot \nabla \vec{U} = -\nabla p' + \frac{1}{Re} \nabla^2 \vec{u'},} \tag{1.10}$$

with $\nabla \cdot \vec{u'} = 0$, $\vec{u'}(t=0) = \vec{u'}_0$ and homogeneous boundary conditions.

A further simplification regarding $\vec{U}$ can be considered. Since the flows of interest related to this study are 2-D boundary layers (e.g. Couette, plane Poiseuille and Hagen-Poiseuille flows), $\vec{U}$ can be assumed to have the form of $\vec{U} = U(y)\hat{i} + 0\hat{j} + 0\hat{k}$. In the case of growing 2-D boundary layers, $\vec{U} = U(x,y)\hat{i} + 0\hat{j} + 0\hat{k}$; but since the dependence on x is much weaker than on y, the simplification is considered valid. Applying this simplification and rewriting (1.10) in its components yields:

$$\left(\frac{\partial}{\partial t} + U\frac{\partial}{\partial x}\right)u' + \frac{dU}{dy}v' = -\frac{\partial p'}{\partial x} + \frac{1}{Re}\left(\frac{\partial^2 u'}{\partial x^2} + \frac{\partial^2 u'}{\partial y^2} + \frac{\partial^2 u'}{\partial z^2}\right), \tag{1.11a}$$

$$\left(\frac{\partial}{\partial t} + U\frac{\partial}{\partial x}\right)v' = -\frac{\partial p'}{\partial y} + \frac{1}{Re}\left(\frac{\partial^2 v'}{\partial x^2} + \frac{\partial^2 v'}{\partial y^2} + \frac{\partial^2 v'}{\partial z^2}\right), \tag{1.11b}$$

$$\left(\frac{\partial}{\partial t} + U\frac{\partial}{\partial x}\right)w' = -\frac{\partial p'}{\partial z} + \frac{1}{Re}\left(\frac{\partial^2 w'}{\partial x^2} + \frac{\partial^2 w'}{\partial y^2} + \frac{\partial^2 w'}{\partial z^2}\right), \tag{1.11c}$$

$$\frac{\partial u'}{\partial x} + \frac{\partial v'}{\partial y} + \frac{\partial w'}{\partial z} = 0. \tag{1.12}$$

In order to remove pressure as a dependent variable, the linearised Navier-Stokes operator is generally expressed in terms of the wall-normal velocity component, v', and the wall-normal vorticity component, $\omega'_y = \partial u'/\partial z - \partial w'/\partial x$. The process to reduce the system of equations (1.11a-1.11c) to two equations, with v' and ω'_y as unknowns, is as follows (Gustavsson & Hultgren, 1980). An equation for p' in terms of v' can be found by manipulating the system (1.11a-1.11c) and combining it with (1.12), that is,

$$\nabla^2 p' = -2\frac{dU}{dy}\frac{\partial v'}{\partial x}, \tag{1.13}$$

which is a linearised Poisson equation for pressure. And then, by applying ∇^2 entirely on (1.11b) and using (1.13), the final equation for v' is obtained:

$$\left(\frac{\partial}{\partial t} + U\frac{\partial}{\partial x}\right)\nabla^2 v' - \frac{d^2U}{dy^2}\frac{\partial v'}{\partial x} - \frac{1}{Re}\nabla^4 v' = 0, \tag{1.14}$$

with homogeneous boundary conditions and where $\nabla^4 \cdot = \nabla^2(\nabla^2 \cdot)$.

The vorticity equation is obtained by applying the curl operator, $\nabla \times (\cdot)$, to (1.10). For these $\vec{U} = U(y)$ flows, the wall-normal vorticity component equation reduces to

$$\left(\frac{\partial}{\partial t} + U\frac{\partial}{\partial x}\right)\omega_y' - \frac{1}{Re}\nabla^2\omega_y' = -\frac{dU}{dy}\frac{\partial v'}{\partial z}, \tag{1.15}$$

with homogenous boundary conditions for wall-bounded flows. Expressions (1.14) and (1.15) are gathered as:

$$\left[\left(\frac{\partial}{\partial t} + U\frac{\partial}{\partial x}\right)\nabla^2 - \frac{d^2U}{dy^2}\frac{\partial}{\partial x} - \frac{1}{Re}\nabla^4\right]v' = 0, \tag{1.16a}$$

$$\left[\left(\frac{\partial}{\partial t} + U\frac{\partial}{\partial x}\right) - \frac{1}{Re}\nabla^2\right]\omega_y' = -\frac{dU}{dy}\frac{\partial v'}{\partial z}. \tag{1.16b}$$

The system (1.16) is the spatial form of the Orr-Sommerfeld-Squire equations, where (1.16a) is the Orr-Sommerfeld equation and (1.16b) the Squire equation. It is important to note that, since $\partial v'/\partial z$ is isolated on the right-hand side of (1.16b), it can be interpreted as a source term. Non-zero $\partial v'/\partial z$ describes the "lift-up" phenomenon (Landahl, 1980), in which v' disturbances cause movement of fluid across the mean velocity gradient dU/dy. As a result, low-speed fluid is pumped away from the wall and high-speed fluid is moved towards the wall. This gives rise to spanwise variation in streamwise velocity, $\partial u'/\partial z$, which in turn produces wall-normal vorticity, ω_y'. In other words, as stated by Kim & Lim (2000), v' behaves as an independent variable whereas ω_y is subject to v' through $\partial v'/\partial z$.

There is a more common form of describing this problem: by means of Fourier-transformed variables. The types of flow considered here can be Fourier transformed in both streamwise and spanwise directions as well as in time, yielding a system of a number of decoupled y-continuous problems for certain Fourier wavenumber pairs (α, β) (Sharma *et al.*, 2006) and angular frequency ϖ. Thus, v' and ω_y' can be generally expressed as

$$v'(x, y, z, t) = \hat{v}'(y)e^{i(\alpha x + \beta z) + \varpi t}, \tag{1.17a}$$

$$\omega_y'(x, y, z, t) = \hat{\omega}'_y(y)e^{i(\alpha x + \beta z) + \varpi t}. \tag{1.17b}$$

Only the real parts are physically meaningful, as pointed out by Butler & Farrell (1992). Combining sets (1.16) and (1.17) yield to the following eigenproblem for $\hat{v'}$ and $\hat{\omega'}_y$:

$$\left(-i\alpha U\widehat{\nabla}^2 + i\alpha\frac{d^2U}{dy^2} + \frac{\widehat{\nabla}^2\widehat{\nabla}^2}{Re}\right)\hat{v'} = \varpi\widehat{\nabla}^2\hat{v'}, \tag{1.18a}$$

$$\left(-i\alpha U + \frac{\widehat{\nabla}^2}{Re}\right)\omega'_y - i\beta\frac{dU}{dy}\hat{v'} = \varpi\hat{\omega'}_y, \tag{1.18b}$$

where $\widehat{\nabla}^2 = \partial^2/\partial y^2 - (\alpha^2 + \beta^2)$. The equations presented in the form of (1.18) are the spectral form of the Orr-Sommerfeld-Squire equations, where (1.18a) is the classical Orr-Sommerfeld equation and thus TS waves are among its solutions (Butler & Farrell, 1992). Rewriting in matrix form system (1.18) leads to

$$\boxed{\varpi\begin{bmatrix}\hat{v'}\\ \hat{\omega'}_y\end{bmatrix} = \mathscr{L}\begin{bmatrix}\hat{v'}\\ \hat{\omega'}_y\end{bmatrix}, \tag{1.19}}$$

$$\boxed{\mathscr{L} = \begin{bmatrix}L_{OS} & 0\\ L_C & L_{SQ}\end{bmatrix}, \tag{1.20}}$$

where $\mathscr{L}$ denotes the linearised Navier-Stokes operator and its terms are:

⋆ Orr-Sommerfeld Operator: $$L_{OS} = \left(\widehat{\nabla}^2\right)^{-1}\left(-i\alpha U\widehat{\nabla}^2 + i\alpha\frac{d^2U}{dy^2} + \frac{\widehat{\nabla}^2\widehat{\nabla}^2}{Re}\right), \tag{1.21}$$

⋆ Squire Operator: $$L_{SQ} = -i\alpha U + \frac{\widehat{\nabla}^2}{Re}, \tag{1.22}$$

⋆ Coupling Operator: $$L_C = -i\beta\frac{dU}{dy}. \tag{1.23}$$

1.3.2 Implications of the Coupling Term

For 2-D disturbances, there exists no $\partial v'/\partial z$ or, in other words, $\beta = 0$, and there is no coupling between $\hat{v'}$ and $\hat{\omega'}_y$. Kim & Lim (2000) numerically studied the effect of the coupling term on the linearised Navier-Stokes operator and showed that $L_C \neq 0$ enhances the non-normality feature of $\mathscr{L}$, as a result of this operator being non-self-adjoint (namely,

$\mathscr{L}^+ \neq \mathscr{L}$, where '$^+$' denotes transpose and conjugate). The authors stated that L_{OS} is, in fact, non-self-adjoint and hence 2-D disturbances can produce a certain transient growth but, nevertheless, it was shown that the presence of $L_C \neq 0$ (3-D disturbances) leads to much larger non-normality and transient growth.

Luchini (1996) pointed out the implications of self-adjointness of an operator where the solution of a linear system of differential equations with constant coefficients comprises a sum of exponential functions (if the eigenvalues of the coefficient matrix are all different), or a sum of exponential functions multiplied by algebraic polynomials in time (if there are multiple eigenvalues), or single polynomials (if the associated eigenvalue is zero). It is also known that the higher the number of eigenvalues tending to each other, the more the behaviour of the solution tends to polynomial form. However, self-adjoint matrices do not exhibit this polynomial behaviour and hence algebraic growth cannot occur. The method of pseudospectra, as described by Trefethen *et al.* (1993), is a tool to quantify how far from self-adjointness an operator is.

Figures 1.8(a) and 1.8(b), both adapted from Kim & Lim (2000), show the time evolution of a turbulent channel flow in terms of, respectively, mean wall shear on both channel walls and streamwise vorticity iso-contours. Blue lines in figure 1.8(a) correspond to the solution with $L_C \neq 0$ on the whole domain, whereas red lines correspond to that with $L_C = 0$ in the upper half of the channel. Figure 1.8(b) shows the time evolution of streamwise vorticity contours for the case of imposing $L_C = 0$ in the upper half of the channel. It can be seen that, in the absence of L_C, there is a remarkable decrease of mean wall shear, which is consistent with the disappearance of streamwise vortices shown in figure 1.8(b). The authors argued that, even if the non-linear terms in the disturbance equations are responsible for the formation of streamwise vortices, the linear coupling term is necessary for the formation of streamwise streaks, which in turn enhance the vortices through a non-linear process. In other words, streamwise vortices, which are formed through non-linear mechanisms, cannot be sustained without the linear coupling term.

This important result has direct implications on feedback flow-control strategies for relaminarisation of turbulent flows and the delay of laminar-to-turbulent transition.

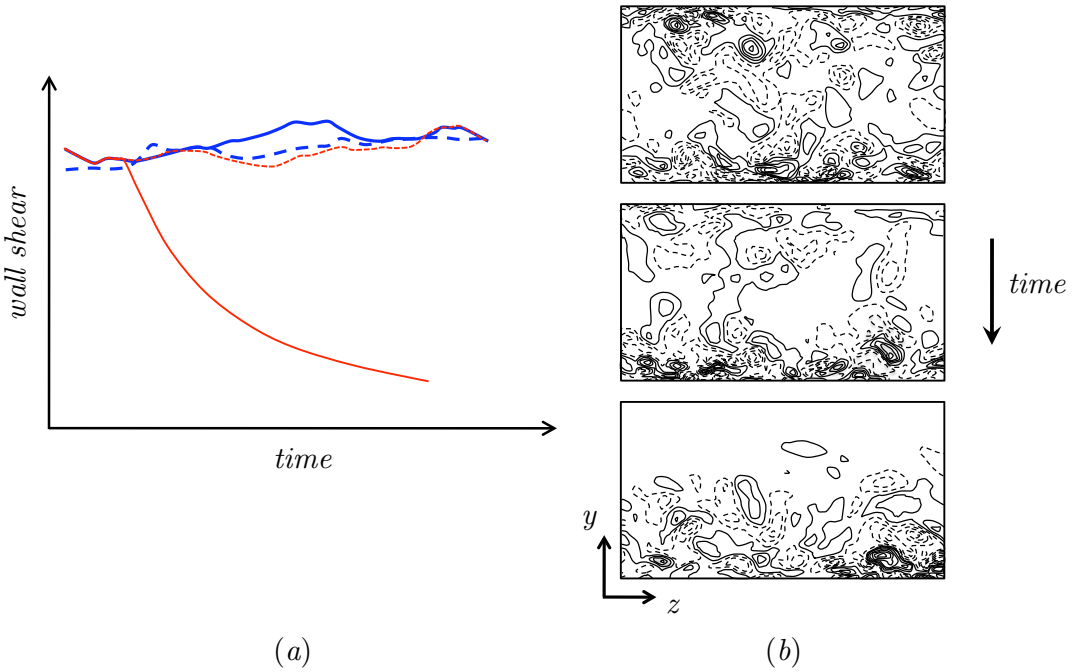


Figure 1.8: (a) Time evolution of mean wall shear in a turbulent channel flow (red lines are for $L_C = 0$ in the upper half of the channel, blue lines for $L_C \neq 0$ in the whole domain; solid lines for the upper wall, dashed lines for the lower wall). (b) Time evolution of streamwise vorticity (iso-contours) in the same turbulent channel flow solved with $L_C = 0$ only in the upper half of the channel (positive vorticity values as solid lines, negative vorticity values as dashed lines). Both illustrations adapted from Kim & Lim (2000).

1.4 Transient Growth

It has been shown that non-normality is a necessary condition for transition to turbulence of laminar boundary layers for Reynolds numbers smaller than those considered critical by the linear stability (eigenvalue) analysis (Henningson & Reddy, 1994).

Transient growth is referred to as the process in which the elemental wavenumbers of perturbations which are solutions of the linearised Navier-Stokes operator initially interact destructively, and then separate in time to reveal considerable growth in integral kinetic energy followed by a decay (Butler & Farrell, 1992). It is important to note that transient growth is dependent on both Reynolds number and initial condition. For a given magnitude of Reynolds number and strength of the incoming perturbations, growth of energy may or not occur. This is explained below.

1.4.1 Condition for Growth

The energy related to a velocity field $\vec{u'}$ is considered as

$$\mathscr{E} = \|\vec{u'}\|^2/2, \tag{1.24}$$

in which the norm $\|\cdot\|$ is chosen to be the inner vector product, that is, $\|\vec{a}\| = (\vec{a}, \vec{a})$, where

$$(\vec{a}, \vec{b}) = \int \vec{a} \cdot \vec{b}\, d\vec{x}. \tag{1.25}$$

Energy growth is considered to occur if a time $t > 0$ exists at which $\mathscr{E}(t) > \mathscr{E}(t = 0)$. The Reynolds number threshold for which energy growth may take place can be estimated using the Reynolds-Orr equation (Henningson & Reddy, 1994). This equation is obtained by applying the dot product between $\vec{u'}$ and expression (1.10) and then integrating with respect to $\vec{x} \in \Omega$, that is,

$$\frac{d\mathscr{E}}{dt} = -\int_{\vec{x}\in\Omega} \vec{u'} \cdot \mathcal{D}\vec{u'}\, d\vec{x} - \frac{1}{Re}\int \left(\nabla\vec{u'}\right) : \left(\nabla\vec{u'}\right)\, d\vec{x}, \tag{1.26}$$

where, adopting the summation convention,

$$\left(\mathcal{D}\vec{u'}\right)_i = \frac{(U_{i,j} + U_{j,i})}{2} u'_j, \tag{1.27}$$

$$\left(\nabla\vec{u'}\right) : \left(\nabla\vec{u'}\right) = u'_{i,j} u'_{i,j}. \tag{1.28}$$

The first term of the right-hand side of expression (1.26) provides a measure of the exchange of energy between the base flow $\vec{U}$ and the disturbance $\vec{u'}$, whereas the second term, which is always negative, is related to the dissipation of energy (Henningson & Reddy, 1994). Note that expression (1.26) is valid for any sort of base flow and hence not constrained to $\vec{U} = U(x, y)\hat{i} + 0\hat{j} + 0\hat{k}$ (simplification applied when deriving the form of the linearised Navier-Stokes operator for wall-bounded flows). For a parallel-shear flow, $\vec{U} = U(y)\hat{i} + 0\hat{j} + 0\hat{k}$, expression (1.26) becomes

$$\frac{d\mathscr{E}}{dt} = -\int_{\vec{x}\in\Omega} \left(\frac{dU}{dy} u'v' + \frac{1}{Re}\mathcal{D}\vec{u'}\right). \tag{1.29}$$

If $d\mathscr{E}/dt \leqslant 0$ for all initial perturbations then there is no energy growth. The largest value of Reynolds number, noted as Re_g, below which growth cannot occur is obtained for the limit $d\mathscr{E}/dt = 0$ of expression (1.26), that is,

$$\frac{1}{Re_g} = \sup_{\vec{u'}} \frac{-\int \vec{u'} \cdot \mathcal{D}\vec{u'}\, d\vec{x}}{\int \left(\nabla\vec{u'}\right) : \left(\nabla\vec{u'}\right)\, d\vec{x}}, \tag{1.30}$$

where "sup" indicates supremum. Therefore, transition is not possible if $Re < Re_g$. Henningson & Reddy (1994) demonstrated that there is no energy growth if $Re < Re_c$ and $Re_g = Re_c$ if $\mathscr{L}$ is normal. In other words, $Re_g < Re_c$ when $\mathscr{L}$ is non-normal.

1.4.2 Nature of Growth

The importance of 3-D perturbations in viscous parallel flows was already identified by Squire (1933). Later on, some further studies on the instability of 3-D perturbations in plane parallel flows appeared, like those of Watson (1960) or Michael (1961). However, it was not until the late 1970s when the nature of growth of 3-D disturbances was analysed in detail. For instance, Gustavsson (1978) studied the growth of initial 3-D disturbances in parallel inviscid flow, and Ellingsen & Palm (1975) demonstrated linear growth in time of initial 3-D disturbances of infinitesimal amplitude and independent of the streamwise direction. But the study which has served as the main reference for many following investigations on the fundamental aspects of transient growth of 3-D disturbances is that of Landahl (1980).

The main finding of Landahl (1980) was that the perturbation kinetic energy of a broad range of localised initial 3-D perturbations in inviscid shear flows grows linearly with time.[2] The starting point of this study was the inviscid limit of the set of expressions (1.11) and the author concluded that, besides the linear growth of perturbation energy, the streamwise extent of the disturbed region also grows linearly, but with the streamwise disturbance velocity remaining bounded as time increases. Landahl claimed that these results hold regardless whether the flow is stable or not to exponential growth of wavelike disturbances. That is, any 3-D disturbance with $v \neq 0$ in a shear parallel inviscid flow exhibits linear growth of kinetic energy. Another important result was that the author had already predicted that 3-D disturbances in shear flows evolve into a distribution of long streamwise streaks of alternating momentum excess and defect, such that, the larger dU/dy is, the stronger this distribution is. To conclude, the author pointed out that the inviscid analysis carried out is valid only for a finite interval of time inversely proportional to the magnitude of the initial perturbation, as viscous effects become important for large times. In fact, he proposed that, for the inviscid analysis to be valid, a time limit is given

[2]This result was achieved for the inviscid limit and in a initial value problem framework, nevertheless further studies revealed similar results for viscous shear flows and from a spatial point of view.

by $l^2/[\nu(dU/dy)^2]$ in the case of a purely convected disturbance (with $v = 0$), where l is a characteristic length of the flow.

If the studies herein mentioned so far regarding non-normality and transient growth (Landahl, 1980; Butler & Farrell, 1992; Trefethen *et al.*, 1993; Henningson & Reddy, 1994; Kim & Lim, 2000) approached the topic within a temporal framework, Luchini (1996) was the first to treat transient growth from a spatial point of view, that is, instead of applying a disturbance at a certain initial time throughout spatial domain and letting it evolve in time, the disturbance is applied at an upstream location for all times and let evolve downstream. Hence the process was seen as an algebraic growth in space rather than in time, and is therefore directly relevant to experiments. Another important contribution of this research is that Luchini (1996) mathematically demonstrated that transient growth can take place regardless of the Reynolds number of the base flow. The reason for it is that the process is governed by Prandtl's standard boundary-layer equations independent of Reynolds number (e.g. Blasius similarity).

Another important feature is that, while in the aforementioned set of works the base flow was considered parallel (essentially, Coutte and Poiseuille flows), Luchini (1996) studied a growing non-parallel boundary layer. He also pointed out that, if for parallel flows the algebraic growth is eventually overcome by exponential viscous decay, in the case of non-parallel base flows the viscous decay is also algebraic and insufficient to prevent the algebraic growth. However, other studies (both numerical and experimental) have shown that whether or not a viscous decay follows the transient growth depends on the amplitude (strength) of the initial/upstream disturbances.

In fact, temporal studies like those of Breuer & Haritonidis (1990) and Breuer & Landahl (1990) focused in particular on the influence of the strength of localised initial disturbances and their subsequent evolution. The main idea was to investigate whether the growth was followed by a viscous decay or triggered secondary instabilities. Breuer & Haritonidis (1990) dealt with a weak 3-D disturbance (a peak-to-peak amplitude of the streamwise component of 0.8% U_∞ at the first measuring station), and showed that viscosity was able to dissipate the transient growth. They identified the transient with the process of formation of a shear layer which is tilted and stretched by the influence of the mean shear as it is convected downtream. The authors observed that

the disturbance, besides its transient (non-normal) portion, also consisted of a residue of unstable Orr-Sommerfeld modes forming a linear dispersive wake packet of considerably lower amplitude than the transient with coherence in the wall-normal direction. Thus a slowly growing wave packet remained after the transient stage. However, despite the good qualitative agreement between inviscid calculations and the experiments in the transient stage, they suggested care in interpreting the process. This is because the vertical vorticity modes are indeed damped and the transient starts its decay as soon as the generation of vertical vorticity finishes. When the Reynolds number of the base flow or the strength of the incoming disturbance is sufficiently high however, the transient growth may be sufficiently intense so that viscosity cannot counteract it. In this situation, the transient itself becomes unstable to secondary instabilities and strong non-linear effects appear, leading to the breakdown of the disturbance and the formation of turbulent spots. This is the scenario studied by Breuer & Landahl (1990) and termed "bypass transition" (Morkovin, 1969*b*).

Breuer & Landahl (1990) dealt with moderately strong 3-D disturbances. For instance, at the first measuring station, where Breuer & Haritonidis (1990) reported an amplitude of the u'-component of 0.8% U_∞, Breuer & Landahl (1990) reported an amplitude of the order of 5% U_∞. The amplitude reached levels of the order of 80% U_∞ at the same station where Breuer & Haritonidis (1990) found that all that remained was a wave packet. Furthermore, the authors observed that, far from decaying, the transient growth eventually formed turbulent spots due to strong non-linear effects. They identified these non-linear effects as mainly two phenomena: the formation of streamwise streaks and the growth of secondary instabilities on the perturbed mean flow. Figure 1.9, adapted from their publication, shows in the left-hand column the time evolution of iso-contours of the v-component on the XZ-plane at $y/\delta_1 = 1.05$, and in the right-hand column contours of the 2-D power spectra corresponding to that velocity component at the same times. From that figure the two non-linearities can be seen:

- **Formation of a cascade of streamwise streaks**. At $tU_\infty/\delta_1 = 43$, the spectrum shows a single peak corresponding to the initial perturbation. The initial streak stretches and splits into successive smaller streaks with sharper spanwise gradients with increasing time. This can also be seen in the evolution of the power spectra, where a cascade of new streaks is noted by the appearance of harmonics. At

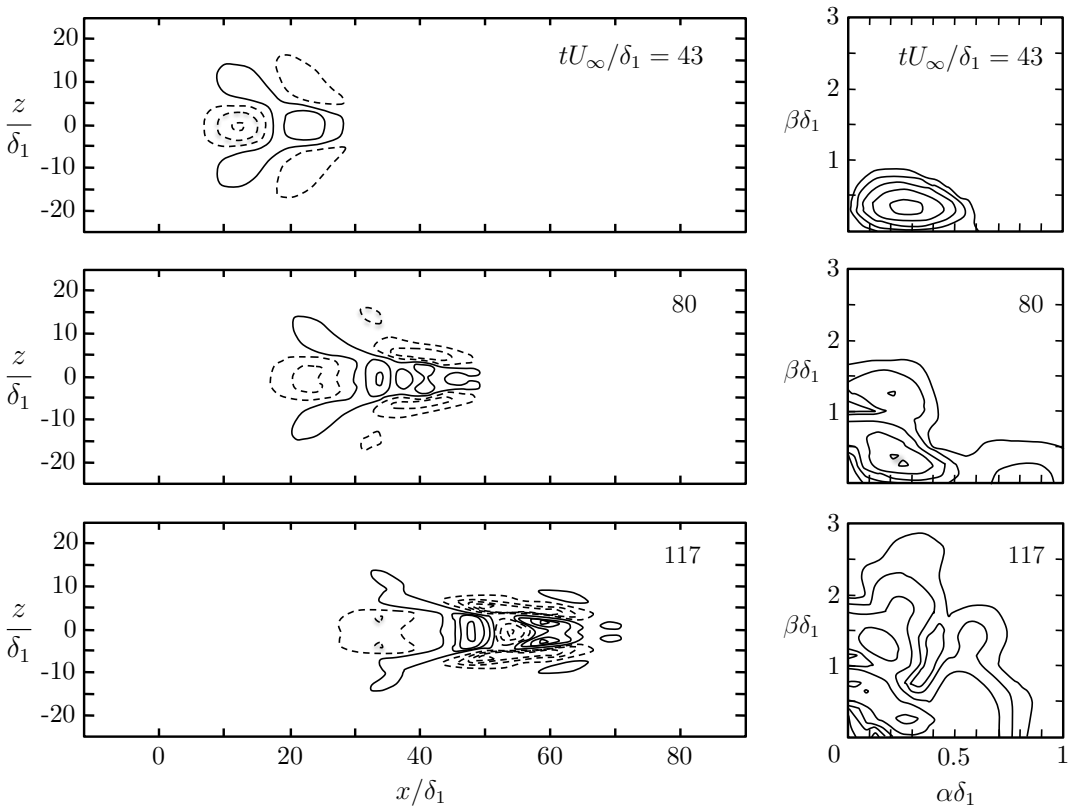


Figure 1.9: Time evolution of the v component in the XZ-plane at $y/\delta_1 = 1.05$. Left hand-side column: iso-contours (spacing $0.002U_\infty$). Right hand-side: 2-D power spatial spectra (contour spacing on an arbitrary logarithmic scale). Figure adapted from Breuer & Landahl (1990).

$tU_\infty/\delta_1 = 80$ a new peak has emerged at about $(\alpha\delta_1 = 0.2, \beta\delta_1 = 1.3)$, due to the two oblique strips of downwash motion on either side of the centre-line as shown in the v iso-contour frame. At $tU_\infty/\delta_1 = 117$ a new oblique structure seems to be emerging at about $(0.2, 2.5)$, which can also be seen in the corresponding v iso-contour plot (at $x/\delta_1 \simeq 70$, $z/\delta_1 \simeq \pm 3.5$), in which the main streak is being divided in two smaller ones with sharper spanwise gradients and hence a higher value of β. The authors did not present plots for $tU_\infty/\delta_1 = 136$ but they claimed that at this time the power spectrum shows peaks at $(0, 0.7)$, $(0.1, 1.3)$ and $(0.2, 2.0)$. They suggested that the non-linearity leads to the introduction of higher harmonics with increasing time, so that each peak serves as a platform for the formation of new peaks of smaller spanwise scale. They then observed that, at later times, the distinct peaks emerged and hypothesised that the spectrum would eventually become continuous and the perturbation would have then transformed into a turbulent spot.

- **Secondary instability growth**. The wave packet which accompanies the 3-D disturbance grows on the back of the disturbed mean profile, stretches in the streamwise direction along with the main structure and also shows the appearance and development of successive smaller instabilities (peaks in the spectra). This also can be seen in figure 1.9. At $tU_\infty/\delta_1 = 43$ the wave packet is not apparent, but at $tU_\infty/\delta_1 = 80$ it can be seen, both in the spectrum and in the v iso-contours, that it starts to emerge at a higher value of α than that of the main structure and at $\beta = 0$ (a 2-D disturbance). With increasing time, the streamwise wavenumbers of the whole disturbance decrease, indicating that it is elongated in the x direction and, by $U_\infty/\delta_1 = 117$, it is clear that the maxima of the wave packet are displaced off the centre-line of the structure (thus $\beta \neq 0$). Also at $tU_\infty/\delta_1 = 117$, a harmonic from the wave packet is emerging at $(\alpha\delta_1 = 0.2, \beta\delta_1 = 1.3)$ and the authors claimed that by $U_\infty/\delta_1 = 136$ a third peak appears at $(0.5, 2)$.

It can be concluded that the non-linear evolution of both the 3-D disturbance and the 2-D wave packet seem to follow the same fashion −the successive appearance of structures at smaller spanwise wavenumbers− and the authors hypothesised that the reason for it is that both evolutions are governed by the same non-linear mechanism.

1.4.3 Optimal Perturbation

An area of transient non-modal growth studies has been focused on optimal perturbations. An "optimal" perturbation is understood, within the context of transient growth, as that which provides maximum energy growth for a given Reynolds number.

Farrell (1988) analysed two aspects associated with the Orr-Sommerfeld equation. One is the optimal excitation of a single wavenumber as an exponential instability. The other is the size of the initial perturbation which provides the maximum energy growth, where no particular wavenumber, but the entire perturbation as a whole, is excited. The author claimed that, owing to the energetic interaction of non-orthogonal modes and the mean flow, much larger transients were found compared to those associated with exponential instabilities. Although the analysis was conducted on finite-amplitude 2-D disturbances in both plane Poiseuille and plane Couette flow, the author acknowledged that 3-D secondary instabilities lead to the sudden growth of transients that dominate the development of the disturbances over the first few hundreds of periods of advection. However, the author

did not present the topology of the disturbances which produced these rapid transient growths.

The theoretical study of Butler & Farrell (1992) provided a step forward in this respect, as they conducted an optimal perturbation analysis this time from the 3-D linearised Navier-Stokes perturbation equations, (1.10). Not only did they apply it to Poiseuille and Couette flows, but also to the Blasius boundary layer. For all the flows that the authors identified, the perturbation which led to the largest energy growth was in the form of streamwise vortices, which rearranged the flow in elongated streamwise streaks (with $\alpha \simeq 0$ after few hundreds time scales). They attributed the formation of the vortices to the lift-up mechanism, although they claimed "vortex-tilting" to be a more accurate term, as the spanwise vorticity of the mean flow ($-dU/dy$) is tilted into the wall-normal direction by the perturbation strain rate $\partial v'/\partial z$, leading to wall-normal vorticity. They furthermore claimed a second mechanism to be also responsible for energy growth: the perturbation Reynolds stress, $\overline{u'v'}$ (where the overbar denotes average over the streamwise direction). The inviscid version of (1.26),

$$\frac{d\mathscr{E}}{dt} = -\frac{1}{2}\int \frac{dU}{dy}\overline{u'v'}dy, \tag{1.31}$$

indicates that, for $d\mathscr{E}/dt > 0$, a disturbance must extract energy from the base flow through the mean shear and the perturbation Reynolds stress. That disturbance produces a larger and more rapid energy growth than that governed solely by streamwise vortices (due to the additional $\overline{u'v'}$ effect), but also decays faster. They also demonstrated that, unlike the streamwise velocity component, the streamwise vorticity related to the vortices can only decay. Besides, it was found that the spanwise scale of the optimal disturbances is of the order of the width of the shear layer. For the specific case of Blasius flow, they found that the global (in the sense of supremum) optimal presented a spanwise wavenumber $\beta = 0.65$ when non-dimensionalised by δ_1 (or $\beta = 0.38$ when normalised by δ).

The optimisation algorithm of Butler & Farrell (1992) was based on finding the wavenumber pair (α, β) that maximised the energy (expressed in variational form) associated with perturbations which satisfy the linearised Navier-Stokes equations. Andersson *et al.* (1999) and Luchini (2000), in turn, approached the optimisation of the perturbed Blasius flow from a "transfer-function" point of view. This involves setting

up $\vec{u}_{out} = M\vec{u}_{in}$, where the output velocity vector $\vec{u}_{out}$ at a certain x-location is the result of acting on the input velocity vector $\vec{u}_{in}$ at an upstream x-location through the linear transfer function M (derived from the linearised Navier-Stokes operator). In transfer-function terms, the optimisation implied maximising the gain of M. Although both studies share a similar approach, they are not identical. In both cases the x-location of $\vec{u}_{in}$ was at the leading edge of the flat plate and the x-location of $\vec{u}_{out}$ was fixed arbitrarily. The main differences are upon how the perturbation energy was formulated. In Andersson *et al.* (1999) the perturbations were considered stationary ($\varpi = 0$), the expression of the perturbation energy expression was formulated with the three velocity components and the variable parameters were the Reynolds number (based on the distance between the leading edge and the x-location of $\vec{u}_{out}$) and β for the upstream perturbation. In the case of Luchini (2000) on the other hand, the perturbation energy expression was formulated in terms of the streamwise velocity component only, the problem was stated as Reynolds-independent (i.e. the $Re \to \infty$ limit), and the variable parameters were β and ϖ (hence unsteady perturbations). Andersson *et al.* (1999) found that for $Re \geqslant 10^5$, the input perturbation that maximised the output energy was obtained for $\beta = 0.45$, in agreement with Luchini (2000). Luchini (2000), in turn, found that the maximum energy gain was produced when $\varpi = 0$. Therefore, according to those studies, it can be concluded that the maximisation of energy growth is given by steady perturbations, with an input spanwise wavenumber of 0.45 for sufficiently large Reynolds numbers, in the form of spanwise-periodic streamwise vortices that evolve into streamwise velocity streaks of alternating sign. The discrepancy in the value of β with respect to that found by Butler & Farrell (1992) may perhaps lie in the optimisation algorithm and in the fact that Butler & Farrell (1992) studied a parallel boundary layer. In the case of the two more recent studies it was a spatially developing boundary layer.

Both Andersson *et al.* (1999) and Luchini (2000) used, for comparison and validation, the experimental results from Westin *et al.* (1994), who generated streamwise streaks in a laminar boundary layer subject to nearly isotropic FST produced by a grid placed upstream of the flat-plate model. Curiously, Westin *et al.* (1994) never referred to the disturbances created in the boundary layer as optimal ones, and in fact, they rather focused on the influence of the level of prescribed FST on the (streaky) structure of the boundary layer and the onset of transition. Moreover, the spanwise wavenumber in Westin

et al. (1994) was $\beta \simeq 0.55$, instead of the theoretical value of 0.45.

In fact, discrepancies between optimal-perturbation theory and experiments in spatially growing boundary layers have been consistent over the years. White (2002) found in his small-amplitude perturbation ($\sim 2.5\%\ U_\infty$) experiments that, although experiments and theory qualitatively matched in terms of general behaviour, significant discrepancies regarding both the energy growth extent and the location of the maxima in the wall-normal profiles of the perturbation were present (overpredicted by the theory). He pointed out that, although the discrepancies did not generally invalidate the transient growth theory, realistic stationary disturbances exhibited a considerable departure from the optimal and hence more work is required for correct prediction of receptivity to practical perturbations.

In the light of the results of White (2002), Fransson *et al.* (2004) conducted large-amplitude perturbation ($\sim 12\%\ U_\infty$) experiments in order to, first, investigate if the non-optimal behaviour for small-amplitude perturbations first detected by White (2002) also held for large-amplitude ones, and second, determine what the main factors for non-optimal experimental perturbations were. A good understanding of those factors could thus lead to feasible practical production of experimental perturbations and, in turn, non-optmimal perturbations could be recreated numerically. However, they warned about the following aspect related to β that makes the comparison between experimental and theoretical perturbations difficult. When generating perturbations by discrete roughness elements (as do the majority of experiments), the spanwise wavenumber of the perturbations is defined as $\beta = 2\pi\delta/\Delta z$, with Δz the spanwise spacing between roughness elements. However, Δz does not necessarily correspond to the fundamental wavenumber of the perturbation, as in the case of White (2002). This, together with the fact that optimal-perturbation theory considers the perturbation formed by one single β, adds to the uncertainty in the comparison of experimental and theoretical results based on β. Their results showed the same discrepancies between experiments and optimal-perturbation theory as those for small-amplitude perturbations of White (2002). Moreover, by comparing the experimental results and numerical simulations conducted with the same code of Andersson *et al.* (1999), they concluded that the main factor that explains those discrepancies is the wall-normal position of the fundamental streamwise vortices that induce the streaks. In the case of experiments, the vortices are embedded in the boundary layer, inducing streaks that grow at a lower rate, attain a lower energy peak

and decay faster (and from a further upstream location) than the predicted theoretical optimal perturbation. Conversely, in the case of the optimal-perturbation theory, the vortices are located further away from the wall, producing streaks that grow over a longer distance and attaining a larger amplitude.

Despite the fact that it is not strictly the type of flow considered in the present study, it is interesting to note the agreement between, on one side, experiments and numerical simulations of perturbations induced in a constant-thickness boundary layer, and, on the other side, optimal-perturbation theory. For instance, the spatially formulated numerical study by Tumin & Reshotko (2001) showed agreement between the optimal disturbance formed by a continuous spectrum of decaying eigenmodes and a TS wave. The experiments with FST over an asymptotic-suction boundary layer of Fransson & Alfredsson (2003) showed good agreement provided that the level of FST was sufficiently high to trigger streamwise streaks in the boundary layer. More recently, Kurian & Fransson (2011), in their experiments on transient growth triggered by a spanwise array of discrete roughness elements in an asymptotic-suction boundary layer, claimed that the optimal-perturbation theory can predict the experimental results for all those modes exhibiting transient growth.

1.4.4 Experimental Generation of Steady Streaks

There are various ways of creating steady and quasi-steady streamwise streaks in laminar boundary layers. One approach is by free-stream perturbations, either sound sources (speakers for instance) or turbulence vorticity generated by a grid upstream of the model (Klebanoff, 1971) where disturbances enter the boundary layer through receptivity mechanisms (Saric *et al.*, 2002). Another means of introducing disturbances from outside the boundary layer is by locating vortex generators above the boundary layer, as done by Tani & Komoda (1962). The vortex generators had the form of small wings and by changing their angle of attack they tuned the circulation of the vortices, which entered the boundary layer and induced steady streamwise streaks. A different approach involves disturbances from inside the boundary layer. In this respect, streamwise streaks can be produced by distributed surface roughness, as in the study by Reshotko (1984). Periodic blowing and suction through the wall, (Kachanov & Tararykin, 1987) among others, is another possible technique. Others include a spherical roughness element (Klebanoff *et al.*, 1955), or a cylindrical roughness element (Tani *et al.*, 1962), or a shallow bump (Gaster

et al., 1994). However, the use of spanwise arrays of discrete roughness elements, in studies of transient growth focused on optimal perturbations, have tended to be used ever since the establishment of the optimal perturbation theory: White (2002) and White & Ergin (2003), Fransson *et al.* (2004) and Fransson *et al.* (2005), Ergin *et al.* (2005), or more recently Lavoie *et al.* (2008), Hanson *et al.* (2010) and Kurian & Fransson (2011), are some of the experimental studies.

Experiments with FST or distributed surface roughness offer situations closer to real-life applications than those experiments involving spanwise arrays of discrete roughness elements. However, the potential of roughness elements lies in the fact that, as pointed out by Reshotko (2001), optimal perturbations can be achieved only if their features are part of the perturbation triggered upstream. Therefore, since all the parameters of roughness element arrays (streamwise location of the array, spacing between roughness elements, and their size) are easily tuneable, it is easier to generate optimal perturbations with roughness element arrays than with FST or distributed surface roughness. Besides, discrete roughness elements trigger perturbations formed by a range of discrete wavenumbers (in the form of damped harmonics), whereas FST or distributed surface roughness provide a wide and continuous spectrum of modes (Kurian & Fransson, 2011). In addition, roughness arrays produce stationary disturbances, which are predicted by optimal perturbation theory as ideal, whereas FST and distributed surface roughness produce disturbances of low frequency, as shown for instance by Westin *et al.* (1994) or Matsubara & Alfredsson (2001). Another practical advantage is that, unlike FST or distributed surface roughness, roughness arrays provide disturbance origins without ambiguity (White, 2002). For all these reasons, disturbances generated by spanwise arrays of roughness elements are unequivocally identified and parameterized. Hence these disturbances can be seen as deterministic processes, unlike those generated by either FST or distributed surface roughness, which are stochastic processes (personal communication with Prof. William S. Saric).

1.5 Contribution of the Present Study

Although theoretical and numerical studies have reported data on the wall-normal and spanwise velocity components, experiments providing measurements of those are minimal or absent in the literature (despite the crucial importance of $\partial v'/\partial z$ being the forcing

term in the non-normal transient growth mechanism). Fransson (2001) reported some measurements of v' by Laser Doppler Anemometry (LDA), but the performance of the LDA probe in terms of spatial resolution was worse than that of a typical single hot wire.

In the present study, a transient growth problem in a zero pressure-streamwise-gradient laminar boundary layer over a flat plate is set up in a wind tunnel. The disturbances are triggered by a spanwise array of cylindrical roughness elements located downstream from the leading edge of the plate. The parameters established for the roughness element array (spacing between elements, diameter and height) are set so that β is near 0.45 at the streamwise location of the array. LDA measurements of both u' and v' are taken simultaneously with a probe whose spatial-resolution performance is better than most single hot-wire probes. Traverses are conducted is such a manner that fine-resolution information of u' and v' in both y and z directions for various x-stations is obtained. Consequently, well-resolved maps of $\partial v'/\partial z$ are derived. The x-stations cover both wake and u'-energy growth regions.

Finite Volume Simulations (FVS) of the same case conducted in the experiments are performed with a commercial package to provide first insights of the flow that help design the structure of the experiments. FVS and LDA results are subsequently compared.

Additionally, since this project is conceived in a flow control research group, a code to carry out 2-D time-marching numerical simulations is developed with the purpose of developing actuators and open-loop control strategies to suppress $\partial v'/\partial z$ that may help devise closed-loop control strategies.

Chapter 2

Experiments

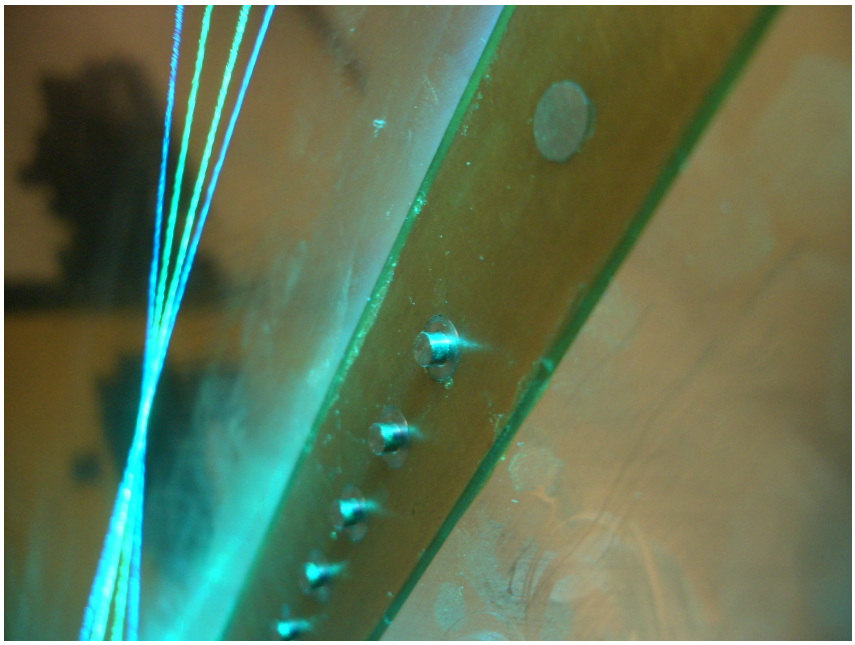


Figure 2.1: LDA beams in the proximity of the roughness element array.

2.1 Experimental Setup and Techniques

All experiments were carried out in the same wind tunnel with a cast aluminium flat-plate used as the test model. Hot-Wire Anemometry (HWA) and Laser Doppler Anemometry (LDA) were used as the main velocimetry techniques.

2.1.1 Wind Tunnel

The experiments were performed in a $3' \times 3'$ (0.91 m $\times$ 0.91 m) cross-section low-speed, closed-loop wind tunnel (top speed $\sim$ 46 m/s), with a 5.5 m long removable test section. Figures 2.2(a) and 2.2(b) show two views of the facility. This wind tunnel in particular, located in the Department of Aeronautics at Imperial College London, was chosen due to its low free-stream turbulence intensity level (with a measured value of $\sim$ 0.05%, see subsection 2.2.1).



(a) (b)

Figure 2.2: $3' \times 3'$ wind tunnel at the Department of Aeronautics of Imperial College London; (a) top view, (b) side view.

As can be seen from figure 2.2(b), the test section has lateral optical access via Perspex® windows with lockgates. The roof consists of a piecewise set of wooden panels. The test section has a built-in 3-D traverse system for hot-wire anemometry measurements, which slides on rails along the roof. The gap left between the wooden panels to locate the traverse is covered by a thin aluminium sheet attached to the traverse frame, and which therefore also slides in the streamwise direction. This sheet has a slot that allows the arm, to which the hot-wire probe is attached, to move in the spanwise

direction. Figures 2.3(a) and 2.3(b) show the traverse arrangement.



(a) (b)

Figure 2.3: 3-D traverse system for hot-wire anemometry in the $3' \times 3'$ wind tunnel; (a) top view, (b) view from inside the tunnel, where the sliding roof can be seen.

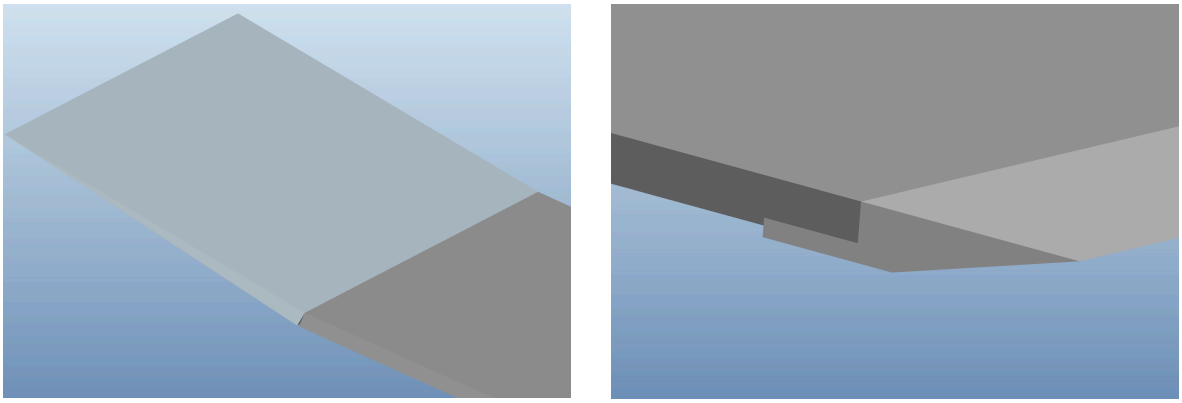
For LDA experiments, several wooden panels of the ceiling were replaced with a 4-mm thick pane of glass for optical access from the top, and the built-in traverse system was moved to the downstream end of the test section.

2.1.2 Flat-Plate and Roughness Element Array

Flat-Plate

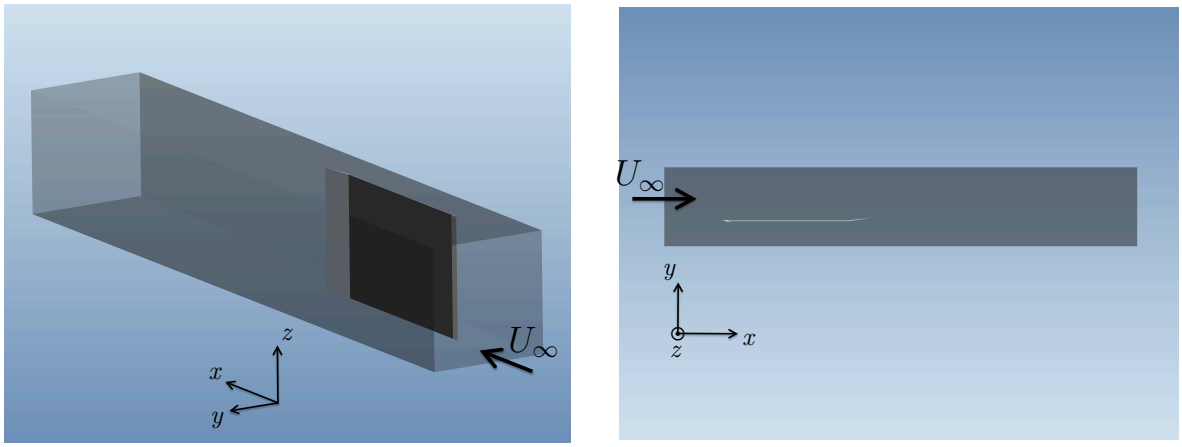
The test plate is fabricated from cast aluminium flat-plate to ensure high flatness and smoothness of the surface. It is the same as used by Lavoie *et al.* (2008) in previous experiments in the same wind tunnel. The plate is 1537 mm long in the streamwise direction, 901 mm wide and 10 mm thick. A sharp leading edge is attached to the model to the upstream edge of the plate. To control the location of the stagnation point, a flap, 500 mm long and with the same span as that of the cast aluminium plate, was attached by means of hinges to the downstream edge of the plate. Besides the stagnation point control, a further aim in using the flap is to achieve an approximately zero streamwise pressure gradient by manipulating the circulation around the plate, as pointed by Tropea *et al.* (2007). The combination of a sharp leading edge and a trailing-edge flap for laminar-to-turbulent boundary layer transition experiments was proven to be successful by the experiments of Lavoie *et al.* (2008) and older studies as that of Klebanoff *et al.* (1962). Figures 2.4(a) and 2.4(b) show, respectively, a detail of the flap and of the leading

edge from a Computer-Aided Design (CAD) model of the assembly.



(a) (b)

Figure 2.4: Views of a CAD simplified model of the flat-plate assembly; (a) detail of the flap, (b) detail of the leading edge.



(a) (b)

Figure 2.5: Full views of a CAD simplified model of the flat-plate assembly placed in the test section of the wind tunnel; (a) isometric view, (b) top view.

The location of the model is the same as that set by Lavoie *et al.* (2008), see figures 2.5(a) and 2.5(b), showing the model with its leading edge at 755 mm downstream from the end of the contraction and at 240 mm from its nearest side-wall. The lateral location of the model is chosen with the aim of achieving minimum influence from induced secondary flows, in the form of corner vortices created by the contraction. To avoid secondary flows, Tropea *et al.* (2007) recommend that the model should not be placed on an axis of symmetry or at locations $1/N$ unit span, with N being a positive integer. In this study, the

location of the model corresponded approximately to 26% span, which is slightly outside the range between 38% and 45% that Tropea *et al.* (2007) state as a good election in most cases. Furthermore, they claim that secondary flows are significant for wind tunnels with contraction ratios greater than 6:1, and in the present study the contraction ratio is 9:1. Despite the possible existence of effects due to secondary flows, improvements in the location of the model in order to minimise these effects were not carried out. This was because replicating the experimental set-up of Lavoie *et al.* (2008) was a premise to enable comparisons between their hot-wire anemometry data and the laser Doppler anemometry ones of the present study.

As shown in figures 2.5(a) and 2.5(b), the model was placed vertically, to avoid any possible curvature of the surface due to the own weight of the plate, and to minimise possible buoyant convection effects from hot wires. To hold the model vertically, a pair of square brackets was used, attached to both the back side of the model and the appropriate wall. Figures 2.6(a) and 2.6(b) show, respectively, the measurement side of the model and its back side.



(a) (b)

Figure 2.6: Model in the wind tunnel; (a) view of the measurement side, (b) view of the back side showing support brackets.

Roughness Element Array

A spanwise slot was cut in the plate once the base-flow characterisation experiments had been performed. An array of 20 spanwise-aligned roughness elements was placed in the slot, figure 2.7. The roughness elements are cylinders, with their axes normal to the plate, with the following dimensions:

- height, $k = 1.5$ mm
- diameter, $d = 2.5$ mm
- spacing, $\Delta z = 10$ mm

These values were fixed throughout the study.

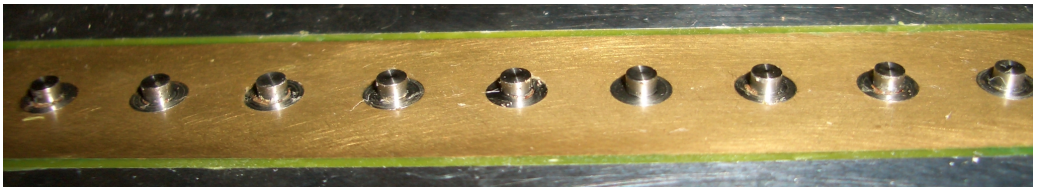


Figure 2.7: Roughness element array.

The optimum location of the roughness element array was determined by trial and error once the base-flow characterisation had been completed. On the one hand, the location should be close enough to the leading edge for there to be sufficient streamwise extent for the perturbation to develop before the onset of natural transition due to Tollmien-Schlichting waves. On the other hand, the boundary layer had to be thick enough so that manufacturing roughness elements of height k equal to a half of the local boundary layer thickness was practically feasible. The roughness element array was placed at $x_k = 200$ mm downstream from the leading edge of the model. The spanwise location of the array was equidistant from the edges of the model.

2.1.3 Hot-Wire Anemometry

Single-component velocity measurements were conducted by Hot-Wire Anemometry (HWA). Basic descriptions of this technique and its fundamentals can be found on Bruun (1996). This technique was employed only to characterise the base flow, i.e. the streamwise development of the laminar boundary layer on the flat-plate. The reason for using HWA was its superior frequency response. Although this feature was not crucial for the laminar boundary layer characterisation, its ease of set-up and use, plus its low cost compared to other techniques make HWA the ideal technique.

The hot wires were always operated in Constant-Temperature Anemometry (CTA) mode because of its ease of use and a similar signal-to-noise ratio to that of the other

mode of operation (Constant-Current), as noted by Bruun (1996). In CTA mode, the anemometer maintains the temperature of the probe virtually constant (and therefore its resistance) by adjusting the current driven through it. The corresponding voltage is then transformed into velocity readings by means of an appropriate calibration.

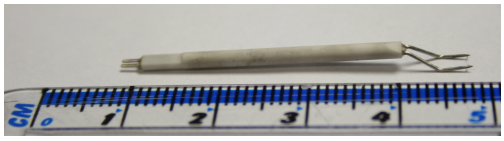
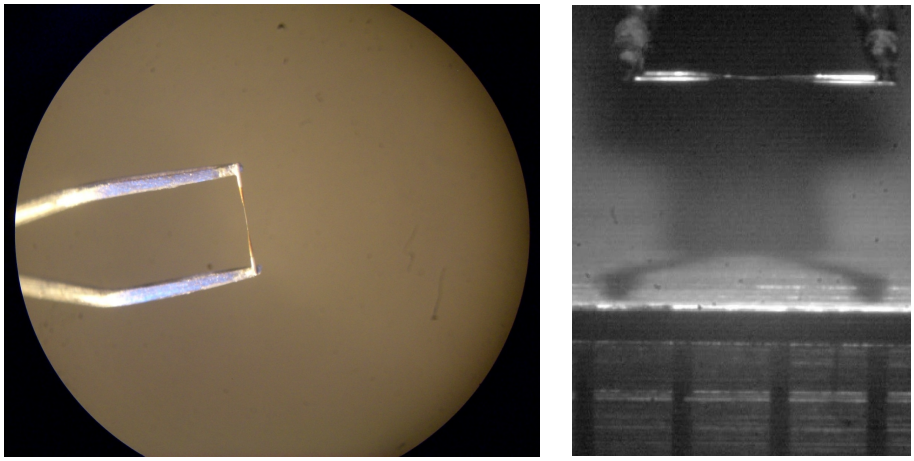


Figure 2.8: Boundary-layer hot-wire probe from AUSPEX.

A boundary-layer probe from AUSPEX was used (figure 2.8). This type of probe permits access very close to the wall without the need of having to incline the probe significantly, so minimising any wake that might affect the readings. The probe was orientated so that its axis was aligned normal to the streamwise direction, resulting in streamwise velocity-component readings. The Wollaston wire (Platinum 10% Rhodium alloy) was of 5-μm diameter (with a silver coating approximately 150-μm thick) and 8.86 Ω/mm of resistivity when etched, from the firm SIGMUND COHN Corp. The length of the etched wire was 1 mm, as recommended by Bruun (1996). The etching process was always performed in-house. Figures 2.9(a) and 2.9(b) show a hot-wire probe through a microscope and a CCD camera, respectively.



(a) (b)

Figure 2.9: Details of a hot-wire probe; (a) view through a microscope, (b) view through a CCD camera (the vertical black lines are 1-mm separation marks of a ruler).

A list of the essential equipment used to conduct the HWA experiments is presented as follows:

- boundary-layer single hot-wire probe, from AUSPEX
- CTA assembly, from TSI Instruments Inc.; power supply module: model 1051-2, variable decade probe-resistance module: model 1056, constant temperature anemometer module: model 1053B
- amplifier and filter unit, built in-house by Dr. D. Birch; internal report reference 06/001,
- traverse system and traverse controller, built in-house, connected to the computer by a serial port
- micromanometer, model FCO510, from FURNESS CONTROLS Limited
- Data Acqusition (DAQ) card, model NI 6229-USB, from NATIONAL INSTRUMENTS
- computer and MATLAB© as control, acquistion and data processing software
- BNC cables for the connections between the anemometer, the amplifier+filter and the DAQ card
- RS232 cable to digitally connect the micromanometer with the computer.

Figure 2.10 shows a schematic of the equipment set-up. Arrows represent connections as well as data-transfer direction. The arrow bifurcation between the anemometer and the amplifier+filter unit indicates the a.c. coupling used for the DAQ card, as will be explained in detail later in section 2.2.

The free-stream velocity in the tunnel was set by a closed-loop feedback PID control algorithm. The way in setting the desired free-stream velocity was by first inputting a voltage which was known to provide a velocity near the set-point and once the readings from the Pitot tube were within a prescribed range ($\pm 2\%$) the PID algorithm was then activated. The tolerance range to consider convergence of the controller was set at $\pm 0.15\%$ of the set-point.

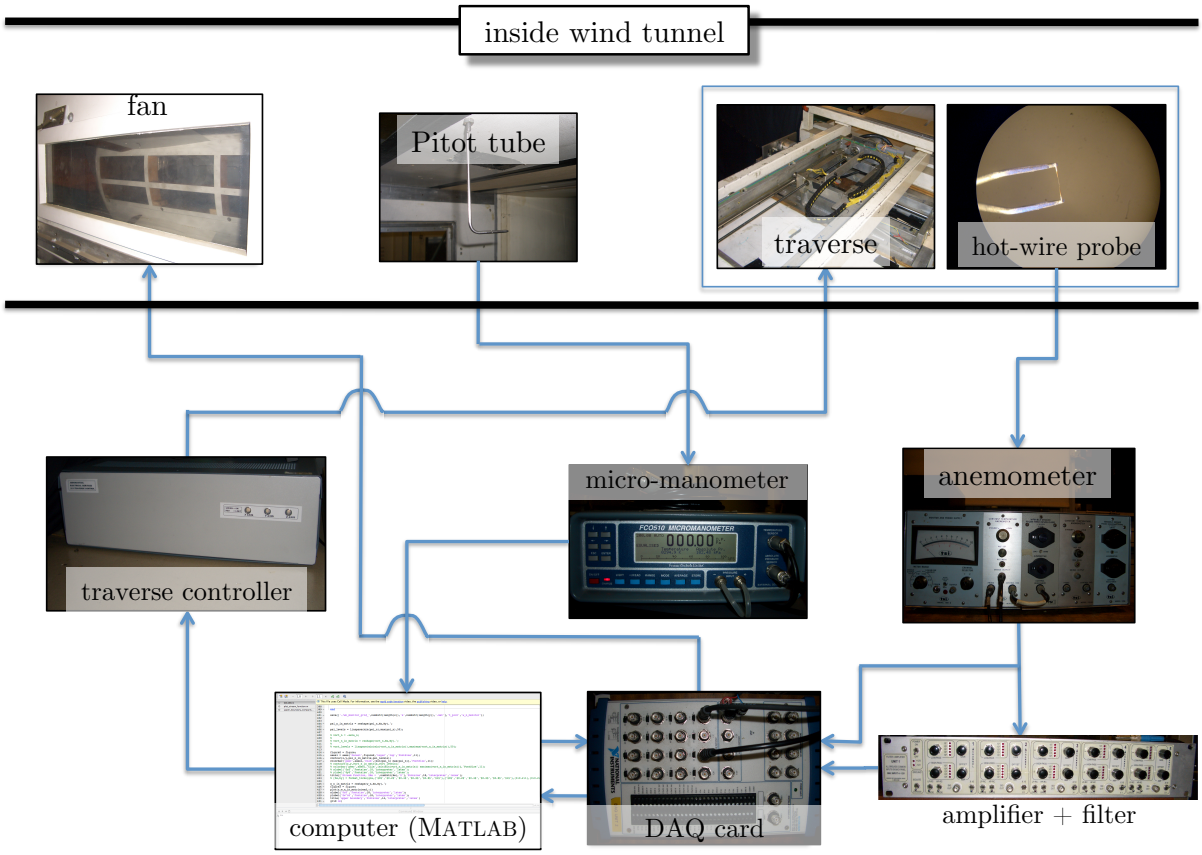


Figure 2.10: Schematic of the HWA rig.

2.1.4 Laser Doppler Anemometry

Simultaneous two-component velocity measurements were conducted by LDA. A brief description of this technique can be found in Appendix A. The reason for conducting LDA instead of HWA for multiple-component velocity measurements is the improved spatial resolution in the wall-normal direction offered by LDA. In the case of HWA, X-probes (two-component velocity measurement probes) are required. These can achieve a spatial resolution only as good as $\sim$160 μm, but leading to issues like thermal-wake interference, prong-wake problems or aerodynamic-disturbance effects, as noted on Bruun (1996). On the other hand, it is possible to achieve probe-volumes of $\sim$50 μm in the wall-normal direction in the case of LDA without significant problems.

It may be argued that HWA could be performed using an arrangement of two single probes, one straight and the other slanted, placed in the same plane parallel to the flat plate. This way the spatial resolution in the wall-normal direction would be as good as that for one-component HWA. For two reasons this option was discarded. First, the complexity of HWA increases in several aspects: the calibration process becomes more laborious; spatial correlation between the data from the two probes is needed and, since the velocity vector angle relative to the slanted wire changes with location in the boundary layer, a suitable rotary mechanism should be attached to the traverse system in order to maximise sensitivity to both velocity components. Lastly the centre of the sensing-length of the probe at the same spatial location has to be maintained introducing an extra error due to the wire co-location. In contrast, 2-D LDA systems record data at one location through two channels simultaneously, thus no spatial correlation is needed. Besides, no voltage-to-velocity calibration is required.

HWA and LDA can be nevertheless seen as complementary techniques. HWA offers good temporal resolution allowing reliable frequency-domain analyses but poor spatial resolution. On the other hand, LDA provides good spatial resolution allowing wavenumber-domain analyses but poor temporal resolution. Efforts have been made by the main LDA equipment manufacturers to incorporate frequency-domain analysis tools in their signal processors. However, they have not been considered in this study because they are mainly based on resampling at a constant data rate conducted at a post-processing stage. Since LDA fundamentally relies on random particle detection occurrence, the technique cannot reliably provide frequency-domain information.

There were also good reasons for choosing 2-component LDA when three components were available. First, there is a significant increase in difficulty of overlapping all the probe-volumes. Second, in order to mount the second probe for the third velocity component, an attachment to the existing traverse system would need to be built and coupled, as shown in figure 2.11. And third, an additional transparent section would be required in the plate to allow the third-component beams to go through it. To avoid the arrangement shown in figure 2.11(b), a 5-beam probe as shown in figure 2.12 could have been used, offering as much simplicity as the arrangement shown in figure 2.11(a), although the difficulty to overlap all the probe volumes is still considerably higher than in the case of 2-component LDA. However, given that a fully functional system to set up

the arrangement of figure 2.11(a) was available, investing in a 5-beam probe would have meant such an effort that it was discarded.

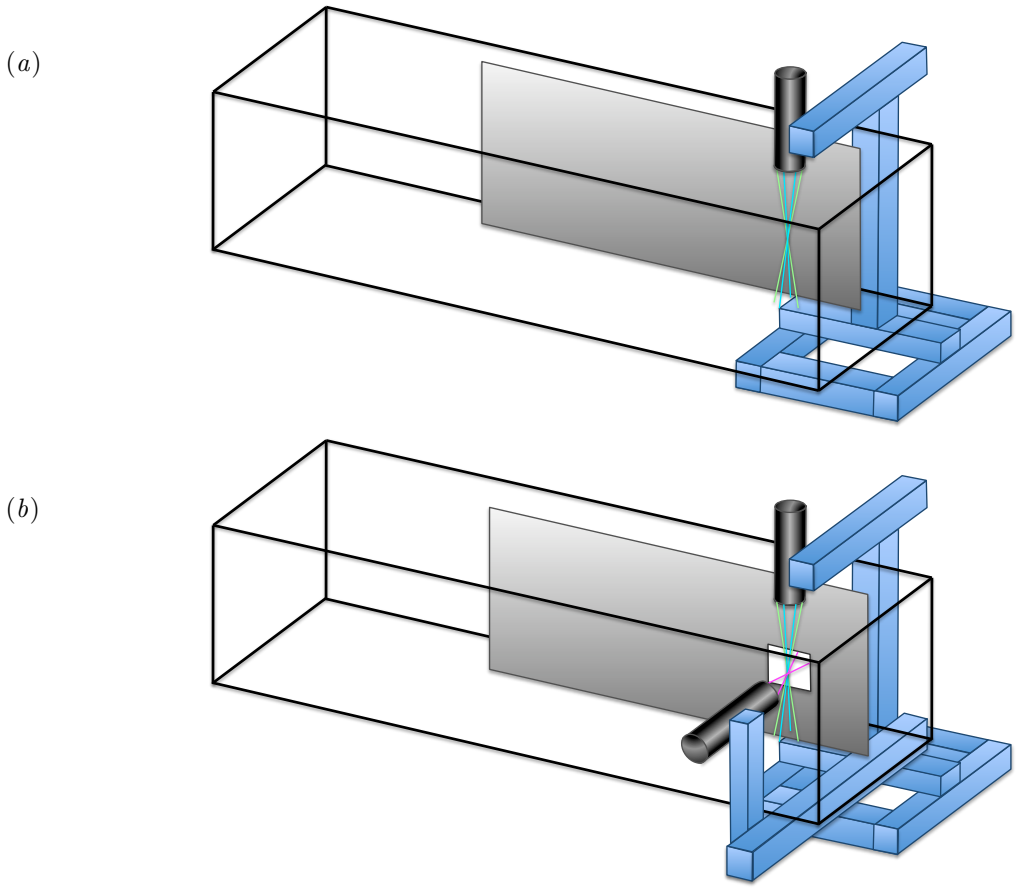


Figure 2.11: Considered LDA arrangements; (a) 2-D measurements (employed), (b) 3-D measurements (discarded).

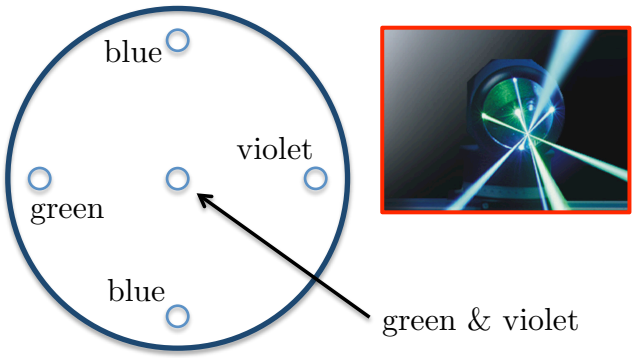


Figure 2.12: Front view of a three-component 5-beam probe (sub-picture courtesy of DANTEC Systems).

Traverse and Probe Alignments

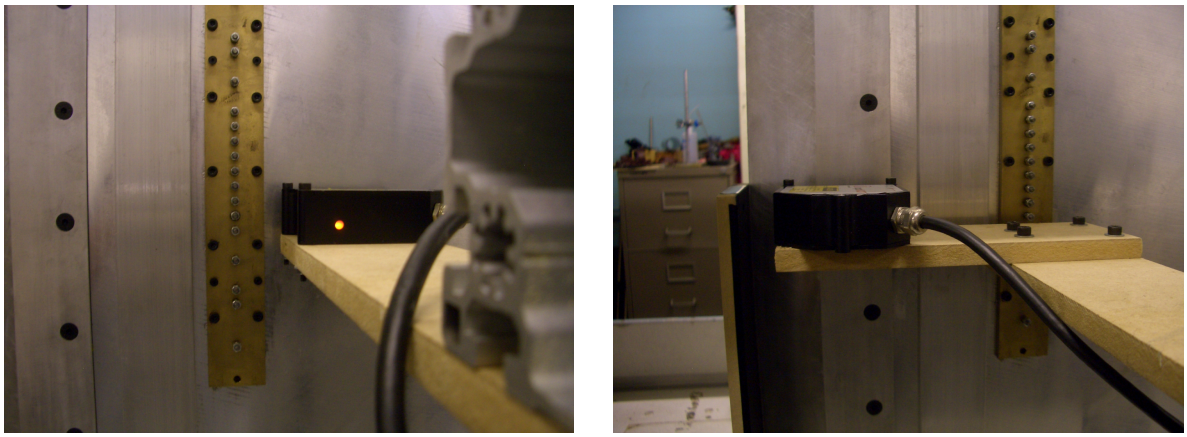
Figure 2.13 shows the traverse system, from the firm ISEL, with which the LDA experiments were conducted. A proper alignment of the traverse with respect to the flat plate had to be carried out in order to ensure that the probe could be moved as required. To do so, a MICRO-OPTRONIC, model optoNCTD2200, laser distance meter was used.



Figure 2.13: Traverse system from the firm ISEL employed to move the probe in the LDA experiments.

The laser distance meter was attached to a wooden platform and mounted on the traverse, as shown in figures 2.14(a) and 2.14(b). Three types of scans were conducted to acquire the three alignment angles (α,β,γ) between the flat-plate coordinate system and the traverse coordinate system. With the arrangement shown in figure 2.14(a), the traverse was moved along the x-direction for the laser distance meter to make measurements in the y-direction (the XY alignment). It was then moved in the z-direction for the meter to make measurements in the y-direction (the YZ alignment). With the arrangement shown in figure 2.14(b), the traverse was moved along the z-direction for the laser distance meter

to make measurements in the x-direction (the XZ alignment).



(a) (b)

Figure 2.14: Laser distance meter attached to a wooden platform mounted on the traverse system and pointing at the back side of the flat-plate; (a) to acquire the XY and YZ alignments, (b) to acquire the XZ alignment.

Figure 2.15 shows the nomenclature followed for the two coordinate systems: (x,y,z) for the flat-plate, (x*,y*,z*) for the traverse and (α,β,γ) for the alignment angles that correlate both coordinate systems, which are defined as (see figure 2.16):

$$\alpha = \tan^{-1}\left(\frac{y^*}{x^*}\right), \tag{2.1}$$

$$\beta = \tan^{-1}\left(\frac{y^*}{z^*}\right), \tag{2.2}$$

$$\gamma = \tan^{-1}\left(\frac{x^*}{z^*}\right). \tag{2.3}$$

In practice, α is obtained from the measured separation in y^* between the laser head and the flat plate when traversing in x^* but not in z^*; β is obtained from the measured separation in y^* between laser head and flat plate when traversing in z^* but not in x^*; and γ is obtained from the measured separation in x^* between laser head and flat plate when traversing in z^* but not in y^*.

The origin of both coordinate systems was arbitrarily set to be the same location when the experiments were carried out, by means of positioning a pinhole through which the LDA probe-volume was made to fit. To avoid accumulation of possible traverse system errors, the coordinate system origin was reset before the start of every run.

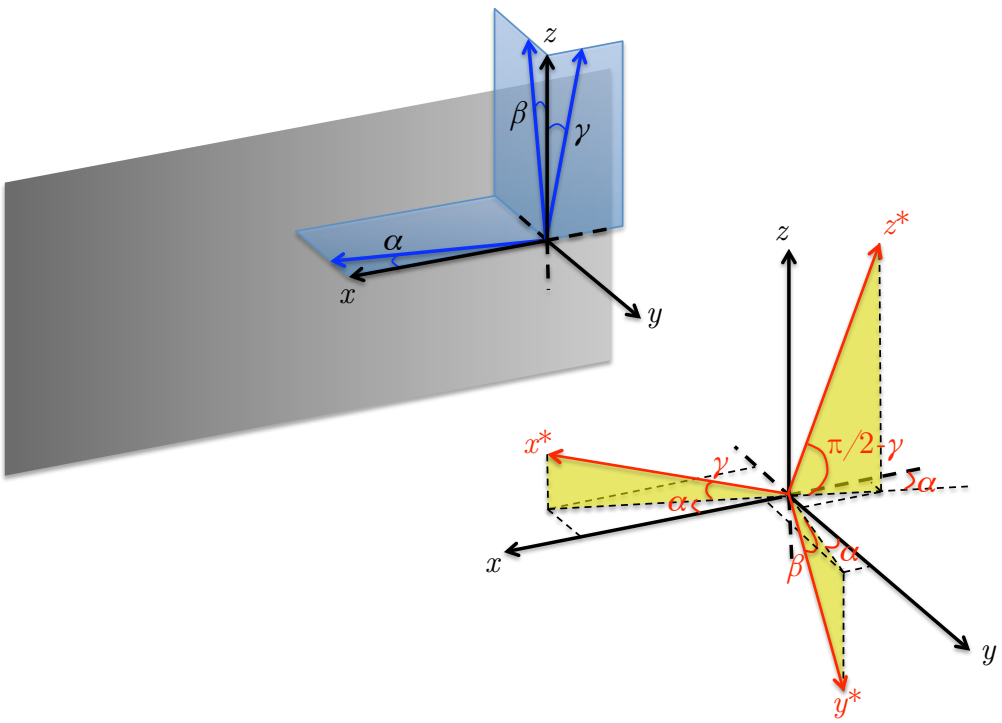


Figure 2.15: Flat-plate (plain notation) and traverse ("*" notation) coordinate systems.

Then, a transformation is needed to convert the position data $\vec{x}$ referred to the flat-plate traverse system into the traverse coordinate system. This is defined as follows:

$$\begin{bmatrix} \vec{x^*} \end{bmatrix}_{\text{traverse}} = P \begin{bmatrix} \vec{x} \end{bmatrix}_{\text{flat-plate}}$$

where $P = M^T$, given by:

$$M = \begin{bmatrix} \cos\gamma\cos\alpha & -\cos\gamma\sin\alpha & \sin\gamma \\ \cos\beta\sin\alpha & \cos\beta\cos\alpha & -\sin\beta \\ -\sin\gamma\cos\alpha & \sin\gamma\sin\alpha & \cos\gamma \end{bmatrix}.$$

An iterative process was used to readjust and wedge the base of the traverse until no more improvement (reduction in the alignment angles) from the laser readings was achievable. The scans (three runs per direction of motion of the traverse) corresponding to the last readjusting/wedging iteration are shown in figure 2.16.

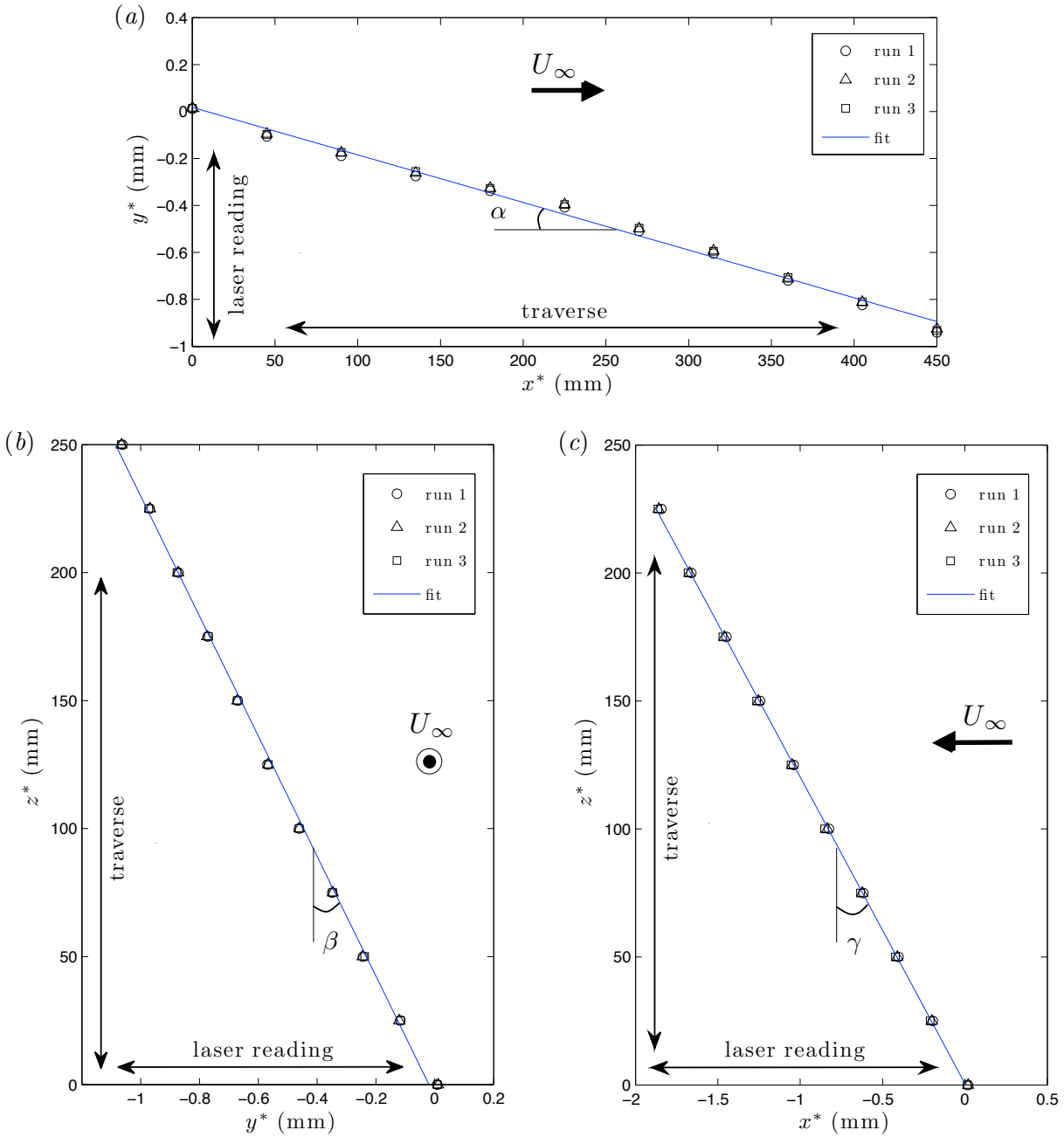


Figure 2.16: Laser distance meter scans (three runs per scan with a linear fit) to determine the alignments; (*a*) XY, (*b*) YZ, (*c*) XZ.

The alignment gradients were obtained from the linear fits and were:

- $XY = 2$ μm/mm; or $\alpha = 0.12°$
- $YZ = 4.3$ μm/mm; or $\beta = 0.24°$
- $XZ = 8.4$ μm/mm; or $\gamma = -0.48°$.

Once the relationship between traverse and flat-plate coordinate systems was determined, the next step was to align the probe.

Since both the wall-normal and spanwise velocity components are considerably smaller than the streamwise component in the boundary layer downstream of the roughness element array, it is necessary to apply a frequency shift on the signal with lower Doppler frequency to obtain an acceptable reading of the velocity. This is explained for a two-component case as follows.

With the transit time, Δt, that a particle, with velocity $\vec{v_o} = (v_x, v_y)$, takes to pass through the probe-volume, the number of cycles of the Doppler signals corresponding to v_x and v_y (or, in other words, the number of fringes crossed in each direction) are:

$$N_x = f_x \Delta t = \frac{v_x}{s_{f_x}} \Delta t, \tag{2.4}$$

$$N_y = f_y \Delta t = \frac{v_y}{s_{f_y}} \Delta t, \tag{2.5}$$

where f_x and f_y are the Doppler frequencies, and s_{f_x} and s_{f_y} the fringe spacings, in x and y, respectively (figure 2.17).

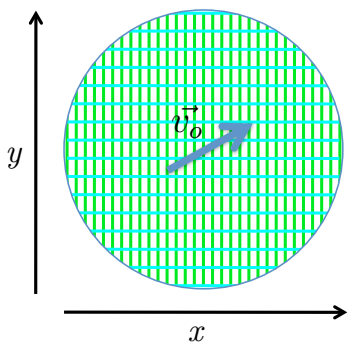


Figure 2.17: Simplification of a 2-D probe-volume.

The signal processor first provides an approximate frequency of the burst and the starting and ending points of it (TSI, 2001). This information is then used to pick the central 256 samples of the 8-bit digitised burst which is then re-sampled at an optimum rate. An optimum rate is considered at least 10-20 samples per cycle over 10-15 cycles around the centre of the burst. A higher number of cycles (in other words, number of fringes crossed) does not really improve the accuracy of the estimation of the velocity, but a lower number of cycles certainly hinders the resolution. Therefore, it can be seen that, the higher the number of fringes that a particle goes through the better, in terms of ensuring a well resolved measurement.

For example, if v_x is a times larger than v_y, thus, assuming $s_{f_x} \sim s_{f_y}$, $N_y \simeq N_x/a$. Therefore, the greater a is, the less accurate the estimation of v_y is. It is ideal to have $N_x \sim N_y$ and to do so, a frequency shift f_s is introduced as:

$$\frac{v_x}{s_{f_x}} = f_x \sim f'_y = \left(f_s + \frac{v_y}{s_{f_y}} \right). \tag{2.6}$$

In terms of resolution, f_s makes the resolution of v_y poorer. If, say, $f_s = kf_y$, the net input to the signal processor is $f'_y = f_s + f_y = (k+1)f_y$. Provided that the resolution of the signal processor is δ (percent of reading), the resolution on acquiring f_y is $(k+1)\delta$, which is worse than δ.

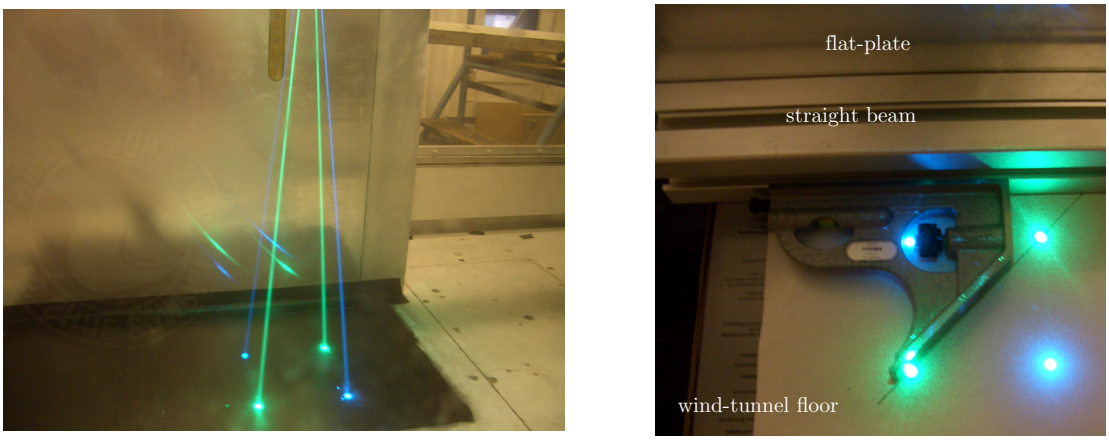
However, an alternative way was employed in this study to achieve $N_x \sim N_y$ without introducing a frequency shift that implies an accuracy penalty. Having initially one channel perfectly aligned with one direction and the other channel with the other direction, the probe was then rotated by 45° with respect to its axis (the third direction). With this configuration, readings of particles crossing a similar number of fringes in both directions were achieved and, therefore, the measurements from both channels had similar resolution.

On the other hand, frequency shifting has to be inevitably introduced when negative velocities are to be measured. In principle, since negative frequencies do not have a physical meaning and LDA offers velocity measurements from Doppler frequency readings, negative velocities cannot be obtained. However, if a shift in the reference frequency (taking a reference frequency as 0 Hz = 0 m/s) is applied, readings of frequency greater than f_s will mean positive velocities, and values lower than f_s will correspond to negative ones. Then, to retrieve the actual Doppler frequency, from which its related particle velocity is

derived, a "downmixing" technique is applied.

Downmixing is a processing technique to reduce the frequency of a signal. To do this, a mixing frequency f_{mix} is introduced and its choice is crucial in terms of data accuracy. Depending on its value, the retrieved Doppler frequencies will be referred to a certain frequency range and the accuracy of the readings will depend on the amplitude of this range. Since this range cannot be exactly known beforehand (because it will depend on the type of flow studied), it has to be set by trial and error.

In this study, having initially the green channel aligned with the streamwise direction and the blue with the wall-normal, the probe was rotated 45° with respect to its own axis. Figure 2.18(a) shows the two pairs of beams impinging on the floor of the wind tunnel once the probe was rotated 45° and figure 2.18(b) shows the accuracy of the 45° rotation.



(a) (b)

Figure 2.18: LDA probe rotated 45° with respect to the free-stream; (a) the two pairs of beams impinging on the wind-tunnel floor, (b) top view of the 45°-check of the two pair of beams.

To retrieve the streamwise and wall-normal velocity components it is enough to locate the probe at a location in the free-stream where there is no v-component and the value that both channels measure is used as a reference value to apply back to the 45° transformation.

A further rotation was needed: in this case with respect to the streamwise direction, in order to be able to take measurements very close to the flat plate. With the probe axis aligned with the spanwise direction, performing measurements at a distance closer to the

wall than $l = L\sin(\theta/2)$ is not feasible, owing to the fact that the beams closer to the flat plate impinge on it before forming the probe volume, figure 2.19(a).

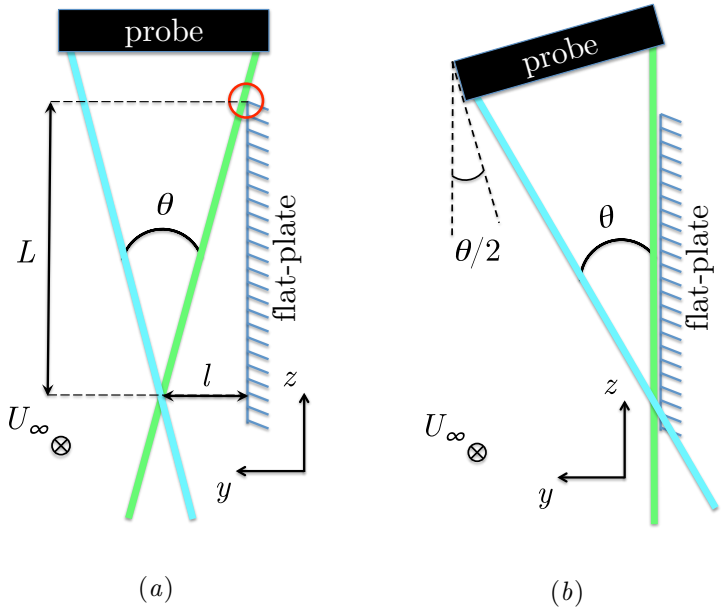
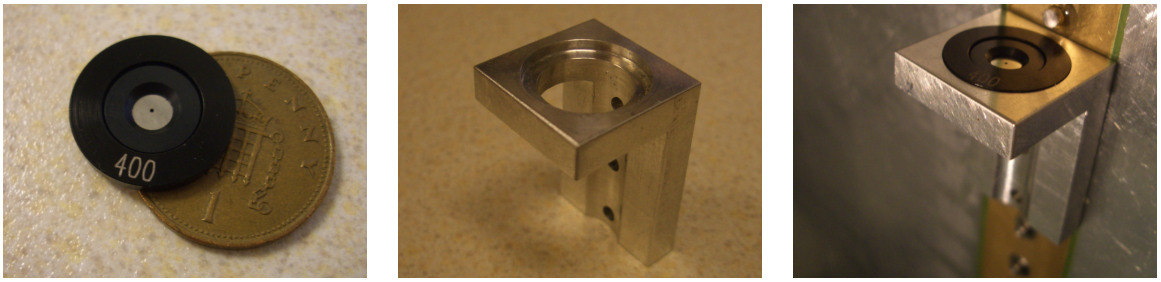


Figure 2.19: Schematic of the streamwise view of the relative positions between probe and flat plate; (a) probe axis aligned with the spanwise direction, (b) probe rotated $\theta/2$ with respect to the streamwise direction.

By rotating the probe, with respect to the streamwise direction by an angle at least equal to $\theta/2$ (with θ the angle formed by each pair of beams), measurements very close to the wall can be made, as shown in figure 2.19(b). With this alignment, the probe-volume lies between the probe and the impingement points. In this situation, the closer the probe-volume is to the wall, the closer the impingement points are to the probe-volume. They all meet when the probe-volume is just touching the surface. Due to the high reflections that occur when this happens, the light intensity that the photo-receptor receives leads to an over-saturated signal and the data are erratic. This only happens within a few tens of micrometers of the surface. Nevertheless, when post-processing the data, the boundary-layer profile origins are obtained aerodynamically, that is, by extrapolation of the near-wall region of the boundary-layer profiles, discarding erratic data. $\theta/2$ was set eventually at 6.2°. Due to this second rotation, another transformation is needed to retrieve the original velocity components. It is important to note that, due the absence of a means to measure the third velocity component, the second rotation implies that the measurements become "contaminated" by the third velocity component. However, since the angle 6.2° is considered small, the contamination is assumed to be negligible.

LDA Positioning with respect to the Reference Origin

The positioning of the LDA probe with respect to an established reference origin was conducted by means of a pinhole. Figures 2.20(a), 2.20(b) and 2.20(c) show, respectively, the pinhole itself, the stand to locate the pinhole, and the assembly aligned with the roughness element array.



(a) (b) (c)

Figure 2.20: Pinhole-stand assembly for LDA probe-volume positioning; (a) pinhole (on top of a one-penny coin, for size comparison purposes), (b) stand, (c) assembly mounted on the roughness element array.

The idea of using a pinhole is that, by making the probe volume pass through the pinhole (leaving, ideally, half a probe volume on each side of the pinhole), and knowing the location of the pinhole with respect to an established reference origin for the traverse system, the location of the probe volume is determined. The reference for the traverse was chosen to be the centre of the base of the 10^{th} roughness element (counting from the bottom of the array). The decision that the probe volume was in the desired position passing through the pinhole was based on visual inspection: by locating a light (preferably white) background behind the pinhole, when all the four beams on the background showed approximately the same intensity (and without scattering due to distortion caused by one or more beams brushing the edge of the pinhole, as shown in figure 2.21), then the probe volume was considered to be located at the correct position.

The diameter of the pinhole was 400 μm and the length of the probe volume was 340 μm for the green beam-pair (320 μm for the blue one). Since the pinhole was positioned so that it was contained in a XY-plane, the uncertainty associated with identifying the position of the probe volume was ± 0.2 mm in both streamwise and wall-normal directions and ± 0.17 mm in the spanwise direction. The combined uncertainty including that derived

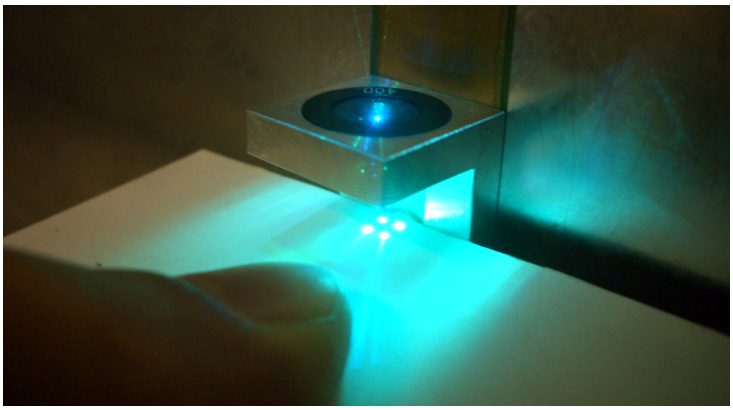


Figure 2.21: Probe-volume position identification by means of a pinhole.

from the manufacturing process of the pinhole to establish the tolerance of its nominal diameter, plus that derived from the in-house manufacturing process of the pinhole stand, had to be added to that derived from the resolution of the stepper motors of the traverse system.

A reduction in the uncertainty of the probe-volume position could have been achieved by employing a pinhole of smaller diameter (since the probe-volume diameter was nearly 10 times smaller than that of the pinhole). In fact, a pinhole of 100 μm of diameter was also used. But, owing to the significant beam-pair angle θ, it was virtually impossible to make all the four beams of the probe-volume pass through the pinhole. It is logical to think that pinholes with diameters between 100 and 400 μm could have been attempted. However, the purchase of off-the-shelf pinholes at realistic prices was not possible.

Data Convergence

Since the reliability of the measurements depends on the number of particles registered per data point, convergence tests were conducted to determine a minimum threshold of the number of particles and associated random uncertainty to ensure statistically independent readings. Figures 2.22 and 2.23 show, respectively, convergence tests of mean velocity readings at two wall-normal locations: 1 mm above the flat-plate surface (in the boundary layer, approximately at 10% of the local boundary layer thickness at that x-location) and 60 mm above (in the free stream). Five runs per location were carried out and both channels were studied. The superscript "*" refers to velocity readings without applying

the angle transformations described in the previous section.

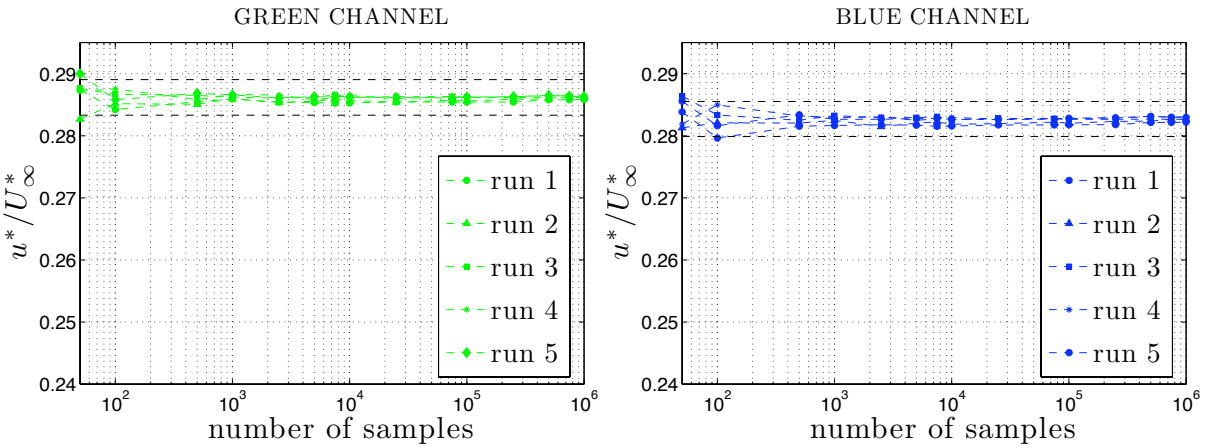


Figure 2.22: Convergence test at a wall-normal location of 1 mm above the wall.

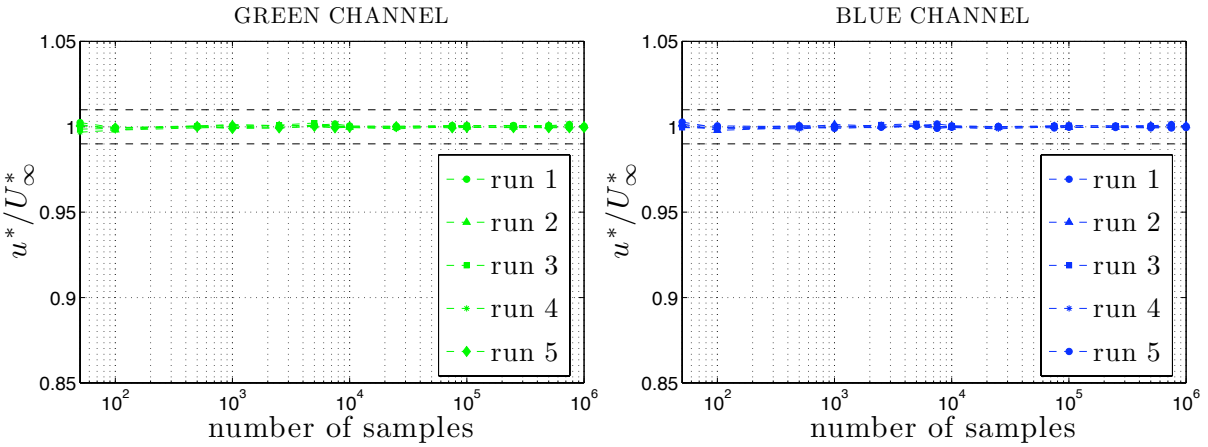


Figure 2.23: Convergence test at a wall-normal location of 60 mm above the wall.

It can be seen that the readings converge rapidly and lie in the range of $\pm 1\%$ (dashed lines) with respect to the reading with the largest number of particles considered. And also that the random uncertainty is smaller in the free stream than in the boundary layer.

Equipment

Here follows a list of the essential equipment required to conduct the experiments:

- Argon-Ion laser generator, model Stabilite 2017 from Spectra-Physics

- Two-component LDA system from TSI Instruments, consisting of:
  - multicolor beam separator, model Fiberlight
  - photo-detector module, model PDM 1000
  - multibit digital processor (signal processing unit), model FSA 4000
  - transmitting/receiving probe, model TRx260, with beam expander, model XPD60-450, resulting in:

wavelength	**514.5 nm (green)**	**488 nm (blue)**
lens focal length	480 mm	480 mm
beam-crossing half-angle ($\theta/2$)	7.78°	7.78°
probe-volume diameter	46 μm	44 μm
probe-volume length	340 μm	320 μm
fringe spacing	1.90 μm	1.80 μm
number of fringes	24	24

Table 2.1: Some relevant optical parameters of the LDA system employed.

  - software FlowSizer as control and acquisition interface
- liquid droplet seeding generator, model 10F03 from DANTEC Dynamics:
  - average droplet size: 2-5 μm
  - mixture: 80% water - 20% polyethylene glycol 600 for synthesis, from the firm Merck Schuchardt OHG
- traverse system, from DANTEC Dynamics. Traverse controller, model Schrittmotor-Controller C142-4, from the firm ISEL. Travel resolution: 6.25 μm per motor step
- micromanometer, model FCO510, from Furness Controls Limited
- DAQ card, model NI 6229-USB, from National Instruments
- LabVIEW© as software for a free-stream PID controller
- RS232 cable to digitally connect the micromanometer with the computer.

Figure 2.24 shows a schematic of the equipment set-up. Arrows represent connections as well as data transfer direction.

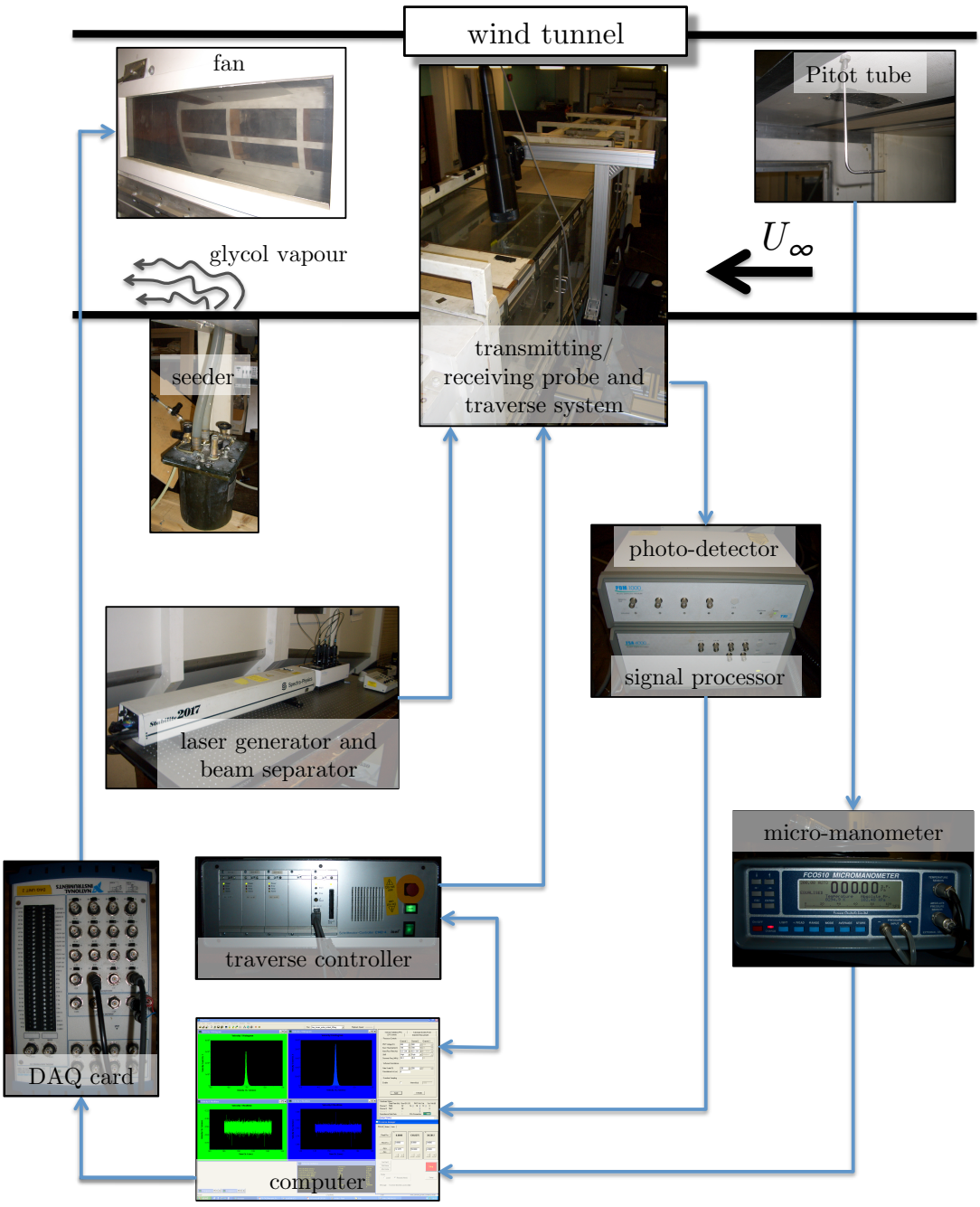


Figure 2.24: Schematic of the LDA set-up.

Velocity-Bias Corrected Statistics

Since in LDA the velocity measurements are based on particle occurrence, the measurements may be velocity biassed. Owing to the fact that more of the faster particles pass through the probe-volume for a given sampling time, the statistics of a measurement can be biassed by these. This cause the velocity mean provided by the measurement to be higher than the actual value and therefore not being representative of the true flow. To avoid this when computing statistics, weighted averages are used. In the present study, every particle reading was weighted with its own transit time (time spent to go through the probe-volume). Therefore, slower particles were more weighted.

2.1.5 Post-Flow Visualisation

The vast number of hours of continuously seeding the wind tunnel with particles for the LDA experiments resulted in another, indirect, experimental technique, so-called "post-flow" visualisation due to seeding deposition. The prefix "post-" is employed because the visualisation was conducted with no flow, once the LDA experiments were performed.

A clear deposition of particles was found on the flat-plate downstream of the roughness element array. A coherent pattern could be distinguished with no need for special lighting. The qualitative analysis of this trace reinforce the conclusions obtained from the LDA experiments, as shown in Chapter 3.

2.2 Design of Experiments

In this section, all the procedures carried out in the experiments are discussed. Aspects such as calibrations, grids of measurement locations, both preparatory and specific experiments, and post-processing strategies are described.

2.2.1 Base Flow Characterisation

As mentioned in section 2.1.3, HWA measurements were carried out to characterise the base flow (an unperturbed Blasius boundary layer). The objectives of these experiments were to ensure that a zero pressure streamwise-gradient laminar boundary layer was

developed on the flat-plate, and to identify the streamwise extension of the laminar region, which was the domain in which the transient growth study was performed.

Calibration

To convert voltage readings from the hot-wire probe into velocity, a calibration procedure was followed. The calibration relationship used was the commonly used King's Law, which is given by:

$$E^2 = A + BU^n. \tag{2.7}$$

By setting known values of free-stream velocity values U, voltage readings E were acquired. By a non-linear regression conducted in MATLAB, coefficients A, B and n were obtained.

Calibrations were performed at the beginning and end of every run. The longest run was over 8 hours long and the small difference between both calibration curves for all the runs was considered a sufficient reason for not having to calibrate in the middle of runs. For the same reason, temperature correction was also discarded: the temperature was monitored but temperature differences were small once the thermal conditions in the tunnel had reached a steady state. Figure 2.25 shows typical calibration curves (data and fits) in the case of the longest run.

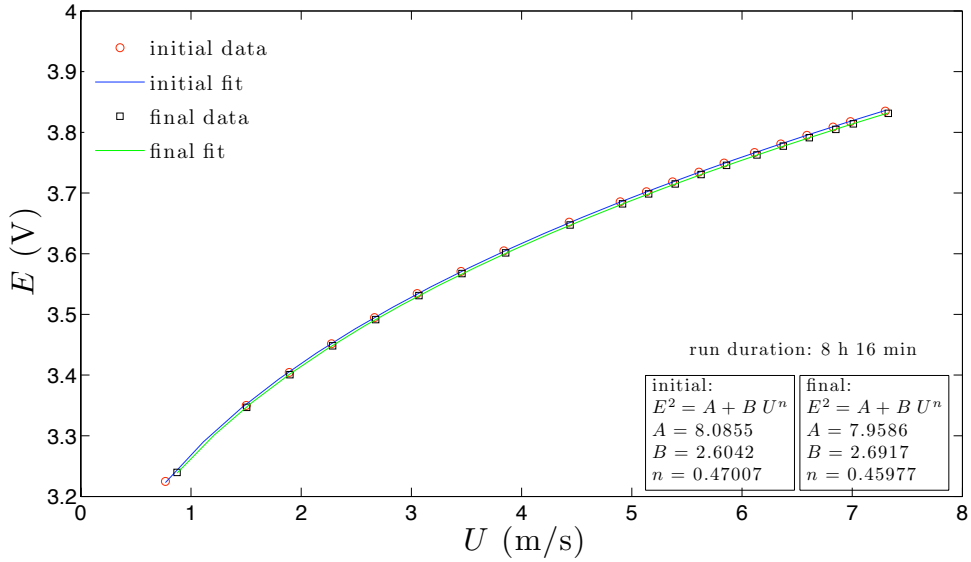


Figure 2.25: Typical calibration curves (data and fits) before and after a run.

As can be seen, the exponent n was near 0.45, which denotes a good calibration, as pointed out by Bruun (1996). The discrepancy between actual calibration data points and fit was always within $\pm 1\%$ for all data points. If this was not the case, the run was repeated.

Finally, the voltage data corresponding to the boundary-layer traverses were converted into velocity data by time-based linear interpolation between both pre- and post-run calibrations (this was possible because the time, with respect to the end of the pre-run calibration, at which every data point of the boundary-layer traverses was acquired was recorded).

Preliminary Experiments – Flat-Plate Flap Angle

Preliminary traverses were conducted to analyse the influence of the angle of the flap on the free-stream turbulence intensity and determine a suitable angle for the flap to ensure that the streamwise pressure gradient was zero and that the stagnation point was on the measuring side of the leading edge.

Three flap angles were considered: 12.8° (maximum angle possible), 9.7° and 6.5°. A check with the flap at both 0° and 6.5° was performed by placing the hot-wire probe inside the boundary layer, 50 mm downstream of the leading edge. The hot-wire voltage readings shown in figure 2.26 clearly indicate that, for the case of 0°, the stagnation point was on the back side of the flat-plate, making the boundary layer turbulent on the measuring side.

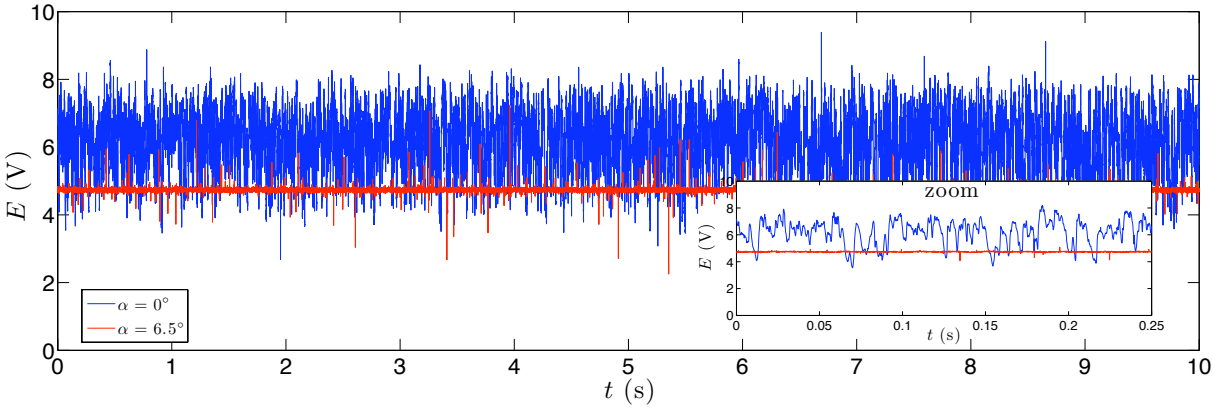


Figure 2.26: Hot-wire voltage time series inside the boundary layer 50 mm downstream of the leading edge at 0° and 6.5°.

Static pressure readings were acquired by taps at three locations on the flat-plate, at $x_1 = 235$ mm, $x_2 = 400$ mm and $x_3 = 560$ mm from the leading edge. Hot-wire readings were taken at x_3. The free-stream turbulence intensity:

$$TI = \frac{[u_\infty(t)]_{rms}}{U_\infty} \times 100, \tag{2.8}$$

was calculated from the velocity spectrum. The rms value of the velocity time series acquired by the hot wire, $[u_\infty(t)]_{rms}$, was computed as:

$$[u_\infty(t)]_{rms} = \left[\frac{1}{N^2} \sum_{f=1}^{f_c} \Phi(f) \right]^{1/2}. \tag{2.9}$$

$\Phi(f)$ is the power spectral density of $u_\infty(t)$, N the number of samples per reading and $f_c \simeq 40$ Hz, a low-pass cut-off frequency to discard mains and environmental noise in the calculations. $[u_\infty(t)]_{rms}$ was also computed by simply performing the rms of the time series. However, since mains and environmental noise are not filtered, this procedure gave quite large values of TI.

The parameters of the experiments were:

- free-stream velocity: $U_\infty = 5$ m/s;
- sampling frequency: $f_s = 10^4$ Hz;
- number of samples: $N = 2^{22}$ (sampling time: $t_s = N/f_s \simeq 6.99$ min).

Three runs per flap angle were conducted. Figure 2.27 shows the spectra of all the cases and table 2.2 summarises all the results.

	6.5°	**9.7°**	**12.8°**
$[\boldsymbol{\Delta P/\Delta L}]_{\boldsymbol{x_1 \leftrightarrow x_2}}$ **(Pa/m)**	0.4154 (0.1506)	1.2142 (0.0543)	1.2284 (0.0605)
$[\boldsymbol{\Delta P/\Delta L}]_{\boldsymbol{x_1 \leftrightarrow x_3}}$ **(Pa/m)**	0.5142 (0.1781)	0.9623 (0.0309)	1.0494 (0.1185)
$\boldsymbol{TI}$ **(%)**	0.0465 (0.0126)	0.0724 (0.0105)	0.1228 (0.0195)

Table 2.2: Streamwise pressure gradients between stations and free-stream turbulence intensity for all the flap angles considered. Mean values (and rms in brackets) out of three runs per angle.

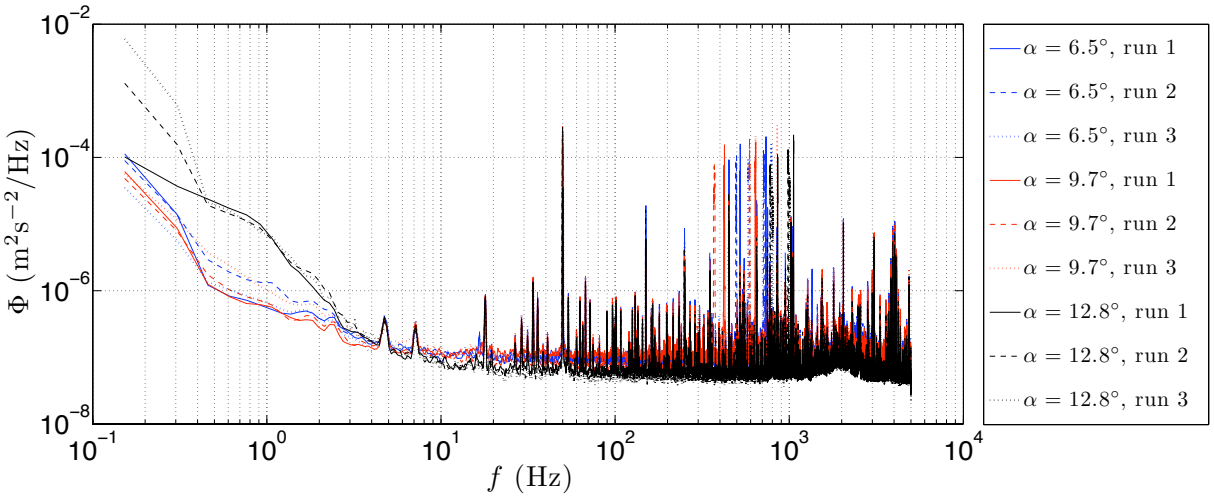


Figure 2.27: Power spectra of all the cases considered. Note that the frequency top end is 5×10^3 Hz, since, by Nyquist theorem, only half of the frequency content of the signal can be recovered.

It can be seen that, while angles 6.5° and 9.7° offer similar levels of velocity fluctuations at low frequencies, 12.8° worsens the situation. In addition, the larger the angle is, the larger the streamwise pressure gradient is. Consequently, the angle adopted for all the further experiments was set at 6.5°, at which the free-stream turbulence intensity is that reported for this wind tunnel. The parameters of the experiments were:

Experiments – Boundary Layer Streamwise Characterisation

The streamwise characterisation of the boundary layer was performed by wall-normal velocity profiles at a number of x-stations and at a single spanwise location (centre-line of the flat-plate). These were:

- **number of x-stations:** 55
- **location of first x-station:** 185 mm downstream of the leading edge
- **spacing between x-stations:** 4.5 mm for the first 53 x-stations, 60 mm between the 53$^{\text{th}}$ and the 54$^{\text{th}}$, and 100 mm between the 54$^{\text{th}}$ and the 55$^{\text{th}}$ (furthest downstream)
- **number of nodes per wall-normal scan:** 70, from the wall outwards:
  - 25 nodes with a spacing of 0.04 mm

  - 15 nodes with a spacing of 0.10 mm
  - 10 nodes with a spacing of 0.20 mm
  - 20 nodes with a spacing of 0.50 mm
- **wall-normal travel:** 15 mm
- **sampling frequency:** 10 kHz
- **sampling time:** 10 seconds per node
- **free-stream velocity:** $U_\infty = 5$ m/s

The profiles were traversed from near the wall outwards. Once a profile was scanned and the probe traversed to the next x-station, the approach of the probe to the vicinity of the wall was conducted carefully in order not to crash the probe onto the wall. This approach was performed in steps, acquiring data and converting them into velocity on the fly based upon the pre-run calibration. The closer to the wall, the smaller the steps between nodes were. This step reduction was based on the velocity gradient between the current position and the previous one. As soon as the mean velocity read by the probe was below 30% U_∞ the approaching stage was stopped and the traverse away from the wall was started.

Since this method of approaching the wall was not subject to a physical reference but related to the boundary layer, the actual location of the probe with respect to the wall for each x-station was unknown until the data were processed. Thus the location of the wall was carried out aerodynamically, in other words, by extrapolating the velocity data down to zero. This extrapolation was performed assuming a linear velocity profile near the wall. Only velocity data at those nodes where the velocity difference between one node and the node below was above 1% with respect to that between the closest two nodes to the wall were considered for the linear fit. This procedure proved successful.

2.2.2 Perturbed Boundary Layer

Traverses

Three types of traverses were carried out:

- ***YZ*-plane traverses at various fixed *x*-locations:**

  These traverses constituted the main core of the experiments and consisted of boundary-layer profile scans (from the wall up to the free stream) evenly spaced in the spanwise direction. Their parameters were:

  - ***x*-locations:** 100, 207, 211, 215, 225, 240, 250, 275 and 300 mm downstream from the leading edge.

    The reason for choosing a station at $x = 100$ mm was based on the aim of checking roughness-induced receptivity features. The remaining stations were chosen using the data from the Finite Volume Simulations (FVS) and the earlier data from Lavoie *et al.* (2008). Both data sets showed that there is a wake region approximately up to $x = 215$ mm and the decay region started approximately at $x = 300$ mm. Since the interest of the present study was focused on the growth region, all the stations were concentrated between the roughness element array (x =200 mm) and $x = 300$ mm. Owing to impingement of the laser beams on the roughness elements for y-locations within the range of the roughness element size, the closest x-location to the roughness element was 207 mm.

  - ***z*-range:** between 3 and 5 roughness-element spacings.

    This range covered those roughness elements in the middle of the array. The reason for choosing between three and five roughness-element separations was to have a sufficient range for wavelength-averaging, and the reason for covering elements in the middle of the array was to ensure periodicity.

  - ***z*-spacing:** $\delta z = \Delta z/16$ ($\delta z = 0.625$ mm), as adopted by Lavoie *et al.* (2008).

  - ***y*-travel:** 18 mm (12 times the roughness element height).

  - ***y*-spacing:** 73 nodes, from the wall outwards:

    * 31 nodes with a spacing of 0.05 mm
    * 20 nodes with a spacing of 0.125 mm
    * 16 nodes with a spacing of 0.5 mm
    * 6 nodes with a spacing of 1 mm

- ***XZ*-plane traverses at two fixed *y*-locations:**

- ***y*-locations:**
  - $y/k = 1$ ($y = 1.5$ mm, at the same height as the top of the roughness elements)
  - $y/k = 8$ ($y = 12$ mm, in the free-stream throughout the streamwise travel covered)
- ***z*-range:** 7 roughness-element spacings (70 mm).

  Likewise the YZ-plane traverses, these ones covered those roughness elements in the middle of the array.
- ***z*-spacing:**
  - $\delta z = \Delta z/16$ for the traverse at $y/k = 1$
  - $\delta z = \Delta z/10$ for the traverse at $y/k = 8$
- ***x*-travel:**
  - from $x = 201.25$ mm (right at the back of the roughness elements) up to $x = 325$ mm (a bit further downstream from the location where the u'-energy peaks), for the traverse at $y/k = 1$
  - from $x = 100$ mm (well upstream from the roughness element array) up to $x = 325$ mm, for the traverse at $y/k = 8$
- ***x*-spacing:**
  - $\delta x = d/2$ (1.25 mm) for the traverse at $y/k = 1$
  - $\delta x = 2d$ (5 mm) for the traverse at $y/k = 8$

- ***XY*-plane traverses at two fixed *z*-locations:**

  One is aligned with the centre of a roughness element and the other is aligned with the centre-line between two roughness elements. Their parameters were:

  - ***x*-travel:** from $x = 175$ mm up to $x = 198.25$ mm (0.5 mm upstream from the front of the roughness element array).
  - ***x*-spacing:**
    - $\delta x = 2d$ from $x = 175$ mm up to $x = 185$ mm
    - $\delta x = d/4$ from $x = 187$ mm up to $x = 198.5$ mm

- ***y*-travel:** identical to that for the YZ-plane traverses.
- ***y*-spacing:** identical to that for the YZ-plane traverses.

Over 59000 positions were used for data gathering by the LDA probe. The LDA sampling parameters were set so that the probe acquired, for each position, either a maximum of 50000 samples or for a maximum of 300 seconds. Whichever of the two conditions occurred first triggered the system to move the probe to the next position. Normally, near the wall the latter condition was met first and, as the probe moved away from the wall, it was the former. On average, for all the boundary-layer profiles scanned, the traverse system was triggered by the former condition for more than 90% of the positions within the boundary-layer region. Nevertheless, after the procedure involving the establishment of the actual wall ($y = 0, u = 0$) from the velocity data (in the same fashion as carried out for the unperturbed flow experiments), for all the positions that were considered to form part of the definitive boundary-layer profiles, the number of samples acquired for each position was over 2000. Therefore, recalling figure 2.22, the data acquired at all the positions met the convergence criterion.

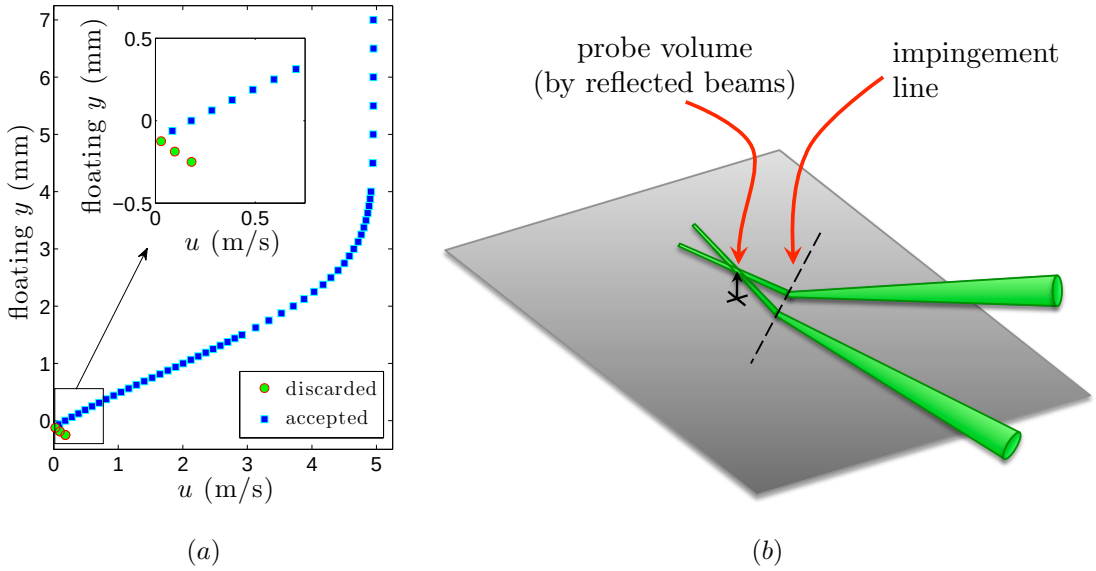
Furthermore, after moving from one position to the next, a time of 10 seconds was left before starting data acquisition. This was done in order to let the oscillations of the LDA probe (produced by the inertia involved in the traverse mechanism when moving and stopping) attenuate. In total, the effective time employed to cover the complete set of traverses was over 3300 hours. Completing a traverse took between 70 and 120 hours (depending on the number of positions covered by a traverse) of non-stop wind-tunnel time. Short interruptions were conducted both within traverse slots to re-optimise the laser power of the beams at the exit of the probe, and between traverses to verify the correct positioning of the probe by means of the pinhole technique described in section 2.1.4.

2.3 Determination of Wall Position

As previously mentioned, determining the no-slip location of the wall ($y = 0, u = 0$) when scanning boundary-layer wall-normal profiles was part of the post-processing stage of the experiments. This wall position was determined by fitting a curve through those

data points near $u = 0$ m/s. The process consisted of two stages. First, degenerate data (as a consequence of performing LDA very near walls and shiny surfaces) were discarded. Second, in an iterative manner, the best curve possible to a number of data points was fitted. Those data points were selected based on the criterion of minimising the standard deviation between the data and the fitted curve. In the case of HWA, only this second stage was performed, as the hot-wire probe never approached the wall so close that thermal convection effects were significant.

Figure 2.28(a) shows, as an example, the data of a boundary layer u-profile distinguishing discarded nodes in the vicinity of $u = 0$ m/s. It can be seen that the discarded nodes show a decrease in u with increasing in y. This was due to the fact that the laser beams impinged on the wall before intersecting, so forming the probe-volume from the reflected beams, as shown in figure 2.28(b).



(a) (b)

Figure 2.28: Degenerate data near the wall; (a) boundary-layer profile with data from all the nodes acquired, (b) schematic of probe-volume generation by reflected beams due to impingement on the wall.

A different strategy would have been to start scanning from a position slightly further away from the wall. On the one hand, this would have saved time from acquiring meaningless data, but on the other hand, it would have reduced the robustness in determining the wall location because the larger the velocity gradient near the wall, the fewer the number of points used in the fit.

Once the degenerate data were removed, the second stage in determining the wall location consisted of finding the best-fit curve through a selected set of points by an iterative procedure. The number of points selected depended on three conditions. First, a starting velocity threshold which ranged between $0.03U_\infty$ and $0.2U_\infty$ was selected. Second, a maximum number of points of 10 was chosen; and third, a maximum velocity threshold, ranging between $0.07U_\infty$ and $0.35U_\infty$ was chosen. If, for a given starting velocity threshold, the number of points was below 10, then the point immediately above the starting threshold was included in the set of points and the threshold was changed to the value for that point just included. This process was repeated up to either 10 points or the maximum velocity threshold was reached. The reason for considering a variable velocity threshold was that the near-wall velocity gradient not only depended on the streamwise position of the boundary-layer profile in question, but also on its proximity to the roughness elements. As an example of the process, figures 2.29(a) and 2.29(b) show boundary-layer profiles at the same streamwise location (x = 207 mm), corresponding to (a) a spanwise location behind a roughness element, and (b) a spanwise location in between roughness elements. In the case of (a), there were 10 nodes before reaching the starting threshold, whereas in the case of (b), the maximum threshold was reached for less than 10 nodes.

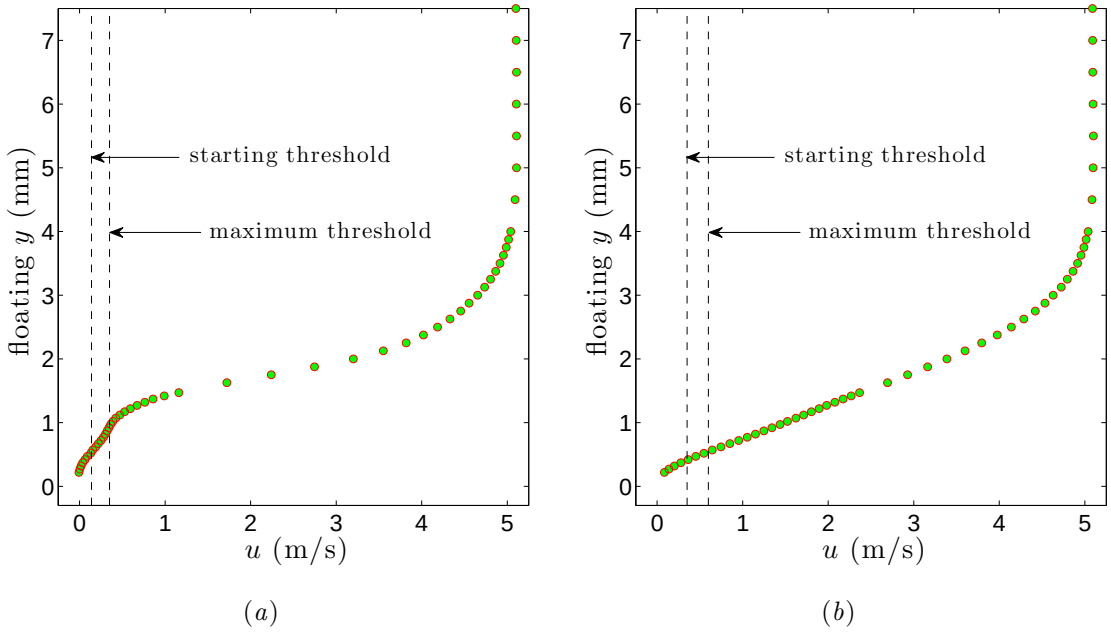


Figure 2.29: Boundary layer profiles of cleaned data and in wall-normal locations for the same streamwise station (x = 207 mm) at two different spanwise locations; (a) there are more than 10 nodes acquired before reaching the adopted starting velocity threshold, (b) the maximum velocity threshold is reached for less than 10 nodes.

Once the set of candidate points was selected through which a curve was to be fitted, the iterative process began. Linear, quadratic and cubic fits were tried simultaneously. The reason for using higher-order polynomials was because, for those boundary-layer profiles in the vicinity of the roughness element array, their near-wall region was far from that of the Blasius boundary layer. Figure 2.29(a) is a good example of this discrepancy with a Blasius profile in the near-wall region. In other words, a linear fit using the velocity threshold for the quasi-linear region of Blasius ($\lesssim 0.3U_\infty$) would have provided an incorrect estimate of the wall location. This process involved, as a first attempt, a selection of only those data points which were within half of the standard deviation of the fit. Then, with only these points, a new fit was performed, and only the points which were within half of the standard deviation of the new fit were selected for a next fit. Once all the data points were within half of the last standard deviation, the process terminated. If, at some point, all the data points were outside the criterion, then the criterion was relaxed so that at least half of the number of data points could fulfil it. Figure 2.30 shows an example of the final result of this process: 15 data points where initially considered (there was no need therefore for increasing the starting threshold) and eventually 7 points (cyan triangular markers) were considered for the fit from which the wall location was obtained.

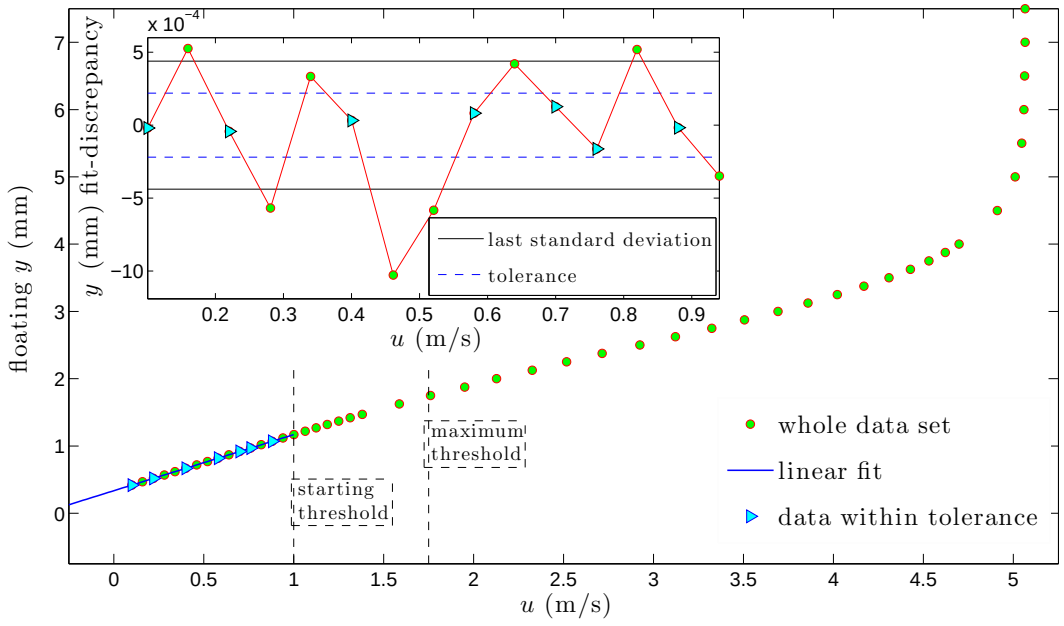


Figure 2.30: Boundary layer profile (at station $x = 275$ mm) in which the wall position was determined by a linear fit. Cyan triangular markers indicate those data points which were eventually considered for the fit that provided the wall location. The inset shows the discrepancy between data points and the fit, the standard deviation given by the last attempted fit and the tolerances are shown.

In the majority of the cases, it was proven that one polynomial clearly provided the best fit in relation to the other two. Figures 2.31(a), 2.31(b), and 2.31(c) show examples in which the best fit curve was, respectively, linear, quadratic and cubic.

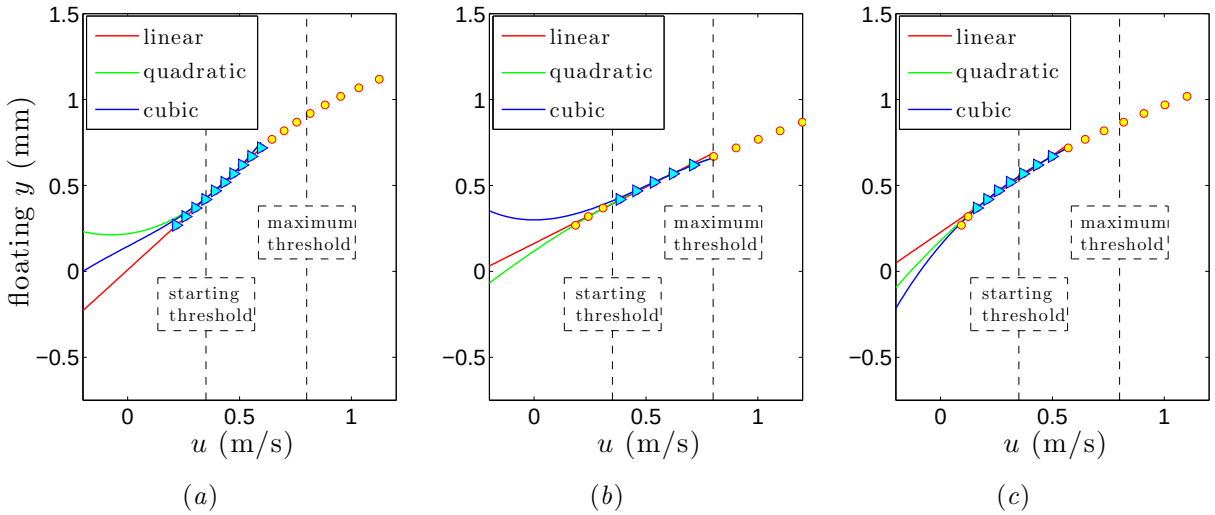


Figure 2.31: Best fit to near-wall region of boundary layer profiles for the same streamwise station ($x = 211$ mm) at different spanwise locations; (a) linear, (b) quadratic, (c) cubic.

In order to check the reliability and robustness of this algorithm, it was compared simultaneously against the method of White (2005) and the locations indicating wall reflection (as shown in figure 2.28) where available. Figure 2.32 shows an example (at $x = 215$ mm) of this comparison.

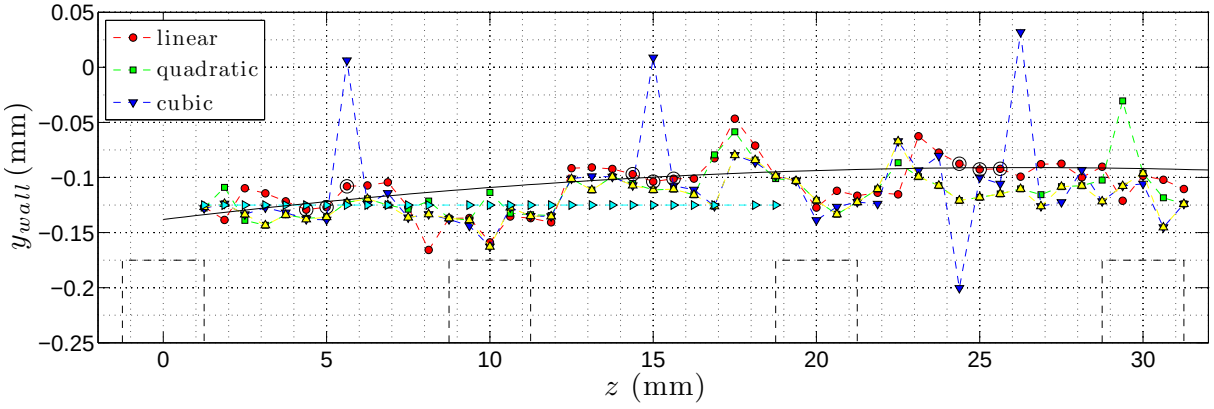


Figure 2.32: Wall estimation comparison at $x = 215$ mm. Red circles, green squares and blue triangles correspond to wall estimations by linear, quadratic and cubic fits, respectively. Yellow triangles indicate the wall estimations eventually adopted. Cyan triangles denote wall reflections where available. The black curve corresponds to a quadratic fit in the spanwise direction according to White (2005).

Red circles, green squares and blue triangles correspond to wall estimations by linear, quadratic and cubic fits, respectively. Yellow triangles indicate the wall estimations eventually adopted. Cyan triangles denote wall reflections at those spanwise locations where available. The black curve corresponds to a quadratic fit along the spanwise direction through those wall estimations by linear fits at locations between roughness elements and one spanwise location before and one after (red circles with black rings around), according to White (2005). It can be seen that the algorithm is fairly robust, avoiding to chose those few wall estimations by quadratic and cubic fits which are clearly out of the trend. In fact, it shows that, for those spanwise locations where wall reflection is available, the best fit is closer to the wall reflection than the other two for most of the spanwise locations. It also shows that, at streamwise locations in the vicinity of the roughness element array (like that of the example, $x = 215$ mm), a wall estimation by linear fit does not necessarily have to be the best one at spanwise locations between roughness elements, when comparing to a wall reflection (note it at $z \simeq 25$ mm in the figure above). Moreover, the spanwise quadratic fit of White (2005) does not seem to be as accurate as the algorithm here presented for spanwise locations aligned with the roughness elements. Nevertheless, the further downstream, the more spanwise locations feature wall estimations by linear fit as the best ones.

Chapter 3

Results

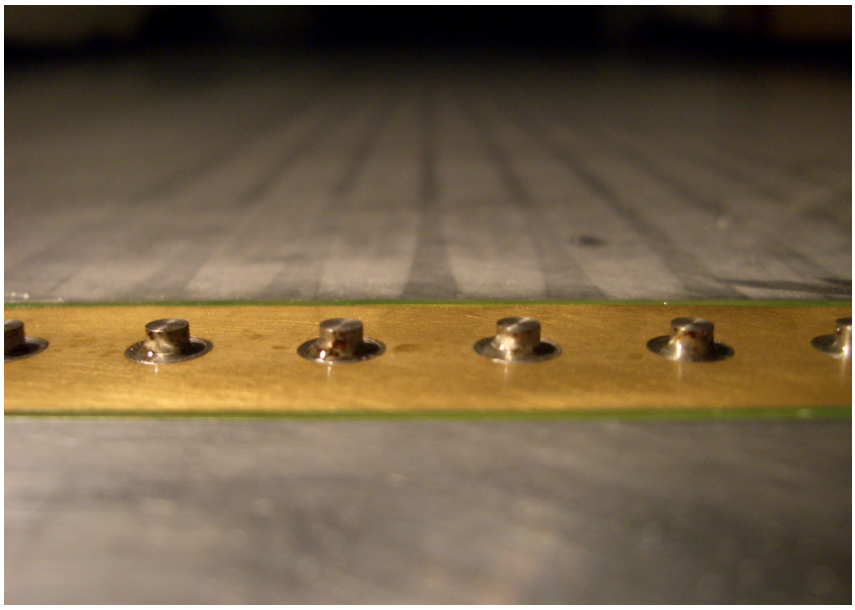


Figure 3.1: View from upstream of the trace left by the roughness element array due to seeding deposition on the surface.

3.1 Unperturbed Boundary Layer

3.1.1 Wall-Normal Velocity Profiles

Figure 3.2 shows the set of wall-normal profiles in self-similarity variables used to determine the boundary layer origin. Only those profiles for which the shape factor was within 2.55 and 2.65 are shown (44 out of 55). It can be seen that the agreement between the experimental data (colour dots) and the theoretical Blasius profile (dashed line) is very good.

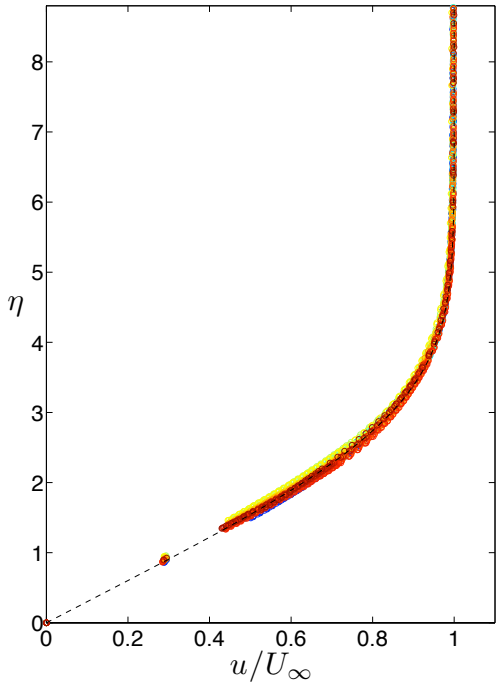


Figure 3.2: Wall-normal velocity profiles (experimental data: dots, theory: dashed line) in self-similarity variables for which $2.55 \leqslant H \leqslant 2.65$.

To further quantify the quality of the boundary layer compared to the theoretical Blasius solution, a discrepancy index, $\epsilon_{Blasius}$, is employed:

$$\epsilon_{Blasius}(\%) = \frac{1}{N-1}\sum_{n=2}^{N}\frac{\left|\left[\frac{u}{U_\infty}\right]_n^{exp} - \left[\frac{u}{U_\infty}\right]_n^{Blasius}\right|}{\left[\frac{u}{U_\infty}\right]_n^{Blasius}} \times 100, \tag{3.1}$$

where N is the number of points per profile. This index is computed for all those profiles for which H ranged between 2.55 and 2.65 (for Blasius, $H = 2.59$). The results are:

- **mean discrepancy:** 2.13%
- **minimum discrepancy:** 1.58%, at 261.5 mm downstream from the leading edge
- **maximum discrepancy:** 3.57%, at 333.5 mm downstream from the leading edge

3.1.2 Streamwise Variation of δ_{99}, δ_1, δ_2 and H

In this subsection, the streamwise evolution of the $0.99U_\infty$ thickness (δ_{99}), displacement thickness (δ_1), momentum thickness (δ_2) and shape factor (H) of the boundary layer established are shown.

- **Streamwise variation of the boundary layer thickness, $\boldsymbol{\delta_{99}}$.**

  The data from the experiments are fitted with a curve of the form

  $$\delta_{99} = a\, x^{1/2}. \tag{3.2}$$

  The constant a is then compared to the theory, shown in equation (1.1).

- **Streamwise variation of the displacement thickness, $\boldsymbol{\delta_1}$.**

  The integral form of δ_1 is shown in expression (1.3). As shown by Schlichting (2000), the numerical results of the Blasius equations are:

  $$\delta_1(x) \simeq 1.72\sqrt{\frac{\nu x}{U_\infty}}. \tag{3.3}$$

  The experimental data are used to compute the evolution of δ_1, and expression (3.3) is used as evidence for a fit of the type

  $$\delta_1 = b\, x^{1/2}, \tag{3.4}$$

  where b is a constant.

- **Streamwise variation of the momentum thickness, $\boldsymbol{\delta_2}$.**

  The integral form of δ_2 is

  $$\delta_2(x) = \int_0^\infty \frac{u(x,y)}{U_\infty}\left[1 - \frac{u(x,y)}{U_\infty}\right] dy. \tag{3.5}$$

For Blasius flow, the numerical solution of δ_2 is

$$\delta_2(x) \simeq 0.664\sqrt{\frac{\nu x}{U_\infty}}. \tag{3.6}$$

Likewise δ_1, the experimental data are used to compute the evolution of δ_2, and expression (3.6) is used as evidence for a fit of the form

$$\delta_2 = c\, x^{1/2}, \tag{3.7}$$

where c is a constant.

- **Streamwise variation of the shape factor, H.**

  The shape factor, H, is defined as

$$H = \frac{\delta_1}{\delta_2}. \tag{3.8}$$

  For Blasius flow, $H = 2.59$. It is generally regarded as a good indicator to evaluate how close to Blasius profile a boundary layer is.

To calculate δ_1, δ_2 and H, the boundary-layer origin, x_0, must be found. By inverting any of expressions (1.1), (3.3) and (3.6), a quadratic relationship with x can be used to estimate the virtual origin. In this study the δ_1 data are fitted through an expression of the form $x = g{\delta_1}^2$ (with g a constant), giving its extrapolation down to $\delta_1 = 0$ the location of the boundary-layer origin with respect to the leading edge of the flat-plate. Only those profiles with $H \in [2.55, 2.65]$ and simultaneously $\epsilon_{Blasius} < 2.5\%$ are considered in the fit $x = g{\delta_1}^2$. According to this calculation, the virtual origin of the boundary layer is located 15 mm (with an accuracy of $\pm$ 0.25 mm) downstream of the leading edge. In non-dimensional terms, using as reference the length of the plate plus flap (L = 2037 mm), $x_0/L = 7.36 \times 10^{-3}$. Figure 3.3 shows together the experimental data, the fits and the Blasius expressions for δ_{99}, δ_1 and δ_2. Those data, along with the determination of η, are based on the boundary-layer virtual origin.

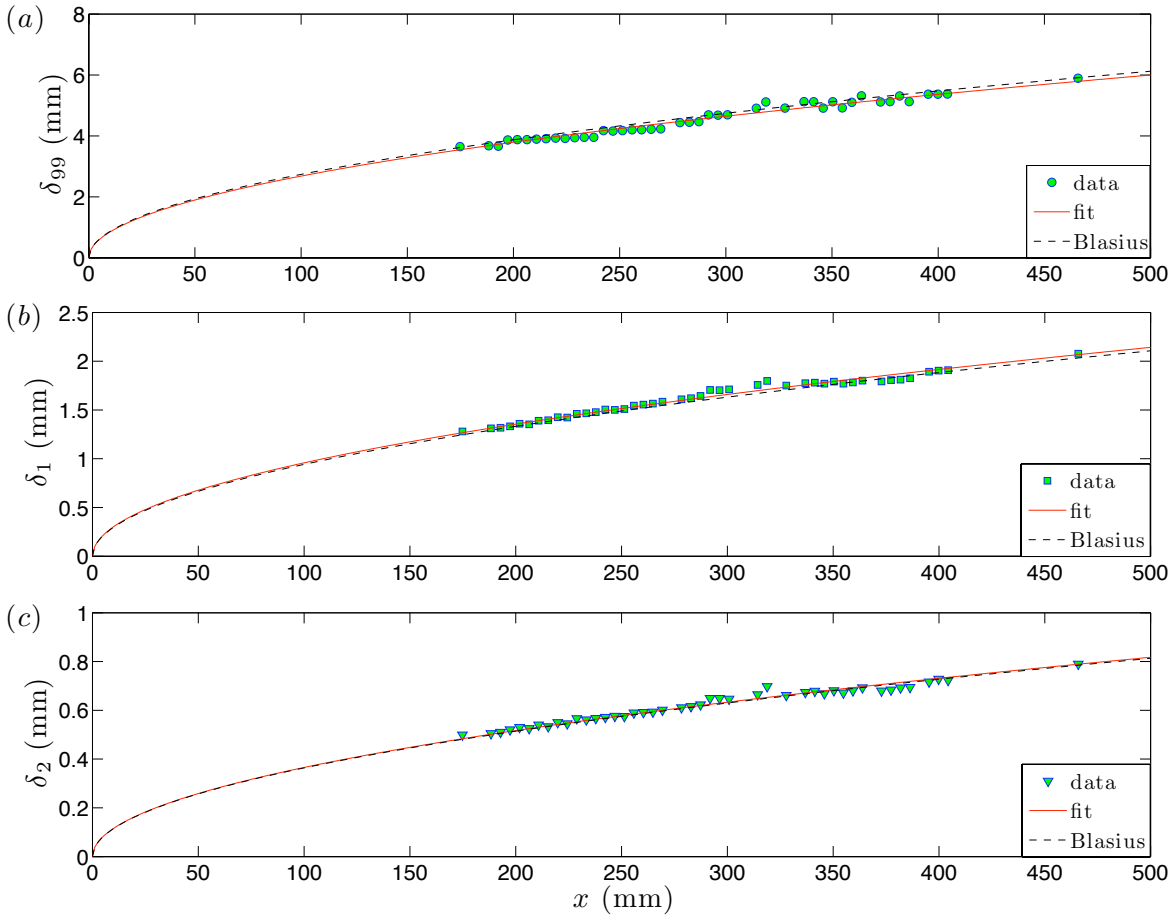


Figure 3.3: Streamwise evolution of the three thicknesses; (a) boundary layer, (b) displacement, (c) momentum. Actual data - symbols, fits - solid lines, Blasius - dashed lines.

As with $\epsilon_{Blasius}$, discrepancy indices for δ_{99}, δ_1 and δ_2 were defined to quantify the accuracy of the data with respect to the theoretical curves. These indices were formulated as follows:

$$\epsilon_{\delta_i}(\%) = \frac{1}{P}\sum_{p=1}^{P}\frac{\left|{\delta_{i,p}}^{theo} - {\delta_{i,p}}^{exp}\right|}{{\delta_{i,p}}^{theo}} \times 100, \tag{3.9}$$

where $i = \{99, 1, 2\}$ and P is the number of boundary-layer profiles. The values of the discrepancy indices are:

- $\epsilon_{\delta_{99}} = 2.04\%$,
- $\epsilon_{\delta_1} = 1.68\%$,
- $\epsilon_{\delta_2} = 0.53\%$.

Compared to the other indices, a larger value of $\epsilon_{\delta_{99}}$ was expected since both δ_1 and δ_2 are integral quantities and therefore less sensitive to experimental error. Nevertheless, the agreement between experimental and theoretical thicknesses suggests that a zero streamwise pressure gradient two-dimensional boundary layer is accurately generated.

Figure 3.4 shows the streamwise evolution H. It shows all the boundary-layer profiles and not only those with a shape factor within 2.55 and 2.65. Considering only those profiles with a shape factor within 2.55 and 2.65, the mean value of H was 2.62, with an rms value of 0.03. It can be seen that, for the furthest x-station, the shape factor drops to 1.48. This denotes that, at that location, the boundary layer was beginning to become turbulent (Schlichting, 2000).

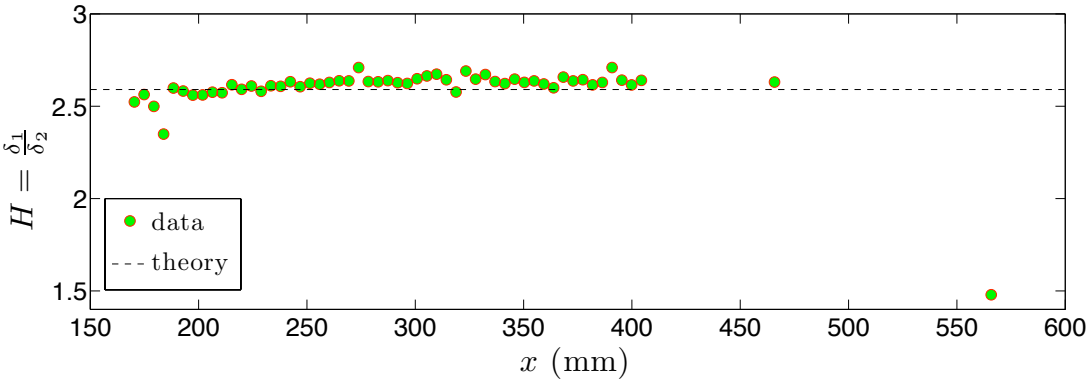


Figure 3.4: Streamwise evolution of the shape factor. Actual data - dots, Blasius - dashed line.

3.2 Perturbed Boundary Layer

The vast majority of these results was obtained from the LDA experiments, but relevant data from the Finite Volume Simulations (FVS) are also included to support those from the LDA. The analysis focuses on u' and v'. Based on expression (1.7), the perturbation velocities can be obtained as

$$u' = u - \langle u \rangle_z, \tag{3.10}$$

where $\langle u \rangle_z$ is the spanwise average (over an integer number of roughness wavelengths) at the same x-location, hence only depending on y.

The Reynolds number based on k and u_k (the velocity at $y = k$) in the absence of roughness elements ($Re_k = u_k k/\nu$) for this study was 318. White (2002) used $Re_k < 90$, and Fransson *et al.* (2004) used $180 < Re_k < 340$. Hence, in the present work, it was reasonable to expect the presence of high-speed streaks behind every roughness element. All the data from LDA, HWA by Lavoie *et al.* (2008) and FVS confirm this.

3.2.1 Free Stream Characterisation

A XZ-plane traverse at $y/k = 8$ (in the free stream) was conducted to characterise the flow above the boundary layer. Figures 3.5(a) and 3.5(b) show, respectively, iso-contours of u and its spanwise-average $\langle u \rangle_z$ measured at each x-location at $y/k = 8$. The traverses covered a significant extension of unperturbed flow, the generation of the perturbation by the roughness element array at $x_k = 200$ mm, the immediate wake region ($200 \lesssim x \lesssim 215$ mm), and the entire region of u'-energy growth ($215 \lesssim x \lesssim 300$ mm) up to the start of its decay ($x \gtrsim 300$ mm).

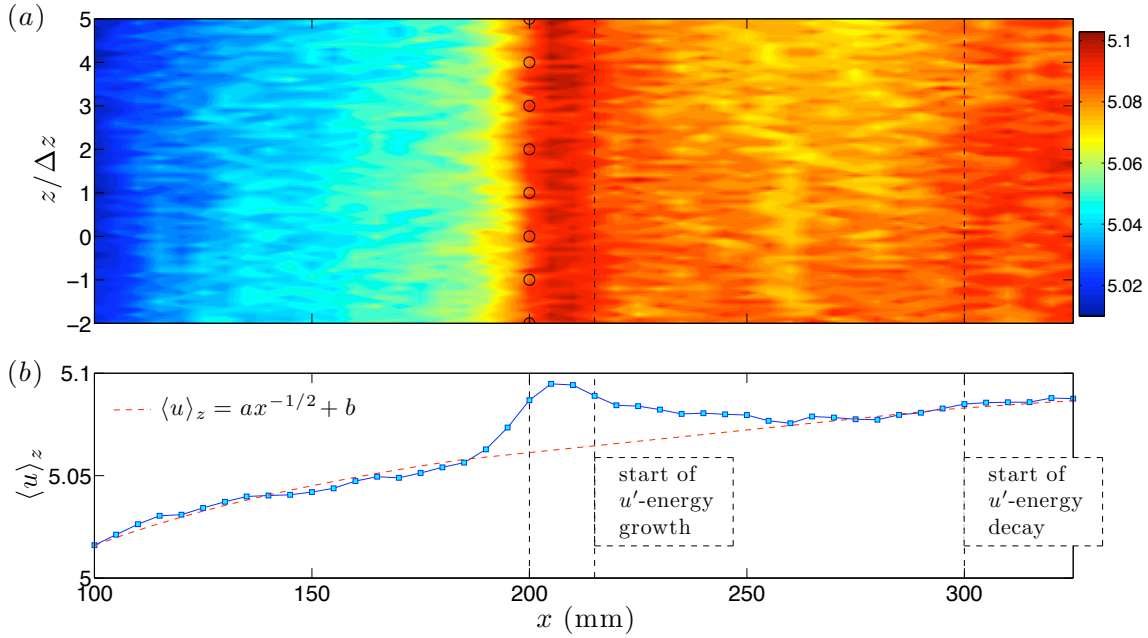


Figure 3.5: Free-stream velocity (in m/s) at $y/k = 8$; (a) iso-contours, (b) spanwise-average. LDA data.

In general terms, there is an overall acceleration throughout the domain analysed. This can be attributed to the growth of the boundary layer. Although the velocity change is small ($\sim$ 1.4% increase), various important features can be detected. For $100 \lesssim x \lesssim 185$ mm the flow progressively accelerates (apparently unaffected by the

presence of the roughness element array). Then, for $185 \lesssim x \lesssim 200$ mm, the flow undergoes a sudden acceleration. This is likely to be due to the blockage of the array, and it is remarkable that this effect can be noticed in the free-stream, at $y/k = 8$. Then the velocity appears constant in the wake region, immediately behind the array. A modest deceleration can be seen as the flow enters the u'-energy growth region ($x \simeq 215$ mm). There is a local minimum at $x \simeq 260$ mm and then the flow slightly accelerates downstream. In figure 3.5(b) a fit of the form $\langle u \rangle_z = ax^{-1/2} + b$ has been included. This fit is based on mass conservation in the free-stream as the boundary layer grows along x, that is, $U_\infty(x)\,[A_{WT} - A_{bl}(x)] = const.$ A_{WT} is the actual cross-sectional area of the wind tunnel (constant along x for these experiments); A_{bl} is that implied by the growth of the boundary layer, i.e. the width of the wind tunnel times the displacement thickness, δ_1. Since $\delta_1 \sim x^{1/2}$, $U_\infty(x) = ax^{-1/2} + b$, with a and b constants. Only the data points outside the interval $185 \lesssim x \lesssim 200$ mm have been used in the fit. The result shows that the acceleration of the flow is caused mainly by the growth of the boundary-layer thickness, with the roughness element array affecting the free stream in a finite and confined manner.

Another important aspect is the streaky structure of the free stream. Figures 3.6(a) and 3.6(b) show, respectively, iso-contours of u' and its rms values with respect to $\langle u \rangle_z$, computed at each x-location:

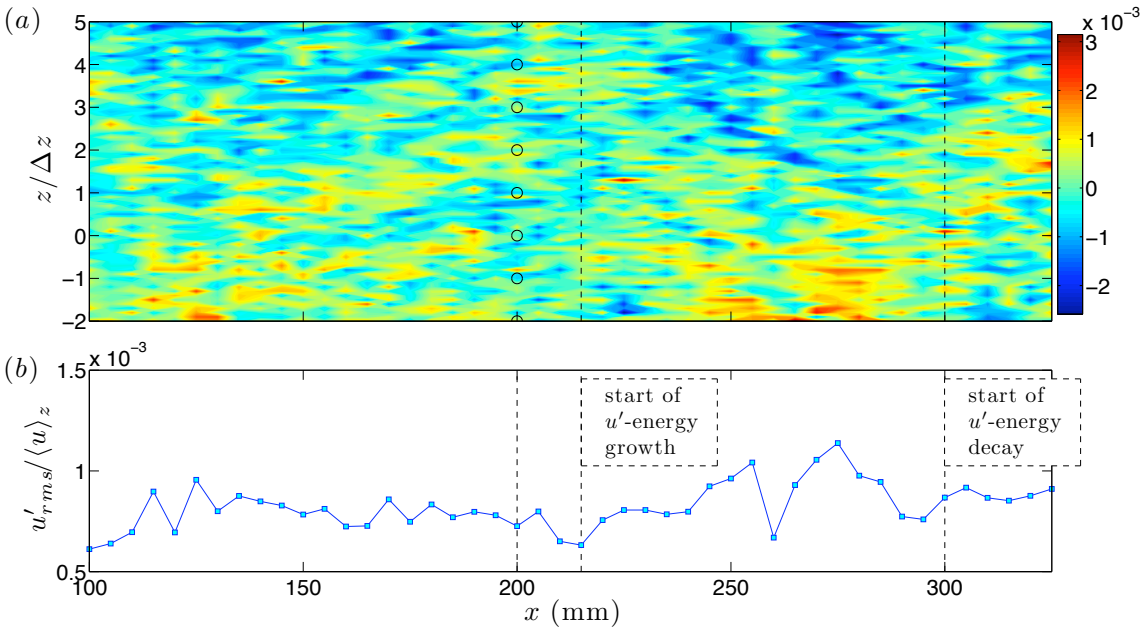


Figure 3.6: Perturbation velocity, u', at $y/k = 8$; (a) iso-contours, (b) rms values. From the LDA data.

Despite the fact that the amplitude of the perturbation velocity (a maximum of $\sim$ 0.11% of $\langle u \rangle_z$) is around two orders of magnitude smaller than that of the perturbation generated by the roughness elements ($\sim$ 11% of $\langle u \rangle_z$ at $x = 300$ mm), two clear features can be seen from figure 3.6:

1. The free stream has a streaky character.

2. The existence of an overall trend in which the upper half of the plane shows predominance of low-speed regions, whereas high-speed regions prevail in the bottom half. This effect can also be seen in the contours of u in figure 3.5(a). The reason for such a pattern might be a systematic/periodic variation in the base flow in the form of secondary flows generated by the wind-tunnel contraction.

It would have been interesting to scan over a larger area in order to check for repeatability of these trends and analyse them in more detail but this was not possible owing to physical constraints related to the experimental rig.

This overall trend seems to affect the perturbation generated by the roughness element array. As an example, figure 3.7 shows the perturbation at $x = 300$ mm ($y/k = 1$, $\eta = 1.57$), where the peak of the rms of u' is located.

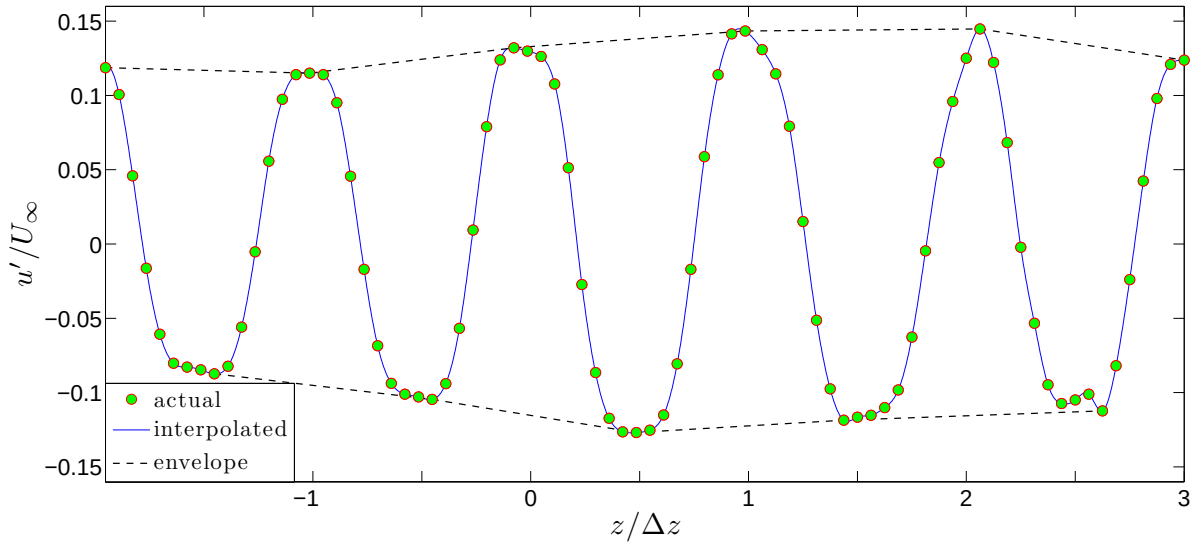


Figure 3.7: u'/U_∞ at $y/k = 1$ ($\eta = 1.57$). LDA data.

The black dashed line connects the maxima (and minima) of the wave, indicating its envelope. It can be seen that there is a modulation of the disturbance. Therefore, variations

in the free stream two orders of magnitude smaller than the amplitude of the perturbation generated by the roughness elements are capable of modulating the perturbation. As mentioned by Fransson *et al.* (2004), changes in the free stream velocity modify the boundary layer scale (δ), therefore altering the ratio k/δ and, as a consequence, the amplitude of the perturbation. Nevertheless, the data were post-processed and analysed by conducting ensemble averages, so that the influence of a non-uniform free stream was reduced.

3.2.2 Overview of the Perturbation

Post-flow visualisation photographs, LDA and FVS data are presented. This qualitative but comprehensive introduction helps understand some features of the perturbation. Regarding the post-flow visualisation technique, the large number of hours seeding the wind-tunnel produced a coherent pattern due to particle deposition on the surface of the plate.

Streaky-Laminar Domain Extension ($215 \lesssim x \lesssim 1000$ mm)

There is a significant feature apparent downstream of the roughness element array. As has been already mentioned, the amplitude of the perturbation in this study is not sufficient to trigger breakdown to turbulence, and that, after a region of growth, it decays due to viscosity. It is interesting to note that the streaky coherence of this decaying perturbation lasts for a long extent downstream. In fact, this coherence is maintained in regions where the HWA data acquired in the unperturbed flow suggest the onset of turbulent flow, as determined by the drop in H at $x \simeq 553$ mm shown in figure 3.4. Similar evidence has already been reported by Fransson *et al.* (2006), investigating the use of streaks to delay the onset of TS wave growth. Figure 3.8 shows a photograph taken near the flap. It can be seen that as far downstream as $x \simeq 1000$ mm, there is still clear evidence of the streaky pattern. This is remarkable because it means that, although triggering quite a large-amplitude perturbation, about one half of the streamwise dimension of the plate has essentially a laminar boundary layer with decaying streamwise vortices.

Streak/Vortex Size in the Decay Region ($x \gtrsim 300$ mm)

There is also a second feature, related to the size of the streaks as they grow and decay downstream. In the decay region, the streaks, or rather their counter-rotating streamwise

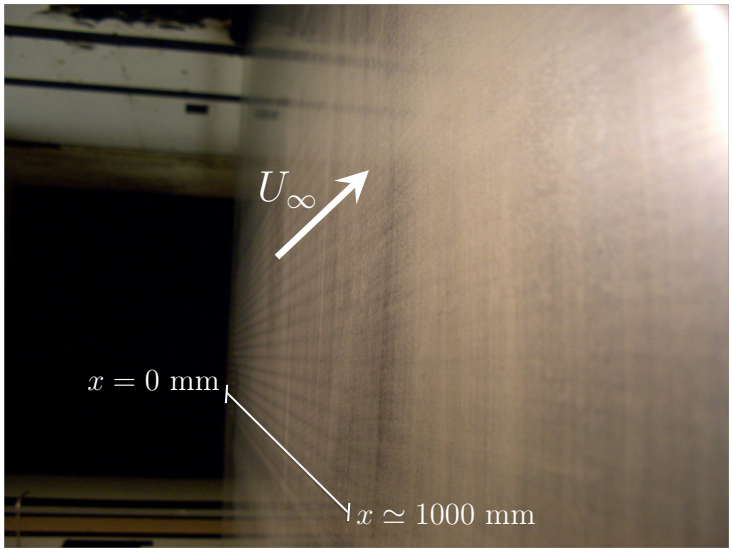
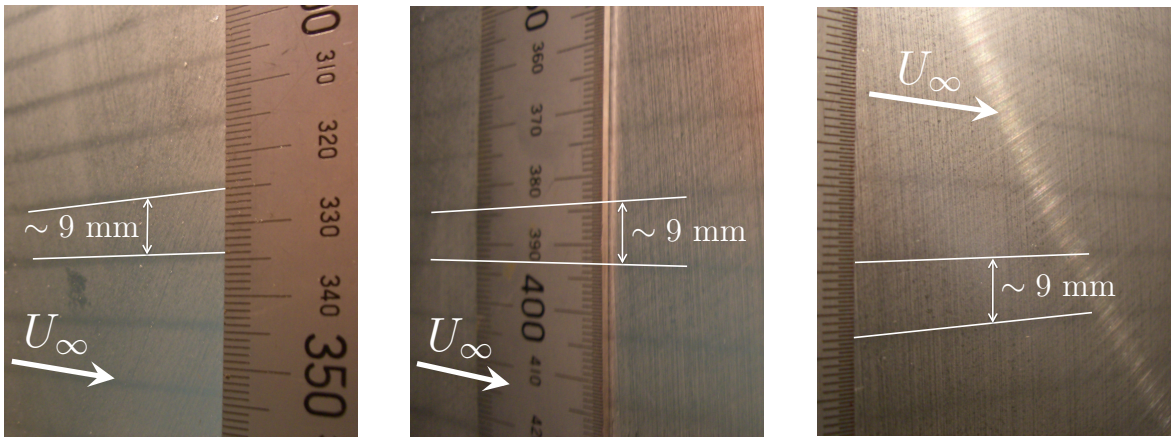


Figure 3.8: Downstream view of streaky pattern by particle-deposition on the flat plate (leading edge at $x = 0$ mm). Note that white line and arrow are not parallels due to the visual effect given by the conic perspective of the photograph.

vortices, appear to reach a constant size. Figure 3.9 illustrates the streaky pattern at locations $x = 300$ mm, $x = 500$ mm, and $x = 700$ mm. It is clear that the width of the deposited-particle regions for the whole streamwise length is fairly constant and approximately equal to 9 mm, that is, close to the roughness spacing ($\Delta z = 10$ mm). Furthermore, the spacing between the centrelines of these regions is 10 mm, i.e. equal to Δz. The particle deposition seems to be due to the downwash motion implied by the streamwise vortices, as they push fluid (and hence particles) towards the wall. It can therefore be hypothesised that the reason for the width of the deposited-particle regions to be approximately constant is that the vortices grow to fill the whole span of the boundary layer covered by the roughness element array. Note that δ_{99} is typically about half Δz, and therefore it is likely that the streamwise vortices fill the whole boundary layer.

Figure 3.10 shows a schematic of the deduced vortex/streak pattern. It shows cross sections at two streamwise locations. The red arrows represent streamwise vortices and the blue thick lines symbolise the particle deposition generated by vortex downwash. The rectangles depicted with dashed lines represent z-locations of the upstream roughness elements. At x_1 the perturbation is growing, whereas at x_2 it is decaying. At x_1, the perturbation is rather a concatenation of discrete disturbances with the vortex pairs having room to grow and expand, while at x_2 the disturbances grow so that the vortex



(a) (b) (c)

Figure 3.9: Streak pattern by particle-deposition on the flat plate, the ruler is placed perpendicular to the streamwise direction; (a) at $x = 300$ mm, (b) at $x = 500$ mm, (c) at $x = 700$ mm. Note that the white lines are not parallels due to the visual effect given by the conic perspective of the photographs.

pairs are adjacent to each other, filling the entire span of the boundary layer covered by the roughness array. At the station where u'-energy reaches its maximum ($x \simeq 300$ mm), the vortices reach the situation described at x_2 (i.e. maximum size), and from thereon they progressively lose strength. This is consistent with what is seen in the post-flow visualisation, where, from $x = 300$ mm onwards, the streak pattern maintains the same shape but becomes progressively lighter (i.e. less particles deposited on the wall) as x increases.

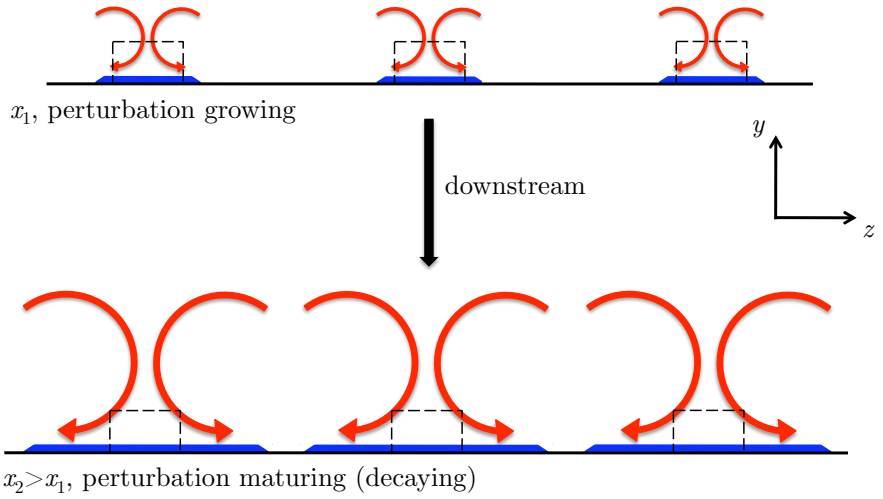


Figure 3.10: Conceptual view of cross-sections at two streamwise locations. At x_1 the perturbation is growing, and at x_2 it is decaying. Red arrows: streamwise vortices; blue thick lines: particle deposition generated by vortex downwash; dashed-line rectangles: silhouettes of roughness elements upstream.

This hypothesis is confirmed by the FVS results. Figure 3.11 shows iso-contours of streamwise streaks (left column) and vorticity (right column) for stations x =250, 300, 500 and 700 mm. It is interesting to note that, at $x = 250$ mm each streak exhibits a pair of closed contours. This seems to be evidence of inner pairs of counter-rotating vortices in addition to the stronger outer ones, as will be shown later on. As x increases, vorticity and streaks expand in both spanwise and wall-normal directions. It seems that, further downstream, the spanwise growth becomes slower. To further analyse this, the spanwise separation, s_z, between the vorticity minimum of a vortex pair and the vorticity maximum of an adjacent vortex is tracked. Figure 3.12(a) shows s_z for the x-stations shown in figure 3.11. The expansion in the wall-normal direction is also analysed by tracking the separation, s_y, of those maxima/minima from the wall, as shown in figure 3.12(b). The purpose of showing exponential fits is only to indicate the typical decay of a vortex in a viscous fluid.

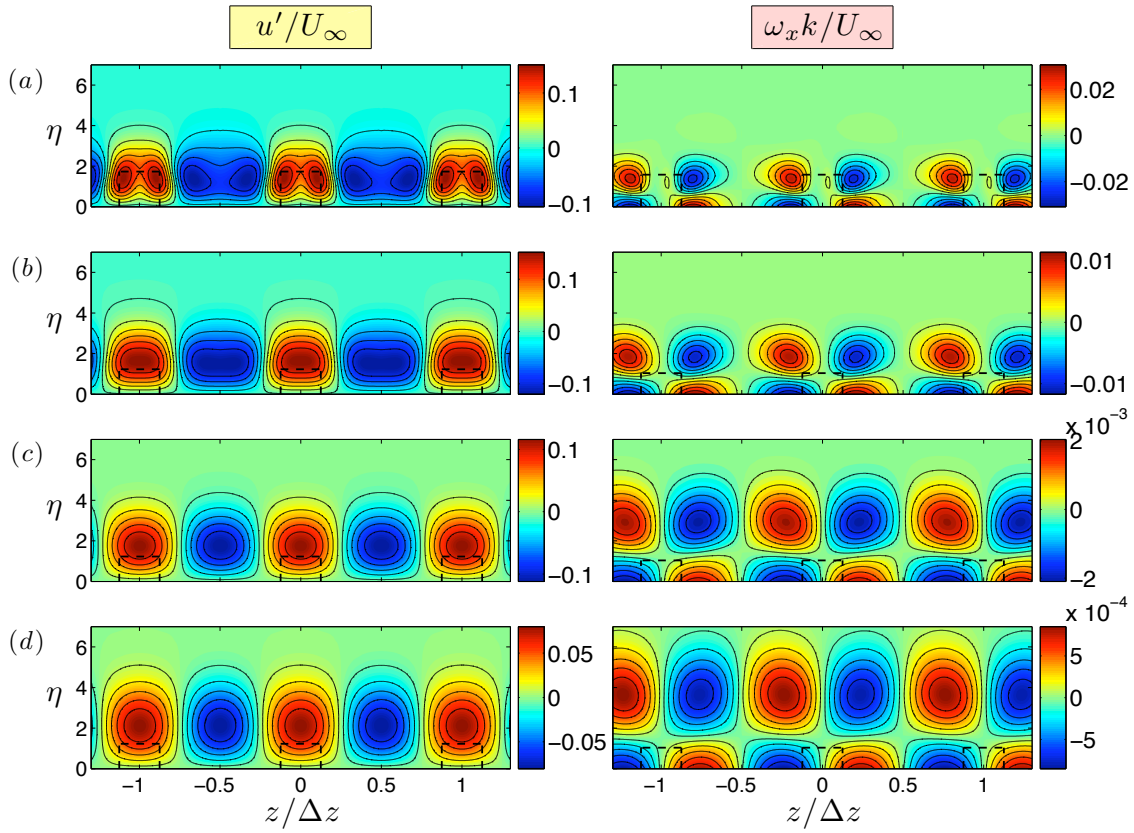
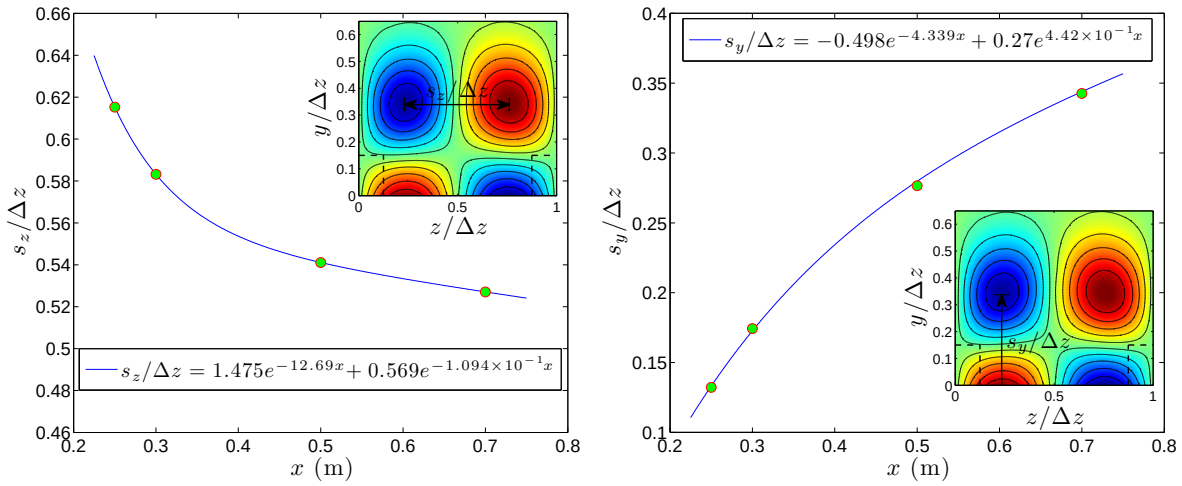


Figure 3.11: Iso-contours of streamwise streaks (left column) and vorticity (right column) from the FVS data at various x-stations. Black-dashed lines indicate the spanwise positions of the roughness elements upstream; (a) $x = 250$ mm, (b) $x = 300$ mm, (c) $x = 500$ mm, (d) $x = 700$ mm



(a) (b)

Figure 3.12: Separations of streamwise vorticity maxima/minima in the viscous decay region (from the FVS data); (a) spanwise, (b) wall-normal.

Flow in the Immediate Vicinity of the Roughness Elements

According to Fransson *et al.* (2004), the ratio k/δ is one of the factors that determines the streak pattern downstream of the roughness elements. The smaller k/δ is, the less incoming spanwise vorticity is strained into streamwise vorticity, and hence the weaker the vortices downstream are. For a sufficiently small value of k/δ, the vortices are not strong enough to overcome the wake behind the roughness element, resulting in a low-speed streak aligned with the element, as seen for instance in White (2002). The flow in the vicinity of the roughness elements is subject to the local blockage due to the elements and shows two major features: a wake (re-circulation) region and a streamwise-vorticity formation mechanism. As can be seen from figure 3.13, the trace left by seeding deposition indicates a stagnation zone upstream of the elements, a low-speed region around them and a twin-core wake behind them (of approximately two roughness diameters in size). The trace reveals that, further downstream, the wake first shrinks (region of re-circulation) and then widens (region of predominant streamwise vorticity).

Figure 3.14 shows, from the FVS data, an iso-surface of positive $Q = \nabla^2 p/2\rho$, the second invariant of the tensor $\nabla\vec{u}$, employed as a criterion (the Q-criterion) for vortex core detection (Hunt *et al.*, 1988). A system of two pairs of counter-rotating streamwise vortices per roughness element can be seen. The outer pair seems to be the result of the natural spanwise vorticity of the boundary layer rolling up around the roughness element

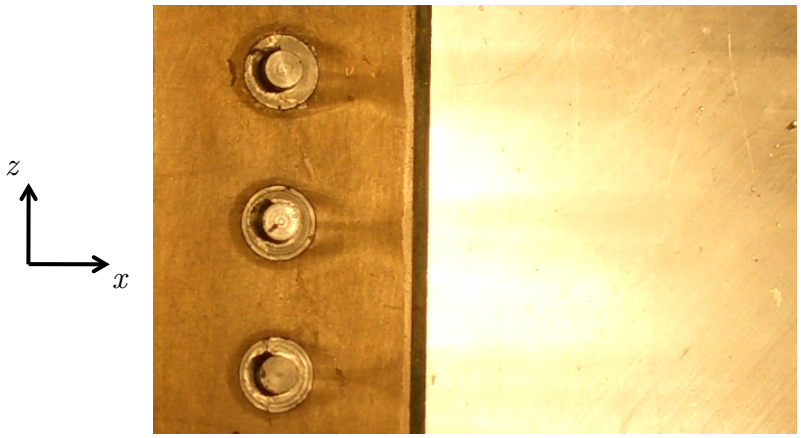


Figure 3.13: Post-flow visualisation by seeding deposition in the vicinity of the roughness element array.

(an annular vortex surrounding the front part of the roughness element). The inner pair shows certain resemblance with the tip vortices emerging from the free face of a cylinder attached to a wall identified by Pattenden *et al.* (2005).

Rizzetta & Visbal (2007) also identified a system of two pairs of streamwise vortices, although in their case they are co-rotating instead of counter-rotating. This discrepancy may be due to the fact of having a much shallower roughness element (k/d much smaller), despite having similar Re_k. Their vortices are all born from the roll-up of the natural vorticity of the upstream boundary layer. Their roughness-wake mode does not seem as strong as that of the present study, not showing any evidences of emergence of tip vortices.

For a clearer illustration of the features present in the flow around the roughness element, in the wake region and further downstream, figure 3.15, from the FVS data, shows surface streamlines on a XZ-plane near the wall. It replicates the pattern shown by the post-flow visualisation and reinforces the reasoning elaborated from figure 3.14. First, the stagnation zone upstream of the element and the low-speed region around can clearly be seen. It also reveals a reversed-flow region between the stagnation zone and the front of the roughness element, indicating the evidence of vortex formation. Then, the flow consequently accelerates outside the low-speed region, reaching a maximum velocity between roughness elements (at the streamwise location aligned with their centres). Once this point is passed, the flow decelerates as the wake shrinks (streamlines expanding outside the wake), accelerating again as the wake starts widening (streamlines compressing outside the wake). An important consequence of this wake-shrinking process

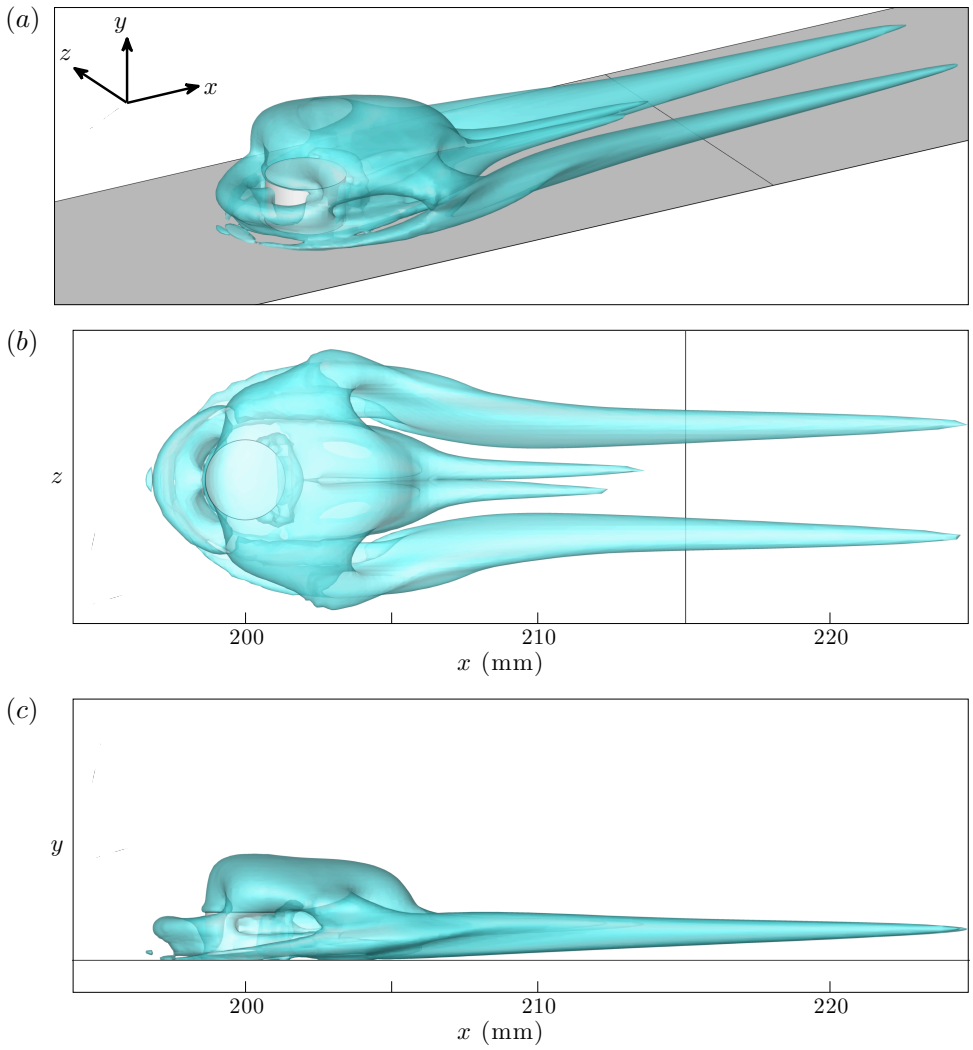


Figure 3.14: Views of vortex cores by means of plotting an iso-surface of $Q > 0$ (from the FVS data) in the vicinity of a roughness element; (*a*) perspective, (*b*) top, (*c*) side. The black solid line depicted in (*a*) and (*b*) indicates the approximate location of the start of the u'-energy growth ($x \simeq 215$ mm).

is the non-uniform expansion between streamlines in the spanwise direction, or in other words, the inducement of $\partial u/\partial z$ (hence the appearance of ω_y). As the wake starts widening, the streamline compression is strongly concentrated at the edge of the wake (indicating a local zone of low pressure, and therefore the presence of the core of a streamwise vortex), remaining like that as the perturbation evolves downstream. This, alongside the shrinking-widening process of the wake and the reversed-flow region in front of the roughness element, is another evidence of the formation of the outer pair of counter-rotating streamwise vortices.

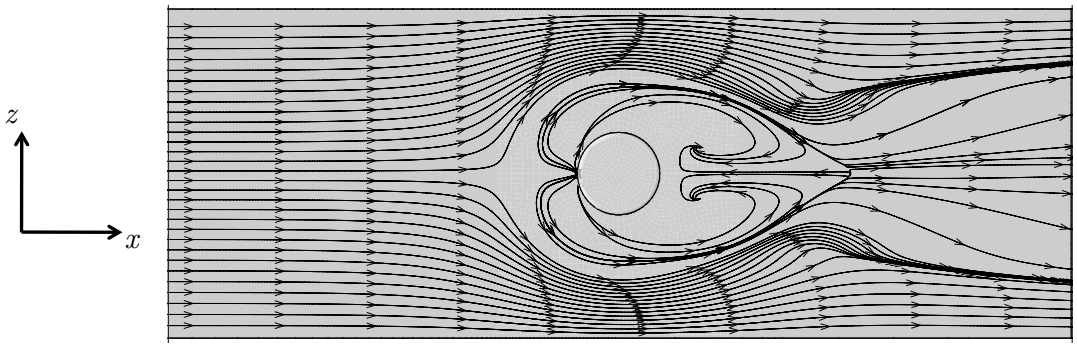


Figure 3.15: Top view of streamlines in the vicinity of the roughness element array on a xz-plane near the wall. FVS data.

Figure 3.16 shows LDA iso-contours of u' and v' on a XZ-plane at $y/k = 1$. It can be seen that the wake region is clearly characterised by a noticeable deficit of u'. Just behind the roughness elements (within one element diameter), the u' deficit co-exists with a core of upwash motion (positive v'). As the wake moves downstream and becomes narrower, the downwash motion that surrounds the upwash motion becomes wider. The former seems to reach its maximum width approximately where the wake stops narrowing and starts widening. Once this point is passed, the side regions of downwash-motion become thinner as the central region of upwash-motion widens in between.

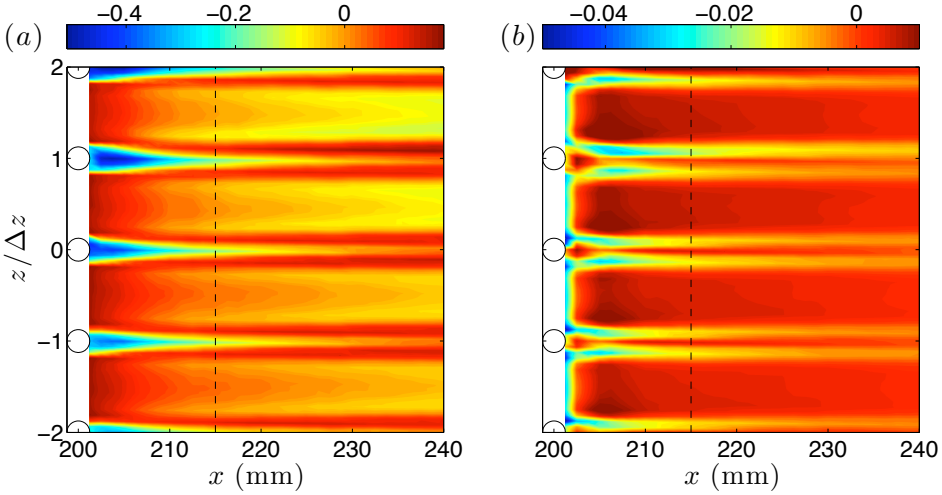


Figure 3.16: LDA iso-contours on a xz-plane at $y/k = 1$; (a) u'/U_∞, (b) v'/U_∞. The dashed line indicates the approximate location of the start of u'-energy growth.

From figure 3.16, it is observed that the growth in u'-energy commences when the downwash and upwash regions are similar in width to each other, that is, when the inner vortex pair fully overcomes the wake region. It is interesting to note that this arrangement

of two pairs of streamwise vortices is similar to that produced by an oscillating dimple (Dearing *et al.*, 2007).

Further evidence of the presence of this inner vortex pair in the early stages of the formation of the disturbance can be extracted from the post-flow visualisation. Figure 3.17 shows a set of photographs in which the inner upwash-motion central region, shown as a thin line of reduced seeding deposition (the red arrows in the figure), can be clearly identified.

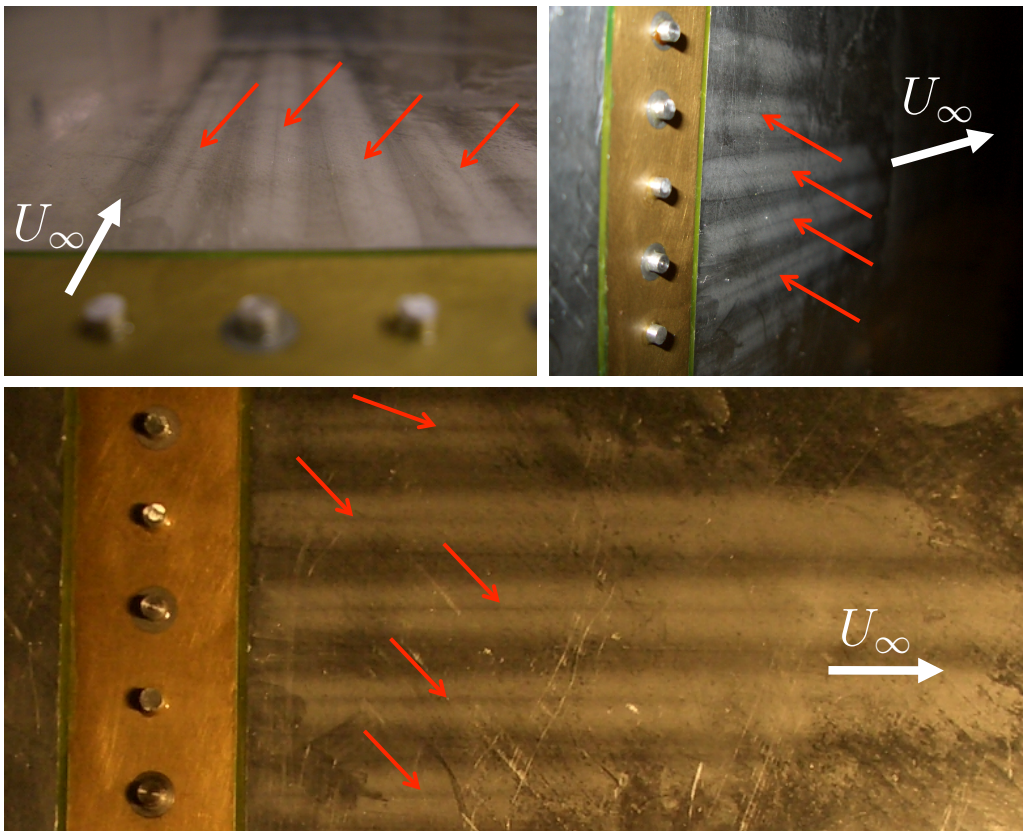


Figure 3.17: Post-flow visualisation photographs showing the existence of a inner streamwise counter-rotating vortex pair, revealed by a thin line of reduced seeding deposition denoting an upwash region (where the red arrows point), in the early stage of the formation of the disturbance.

Fransson *et al.* (2004), Lavoie *et al.* (2008), and others, have claimed that the formation of the outer counter-rotating vortex pair is a result of the incoming natural spanwise vorticity of the boundary layer being strained by the presence of the roughness element and wrapped around its upstream edge. Figure 3.18(a) shows FVS iso-contours of wall-normal velocity on a XZ-plane at $y/k = 0.67 \times 10^{-3}$. This shows a similar result. There is a

downwash region surrounding the upstream edge of the roughness element, and in turn being surrounded by an outer upwash region. This, together with the stagnation region (figure 3.15), is clear evidence of a vortical structure being wrapped around the upstream edge of the roughness element and then turned downstream, figure 3.18(b).

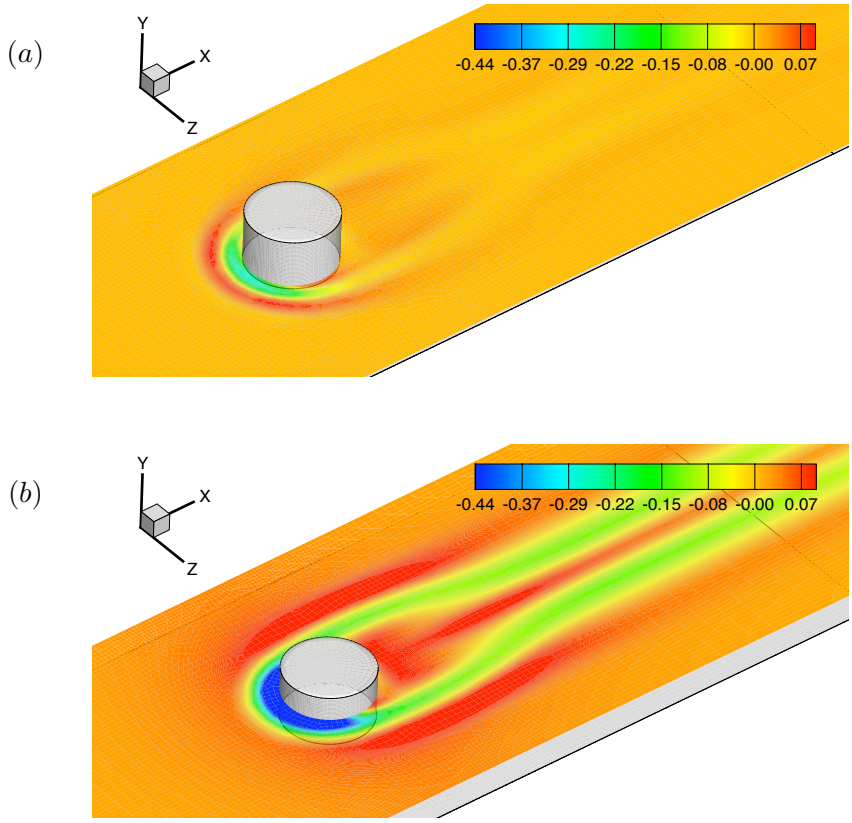


Figure 3.18: Iso-contours of v' (m/s), from the FVS data, on two xz-planes; (a) at $y/k = 0.67 \times 10^{-3}$, ($b$) at $y/k = 0.5$.

LDA data upstream of the roughness element array were acquired to compare with the FVS data. Figure 3.19 shows LDA iso-contours of u and v' on two xy-planes upstream of the array, figures (a) and (c) corresponding to a plane aligned with a roughness element centre and (b) and (d) corresponding to a plane equidistant from two elements. In figure 3.19(a) it can be seen that u shows a deceleration in the vicinity of the roughness element. A recirculation region can be seen near the wall. On the other hand, in 3.19(b) the u component experiences a slight acceleration immediately upstream of the roughness element. Both figures are in reasonably good agreement with the FVS data (figure 3.18). 3.19(c) shows the v' component near the wall and in the vicinity of the roughness element.

This is also in good agreement with the FVS results, where an annulus of upwash motion surrounds an inner annulus of downwash motion. 3.19(d) shows that the influence of the roughness elements on v' is minimal in that zone. Unfortunately, owing to laser beam impingement on the roughness elements, reliable data could not be acquired nearer the array. That information is provided by the FVS data, see figure 3.20. Note the good agreement in the flow features on those planes between LDA and FVS data.

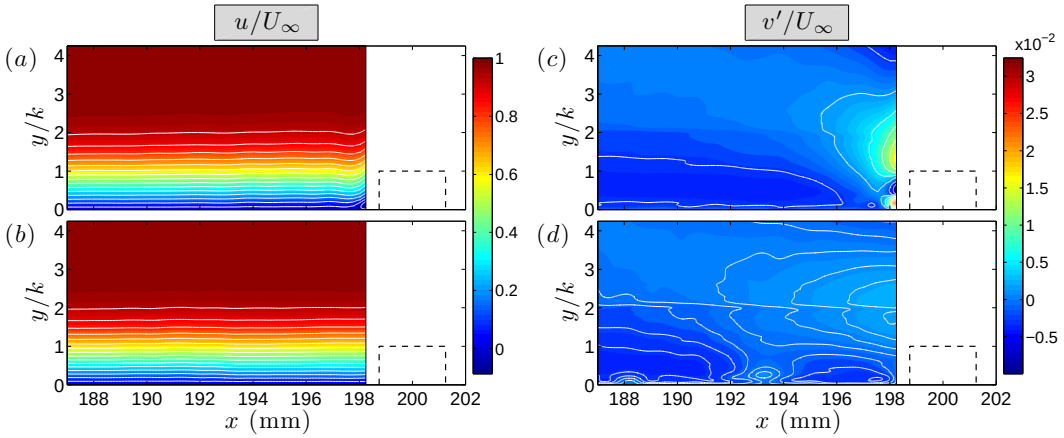


Figure 3.19: LDA iso-contours of u and v' on xy-planes upstream of the roughness element array; (a) and (c) aligned with a roughness centre, (b) and (d) equidistant between roughness elements.

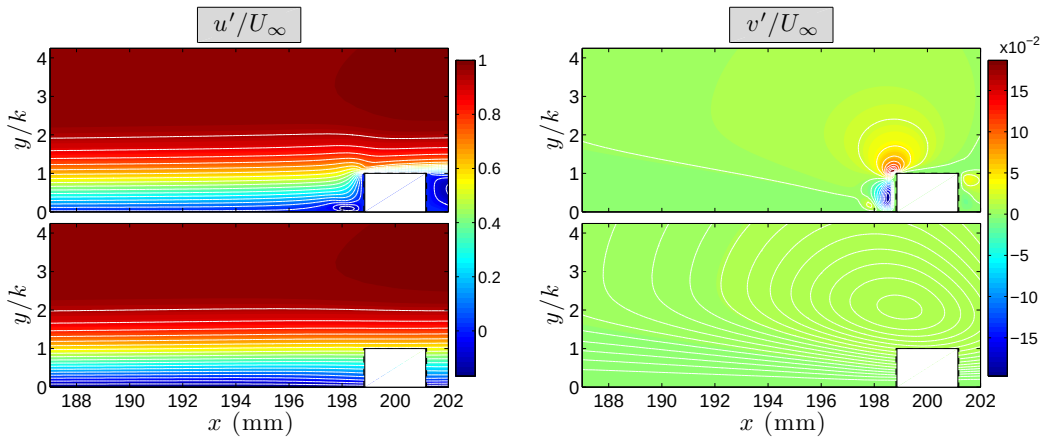


Figure 3.20: FVS iso-contours of u and v' on xy-planes upstream of the roughness element array; (a) and (c) aligned with a roughness centre, (b) and (d) equidistant between roughness elements.

Energy Growth Region

Figure 3.21 shows LDA iso-contours of u' and v' in the growth region (these are the same data shown in figure 3.16 but continued up to $x = 325$ mm). Both u' and v' fields

show, as expected, a similar shape, since upwash (downwash) motion implies a pattern of alternating low-(high-)speed streaks. However, the amplitude of u' increases in this region whereas that of v' decreases monotonically. An interesting feature is that the streamwise extent of the growth appears to coincide with the "life time" of the inner vortex pair. In other words, the growth region seems to start when the inner vortex pair fully overcomes the wake region. And it seems to end when the inner vortex pair dies out.

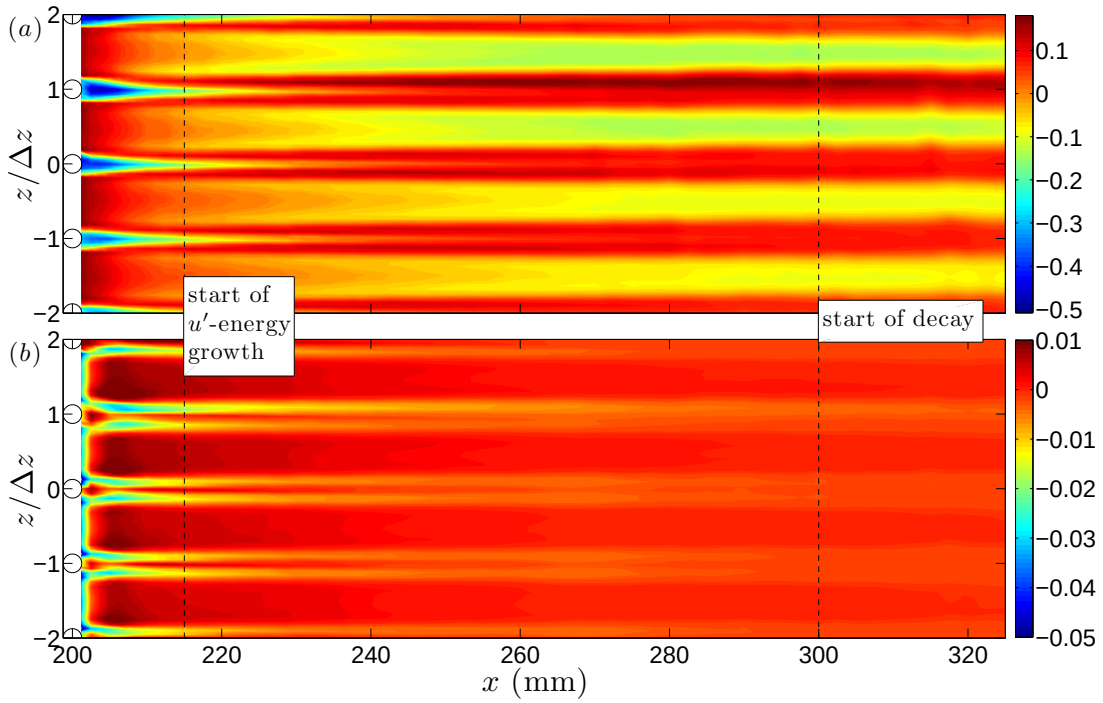


Figure 3.21: LDA iso-contours of (a) u'/U_∞ and (b) v'/U_∞ on a xz-plane at $y/k = 1$.

3.2.3 Mean Boundary Layer Profiles

Figures 3.22(a) and 3.22(b) show those profiles, from the LDA data, in which the wall-normal axis is non-dimensionalised respectively by the roughness element height and the self-similarity variable.

It can be seen that the results at $x = 100$ mm show a remarkable agreement with Blasius, with no evidence of perturbation. However, a consistent region of velocity deficit can be seen not only in the wake region, but also throughout the u'-energy growth region. For the peak u'-energy x-location ($x = 300$ mm), a slight deficit with respect to Blasius

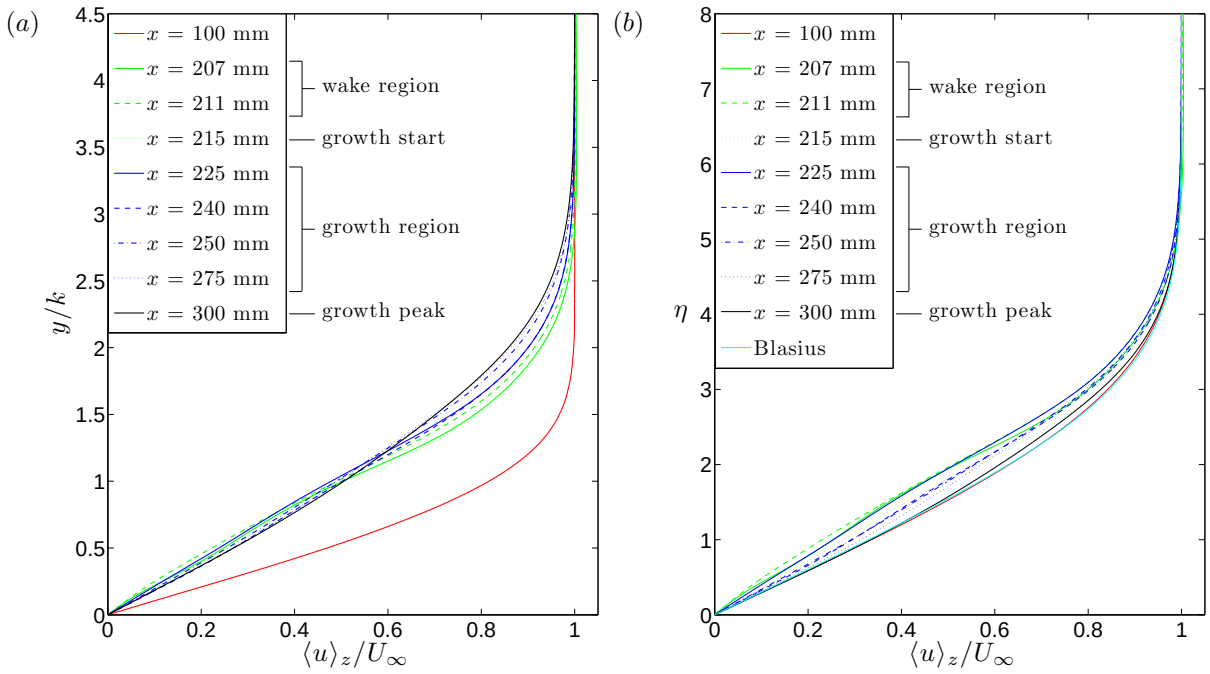


Figure 3.22: Mean boundary-layer profiles at all the x-stations where LDA data were acquired; wall-normal direction non-dimensionalised by, (a) the roughness-element height, (b) the self-similarity variable.

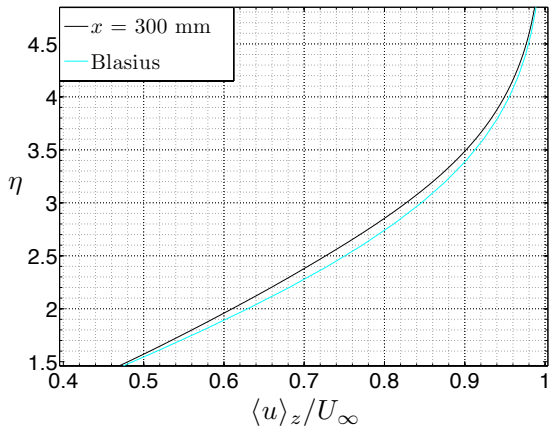


Figure 3.23: Detailed view of figure 3.22(b), showing only data at x =300 mm and Blasius.

persists (figure 3.23). This is also apparent in the data of Lavoie *et al.* (2008), who show results from $x = 300$ mm downstream and, focusing on x-locations in the decay region, show good agreement between their mean boundary layer profiles and Blasius. However, as can be seen here, the deficit at $x = 300$ mm is not due to experimental uncertainty, but a result of the perturbation. This suggests that the base flow is an energy source for the perturbation to grow, with the velocity deficit decreasing in the growth region.

3.2.4 Ensemble Averages

The full-span data were subsequently ensemble-averaged over an integer number (between 3 and 5) of spanwise intervals equal to the fundamental wavelength or the roughness element spacing, Δz. This was done to reduce experimental uncertainty. As an example, figure 3.24 shows full-span iso-contours of u, u' and v' data at $x = 300$ mm (vertical solid black lines indicate the divisions over which the ensemble average was performed), and figure 3.25 the iso-contours of their corresponding ensemble averages.

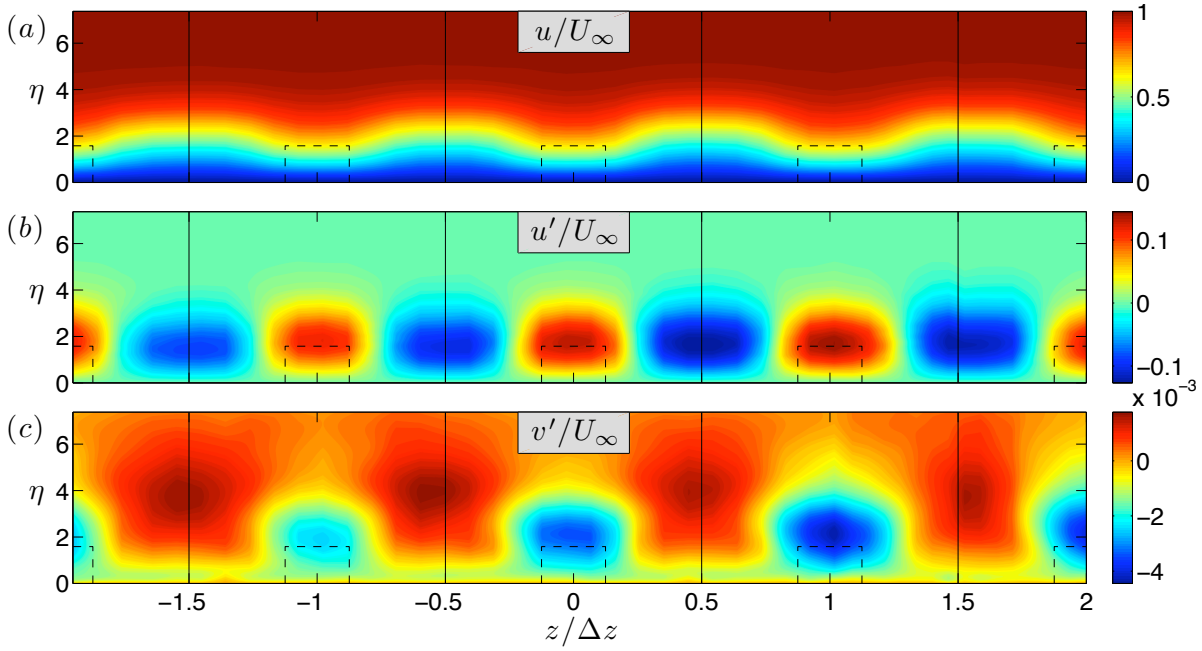


Figure 3.24: Iso-contours of full-span data of (a) u, (b) u' and (c) v' data at $x = 300$ mm. Vertical solid black lines indicate the divisions over which the wavelength-average was performed. Dashed lines indicate the roughness element positions.

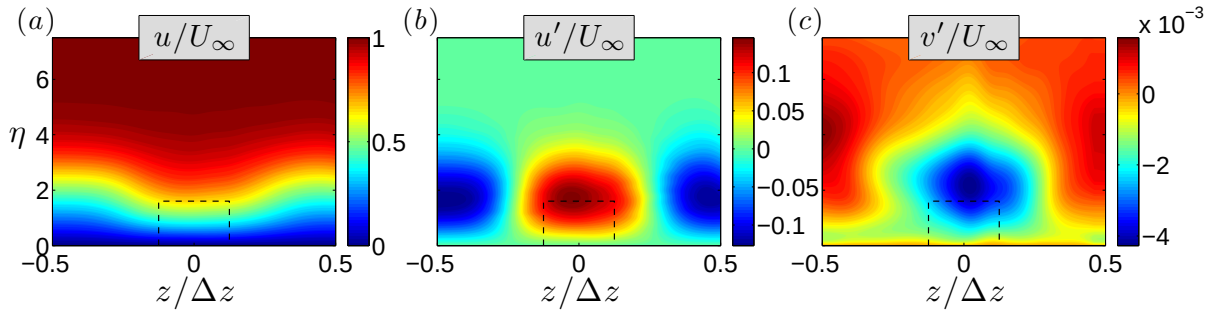


Figure 3.25: Iso-contours of ensemble averages of (a) u, (b) u' and (c) v' at $x = 300$ mm, from the data shown in figure 3.24.

The ensemble-averaged iso-contours in yz-planes of u, u', v', and the angle $\theta = \tan^{-1}(v'/u')$, as well as $\partial v'/\partial z$, $\partial u'/\partial z$ and $\partial u'/\partial y$, as components of the vorticities ω'_x, ω'_y and ω'_z respectively, are now considered in detail.

- **Iso-contours of ensemble-averaged u**:

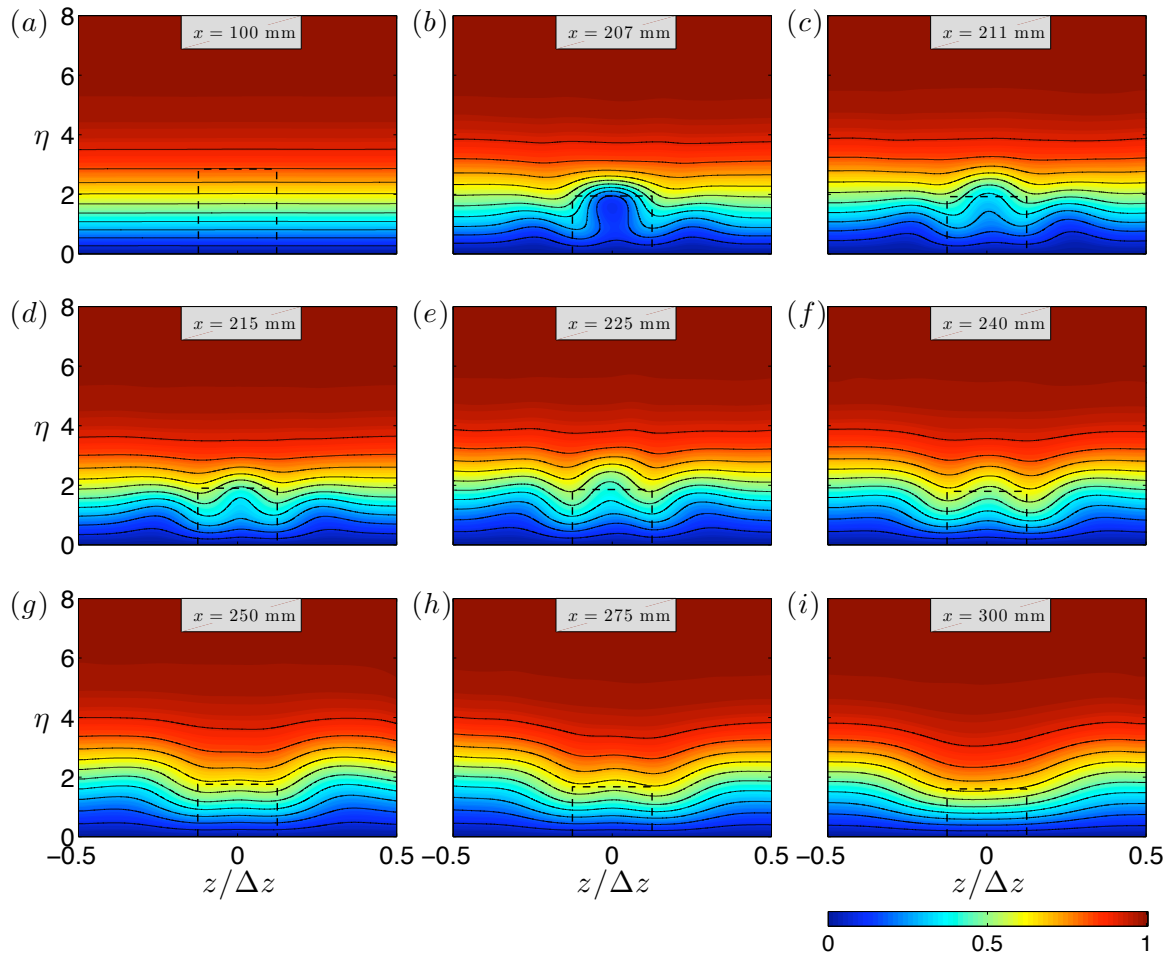


Figure 3.26: Iso-contours of ensemble-averaged u/U_∞; x = (a) 100 mm, (b) 207 mm, (c) 211 mm, (d) 215 mm, (e) 225 mm, (f) 240 mm, (g) 250 mm, (h) 275 mm, (i) 300 mm. Dashed lines: roughness element (at $x = 200$ mm).

Figure 3.26 shows features consistent with results of the previous section. The roughness elements are at $x = 200$ mm. At $x = 100$ mm evidence of the downstream perturbation has not yet appeared. The wake region, characterised by a velocity deficit, is clear at $x = 207$ mm. It is interesting to note that the height of this deficit is approximately the same as that of the roughness element. As will be shown later, the u'-energy starts to grow at $x \simeq 215$ mm. At this location it can be seen that the downwash region behind

the roughness element starts to appear, and becomes stronger further downstream. This downwash region is created by the outer counter-rotating vortex pair, a perturbation with a spanwise wavelength $\lambda_z = \Delta z$. Therefore it can be concluded that the u'-energy starts to grow as the fundamental wavelength Δz. A spectral analysis follows this section.

- **Iso-contours of ensemble-averaged u'**:

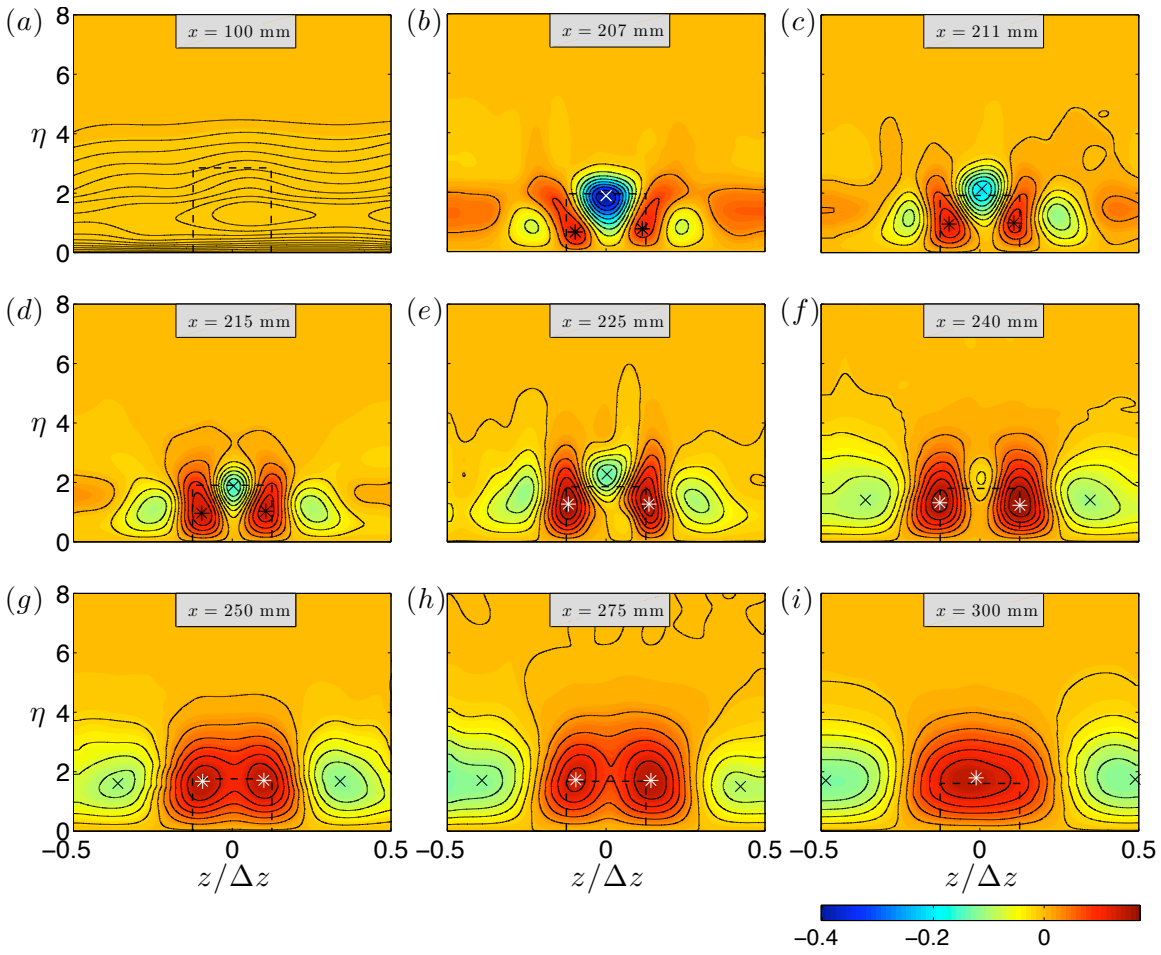


Figure 3.27: Iso-contours of ensemble-averaged u'/U_∞; x = (a) 100 mm, (b) 207 mm, (c) 211 mm, (d) 215 mm, (e) 225 mm, (f) 240 mm, (g) 250 mm, (h) 275 mm, (i) 300 mm. Dashed lines: roughness element (at $x = 200$ mm).

Figure 3.27 shows how the perturbation evolves through a competition of structures occurring in the wake region. As soon as the high-speed cores reach an amplitude similar to that of the central low-speed one, the u'-energy starts to grow. Figure 3.28 shows maxima and minima (in absolute values) of the corresponding high- and low-speed cores of u' at each x-location (marked in figure 3.27 as stars and crosses respectively).

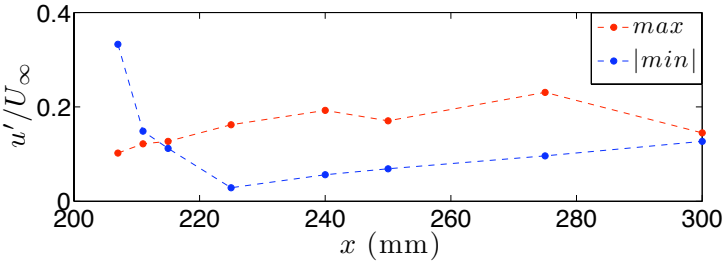


Figure 3.28: Maxima and minima (absolute values) of u'/U_∞ at each x-location.

- **Iso-contours of ensemble-averaged v':**

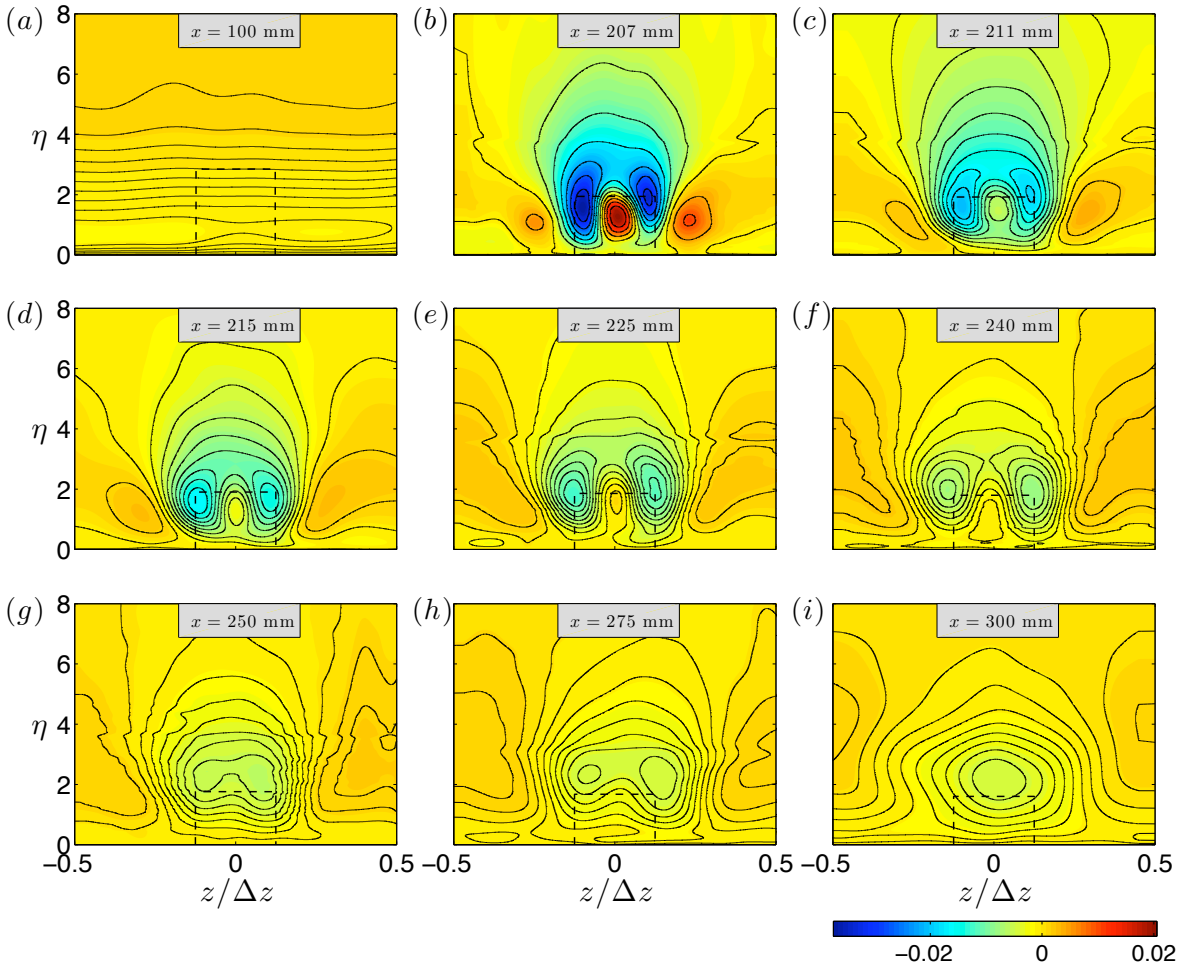


Figure 3.29: Iso-contours of ensemble-averaged v'/U_∞; x = (*a*) 100 mm, (*b*) 207 mm, (*c*) 211 mm, (*d*) 215 mm, (*e*) 225 mm, (*f*) 240 mm, (*g*) 250 mm, (*h*) 275 mm, (*i*) 300 mm. Dashed lines: roughness element (at $x = 200$ mm).

Figure 3.29 illustrates the downwash and upwash distributions, which are consistent with the interpretations made from the iso-contour maps of both u and u'. Again, the u'-energy

region seems to be characterised by the suppression of the upwash core in the plane of the roughness element, as well as the emergence of a dominant wavelength Δz for v'. Interestingly, the maximum and minimum values of v' evolve towards different wall-normal locations. This can also be seen in figure 3.25: for instance at $x = 300$ mm, both maxima and minima of u' are located at $\eta \simeq 2$, whereas in the case of v', the minimum is at $\eta \simeq 2$ but the maximum is at $\eta \simeq 4$. Furthermore, the amplitude of the perturbation decays monotonically, figures 3.21 and 3.29.

- **Iso-contours of ensemble-averaged $\partial v'/\partial z$**:

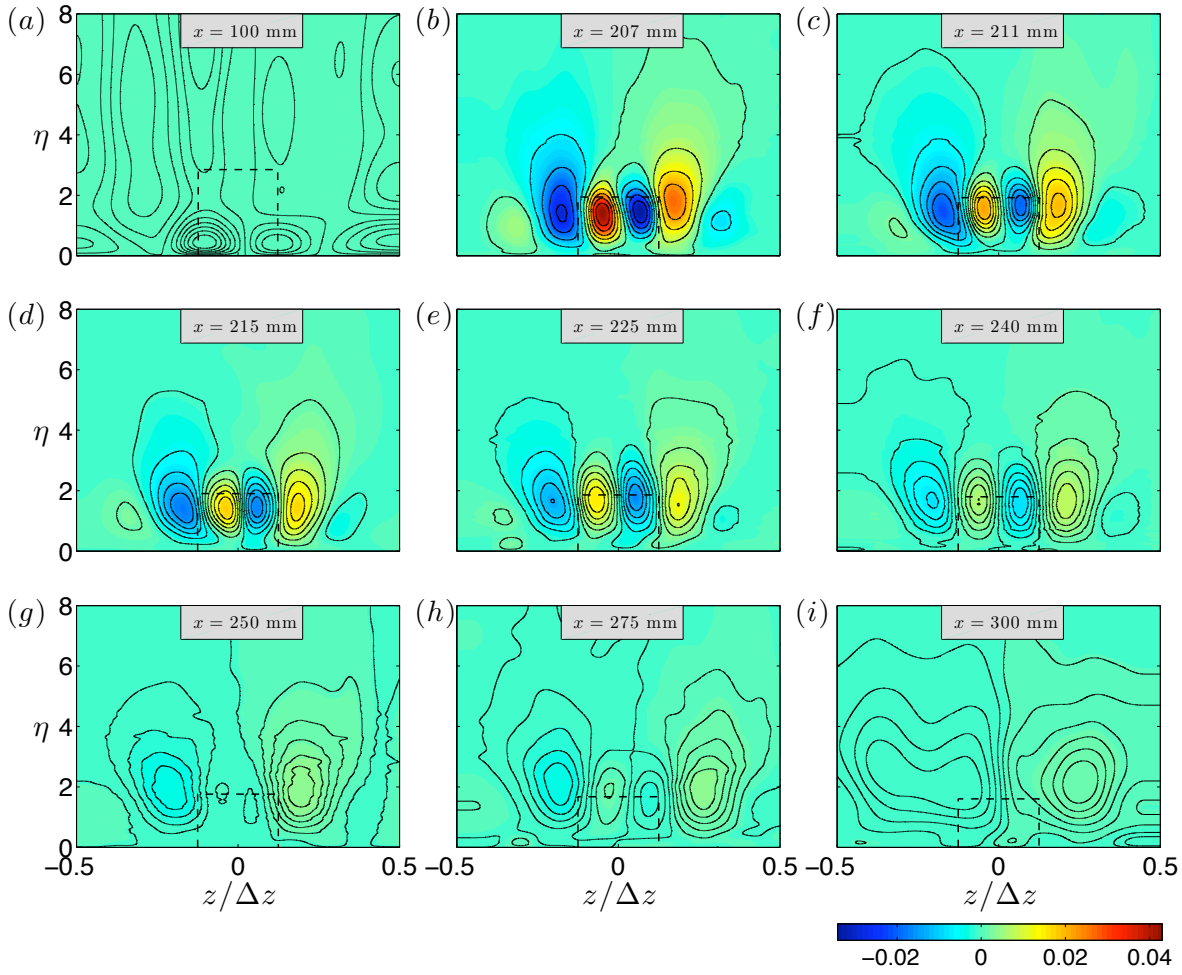


Figure 3.30: Iso-contours of ensemble-averaged $(\partial v'/\partial z)/(U_\infty/\Delta z)$; $x =$ (*a*) 100 mm, (*b*) 207 mm, (*c*) 211 mm, (*d*) 215 mm, (*e*) 225 mm, (*f*) 240 mm, (*g*) 250 mm, (*h*) 275 mm, (*i*) 300 mm. Dashed lines: roughness element (at $x = 200$ mm).

Figure 3.30 shows iso-contours of $\partial v'/\partial z$ non-dimensionalised by $U_\infty/\Delta z$. It can also be seen that, up to $x = 250$ mm, the perturbation is characterised by two high-speed

streaks growing on each side of the wake core. Both spanwise and wall-normal scales of this structure appear approximately constant up to $x = 250$ mm. This holds not only for the u' contours, but also for those of v' and $\partial v'/\partial z$. Then, downstream of $x = 250$ mm, this structure starts to merge and the dual-core feature disappears to become a single high-speed streak with one single peak. As v', $\partial v'/\partial z$ decays monotonically, and at $x \simeq 300$ mm it is near zero, indicating that the perturbation has run out of "engine" to continue growing, implying the end of the u'-energy growth region. Note that $\partial v'/\partial z$ has not been considered to be approximate to ω'_x since, as noticed from the FVS results, $\partial v'/\partial z \sim \partial w'/\partial y$.

- **Iso-contours of ensemble-averaged $\boldsymbol{\partial u'/\partial z}$ ($\boldsymbol{\simeq \omega'_y}$)**:

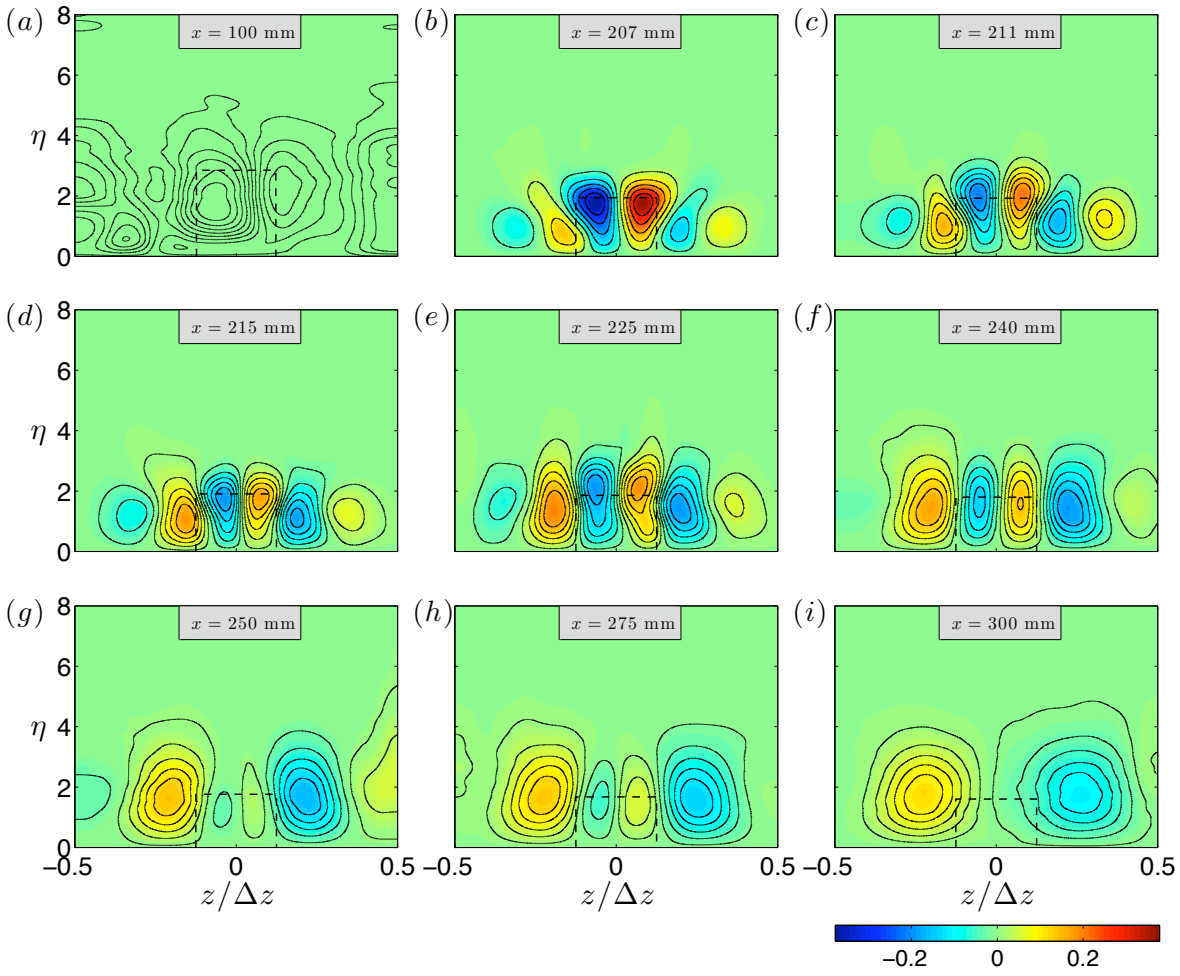


Figure 3.31: Iso-contours of ensemble-averaged $(\partial u'/\partial z)/(U_\infty/\Delta z)$; $x =$ (a) 100 mm, (b) 207 mm, (c) 211 mm, (d) 215 mm, (e) 225 mm, (f) 240 mm, (g) 250 mm, (h) 275 mm, (i) 300 mm. Dashed lines: roughness element (at $x = 200$ mm).

Figure 3.31 shows iso-contours of $\partial u'/\partial z$ non-dimensionalised by $U_\infty/\Delta z$. It reveals features similar to those of $(\partial v'/\partial z)/(U_\infty/\Delta z)$, namely that both the spanwise and wall-normal scales of the perturbation maintain approximately constant up to $x = 250$ mm, and further downstream the outer structure starts to overcome the inner one. Interestingly, the sign of $\partial u'/\partial z$ is consistently opposite to that of $\partial v'/\partial z$. Noting that, first, $\omega_y = \partial u'/\partial z - \partial w'/\partial x$ and second, that $\partial w'/\partial x \ll \partial u'/\partial z$, it can be said that $\omega_y \simeq \partial u'/\partial z$. According to figure 3.31, it can be concluded that the system formed by an inner pair of counter-rotating streamwise vortices surrounded by an outer pair is consistent with the distribution of ω_y.

- **Iso-contours of ensemble-averaged $\boldsymbol{\partial u'/\partial y}$ ($\boldsymbol{\simeq -\omega_z'}$)**:

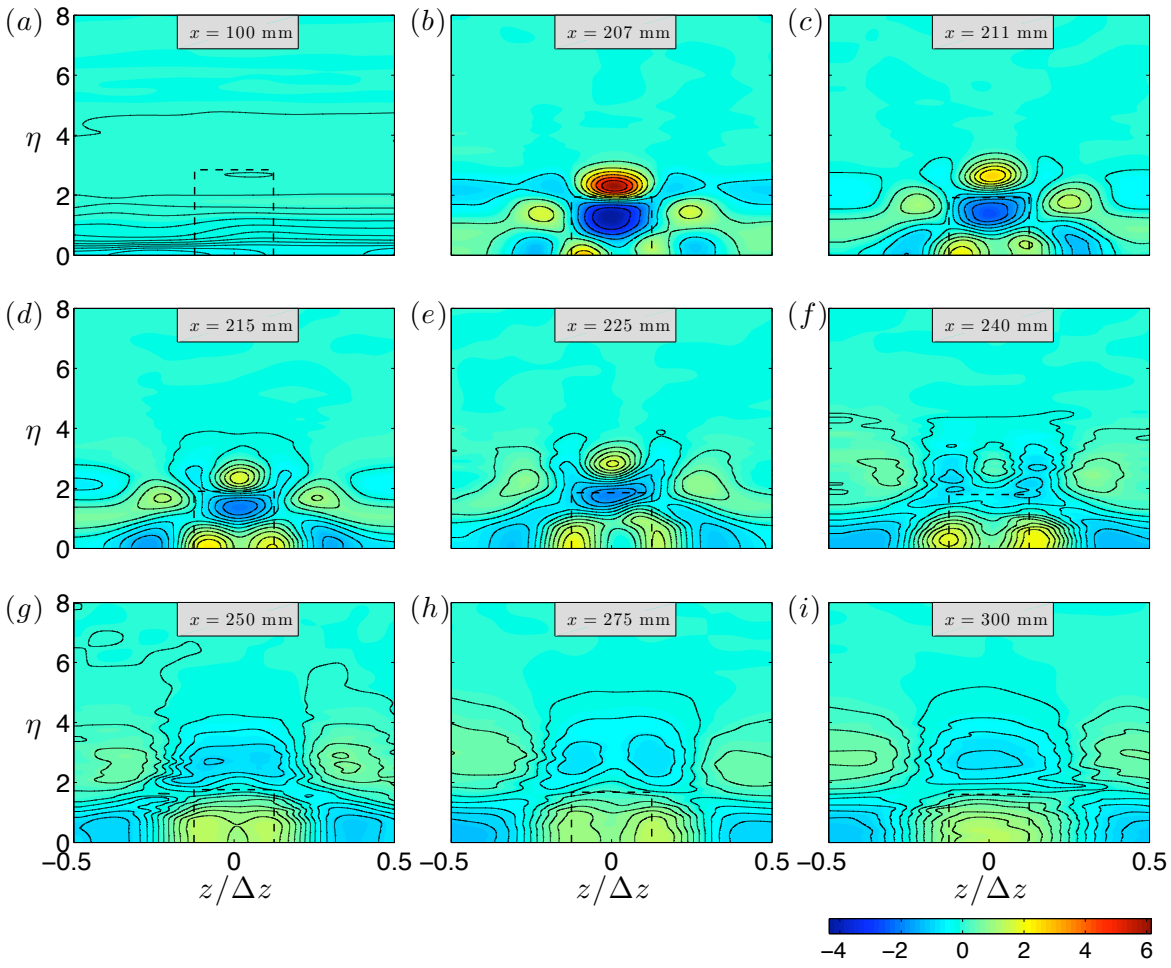


Figure 3.32: Iso-contours of ensemble-averaged $(\partial u'/\partial y)/(U_\infty/\Delta z)$; $x =$ (a) 100 mm, (b) 207 mm, (c) 211 mm, (d) 215 mm, (e) 225 mm, (f) 240 mm, (g) 250 mm, (h) 275 mm, (i) 300 mm. Dashed lines: roughness element (at $x = 200$ mm).

Figure 3.32 depicts iso-contours of $\partial u'/\partial y$ non-dimensionalised by $U_\infty/\Delta z$. It clearly shows that a strong shear layer forms right behind the roughness element, in the same fashion as identified for instance by White (2002) or Rizzetta & Visbal (2007) but for smaller Re_k. The centreline of this shear layer coincides in height with the top of the roughness element. The magnitude of $\partial u'/\partial y$ falls with x and, interestingly, changes signs in the zone behind the roughness element from $x \simeq 250$ mm downstream, precisely where the inner pair of counter-rotating vortices is overcome by the outer one. The approximation $\omega_z = \partial v'/\partial x - \partial u'/\partial y \simeq -\partial u'/\partial y$ is considered valid because $|\partial v'/\partial x| \ll |\partial u'/\partial y|$.

- ***Rms* profiles**:

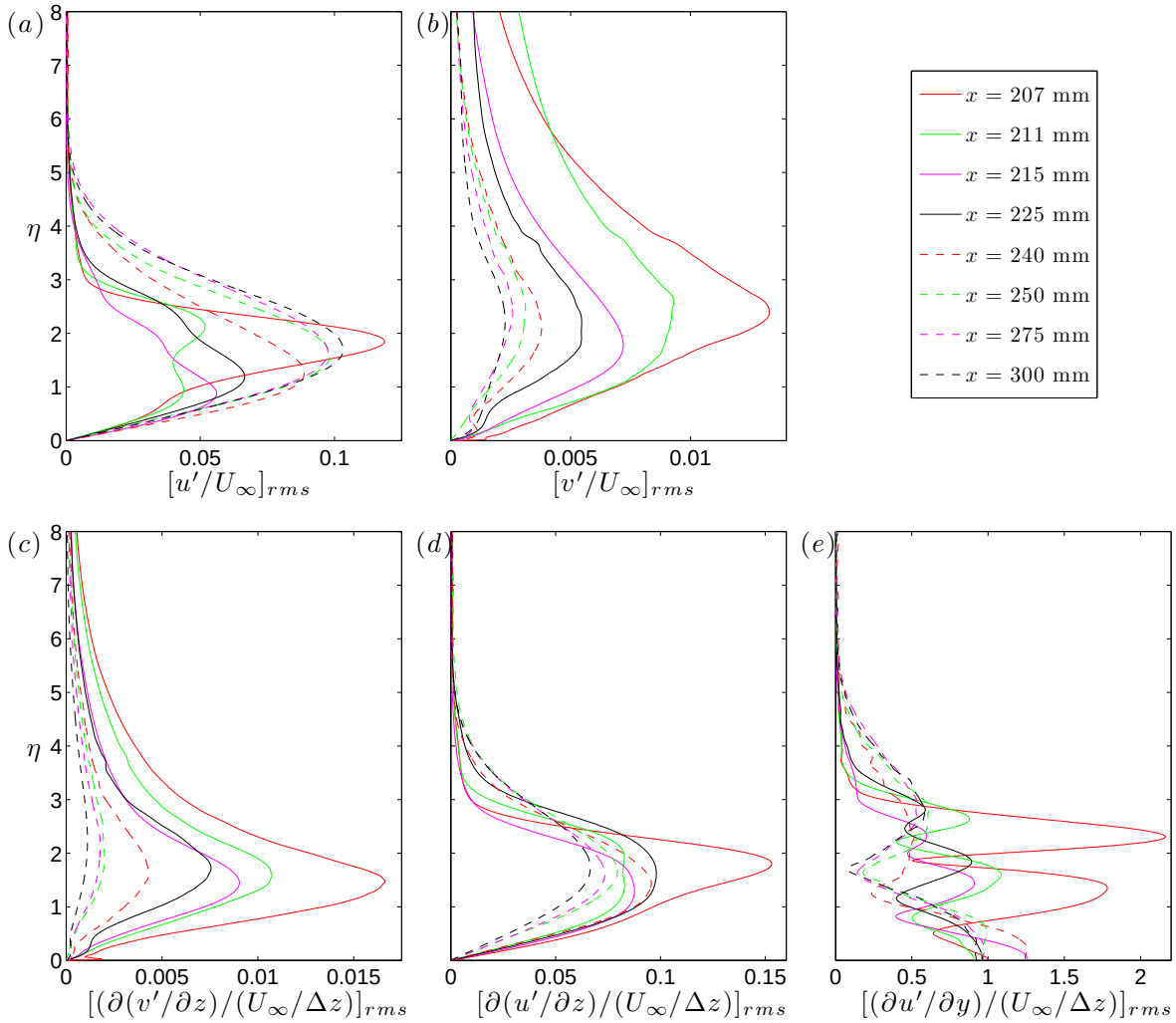


Figure 3.33: Wall-normal profiles of the spanwise *rms* of, (*a*) u', (*b*) v', (*c*) $\partial v'/\partial z$, (*d*) $\partial u'/\partial z$, and (*e*) $\partial y'/\partial y$.

Figure 3.33 shows the wall-normal profiles of *rms* quantities (*a*) u', (*b*) v', (*c*) $\partial v'/\partial z$, (*d*) $\partial u'/\partial z$, and (*e*) $\partial y'/\partial y$, for all the x-locations downstream from the roughness element array. The peaks of the *rms* profiles (and the area of these profiles with respect to η) of u' exhibit an initial drop (the wake region) and then increase (the transient growth region). Conversely, the peaks and areas beneath the distributions for both v' and $\partial v'/\partial z$ exhibit monotonic decay. The *rms* profiles of $\partial u'/\partial z$ initially evolve similarly to those of u' but, intriguingly, instead of continuing to grow downstream of $x \simeq 225$ mm, they decay. The *rms* profiles of $\partial u'/\partial y$ clearly show the shear layer produced by the top surface of the roughness elements (for instance, at $\eta \simeq 1.86$ for $x = 207$ mm) and the change of sign at $x \simeq 250$ mm.

3.2.5 Energy

The local energy, e, carried by $\vec{u}$ over a spanwise extent, L_z, is given by

$$e(x,y) = \frac{1}{L_z}\int_{-L_z/2}^{L_z/2}\left(u'^2 + v'^2 + w'^2\right)dz. \tag{3.11}$$

To quantify an averaged value of the perturbation energy contained in the entire thickness of the boundary layer, E, the local values are integrated in the wall-normal direction up to $\eta = 5$ (edge of the boundary layer), that is,

$$E(x) = \frac{1}{5}\int_0^5 e\, d\eta. \tag{3.12}$$

The energy carried by u' and v' is calculated according to (3.12). Figure 3.34(a) shows a comparison of the streamwise evolution of $E_{u'}/U_\infty^2$ from the LDA, HWA (Lavoie *et al.*, 2008) and FVS data. Likewise, Figure 3.34(b) shows the streamwise evolution of $E_{v'}/U_\infty^2$ from the LDA data. The FVS data are not included in this case due to some anomalies in the computation of v' by the FVS (see Appendix E). It can be seen that, as anticipated, the agreement with the FVS results is remarkably good.

It can be seen that, while $E_{v'}$ decays monotonically, $E_{u'}$ goes through three stages: the wake region ($200 \lesssim x \lesssim 215$ mm), characterised by a severe drop in energy; the transient growth region ($215 \lesssim x \lesssim 300$ mm), where all the measurements were concentrated; and the decay region ($x \gtrsim 300$ mm). Measurements in the decay region were not conducted

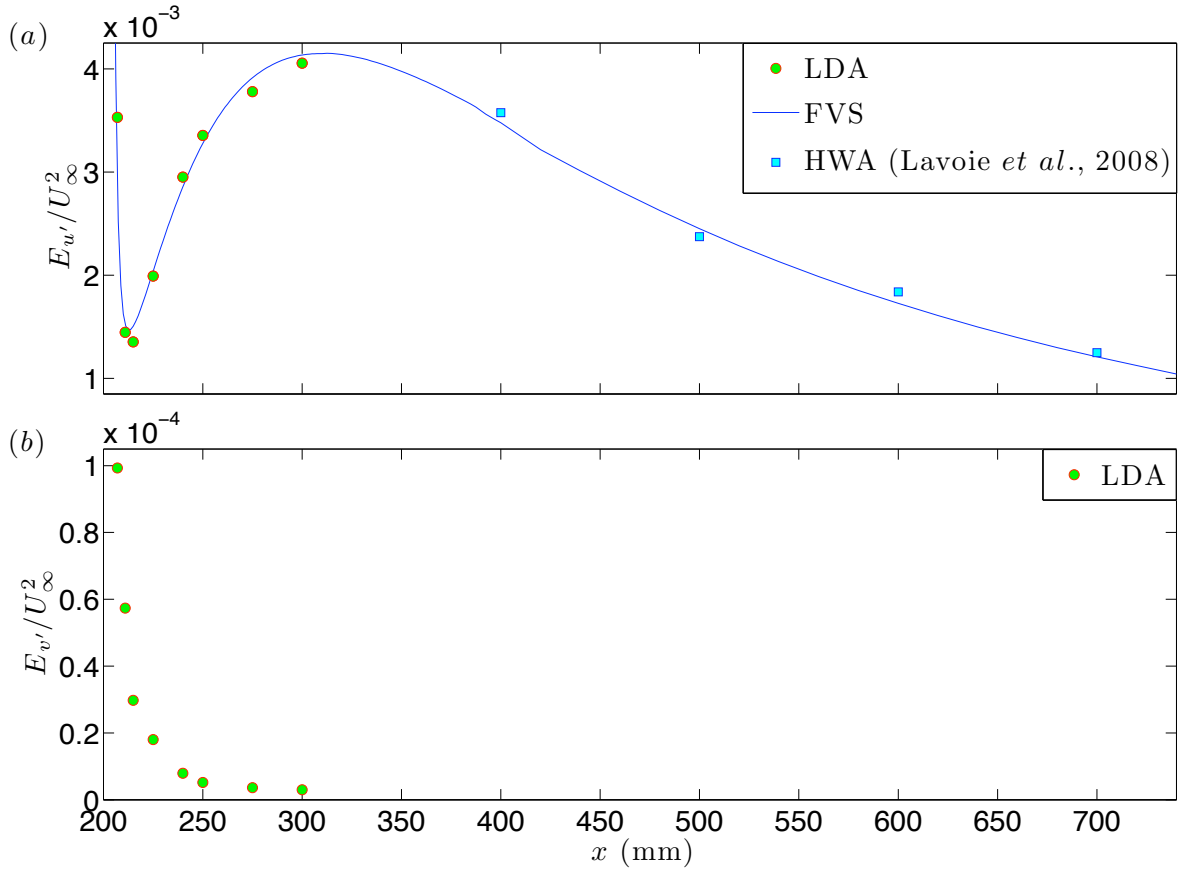


Figure 3.34: Streamwise evolution of, (*a*) $E_{u'}/U_\infty^2$ and, (*b*) $E_{v'}/U_\infty^2$.

because this was already studied by Lavoie *et al.* (2008). Figure 3.34 confirms the results of Butler & Farrell (1992) in two aspects. First, the drop in u'-energy in the wake region is in agreement with the initial destructive interaction between the elemental wavenumbers of the perturbation that the authors stated. Second, when v', as the "engine" of the growth, is sufficiently attenuated, such that the transport of momentum cannot counteract the dissipation of u', the perturbation can no longer grow and so starts to decay.

3.2.6 Spectral Analysis

A spectral analysis of the spanwise averaged LDA data is conducted to further investigate the behaviour of the perturbation. Studying energy processes in the spectral domain is particularly useful because it provides information concerning the energy content at each wavenumber, whereas studying energy in the physical domain alone provides information on the variation of energy in space. This is possible because, according to Parseval's

relation, the energy in the physical and Fourier domains is conserved.

The spectrum $\phi_{u'u'}$ in the spanwise direction at a given wall-normal location is defined by the integral

$$u'(\eta)^2 = \int_0^\infty \phi_{u'u'}(k_z; y) dk_z, \tag{3.13}$$

where k_z is the spanwise wavenumber. This means that the area under the spectrum provides a direct measure of the energy content of u'. The power spectrum can be determined by the Fourier Transform (FT) of u', that is,

$$\phi_{u'u'} = |\mathrm{FT}\{u'\}|^2. \tag{3.14}$$

The wavenumber spacing is defined as

$$\delta k_z = \frac{2\pi}{\Delta z} = \frac{2\pi}{N \delta z}, \tag{3.15}$$

thus wavenumbers are defined as

$$k_z(p) = \frac{p \delta k_z}{2\pi}, \quad p = 0, 1, 2, ..., \tag{3.16}$$

where the 2π in the denominator is introduced in order to provide integer wavenumbers, i.e. $k_z(p)\Delta z = p$.

Parseval's relation for a discrete signal at a specific wall-normal location is:

$$\sum_{n=0}^{N-1} |u'(n; y)|^2 = \frac{1}{N} \sum_{p=0}^{N-1} |\mathrm{DFT}\{u'(p; y)\}|^2 = \frac{1}{N} \sum_{p=0}^{N-1} \phi_{u'u'}[k_z(p); y], \tag{3.17}$$

where $\mathrm{DFT}\{u'\}$ is the Discrete Fourier Transform of u', n is the position index and p is the wavenumber index. In the present study, since $|u'|^2 = u'^2$, combining the discrete form of (3.11) and (3.17) yields:

$$e = \frac{1}{N} \sum_{p=0}^{N-1} (u'^2 + v'^2 + w'^2) = \frac{1}{N} \sum_{p=0}^{N-1} (\phi_{u'u'} + \phi_{v'v'} + \phi_{w'w'}). \tag{3.18}$$

Strictly, by Nyquist theorem, only $N/2$ unique wavenumbers can be identifed, hence (3.18) becomes:

$$\boxed{e(y) = \frac{2}{N} \sum_{p=0}^{\frac{N}{2}-1} \{\phi_{u'u'}[k_z(p); y] + \phi_{v'v'}[k_z(p); y] + \phi_{w'w'}[k_z(p); y]\}.} \tag{3.19}$$

Consequently, the average energy over the entire boundary layer can be calculated by integrating ϕ over the thickness of the boundary layer, that is,

$$E = \frac{2}{N} \sum_{p=0}^{\frac{N}{2}-1} \langle \phi_{u'u'}[k_z(p)] \rangle_\eta + \langle \phi_{v'v'}[k_z(p)] \rangle_\eta + \langle \phi_{w'w'}[k_z(p)] \rangle_\eta, \tag{3.20}$$

where

$$\langle \phi[k_z(p)] \rangle_\eta = \frac{1}{5} \int_0^5 \phi[k_z(p); \eta] \, d\eta. \tag{3.21}$$

Although it is not shown here, equation (3.20) recovers the results of figure 3.34 with a remarkable level of accuracy. This was conducted as a check for the accuracy of the DFT algorithm.

Figures 3.35 and 3.36 show, respectively, the streamwise evolution of iso-contours of $\phi_{u'u'}$ and $\phi_{v'v'}$, non-dimensionalised by U_∞^2. The ordinate of these plots is the wall-normal, self-similarity variable, η, and the abscissa is the spanwise wavenumber, k_z, non-dimensionalised by the roughness element spacing, Δz. The spectra in both the wake region and the first stages of the growth region exhibit a heterogeneous distribution of energy across the thickness of the boundary layer, with the peaks of the spectra occurring for a number of wavenumbers at different wall-normal locations. Further downstream, the energy evolves towards one single peak (at $k_z \Delta z = 1$) for both u' and v', and focussed on a near-constant wall-normal location ($\eta \simeq 1.7$ for u', and $\eta \simeq 2.3$ for v').

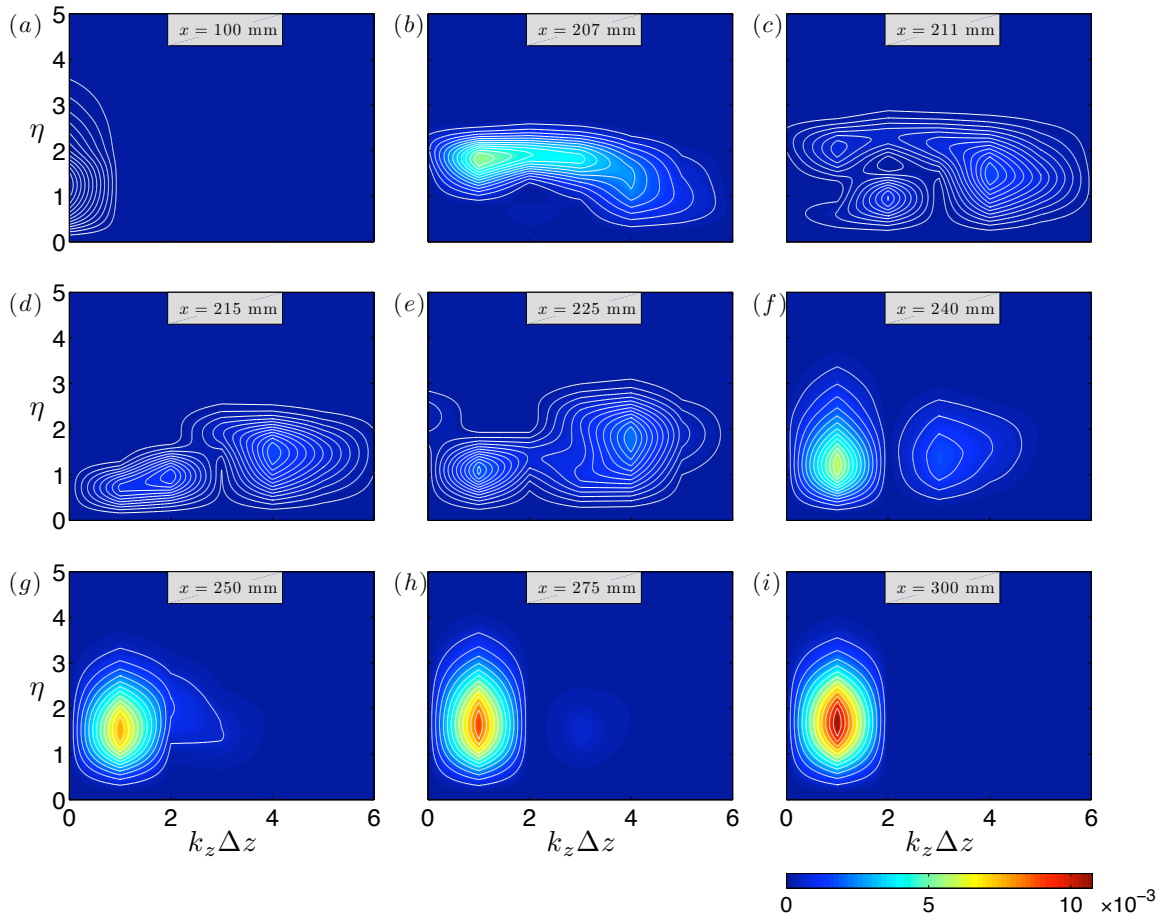


Figure 3.35: $\phi_{u'u'}/U_\infty^2$ Iso-contours of ensemble-averaged u' data; $x =$ (a) 100 mm, (b) 207 mm, (c) 211 mm, (d) 215 mm, (e) 225 mm, (f) 240 mm, (g) 250 mm, (h) 275 mm, (i) 300 mm.

Figure 3.37 shows, (a) the streamwise evolution of $\phi_{u'u'}/U_\infty^2$ versus wavenumber integrated over a wall-normal extent of $\eta = 5$, and (b) at the wall-normal location where u'_{rms} peaks. Figures 3.38 shows the same for the case of $\phi_{v'v'}/U_\infty^2$.

The iso-contours of $\phi_{u'u'}$ confirm the complexity of the perturbation in the vicinity of the roughness element array. It is characterised by its broad-band nature, without a clear predominance of any wavenumber, with their peaks moving around. As stated by Butler & Farrell (1992) and Fransson *et al.* (2004) and as can be seen in both figures 3.35 and 3.37, the competition between wavenumbers in the wake region has a destructive nature, producing a drop in the overall level of u'-energy. Recalling figure 3.5, it can be argued that there is an overall transfer of energy from the perturbation to the free stream for that stage of the perturbation evolution. But as soon as the outer streamwise vortex pair

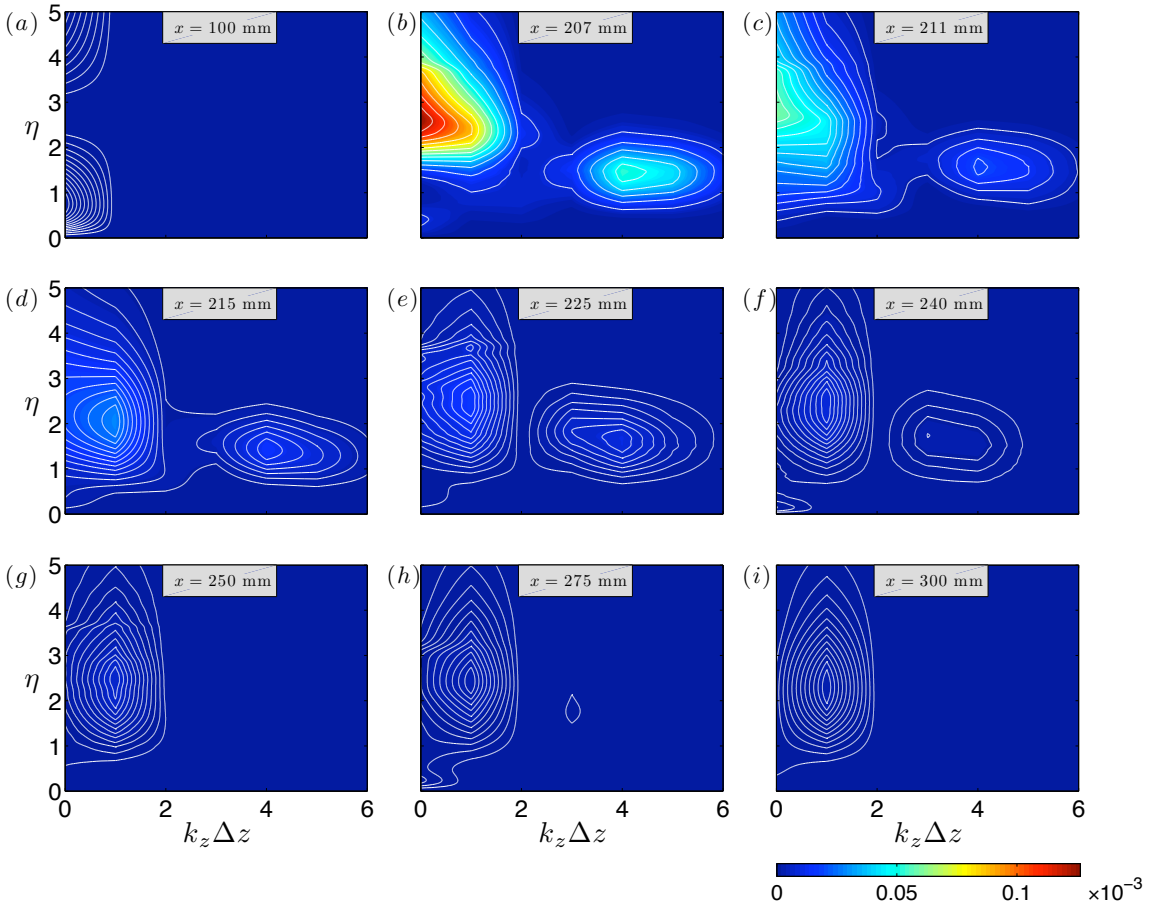


Figure 3.36: $\phi_{v'v'}/U_\infty^2$ Iso-contours of ensemble-averaged v' data; $x =$ (a) 100 mm, (b) 207 mm, (c) 211 mm, (d) 215 mm, (e) 225 mm, (f) 240 mm, (g) 250 mm, (h) 275 mm, (i) 300 mm.

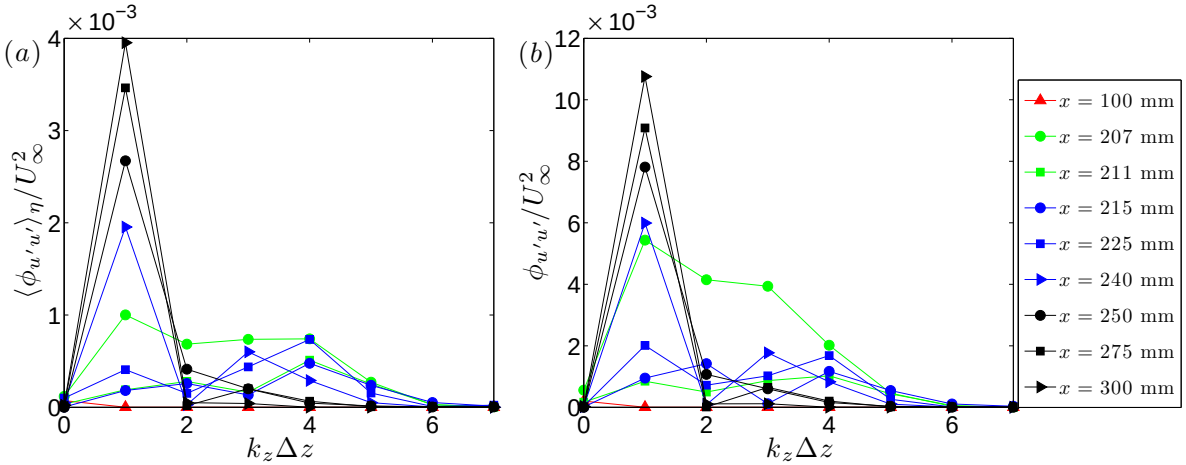


Figure 3.37: $\phi_{u'u'}/U_\infty^2$; (a) integrated over $0 \leqslant \eta \leqslant 5$, ($b$) at the wall-normal location where u'_{rms} peaks (at different η-locations).

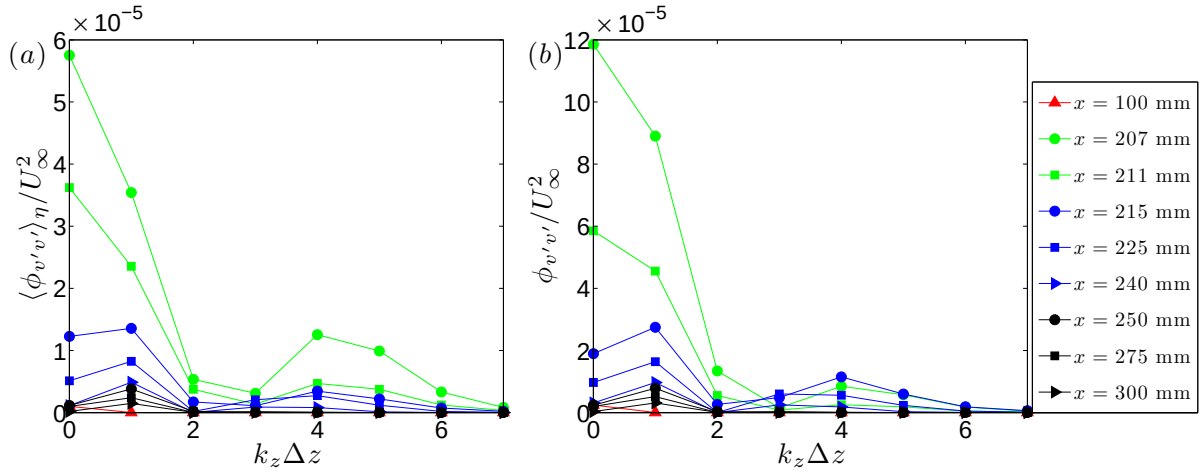


Figure 3.38: $\phi_{v'v'}/U_\infty^2$; (a) integrated over $0 \leqslant \eta \leqslant 5$, ($b$) at the wall-normal location where v'_{rms} peaks (at different η-locations).

overcomes the velocity deficit characterising the wake region (at $x \simeq 215$ mm), the energy transfer is inverted and the perturbation energy starts to grow. It is not until $x \simeq 225$ mm when the fundamental wavenumber ($k_z \Delta z = 1$) emerges and prevails over the rest of wavenumbers.

The features of the v'-component spectra (figure 3.38) are substantially different to those of the u'-component. First, there is an overall monotonic decay of the power spectrum moving downstream, in agreement with the monotonic decrease in amplitude of v' shown in figure 3.29. Second, there is a clear predominance of the component at zero wavenumber of the perturbation, related to the velocity deficit, which is not overcome by the fundamental wavenumber ($k_z \Delta z = 1$) until $x \simeq 215$ mm, precisely when the u'-energy starts to grow. Third, the second-most dominant wavenumber is the fundamental one, which becomes most dominant from $x \simeq 215$ mm onwards and remains as such for all the full streamwise extent. Fourth, the wavenumber $k_z \Delta z = 3$ seems not to contribute importantly to the v'-field at any stage, although it exhibits a slight transient growth between $x = 215$ mm and $x = 225$ mm (as can be seen in figure 3.40). The wavenumber $k_z \Delta z = 4$ survives the wake stage and starts to become negligible only when the perturbation reaches $x \simeq 250$ mm, where the u'-energy growth loses its linear character. Interestingly, this same behaviour occurs for the wavenumber $k_z \Delta z = 4$ of the u'-field of the perturbation. According to these evidences, it seems that $k_z \Delta z = 4$ is

related to the inner pair of counter-rotating vortices.

Figure 3.39 shows, (a) the streamwise evolution of $\phi_{v'_z v'_z}\Delta z^2$ (the non-dimensional power spectral density of $\partial v'/\partial z$) versus wavenumber integrated over a wall-normal extent of $\eta = 5$, and (b) at the wall-normal location where u'_{rms} peaks. The predominance of the wavenumber $k_z\Delta z = 4$ is remarkable. The power spectral density peak at this wavenumber is larger than that at $k_z\Delta z = 1$ for about half of the streamwise extent. It is interesting to note that the peak at $k_z\Delta z = 4$ shifts from $k_z\Delta z = 4$ to $k_z\Delta z = 3$ between $x = 215$ mm and $x = 225$ mm and stays at $k_z\Delta z = 3$ further downstream. This process must be related to the small transient growth in v'-energy at $k_z\Delta z = 3$ seen between those x-locations. It is not until $x = 250$ mm when $k_z\Delta z = 1$ overcomes $k_z\Delta z = 3$, precisely the station at which the outer pair of counter-rotating vortices overcomes the inner one, identified in the spatial domain analysis.

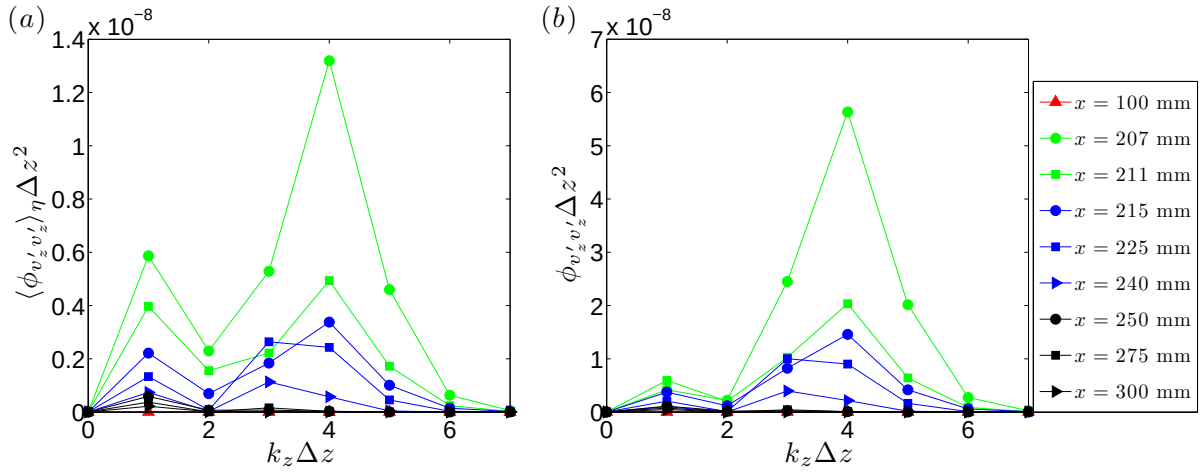


Figure 3.39: $\phi_{v'_z v'_z}\Delta z^2$; (a) integrated over $0 \leqslant \eta \leqslant 5$, (b) at the wall-normal location where v'_{rms} peaks (at different η-locations).

Summarising, it can be concluded that $k_z\Delta z = 4$ plays a crucial role in the behaviour of the disturbance. It corresponds to the inner pair of counter-rotating vortices, and the transfer of energy from that wavenumber to $k_z\Delta z = 3$ and then to $k_z\Delta z = 1$ confirms the process of the outer pair of counter-rotating vortices overcoming the inner one, culminated at $x = 250$ mm.

The streamwise evolution of $\phi_{u'u'}$ and $\phi_{v'v'}$ can be seen more clearly in figures 3.40(a) and 3.40(b), respectively. Most of the energy appears at $k_z\Delta z = 1$. In terms of u'-energy, $k_z\Delta z = 1$ is the one which experiences growth, while the others generally decay. It also exhibits, as do the rest of the modes, a drop in energy in the wake region, as already pointed out. $k_z\Delta z = 1$ is the wavenumber which also carries most of the v'-energy and its decay rate is the most rapid (and similar to that of the zero wavenumber). As anticipated, the small transient growth of the mode $k_z\Delta z = 3$ between $x = 215$ mm and $x = 225$ mm can be seen, see insert in figure 3.40(b).

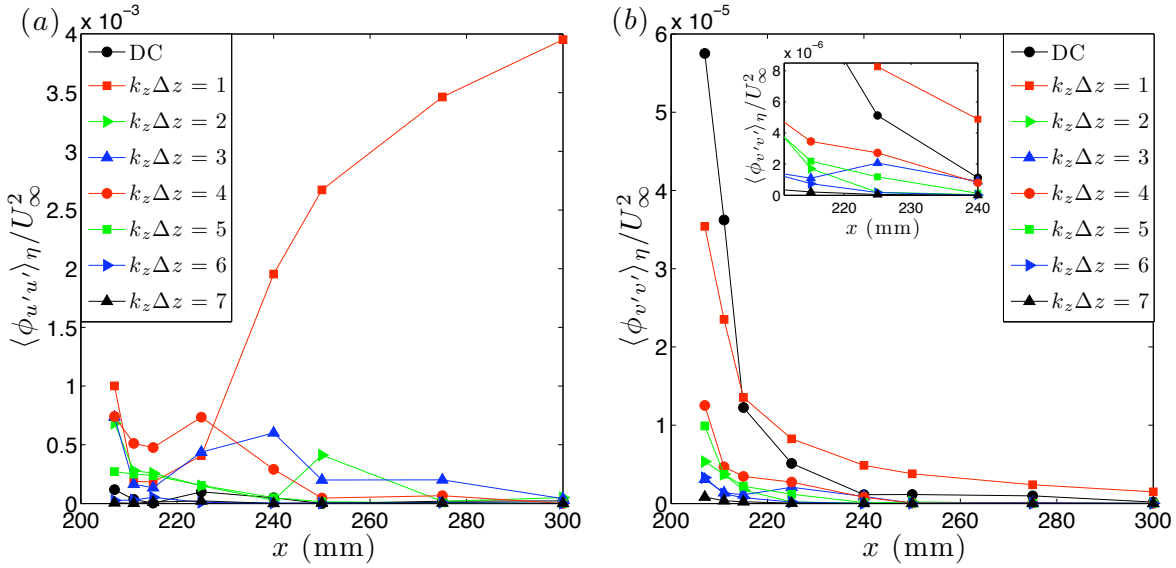


Figure 3.40: (a) $\phi_{u'u'}/U_\infty^2$ and (b) $\phi_{v'v'}/U_\infty^2$ separated in modes and integrated over $0 \leqslant \eta \leqslant 5$.

But perhaps the most interesting aspect of the spectral analysis is what happens at higher wavenumbers of u'. It has been said that they follow a general trend of decay. However, it can be seen in figure 3.40(a) that wavenumbers up to $k_z\Delta z = 4$ exhibit regions of finite growth. The role of $k_z\Delta z = 4$ in $\partial v'/\partial z$ can be clearly noticed also in the evolution of u', as the second number number at which u'-energy grows the most. In fact, at $x = 225$ mm, $k_z\Delta z = 4$ is stronger than $k_z\Delta z = 1$. In addition to this, a secondary effect appears to be the transfer of energy from higher to lower wavenumbers as x increases: thus a secondary peak at ($k_z\Delta z = 4$, $x = 225$ mm) passes to ($k_z\Delta z = 3$, $x = 240$ mm) and then to ($k_z\Delta z = 2$, $x = 250$ mm). The behaviour of the secondary peaks in $\phi_{u'u'}$ with increasing distance suggests transfer of energy between wavenumbers while that energy is transported downstream, $225 \lesssim x \lesssim 250$ mm, that is, in the region of

most rapid transient growth. This region of transient growth, together with the fact that energy increases at some wavenumbers at the expense of energy at others (figures 3.37, 3.38 and 3.39), indicates that there is an underlying non-linear process in the streamwise evolution of the disturbance.

To demonstrate this process, a simple but illustrative example based on transfer functions is presented in Appendix B.

3.2.7 Wavelet Analysis

In order to provide a dual space-wavenumber description, a wavelet analysis using the 1-D Continuous Wavelet Transform (CWT) was conducted on the ensemble-averaged LDA data. Of particular interest is the region close to the roughness element array, where the disturbance seems to be described by a periodic array of discrete (local) structures of different scales, as shown by the spectral analysis, rather than a continuous periodic perturbation. The wavelet analysis is complementary to the spectral one. This is because, while the Fourier transform requires the signal to be of infinite or periodic extent in the physical domain, the wavelet transform does not. In fact, the wavelet transform maps the information of the physical domain into coefficients that are directly related to both the spatial location of the structures as well as their scales. Therefore, the transform is suitable for the identification of coherent structures.

The 1-D CWT is:

$$\tilde{f}(s, z_0) = \frac{1}{s^{1/r}} \int_{-\infty}^{\infty} f(z)\ \psi^* \left(\frac{z - z_0}{s} \right) dz, \tag{3.22}$$

where z_0 is the wavelet position offset, s is the wavelet scale, and ψ^* is the conjugate of the wavelet, ψ. Hence the wavelet ψ acts as a "mathematical microscope", with magnification s^{-1} and point of focus z_0 (Farge, 1992; Morrison & Westbury, 1996). The parameter r refers to the scaling considered for the wavelet transform; $r = 1$ specifies the L_1-norm whereas $r = 2$ specifies a transform in L_2-norm. L_1-norm conserves wave amplitude, whereas L_2-norm conserves wave energy (i.e. the wavelet does not contribute to the energy of the transformed function). Hence integration of the L_2-norm wavelet transform with respect to position produces conventional wavenumber spectra. In the present study only

the L_2-norm is considered.

There is a number of "mother" wavelets (Farge, 1992). Here the mother wavelet chosen is the Morlet, which is a wave modulated by a Gaussian envelope of unit width, and given by

$$\psi(z) = \pi^{-1/4} e^{ik_\psi z} e^{-z^2/2}, \tag{3.23}$$

where k_ψ is the wavenumber and the factor $\pi^{-1/4}$ is introduced to ensure unit energy (Torrence & Compo, 1998). The Morlet does not strictly satisfy one condition of a wavelet, namely the condition of admissibility (zero average). As indicated by Farge (1992), by adding some corrections terms, admissibility can be satisfied. In practice, if $k_\psi = 6$, no correction terms are necessary. Another way of guaranteeing admissibility is to force the Fourier transform of the wavelet, $\hat{\psi}(k_z)$, to be zero for negative wavenumbers, that is:

$$\psi(k_z) = \pi^{-1/4} e^{-(k_z - k_\psi)^2/2} H(k_z), \tag{3.24}$$

where $H(k_z)$ is the Heaviside step fuction, namely $H(k_z) = 1$ for $k_z > 0$ and $H(k_z) = 0$ otherwise. Figures 3.41(a) and 3.41(b) show the Morlet in physical space and its spectrum, respectively.

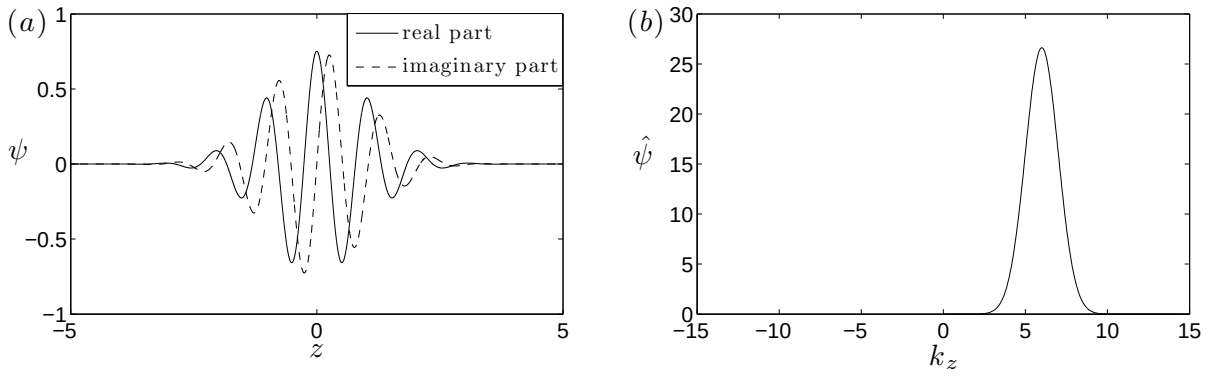


Figure 3.41: Morlet wavelet, (a) in physical domain, (b) in spectral domain.

Once the wavelet is chosen, the second choice is that of scales. As suggested by Torrence & Compo (1998), it is best to choose scales as fractional powers of two, that is,

$$s_j = s_0 2^{j\xi}, \quad j = 0, ..., J, \tag{3.25}$$

with s_0 the minimum resolvable scale, $J+1$ the total number of scales, and ξ an adjustable parameter. Since the wavelet transform is conducted with respect to the z direction, and

the ensemble averaged data consists of 17 data points, J is set at 8 (by Nyquist's theorem). The minimum resolvable scale is set at the spanwise discretisation, that is, $s_0/\Delta z = 1/16$. The parameter ξ is set by trial-and-error at 0.5. These choices provide the best results for the present case, with $s/\Delta z$ ranging from 1/16 to 1. Regarding the position offsets, z_0, they are at the same values as the spanwise discretisation of the ensemble-averaged data, that is, $z_0/\Delta z$ ranging from -0.5 to 0.5 in constant steps of 1/16.

Since the LDA data were acquired both in z and y directions, the 1-D CWT was performed at the wall-normal location where both u'_{rms} and v'_{rms} are at their maximum. Figures 3.42 and 3.43 show, respectively, the streamwise evolution of u'/U_∞ and v'/U_∞ at these locations. To check the accuracy of the Morlet transform algorithm, the original data are recovered conducting the inverse transform and are compared with the original. Figures 3.42 and 3.43 shown the original and recovered data superimposed.

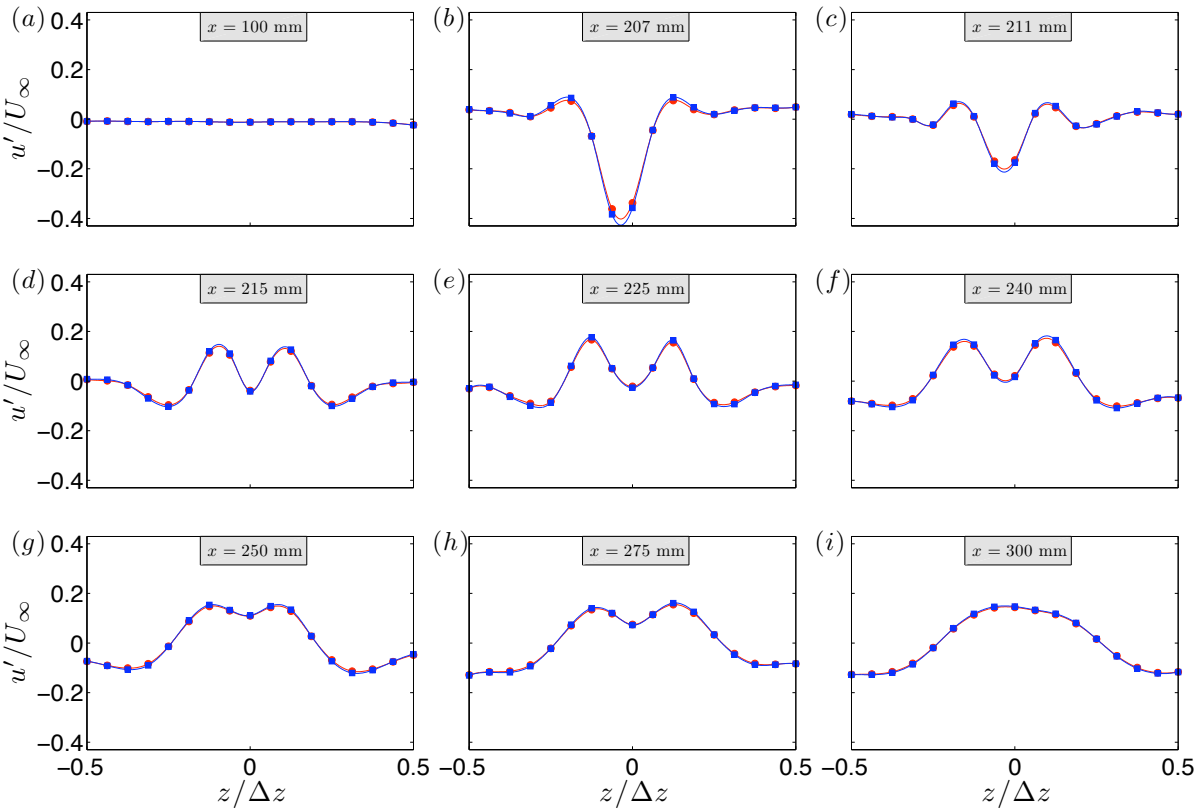


Figure 3.42: Streamwise evolution of u'/U_∞ at the wall-normal location where u'_{rms} peaks. Original data (•) and recovered data after applying the inverse wavelet transform (■); x = (*a*) 100 mm, (*b*) 207 mm, (*c*) 211 mm, (*d*) 215 mm, (*e*) 225 mm, (*f*) 240 mm, (*g*) 250 mm, (*h*) 275 mm, (*i*) 300 mm. The curves are interpolations between data points.

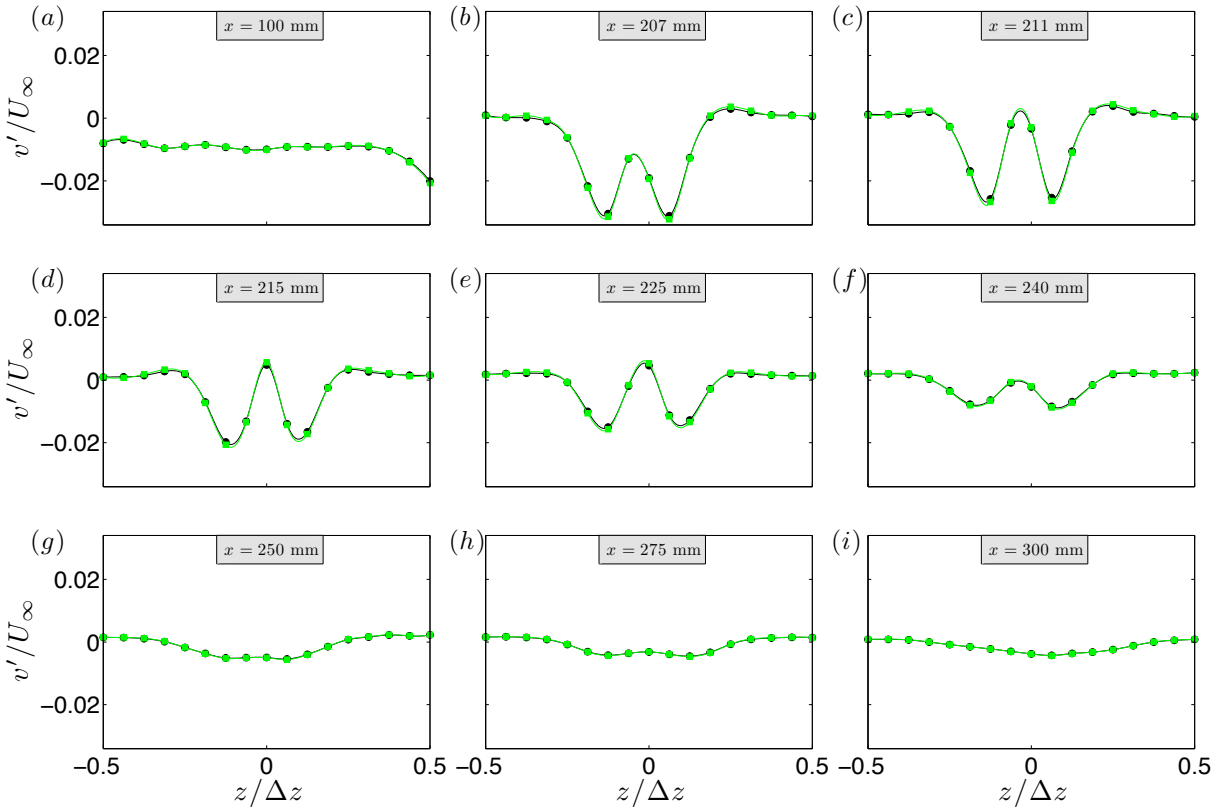


Figure 3.43: Streamwise evolution of v'/U_∞ at the wall-normal location where u'_{rms} peaks. Original data (•) and recovered data after applying the inverse wavelet transform (■); $x =$ (*a*) 100 mm, (*b*) 207 mm, (*c*) 211 mm, (*d*) 215 mm, (*e*) 225 mm, (*f*) 240 mm, (*g*) 250 mm, (*h*) 275 mm, (*i*) 300 mm. The curves are interpolations between data points.

Figure 3.44 shows the streamwise evolution of the magnitude of the L_2-norm coefficients of u'/U_∞, $|\{u'/U_\infty\}_2|$. At first sight, the global picture reveals good agreement with what seen in the spectral analysis. That is, just downstream of the roughness element ($x = 207$ mm) the energy is concentrated in the intermediate and large scales. Then it abruptly decays up to $x = 215$ mm (the end of the wake region). From there on, there is a distinctive increase in energy at scale $s/\Delta z \simeq 0.25$ (which reaches its growth peak at $x \simeq 225$ mm and then decays), but mostly at scale $s/\Delta z = 1$, which continuously grows up to $x = 300$ mm. In spectral terms, these scales correspond to the wavenumbers $k_z\Delta z = 4$ and $k_z\Delta z = 1$, respectively. The additional piece of information that the CWT analysis provides and the spectral one does not is the localisation in space of these scales. This is most apparent in figure 3.44(*e*). That is, while the outer pair of counter-rotating vortices cover the full spanwise extent (i.e. $s/\Delta z = 1$ or $k_z\Delta z = 1$), the inner pair, centred at $z/\Delta z = 0$, covers a span of $z/\Delta z = \pm 0.25$ (i.e. $s/\Delta z \simeq 0.25$ or $k_z\Delta z = 4$). Note that

$s/\Delta z = 0.25$ corresponds to the diameter of the roughness element. The CWT analysis shows, as does the spectral one, that the inner pair of counter-rotating vortices dies out from $x \simeq 225$ mm on.

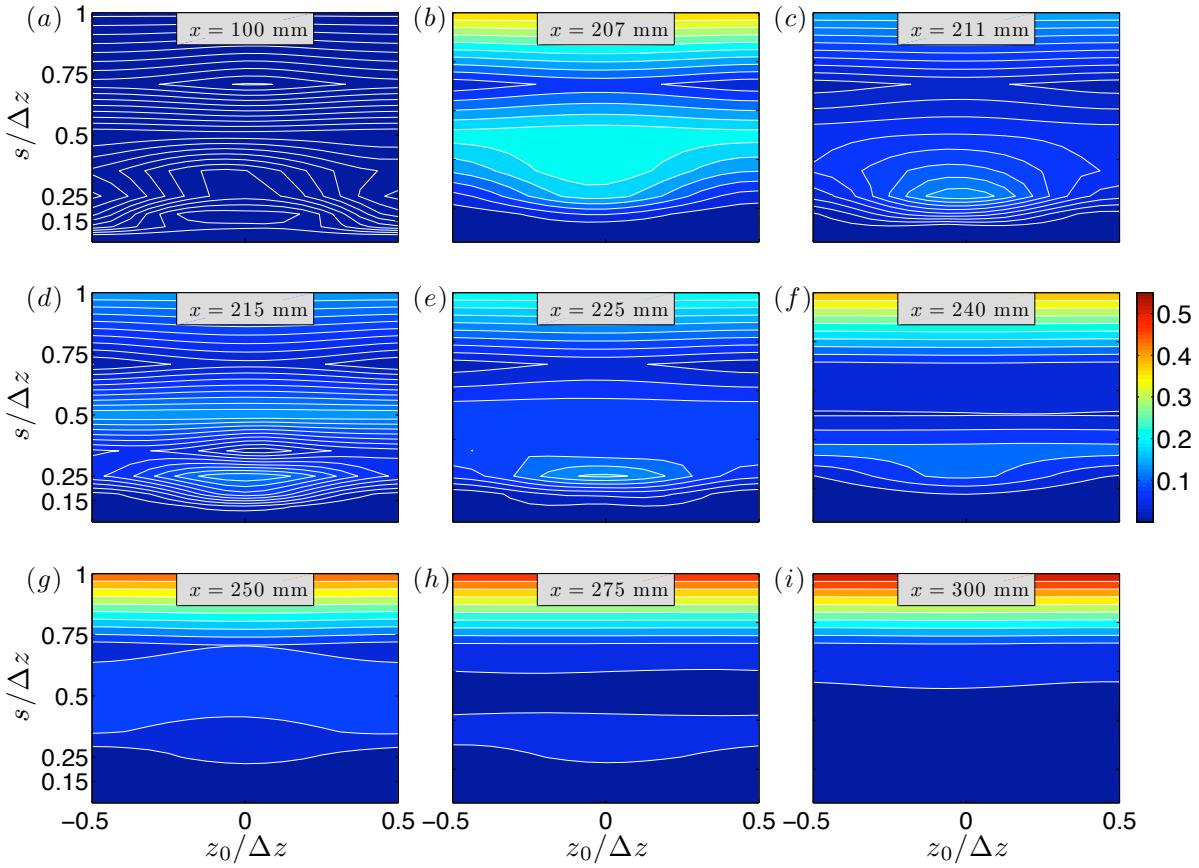


Figure 3.44: Modulus of the wavelet coefficients of the u'/U_∞ signals in figure 3.42; $x =$ (a) 100 mm, (b) 207 mm, (c) 211 mm, (d) 215 mm, (e) 225 mm, (f) 240 mm, (g) 250 mm, (h) 275 mm, (i) 300 mm.

Figure 3.45 shows the corresponding magnitude of the L_2-norm CWT of v', that is, $|\{v'/U_\infty\}_2|$. In agreement with the results obtained in the physical space, the modulus of the coefficients decreases monotonically downstream of the roughness array. Another expected feature is the lower order of magnitude of $|\{v'/U_\infty\}_2|$ compared to that of $|\{u'/U_\infty\}_2|$. But perhaps the most interesting feature is the good agreement in shape between the contours of $|\{v'/U_\infty\}_2|$ and $|\{u'/U_\infty\}_2|$ from $x = 211$ mm onwards. This indicates, first, that the early stages of the perturbation are not only coherent in u', but also in v'. Second, that, despite the monotonic decay of its amplitude, v' morphologically evolves as u', in the sense of the lift-up mechanism induced by pairs of counter-rotating

vortices introduced by Landahl (1980). In other words, these contours of $|\{u'/U_\infty\}_2|$ confirm that the two pairs (inner and outer) of counter-rotating streamwise vortices are the major roles in the evolution of the perturbation.

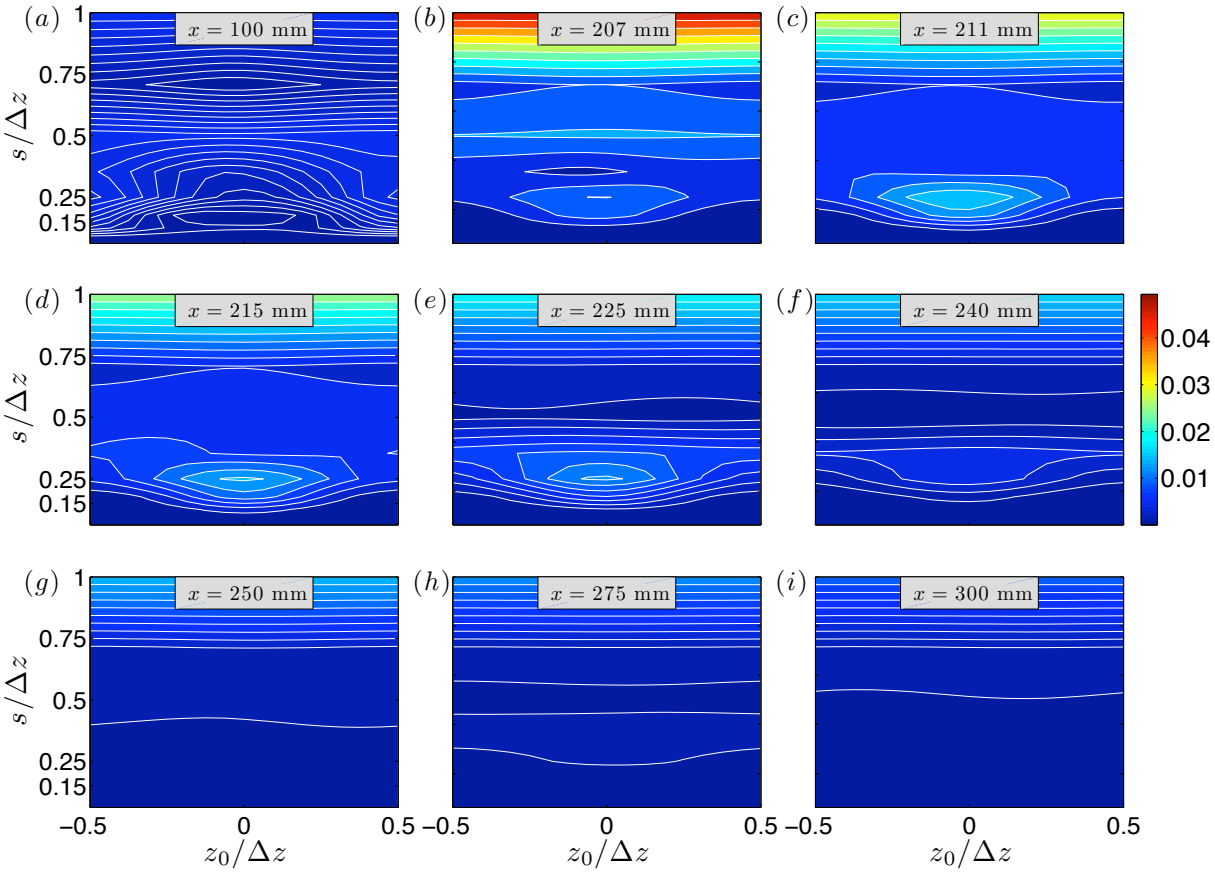


Figure 3.45: Modulus of the wavelet coefficients of the v'/U_∞ signals in figure 3.43; x = (a) 100 mm, (b) 207 mm, (c) 211 mm, (d) 215 mm, (e) 225 mm, (f) 240 mm, (g) 250 mm, (h) 275 mm, (i) 300 mm.

Figures 3.46 and 3.47 show the magnitude of the wavelet coefficients of both u' and v' versus the position offset, z_0, separated in scales and for all the streamwise locations. The interesting aspect of these figures is that the locality of the components of the perturbation is shown explicitly. It can be seen that, for both velocity components, in the wake region and the first stages of the growth region, the smaller scales have hump-shaped profiles, symmetrical with respect to $z_0/\Delta z = 0$. The larger scales are predominant at further distances downstream and tend to cover the whole extent of $z_0/\Delta z$. Interestingly, at the location of the start of the u'-energy growth ($x \simeq 215$ mm), the three smallest scales show a double-bumped profile symmetric with respect to the centreline in the case of u',

indicating the relative absence of those scales right behind the roughness elements.

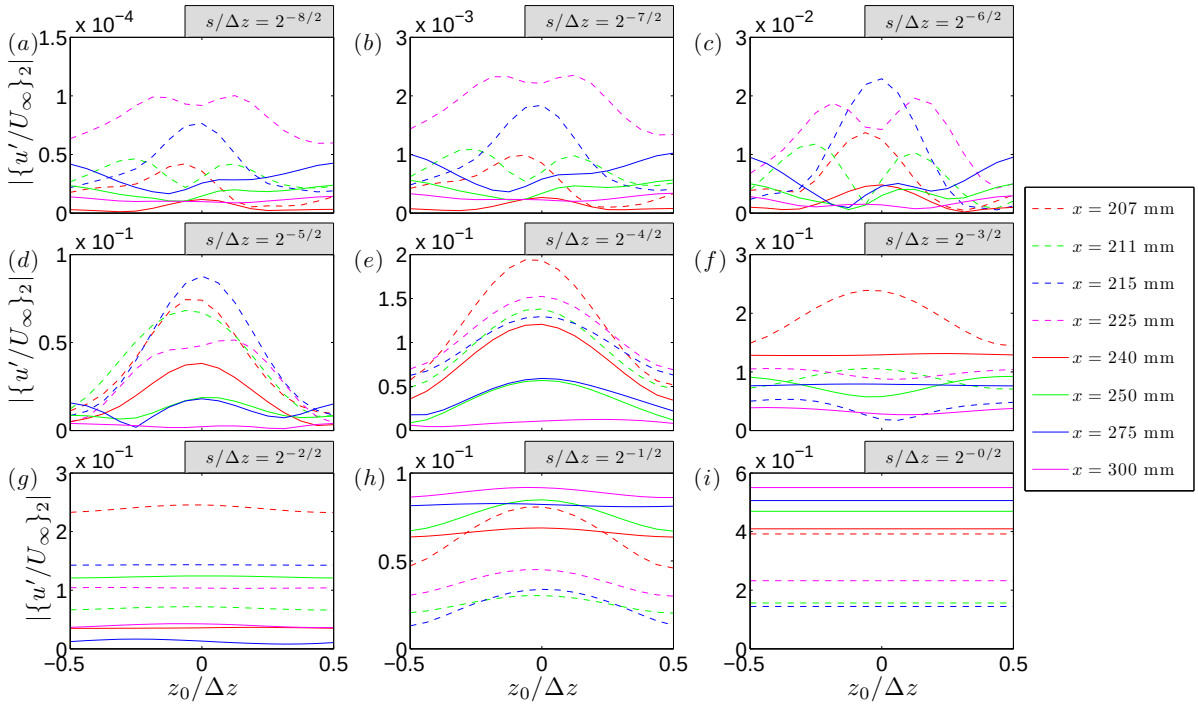


Figure 3.46: Modulus of the wavelet coefficients of the u'/U_∞ signals in figure 3.42 versus $z_0/\Delta z$; for $s/\Delta z = (a)\ 2^{-8/2}$, $(b)\ 2^{-7/2}$, $(c)\ 2^{-6/2}$, $(d)\ 2^{-5/2}$, $(e)\ 2^{-4/2}$, $(f)\ 2^{-3/2}$, $(g)\ 2^{-2/2}$, $(h)\ 2^{-1/2}$, $(i)\ 2^{-0/2}$.

Summarising the behaviour of the magnitude of the wavelet coefficients shown in figures 3.44 and 3.45 at $z_0/\Delta z = 0$ (the centreline), for all the scales, figures 3.48 and 3.49 show the energy passing from one scale to another at each x. It can be seen for both perturbation velocities that, despite the fact that the initial response shows energy over a range of scales, as x increases the most powerful scale for all the streamwise locations is $s/\Delta z = 1$, illustrating the periodic character of the perturbation. Interestingly, the evolution of the magnitude of the wavelet coefficients with respect to x also features crossings, that is, the magnitude of the wavelet coefficients does not increase or decrease with x for all the scales, but increases for some scales and decreases for others. As an example, in figure 3.48 from $x = 215$ mm to $x = 240$ mm, the magnitude of the wavelet coefficients at $s/\Delta z = 2^{-3/2}$ increases, whereas at $s/\Delta z = 2^{-1}$ decreases. A similar behaviour has been detected in the power spectral density and, as demonstrated in the previous section, this constitutes an evidence of an existing underlying non-linear process. Besides, in figure 3.49, the magnitude of the wavelet coefficients at $s/\Delta z = 2^{-2}$ increases

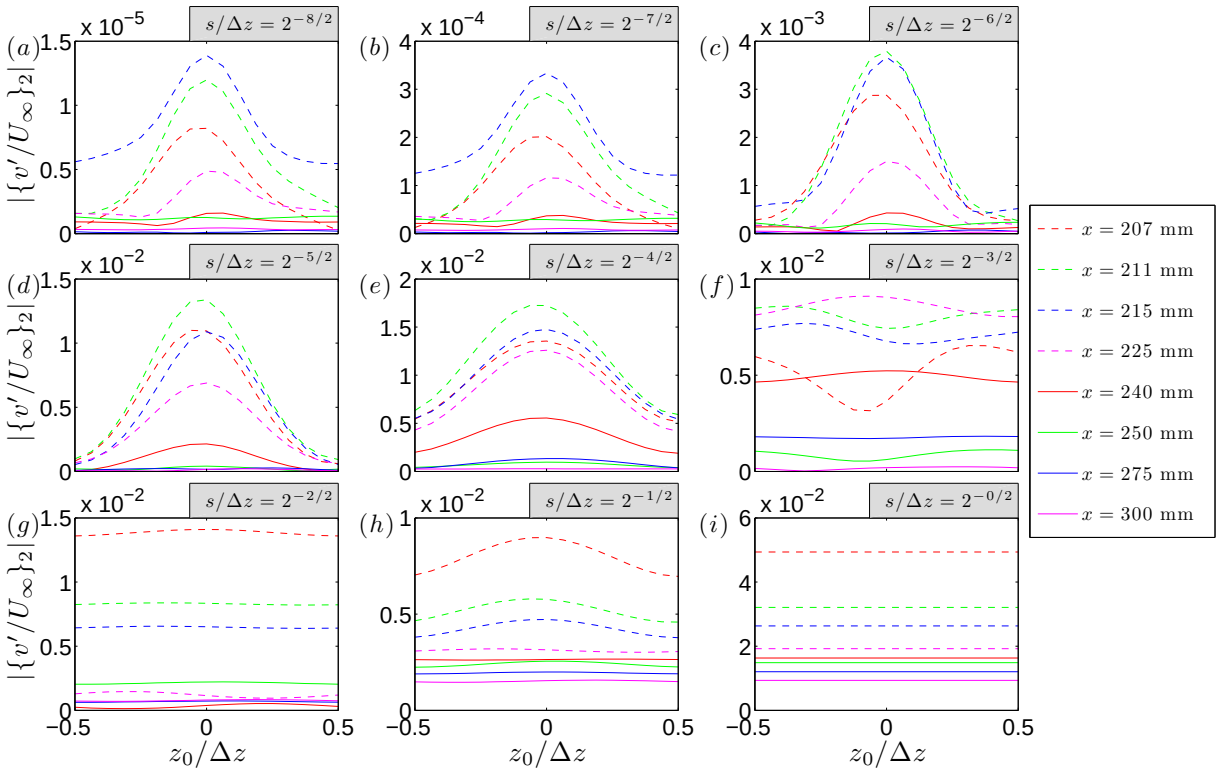


Figure 3.47: Modulus of the wavelet coefficients of the v'/U_∞ signals in figure 3.43 versus $z_0/\Delta z$ for each $s/\Delta z$; for $s/\Delta z =$ (*a*) $2^{-8/2}$, (*b*) $2^{-7/2}$, (*c*) $2^{-6/2}$, (*d*) $2^{-5/2}$, (*e*) $2^{-4/2}$, (*f*) $2^{-3/2}$, (*g*) $2^{-2/2}$, (*h*) $2^{-1/2}$, (*i*) $2^{-0/2}$.

between $x = 207$ and 211 mm, possibly indicating that the inner pair of counter-rotating vortices is acquiring coherence.

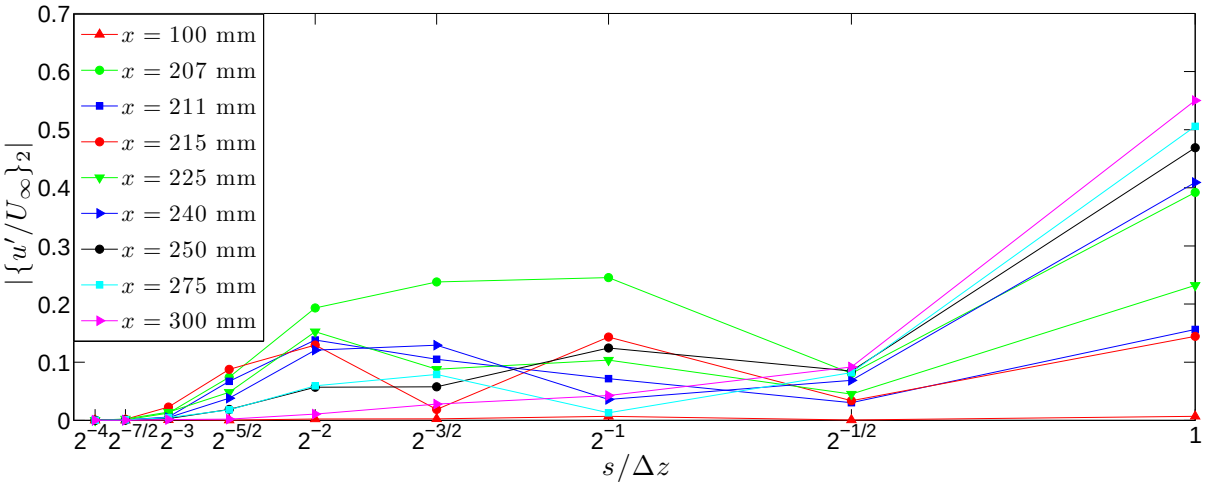


Figure 3.48: Modulus of the wavelet coefficients of u'/U_∞ shown in 3.44, at $z_0/\Delta z = 0$, versus $s/\Delta z$.

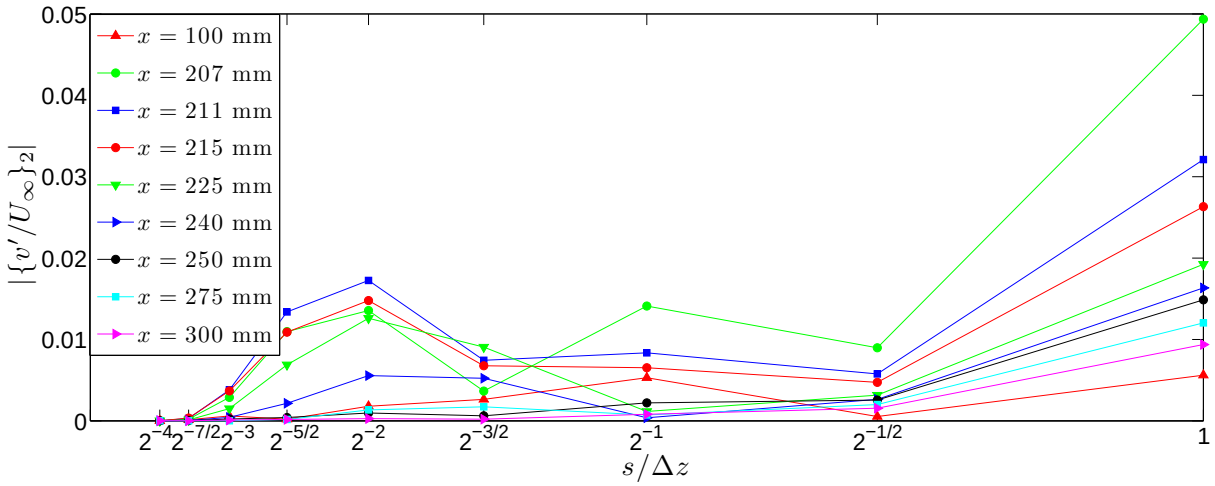


Figure 3.49: Modulus of the wavelet coefficients of v'/U_∞ shown in 3.45, at $z_0/\Delta z = 0$, versus $s/\Delta z$.

Figures 3.50 and 3.51 show, respectively, the streamwise evolution of the wavelet coefficients of u' and v' at each scale at $z_0/\Delta z = 0$. These are the coefficients shown in figures 3.44 and 3.45 at $z_0/\Delta z = 0$, decomposed by scales. Five interesting aspects can be appreciated regarding u'. First (also seen in the spectral analysis), once the wake region is passed, the further downstream, the more energy is carried by the largest scale in relation to the others. Second, at the beginning of the u'-energy growth region ($x \simeq 215$ mm), and at the wall-normal location where the 1-D CWT is performed, the inner pair of counter-rotating vortices ($s/\Delta z = 2^{-2}$) and scale $s/\Delta z = 2^{-1}$ are as strong as the outer pair ($s/\Delta z = 1$). In fact, according to the spectral analysis . Third, scales $s/\Delta z = 2^{-3}, 2^{-5/2}, 2^{-1}, 2^{-1/2}$ exhibit transient growth in the wake region. Fourth, scale $s/\Delta z = 2^{-1/2}$ not only shows growth in the wake region, but also downstream and continuously up to $x = 300$ mm, ending as the second strongest scale. And fifth, the streamwise location of the energy maxima of those scales which present transient growth beyond the wake region increases as $s/\Delta z$ increases, corroborating the results shown in figure 3.40.

With regard to v', the general decay and the slight growth between $x = 215$ and 225 mm are also revealed here. However, interestingly, and in contrast with the spectral analysis, this wavelet analysis also reveals transient growth in the wake region for scales $s/\Delta z = 2^{-3}, 2^{-5/2}$, 2^{-2} and $2^{-3/2}$. Moreover, scale $s/\Delta z = 2^{-3/2}$ presents a second stage of growth just after the wake region (between $x = 215$ and 225 mm), and scale $s/\Delta z = 2^{-1}$

also exhibits growth between $x = 240$ and 250 mm.

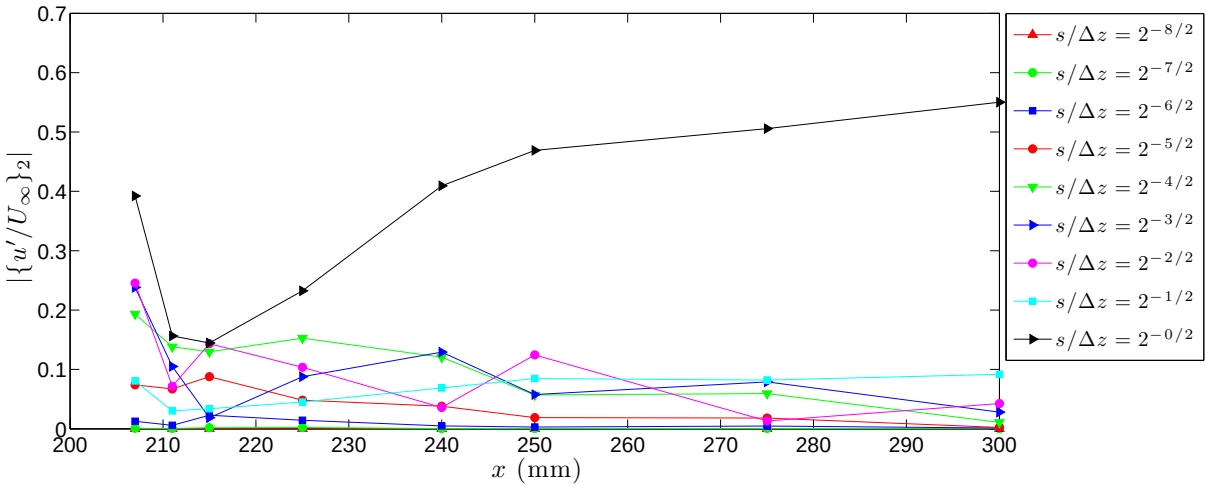


Figure 3.50: Modulus of the wavelet coefficients of u'/U_∞ shown in 3.44, at $z_0/\Delta z = 0$, versus x.

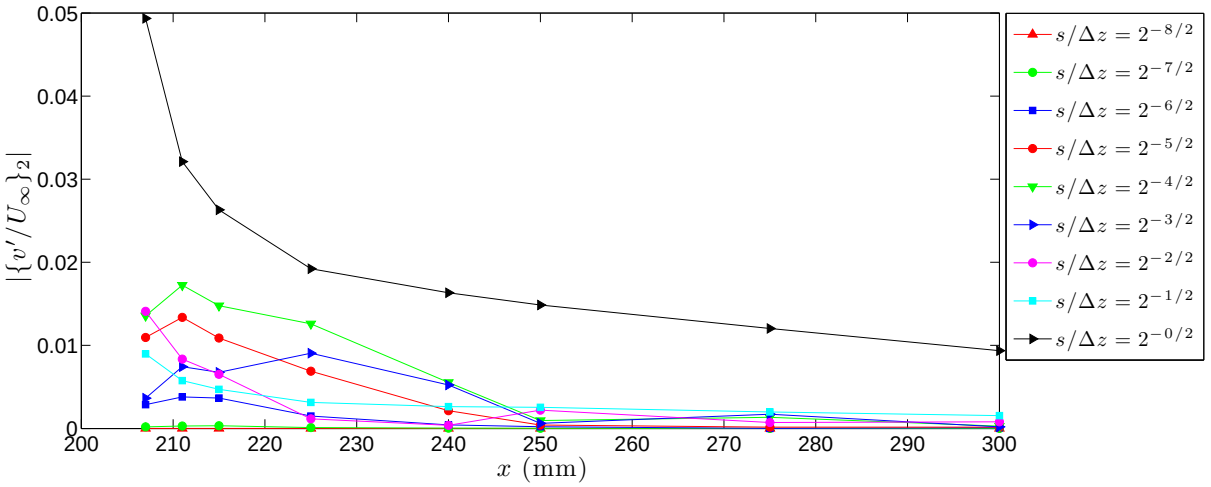


Figure 3.51: Modulus of the wavelet coefficients of v'/U_∞ shown in 3.45, at $z_0/\Delta z = 0$, versus x.

Chapter 4

Discussion and Conclusions

4.1 Discussion

The perturbation is typified by the streamwise component, u', experiencing, first, a severe drop (the wake region), then a transient growth stage and finally a decay. In this process, the wall-normal component, v', decays monotonically from just downstream of the roughness element array. The u' component is contained within the boundary layer ($\eta \leqslant 5$), whereas v' protrudes into the free stream. Another interesting feature of the perturbation is that, up to $x \simeq 250$ mm, most of the information of the disturbance behind every roughness element seems to be local, i.e. u' and v' are finite for $z < \Delta z$ (see figures 3.42 and 3.43).

In the vicinity of a roughness element, a wake region, characterised by two downwash cores on either side of a strong upwash central one, is created. This upwash central core features a strong shear layer at the same height as the top edge of the roughness element. The downwash cores are in turn surrounded by two weak upwash cores. This distribution is consistent with the existence of an outer counter-rotating streamwise vortex pair formed by the roll-up of the natural spanwise vorticity of the incoming boundary layer, and an inner streamwise vortex pair derived from the wake of the roughness element. It is not until $x \simeq 215$ mm (6 diameters mm downstream from the roughness element centre), that the maxima of the downwash cores become larger than the minimum (in absolute value) of the upwash central core. In other words, it is not until $x \simeq 215$ mm that the outer vortex pair (pushing fluid towards the wall in the region behind the roughness element) starts acquiring predominance over the inner pair (pushing fluid away from the wall in the

region behind the roughness element). As mentioned by Fransson *et al.* (2004), it seems that the strength of this outer vortex pair and thus its capability of overcoming the wake flow depends on the ratio of the roughness element height to the boundary layer thickness at the x-location of the roughness array. Despite the fact that the growth of u'-energy starts when the outer vortex pair start to overcome the inner one, the latter seems to play an important role in the growth, because it is not until its complete disappearance (at $x \simeq 300$ mm, clearly seen in figure 3.27(i), where the high-speed streak no longer exhibits pairs of closed contours) that the u'-energy starts to decay. For $x > 250$ mm, the two downwash cores merge, evolving towards a single-core high-speed streak, which spreads across the whole span, as exhibited at $x = 300$ mm. The evolution of $\partial v'/\partial z$ and $\partial u'/\partial z$ reveals that both the spanwise and wall-normal scales of the perturbation maintain approximately constant up to $x \simeq 250$ mm. Further downstream the outer structure starts to merge with the inner one. This is accompanied by a change of sign of the shear layer aligned with the top of the roughness element, as revealed by the evolution of $\partial u'/\partial y$. This shear layer, associated to the wake behind the roughness element is consistent with that identified by White (2002) or Rizzetta & Visbal (2007) at smaller Re_k. According to the inviscid study of Landahl (1980), it can be concluded that up to $x \simeq 250$ mm, the evolution of the perturbation is essentially inviscid, with the effects of viscosity becoming more important further downstream. As v', $\partial v'/\partial z$ also decays monotonically, and by $x \simeq 300$ mm $\partial v'/\partial z \simeq 0$. This indicates that the perturbation has run out of "engine" to continue growing, implying the end of the u'-energy growth region.

Both spectral and wavelet analyses provide important findings. First, the complexity of the perturbation in the vicinity of the roughness element array, characterised by a broad-band response (figures 3.37 and 3.48), is evident; without a clear predominance of any wavenumber/scale, and the competition between them, with their energy peaks moving around. In terms of u', this competition between wavenumbers/scales in the wake region has a destructive nature, producing a drop in the overall level of u'-energy (figures 3.35 and 3.37), as reported in the literature. There is an overall dissipation of energy from the perturbation to the free stream for that stage of the perturbation evolution (figure 3.5). But as soon as the outer streamwise vortex pair overcomes the velocity deficit characterising the wake region (at $x \simeq 215$ mm), the energy transfer is inverted and the perturbation energy starts to grow. It is after $x \simeq 225$ mm when the fundamental wavenumber/scale ($k_z\Delta z = s/\Delta z = 1$) emerges and prevails over the rest

of wavenumbers/scales. In fact, in terms of the spectra of u', $k_z\Delta z = 4$ is stronger than $k_z\Delta z = 1$ at $x \simeq 225$, see figure 3.40(a).

In terms of v', the behaviour is substantially different to that of u'. It is characterised by a clear predominance of a velocity deficit (zero wavenumber) in the wake region and an overall monotonic decay in v'-energy moving downstream. However, the energy at $k_z\Delta z = 3$ exhibits a small growth between $x = 215$ and $x = 225$, see figure 3.40(b). Apart from the zero wavenumber, the next dominant wavenumber/scale is the fundamental one. This wavenumber/scale becomes the most dominant precisely when the u'-energy starts to grow ($x \gtrsim 215$ mm), see figure 3.40(b). In other words, the u'-energy starts to grow only beyond the wake region.

An interesting aspect of the evolution of the perturbation is what happens with the higher wavenumbers. A spectral analysis on $\partial v'/\partial z$ reveals the remarkable predominance of the wavenumber/scale $k_z\Delta z = 4$ and $s/\Delta z = 0.25$ in the initial stages of the disturbance formation. This indicates that one of the roughness characteristic lengths (the diameter, the other is the height) plays a crucial role in creating three-dimensional disturbances, hence in generating $\partial v'/\partial z \neq 0$. In fact, $k_z\Delta z = 4$ is related to the inner pairs of counter-rotating vortices, which are fully overcome by the outer pair at $x \simeq 250$ mm, precisely where $k_z\Delta z = 4$ ceases to be the second most important wavenumber. Going downstream the predominance seems to shift from $k_z\Delta z = 4$ to $k_z\Delta z = 3$ ($s/\Delta z \simeq 2^{-1.5}$), and then to $k_z\Delta z = 1$, see figure 3.39. The disappearance of the inner pair of counter-rotating vortices must be related to the lose of u'-energy growth rate from $x \simeq 250$ mm downstream (see figure 3.34). This shift to $k_z\Delta z = 3$ may be the cause of the shy transient growth exhibited by v' for that particular wavenumber, see figure 3.40(b). According to the wavelet analysis, which provides the extra information about locality, those scales in terms of u' are predominant mainly in the region aligned with the centreline of the roughness elements, up to $x \simeq 240$ mm, dying out as moving downstream.

But what perhaps is the most interesting aspect related to the higher wavenumbers is the existence of secondary transient growths of u' for $1 < k_z\Delta z \leqslant 4$ (or $0.25 \leqslant s/\Delta z < 1$). The spectral analysis reveals that, within a general trend of decay, the energy at those wavenumbers exhibits stages of finite transient growth over different regions, see figure 3.40(a). The wavelet analysis provides similar information, see figure 3.50. In other words,

a secondary effect seems to exist in the form of energy transfer from higher to lower wavenumbers as x increases, so that a secondary energy peak moves from $k_z\Delta z = 4$ ($s/\Delta z = 0.25$) at $x = 225$ mm to $k_z\Delta z = 3$ ($s/\Delta z \simeq 2^{-1.5}$) at $x = 240$ mm, and from $k_z\Delta z = 3$ ($s/\Delta z \simeq 2^{-1.5}$) at $x = 240$ mm to $k_z\Delta z = 2$ ($s/\Delta z \simeq 2^{-1}$) at $x = 250$ mm. It can be seen that this occurs for $225 \lesssim x \lesssim 250$ mm, that is, in the first half of the u'-energy growth region, see figure 3.34(a). This secondary transient growth, together with the spectrum crossings shown in figures 3.37, 3.38 and 3.39, or in the wavelet coefficients of figures 3.48 and 3.49, indicate that there exists an underlying non-linear process in the streamwise evolution.

A simple exercise consisting of comparing the streamwise evolution of the spectra of a linear process with that of a non-linear one is conducted in Appendix B. The exercise demonstrates the relationship between spectrum crossings (as those for instance shown in figure 3.37) and non-linearity.

An analysis of the skewness and kurtosis conducted on the time series of LDA data acquired at a plane parallel to the wall at $y/k = 1$ (see Appendix C) also reveals streak-like patterns. Large skewness in the wake region suggest the possibility of existence of unsteady processes. The streamwise-elongated streak-like regions of finite skewness are aligned with the roughness element, and have a spanwise scale of approximately two roughness diameters. Everywhere else the skewness is approximately zero. Just downstream of the roughness elements, in the regions of finite skewness, this suddenly grows and then progressively decays. There is a local increase in skewness at $x \simeq 290$ mm, just before the end of the u'-energy growth region. This increase, however, does not reach the level of that in the wake region. Like the skewness, the kurtosis follows streamwise-elongated streaky patterns, also with high levels aligned with the roughness elements and with a spanwise scale of two roughness diameters. Within the streaks, the level of kurtosis of v are higher than those of u. Everywhere else, the predominant value of kurtosis of u is near 3 (Gaussian), whereas in the case of v it is near 6. Another interesting aspect occurs at the perimeter of the roughness element ($z/\Delta z = \pm 0.125$): while the kurtosis of u evolves similarly at each side of the roughness element throughout x, the kurtosis of v, particularly in the wake region, has a marked antisymmetric behaviour, characterised by a distinctive peak value.

4.2 Conclusions

4.2.1 LDA Experiments

2-D Laser Doppler Anemometry (LDA) measurements were conducted on transient growth in a zero streamwise pressure gradient laminar boundary layer over a flat plate in a wind tunnel of low free-stream turbulence intensity. Hot-Wire Anemometry experiments were also carried out to characterise the base (unperturbed) flow. The model employed was a flat plate with a sharp leading edge, with a trailing-edge flap to locate the stagnation point on the measuring side. The perturbation was generated by a spanwise array of discrete cylindrical roughness elements, placed downstream of the leading edge. The conditions of the experiments were set at a single case of free-stream velocity and configuration of the roughness element array (spacing between roughness elements, their diameter and their height). The LDA provided simultaneous readings of both u and v. The majority of the experiments consisted of fine-resolution traverses on YZ-planes for various x-stations. Those stations were concentrated in the wake and u'-energy growth regions.

The experiments demonstrate that the wake region is characterised by a severe drop in u'-energy which lasts for about six roughness-element diameters. The u'-energy growth region covers approximately 34 diameters. Then the u'-energy decays monotonically. Conversely, the v'-energy decays monotonically as soon as the disturbance is created. The drop in u'-energy in the wake region is attributed to a destructive competition between the wavenumbers forming the perturbation. The results also show that the u'-energy does not start growing until the amplitude of the high-speed cores is larger than that of the low-speed ones.

The disturbance generated has three distinct features. One is a velocity deficit just behind the roughness elements, which covers the wake region. Another is an outer pair of counter-rotating streamwise vortices with common flow towards the wall, formed as a result of the wrap-up of the natural spanwise vorticity of the incoming laminar boundary layer around the roughness elements. The third consists of an inner pair of counter-rotating vortices, whose circulations are opposite to those of the outer pairs, which emerge from the wake of the roughness elements. The u'-energy growth region starts where these inner pairs of vortices fully emerge, and finishes when they are overcome by the more powerful

downwash motion of the outer pairs. The action of the outer vortex pairs make the disturbance evolve towards spanwise-periodic streamwise streaks with wavelength equal to the spacing between roughness elements. However, it is clear that streaks featuring single maxima/minima per cycle, or in other words, dominated by one single wavenumber, are not formed until the flow enters the u'-energy decay region. Both u' and v' fields exhibit this feature. However, while the maxima of the u'-streaks occur at the same wall-normal location as their minima, this does not hold for the v'-streaks.

Although the fundamental wavenumber (corresponding to the outer pair of streamwise vortices) is that which undergoes the largest growth in u'-energy, higher wavenumbers also exhibit growth. The perturbation component corresponding to the inner pair of streamwise vortices plays a crucial role in the growth in u'-energy. It is only when this component disappears that the u'-energy growth rate starts to decay. Further downstream, when there is no longer supply of $\partial v'/\partial z$, the end of u'-energy growth occurs. Besides, there exists transfer of energy between wavenumbers over the u'-energy growth region, for both u' and v', which follows a non-linear process.

4.2.2 Numerical Simulations

A simple 2-D time-marching numerical simulation code was written in MATLAB© with the purpose of serving as a workbench to test different configurations of the parameters of active surfaces for flow control, see Appendix D.

Two types of surface-mounted actuators were designed and tested in stagnant flow. Type-A actuators, which perform spanwise periodic expansions and contractions with respect their centreline, and type-B actuators, which perform spanwise periodic oscillations. A possible way of manufacturing these devices could be by using pre-stretched sheets of electro-active polymers with compliant electrodes printed on them and contained within a rigid frame. The distribution of deflections across the actuators was modelled linearly, all the structural parameters of the actuators were maintained unvaried for the cases studied and only the driving frequency was varied (10 and 100 Hz). The most important feature is the creation of streaming by both types of actuators. It is found that type-A actuators produce a pair of alternating counter-rotating streamwise vortices aligned with the actuator centreline, whereas type-B actuators produce a single

alternating streamwise vortex. Also, for both types, the higher the forcing frequency, the thinner the penetration depth becomes, as happens in the Stokes 2$^{\text{nd}}$ Problem. Type-A actuators produce an upwash-motion region aligned with the actuator centreline with downwash-motion regions side by side, whereas type-B actuators create the opposite. Since the wake region behind the roughness elements of the present study is characterised by a downwash-motion core aligned with the elements, which evolves towards an upwash-motion region, a possible open-loop strategy to suppress transient growth by counter-action could be to place type-A actuators in the wake region and/or type-B actuators in the u'-energy growth region, and tune the forcing parameters of the actuators so that the induced flow by the actuators matches the order of magnitude of the incoming flow.

A commercial package for FVS was employed. The main purpose of this was to provide preliminary insights of the flow to help design the LDA experiments. The FVS code is able to accurately predict the evolution of the streamwise velocity component. However, the prediction of the wall-normal component shows some unphysical anomalies, and hence the FVS were not considered for further analyses.

4.3 Future Work

Regarding the LDA experiments, the logical step forward is to implement a full 3-D system to simultaneously capture u, v and w. If traverses with fine streamwise resolution are added to the design of experiments presented in this study, accurate determination of $\omega'_y = \partial w'/\partial x - \partial u'/\partial z$ could be provided, and hence the experimental characterisation of transient growth could be fully accomplished. Moreover, it would be interesting to conduct experiments varying the spanwise spacing, diameter and height of the roughness elements and the free-stream velocity, to carry out a parameterised study, not only on u', as already reported in the literature, but also on $\partial v'/\partial z$ and ω'_y.

Regarding open-loop flow control, the next stage would be to characterise type-A and -B actuators as suggested in this study for a wide range of forcing frequencies and deflection amplitudes, and perhaps also for various electrode widths, by means of the numerical simulation code. These designs could then be implemented in an experiment to cancel transient growth. LDA seems to be the ideal technique to measure the resultant

flow because, in contrast to Hot-Wire Anemometry (HWA), which may incur the risk of impinging the actuators with the probe while measuring near the wall, LDA is not intrusive and hence there exists no risk of damaging the actuators.

Bibliography

Abu-Ghannan, B.J. & Shaw, R. 1980 Natural transition of boundary layers - the effects of turbulence, pressure gradient, and flow history. *Journal Mechanical Engineering Science* **22**, 213–228.

Ames, W.F. 1992 *Numerical Methods for Partial Differential Equations*, 3rd edn. Academic Press.

Anderson, J.D. 2001 *Fundamentals of Aerodynamics*, 3rd edn. McGraw Hill.

Andersson, P., Berggren, M. & Henningson, D.S. 1999 Optimal disturbances and bypass transition in boundary layers. *Physics of Fluids* **11** (1), 134–150.

Benjamin, T.B. 1960 Effects of a flexible boundary on hydrodynamic stability. *Journal of Fluid Mechanics* **9**, 513–532.

Bertolotti, F.P., Herbert, T. & Spalart, P.R. 1992 Linear and nonlinear stability of the Blasius boundary layer. *Journal of Fluid Mechanics* **242**, 441–474.

Braslow, A.L. & Visconti, F. 1950 Further experimental studies of area suction for the control of the laminar boundary layer on a porous bronze NACA 64A010 airfoil. *NACA*. Technical note 2112.

Breuer, K.S. & Haritonidis, J.H. 1990 The evolution of a localized disturbance in a laminar boundary layer. part 1. weak disturbances. *Journal of Fluid Mechanics* **220**, 569–594.

Breuer, K.S. & Landahl, M.T. 1990 The evolution of a localized disturbance in a laminar boundary layer. part 2. strong disturbances. *Journal of Fluid Mechanics* **220**, 595–561.

Bruneau, C.-H., Ruiz-Rivas, U. & Saad, M. 2006 The 2D lid-driven cavity problem revisited. *Computers and Fluids* **35**, 326–348.

Bruun, H.H. 1996 *Hot-Wire Anemometry. Principles and Signal Analysis*. Oxford University Press.

Butler, K.M. & Farrell, B.F. 1992 Three-dimensional optimal perturbations in viscous shear flow. *Physics of Fluids* **4** (8), 1637–1650.

Dearing, S.S., Lambert, S. & Morrison, J.F. 2007 Flow control with active dimples. *The Aeronautical Journal* **111(1125)**, 705–714.

Dearing, S.S., Morrison, J.F. & Iannucci, L. 2010 Electro-active polymer (eap) "dimple" actuators for flow control: Design and characterisation. *Sensors and Actuators A: Physical* **157**, 210–218.

Dhawan, S. 1953 Direct measurements of skin friction. *NACA* **1121**, 281–300.

Drain, L.E. 1980 *The Laser Doppler Technique*. John Wiley & Sons.

Ellingsen, T. & Palm, E. 1975 Stability of linear flow. *Physics of Fluids* **18** (4), 487–488.

Ergin, F.G., Choudhari, M.M., Fischer, P. & Tumin, A. 2005 Transient growth: experiments, DNS and theory. *Proceedings of the 4th international symposium on turbulence and shear flow phenomena,* pp. 1–6.

Farge, M. 1992 Wavelet transforms and their applications to turbulence. *Annual Review of Fluid Mechanics* **24**, 395–457.

Farrell, B.S. 1988 Optimal excitation of perturbations in viscous shear flow. *Physics of Fluids* **31** (8), 2093–2102.

Fluent 2004 *Gambit 2.2.30, Modeling Guide*. Fluent, Inc.

Fluent 2006 *Fluent 6.3, User's Guide*. Fluent, Inc.

Fransson, J.H.M. 2001 Investigations of the asymptotic suction boundary layer. PhD thesis, Kungliga Tekniska Högskolan (KTH), Stockholm.

Fransson, J.H.M. & Alfredsson, P.H. 2003 On the disturbance growth in an asymptotic suction boundary layer. *Journal of Fluid Mechanics* **482**, 51–90.

Fransson, J.H.M., Brandt, L., Talamelli, A. & Cossu, C. 2004 Experimental and theoretical investigation of the nonmodal growth of steady streaks in a flat plate boundary layer. *Physics of Fluids* **16 (10)**, 3627–3638.

Fransson, J.H.M., Brandt, L., Talamelli, A. & Cossu, C. 2005 Experimental study of the stabilization of Tollmien-Schlichting waves by finite amplitude streaks. *Physics of Fluids* **17** (5).

Fransson, J.H.M., Talamelli, A., Brandt, L. & Cossu, C. 2006 Delaying transition to turbulence by a passive mechanism. *Physical Review Letters* **96** (064501).

Gaster, M. 1974 On the effects of boundary-layer growth on flow stability. *Journal of Fluid Mechanics* **66**, 465–480.

Gaster, M., Grosch, C.E. & Jackson, T.L. 1994 The velocity field created by a shallow bump in a boundary layer. *Physics of Fluids* **6** (9), 3079–3085.

Goldstein, M.E. 1985 The evolution of tollmien-schlichting waves near a leading edge. *Journal of Fluid Mechanics* **127**, 59–81.

Gouder, K. 2010 *Turbulent friction drag reduction using electroactive polymer surfaces*. PhD thesis. Imperial College London.

Gouder, K., Potter, M. & Morrison, J.F. 2012 Turbulent friction drag reduction over electroactive polymer and electromagnetically driven actuators. *Experiments in Fluids - Special Issue on Flow Control*. To be published.

Gustavsson, L.H. 1978 On the evolution of disturbances in boundary layer flows. *Technical report TITRA-MEK* pp. 78–02.

Gustavsson, L.K. & Hultgren, L.S. 1980 A resonance mechanism in plane Couette flow. *Journal of Fluid Mechanics* **98** (1), 149–159.

Hammerton, P.W. & Kerschen, E.J. 1996 Boundary-layer receptivity for a parabolic leading edge. *Journal of Fluid Mechanics* **310**, 243–267.

Hansen, M. 1928 Die Geschwindigkeitsverteilung in der Grenzschicht an einer eingetauchten Platte. *Zeitschrift für Angewandte Mathematik und Mechanik* **8**, 185–199.

Hanson, R.E., Lavoie, P., Naguib, A.M. & Morrison, J.F. 2010 Control of transient growth induced boundary layer transition using plasma actuators. *7^{th} IUTAM Symposium on Laminar-Turbulent Transition* **18** (2), 183–188.

Henningson, D.S. & Reddy, S.C. 1994 A linear process in wall-bounded turbulent shear flows. *Physics of Fluids* **6** (3), 1396–1398.

Hunt, J.C.R., Wray, A.A. & Moin, P. 1988 Eddies, stream, and convergence zones in turbulent flows. *Report CTR-S88, Center For Turbulence Research.*

Joslin, R.D. 1998 Prediction and control of transition in supersonic and hypersonic boundary layers. *Annual Review of Fluid Mechanics* **30**, 1–29.

Kachanov, Y. S. & Tararykin, O. I. 1987 Experimental investigation of a relaxing boundary layer. *Izv. SO AN SSSR, Ser. Tech. Nauk* **18** (9).

Kim, J. & Lim, J. 2000 A linear process in wall-bounded turbulent shear flows. *Physics of Fluids* **12** (8), 1885–1888.

Klebanoff, P.S., Schubauer, G.B. & Tidstrom, K.D. 1955 Measurements of the effect of two-dimensional and three-dimensional roughness elements on boundary-layer transition. *Journal of Aerospace Sciences* **22**, 803–804.

Klebanoff, P. S. 1971 Effect of freestream turbulence on the laminar boundary layer. *Bulletin of the American Physical Society* **10**, 1323.

Klebanoff, P. S., Tidstrom, K. D. & Sargent, L. M. 1962 The three-dimensional nature of boundary-layer instability. *Journal of Fluid Mechanics* **12**, 1–34.

Kurian, T. & Fransson, J.H.M. 2011 Transient growth in the asymptotic suction boundary layer. *Experiments in Fluids* **51**, 771–784.

Landahl, M.T. 1980 A note on an algebraic instability of inviscid parallel shear flows. *Journal of Fluid Mechanics* **98** (2), 243–251.

Laurien, E. & Kleiser, L. 1988 Numerical simulation of boundary-layer transition and transition control. *Journal of Fluid Mechanics* **199**, 403–440.

Lavoie, P., Naguib, A. M. & Morrison, J.F. 2008 Transient growth induced by surface roughness in a Blasius boundary layer. In *XXII ICTAM, 25-29 August 2008, Adelaide, Australia*.

Loftin Jr., L.K. & Burrows, D.L. 1949 Investigations relating to the extension of laminar flow by means of boundary-layer suction through slots. *NACA*. Technical note 1961.

Luchini, P. 1996 Reynolds-number-independent instability of the boundary layer over a flat surface. *Journal of Fluid Mechanics* **327**, 101–115.

Luchini, P. 2000 Reynolds-number-independent instability of the boundary layer over a flat surface: optimal perturbations. *Journal of Fluid Mechanics* **404**, 289–309.

Malik, M.R. 1989 Prediction and control of transition in supersonic and hypersonic boundary layers. *AIAA* **27**, 1487–1493.

Matsubara, M. & Alfredsson, P.H. 2001 Disturbance growth in boundary layers subjected to free-stream turbulence. *Journal of Fluid Mechanics* **430**, 149–168.

Michael, D.H. 1961 Note on the stability of plane parallel flows. *Journal of Fluid Mechanics* **10**, 525–528.

Morkovin, M.V. 1969*a* Critical evaluation of transition from laminar to turbulent shear layers with emphasis on hypersonically traveling bodies. *Air Force Flight Dynamics Laboratory, Wright-Patterson AFB, Ohio. AFFDL-TR-68-149* .

Morkovin, M.V. 1969*b* On the many faces of transition. In *Viscous Drag Reduction* (ed. CS Wells), pp. 1–31. New York: Plenum.

Morrison, J.F. & Westbury, P.S. 1996 Perspectives on wall turbulence: The use of complementary techniques. *Experimental Thermal and Fluid Science* **13**, 211–222.

Ortega-Casanova, J. & Fernandez-Feria, R. 2002 *Introduccion a la Mecanica de Fluidos Computacional*. Universidad de Malaga, Malaga.

Pattenden, R.J., Turnock, S.R. & Zhang, X. 2005 Measurements of the flow over a low-aspect-ratio cylinder mounted on a ground plane. *Experiments in Fluids* **39**, 10–21.

Potter, M., Gouder, K. & Morrison, J.F. 2011 A numerical model for electro-active polymer actuators with experimental validation. *Sensors and Actuators A: Physical* **170**, 121–130.

Reshotko, E. 1984 Disturbances in a laminar boundary layer due to distributed surface roughness. *Turbulence and chaotic phenomena in fluids; Proceedings of the International Symposium, Kyoto, Japan, September 5-10, 1983 (A85-24951 10-34). Amsterdam, North-Holland, 1984,* pp. 39–46.

Reshotko, E. 2001 Transient growth: A factor in bypass transition. *Physics of Fluids* **13** (5), 1067–1075.

Rizzetta, D.P. & Visbal, M.R. 2007 Direct numerical simulations of flow past an array of distributed roughness elements. *American Institute of Aeronautics and Astronautics Journal* **45**, 1967–1976.

Ruban, A.I. 2010 *Receptivity theory*. Imperial College London (personal communication).

Saric, W.S., Reed, H.L. & Kerschen, E.J. 2002 Boundary-layer receptivity to freestream disturbances. *Annual Review of Fluid Mechanics* **34**, 291–319.

Saric, W.S., Reed, H.L. & White, E.B. 1999 Boundary-layer receptivity to freestream disturbances and its role in transition. *American Institute of Aeronautics and Astronautics Journal. 30th AIAA Fluid Dynamics Conference* pp. 99–3788.

Schlichting, H. 2000 *Boundary Layer Theory*. 8th edn. Springer-Verlag, Berlin.

Sharma, A.S., Limebeer, D.J.N., McKeon, B.J. & Morrison, J.F. 2006 Stability control laws for the incompressible navier-stokes equations using sector stability theory. In *3rd AIAA Flow Control Conference*, *AIAA 2006* 3695.

Squire, H.B. 1933 On the stability for three-dimensional disturbances of viscous fluid flow between parallel walls. *Proceedings of the Royal Society of London* **142**, 621–628.

Tani, I. & Komoda, H. 1962 Boundary layer transition in the presence of streamwise vortices. *Journal of Aerospace Sciences* **29** (440).

Tani, I., Komoda, H., Komatsu, Y. & Iuchi, M. 1962 Boundary-layer transition by isolated roughness. *Aeronautical Research Institute. University of Tokyo. Report No. 375* .

Torrence, C. & Compo, G.P. 1998 A practical guide to wavelet analysis. *Bulletin of the American Meteorology Society* **79** (1), 61–78.

Trefethen, L.N., Trefethen, A.E., Reddy, S.C. & Driscoll, T.A. 1993 Hydrodynamic stability without eigenvalues. *Science* **261** (5121), 578–584.

Tropea, C., Foss, J. & Yarin, A. 2007 *Handbook of Experimental Fluid Mechanics*. Springer.

TSI 2001 *Instruction Manual, LDV/PDPA System: FSA 3500/4000 Signal Processor, PDM 1000 Photo Detector Module*. TSI Instruments.

Tumin, A. & Reshotko, E. 2001 Spatial theory of optimal disturbances in boundary layers. *Physics of Fluids* **13** (7), 2097–4439.

Watson, J. 1960 Three-dimensional disturbances in flow between parallel planes. *Proceedings of the Royal Society of London. Series A, Mathematical and Physical Sciences* **254**, 562–569.

Westin, K.J.A., Boiko, A.V., Klingmann, B.G.B. & Kozlov, V.V. 1994 Experiments in a boundary layer subjected to free stream turbulence. part 1. boundary layer structure and receptivity. *Journal of Fluid Mechanics* **281**, 193–218.

White, E.B. 2002 Transient growth of stationary disturbances in a flat plate boundary layer. *Physics of Fluids* **14** (12), 4429–4439.

White, E.B. & Ergin, F.G. 2003 Receptivity and transient growth of roughness-induced disturbances. In *American Institute of Aeronautics and Astronautics Journal. 33rd AIAA Fluid Dynamics Conference*, *AIAA 2003* 4243.

White, E. B. 2005 Experiments in transient growth and roughness-induced bypass transition. Final Report for AFOSR Grant F49620-02-1-0058.

White, F.M. 2003 *Fluid Mechanics*, 5th edn. McGraw Hill.

Appendices

Appendix A

Brief Description of the Laser Doppler Anemometry Technique

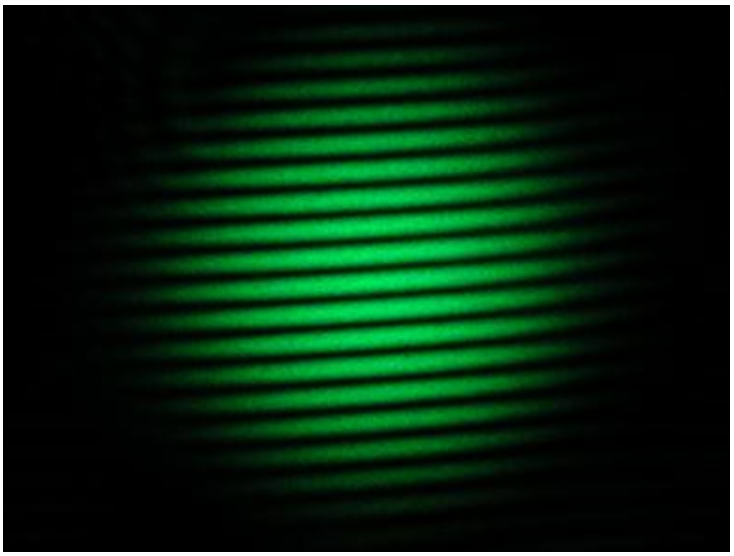


Figure A.1: LDA 514.5 nm-wavelength beam fringe pattern (courtesy of TSI Instruments).

A.1 Introduction

In this appendix, a brief description of the LDA technique is presented. More detailed explanations can be found on any book about the matter or on the user manuals of the firms which manufacture LDA systems. In the case of this study the system employed was from TSI Instruments.

Figure A.2 shows a schematic of the essential elements of a single-component LDA system.

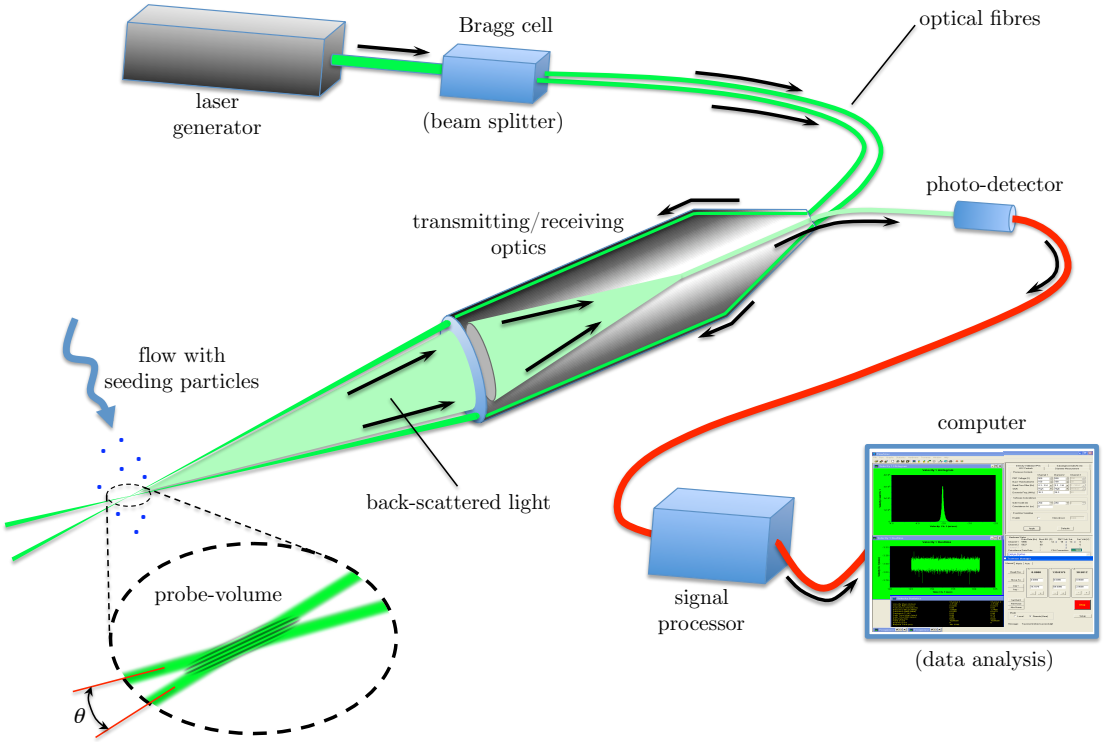


Figure A.2: Schematic of the principles and components of a 1D LDA system.

A.2 Doppler Shift

This technique relies on several aspects. The most important is the fact that particles (either naturally resident in the flow or artificially introduced by means of seeding) are assumed to follow the flow and to be able to scatter light. When a particle goes through

the probe-volume, formed by the intersection of two beams of monochromatic light (laser) of equal intensity, light is scattered in all directions. By having a light detector (also called photodetector) in place, this scattered light event (light "burst") is received and eventually transformed into a component of the velocity of the particle with respect to a determined reference system.

A.3 Interference Phenomenon

The LDA technique is based on the wave nature of light. Frequency (or Doppler) shifts take place due to movement of any of these entities: wave source, wave receptor, medium of propagation, intervening reflector or scatterer. In the LDA technique, the shifts are only produced by particles capable of scattering light from the source which is captured by a receiver. This is the same principle as used in radar transmissions, but in a region of the electromagnetic spectrum of much higher frequency (Drain, 1980).

In the region of the intersection of two laser beams of the same wavelength and with a consistent phase relation, an electromagnetic interference pattern is formed. This pattern can be seen as a succession of light and dark fringes, as shown in figure A.1.

The probe-volume is a region of alternating electromagnetic fields of the intersection of both beams. Where alternations are in phase, the amplitude of the resultant electromagnetic field is the sum of the amplitudes from the two beams and therefore the intensity of the light is increased. Where the fields are out of phase, the resultant electromagnetic field is the subtraction of the amplitudes and light intensity is reduced. The spacing between fringes is given by the following expression:

$$s_f = \frac{\lambda}{2\sin\left(\frac{\theta}{2}\right)}, \tag{A.1}$$

where λ is the wavelength of the beams and θ is the angle between beams. Details of the derivation of expression (A.1) can be found in Drain (1980).

When a particle passes through the probe-volume, the intensity of the light that it scatters will be determined by the fringe pattern. The photodetector, which transforms the light intensity received into voltage, will provide a sinusoidal signal which will reveal

the interference pattern behaviour.

The raw voltage signal of a light burst received by the photodetector due to a particle passing through the probe-volume looks like that shown in figure A.3(a). Then a low-pass filter (which must be greater than the Doppler frequency in order to avoid filtering the Doppler signal) is applied to remove the high-frequency background noise, resulting in the signal shown in figure A.3(b). The low-frequency component (commonly called "pedestal") of the burst signal, shown in figure A.3(b) as a red trace, is removed using a high-pass filter, resulting in the signal shown in figureA.3(c). From this last signal the Doppler shift frequency f_D is obtained.

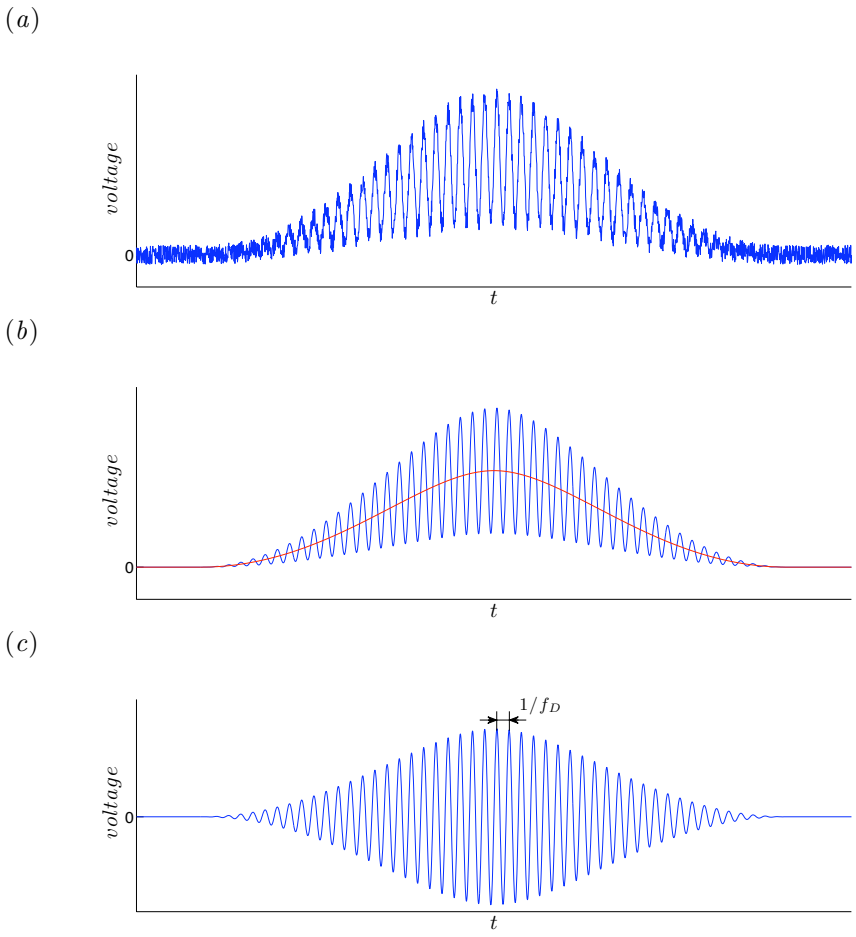


Figure A.3: Steps performed on the photodetector signal of a burst to obtain the Doppler shift frequency f_D – (a) raw burst signal; (b) burst signal with high-frequency noise removed; (c) burst signal with the pedestal component removed ready for f_D to be extracted.

Once f_D is determined (by a Fourier analysis), the velocity v_λ of the particle is straightforward obtained by just multiplying f_D by s_f, hence:

$$v_\lambda = f_D \times s_f = f_D \frac{\lambda}{2\sin\left(\frac{\alpha}{2}\right)}. \tag{A.2}$$

The subscript λ in v_λ indicates that the velocity obtained is the projection of the velocity vector $\vec{v}$ in the plane of the fringes and perpendicular to these, formed by two beams of wavelength λ . The usual wavelengths employed are 514.5 nm (green), 488 nm (blue) and 476.5 nm (violet). If the probe-volume is orientated so that the fringes are perpendicular to the streamwise direction, then the readings of velocity will correspond to streamwise component measurements. Conversely, if the probe-volume is orientated so that the fringes are parallel to the streamwise direction, then the readings of velocity will correspond to one of the normal components of $\vec{v}$.

A.4 Coincidence

To obtain simultaneous readings of several components of $\vec{v}$, more beam pairs have to be added to the system and a data-coincidence criterion must be established. Figure A.4 shows a schematic of the configuration of three probe-volumes for acquiring three orthogonal components of $\vec{v}$.

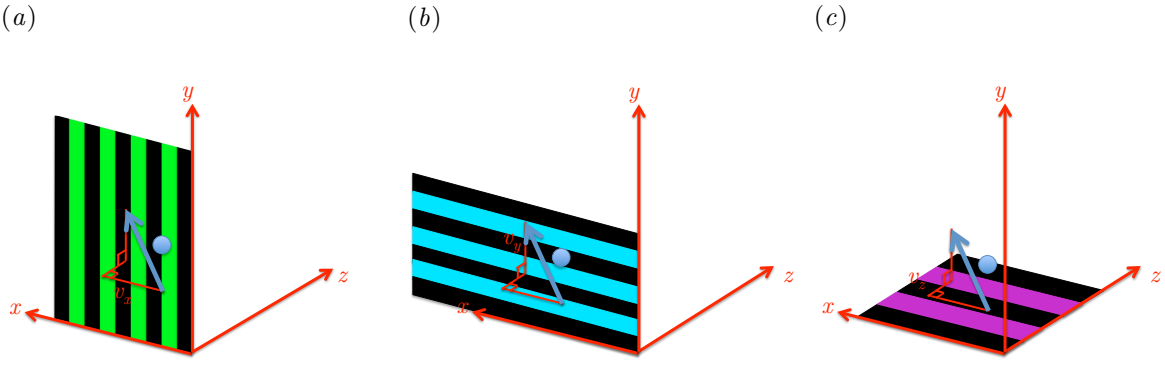


Figure A.4: Schematic of fringe pattern and corresponding measured velocity components for a 3D system; (a) v_x reading, (b) v_y reading and (c) v_z reading.

Simplifying the explanation for a 2D system, "coincidence" (or "simultaneity") refers to the fact that a burst registered on one channel and another burst registered on the other channel correspond to the same particle. Ideally, a particle should give two bursts simultaneously on each acquisition channel. However, if there is a poor alignment of the

optics so that the probe-volumes do not perfectly overlap, or if a particle passes first through a probe-volume and then through the other, there will be a time lag between bursts.

Every time a voltage reading from the photodetector is above an established threshold, a burst is considered to have occurred and a "burst gate" is opened for the occurrence of the burst to register its length in time (see figure A.5). The slower a particle, the longer its transit time, hence the burst gate is open for longer. To determine if two burst (one on each channel) correspond to the same particle, a tolerance width or "acceptance region" is applied to each burst gate. If an overlapping region exists between the two acceptance regions, it is concluded that both bursts correspond to the same particle. The most restrictive situation would be that in which both acceptance regions are as wide as their corresponding burst gates. In that case, the acceptance of coincidence would only occur if both burst gates fully overlap (for instance, the case shown in figure A.6). A situation as that shown in figure A.7 could be considered either as a coincidence case or not, depending on the chosen width of each acceptance region (see figure A.5).

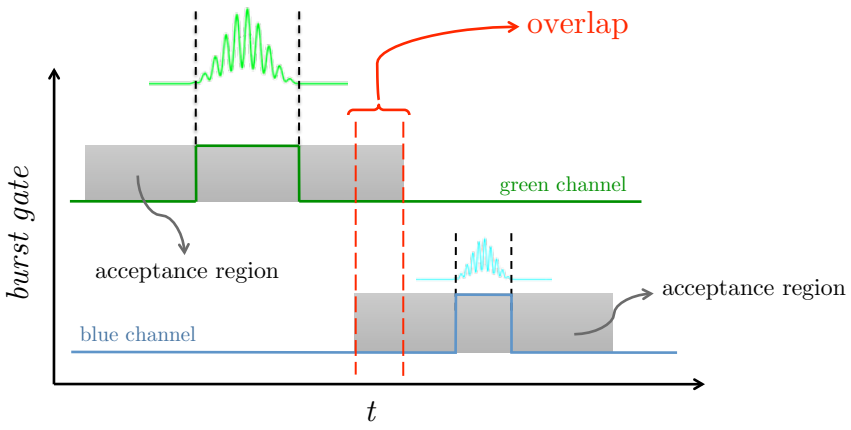


Figure A.5: Schematic of overlap burst gate given a certain acceptance region criterion (in the example, with different acceptance region widths for each channel).

The narrower the acceptance regions are, the more reliable the measurements are from the point of view of simultaneous data. However, the subsequent acquisition rate of valid data is lower. On the contrary, the wider the acceptance regions are, the higher the data rate is, but also the more likely it is to have erratic or inconsistent data.

Figure A.6 shows a time sequence of a particle passing through the overlapping region of two probe-volumes. In this particular case, a particle passes through the overlapping region of probe-volumes simultaneously or, in other words, enters and leaves both the green and blue probe-volumes at the same times. The corresponding burst signals perfectly coincide in time regardless of the chosen acceptance region and it can be reliably concluded that both bursts correspond to the same particle.

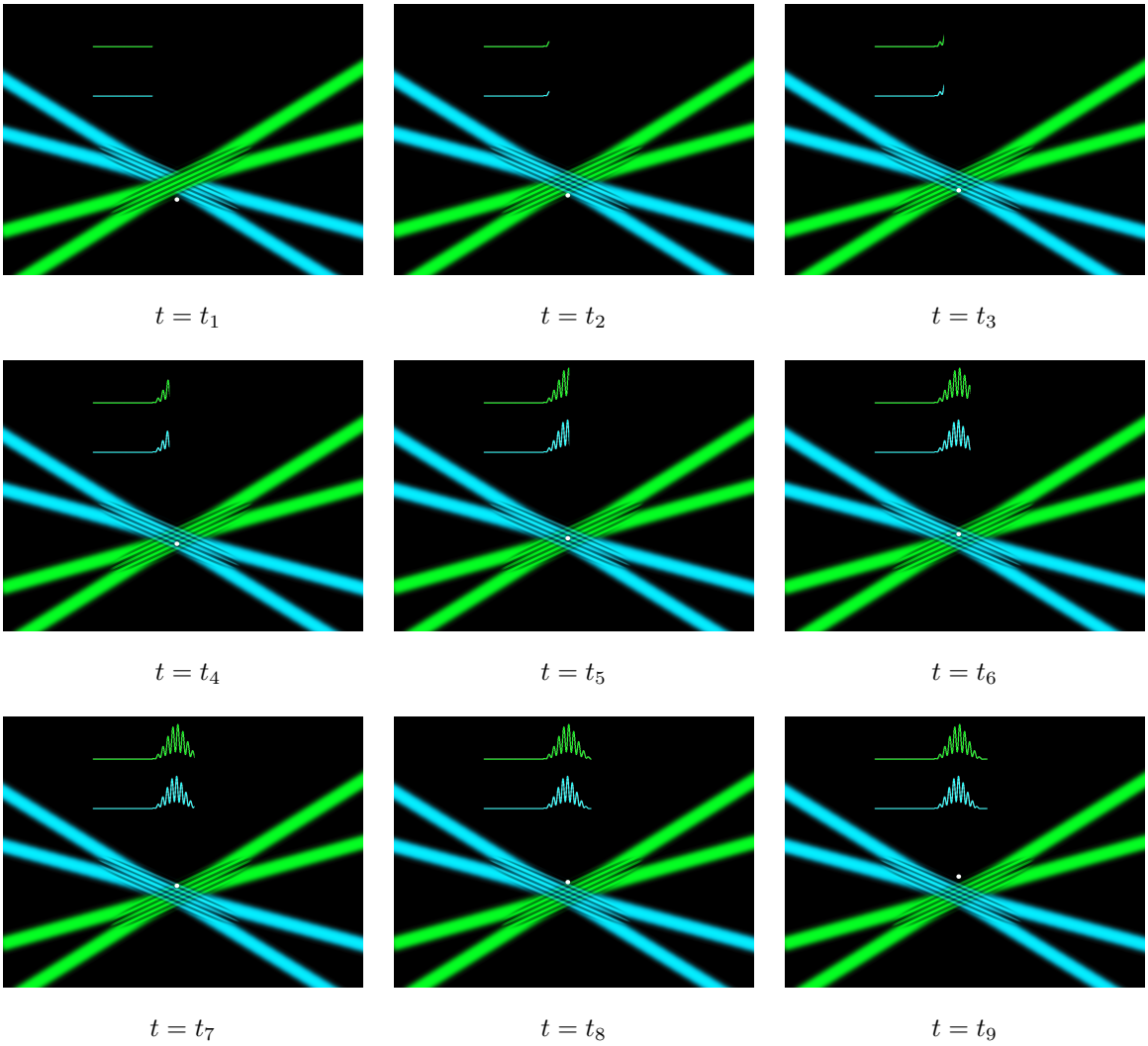


Figure A.6: Time sequence schematic of a particle passing simultaneously through the overlapping region of two probe-volumes. Note particle in white and resulting burst signals.

Figure A.7 shows a time sequence of a particle passing first through one probe-volume and then through the other. In this particular case, a particle first enters the green probe-volume, leaves it and then enters the blue one. The corresponding signals show

a time lag between bursts and it will depend on the width of the acceptance regions as to whether that combination of burst signals corresponds to the same particle. There may be the case in which a particle enters the green probe-volume with a certain direction so that when it leaves, it does not pass through the blue probe-volume and, subsequently, another particle which did not pass through the green probe-volume does go through the blue. In this situation the burst signal combination might be as that shown in figure A.7: if the considered acceptance region is wide enough to have a signal overlap zone, then the combination would be interpreted as that created by one single particle and would provide misleading data.

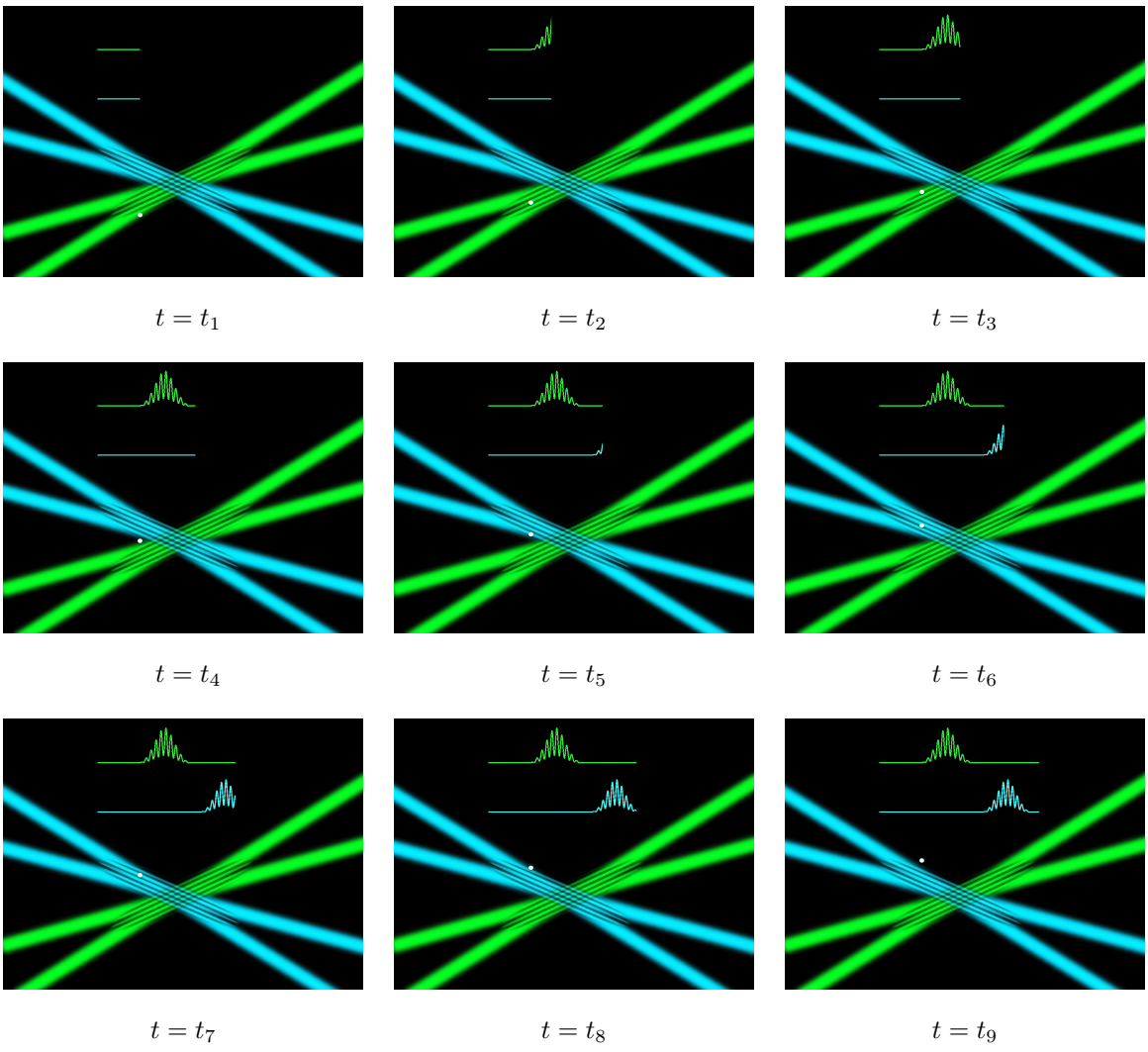


Figure A.7: Time-sequence of schematics of a particle passing first through one probe-volume and then through the other.

Appendix B

Determination of Non-Linear Processes by Spectral Analysis

Let a linear process be represented as:

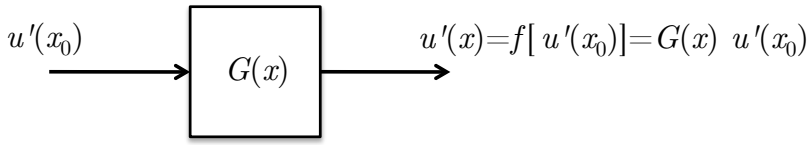


Figure B.1: Schematic of a linear process.

That is, the wave $u'(x)$ at a streamwise location, x, results from a linear process applied on a wave at a certain streamwise location, x_0. If the gain of the process, $G(x)$, increases with x, the wave is amplified. If $G(x)$ decreases with x, the wave decays.

Let the example be:

- Three streamwise locations: $x = x_0, x_1, x_2$; with $x_0 < x_1 < x_2$.
- The wave spans as: $z/\Delta z \in [-0.5, 0.5]$.
- The wave is formed by three wavenumbers: $k_z \Delta z = 1, 3, 6$.
- The wave at $x = x_0$ is, for instance:

$$u'(x_0, z) = \cos(2\pi z/\Delta z) + 0.75\cos(2\pi 3z/\Delta z) + 0.6\cos(2\pi 6z/\Delta z).$$

- The gain $G(x)$ is assumed to increase with x, such that, for instance:

- $G(x_0) = 1$,
- $G(x_1) = 2$,
- $G(x_2) = 3$.

Consequently:

$$u'(x_1, z) = 2u'(x_0, z), \tag{B.1}$$

$$u'(x_2, z) = 3u'(x_0, z). \tag{B.2}$$

Figures B.2(a) and B.2(b) show, respectively, the three modes of the wave considered and the application of the linear process. The power spectral density of the waves in figure B.2(b) is depicted in figure B.3. It can be seen that the energy at all the wavenumbers amplifies with x and the amplification does not lead to energy transfer between wavenumbers.

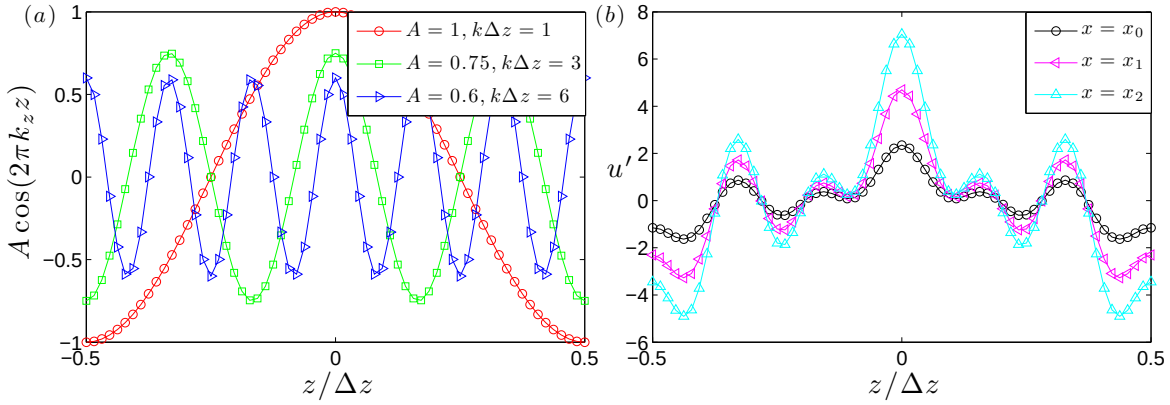


Figure B.2: (a) wavenumber decomposition of u' at $x = x_0$, (b) the linear amplification process considered on u'.

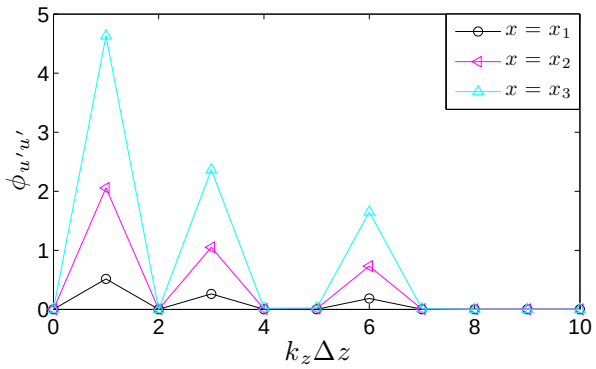


Figure B.3: Power spectral density of the waves in figure B.2(b).

If the above example is altered so that now $G = G(x; u)$, the process is no longer linear. Considering, for instance:

- $G(x_0) = 1$,
- $G(x_1) = 2u'$,
- $G(x_2) = 3u'$,

the transformation is now quadratic:

$$u'(x_1, z) = 2{u'}^2(x_0, z), \tag{B.3}$$

$$u'(x_2, z) = 3{u'}^2(x_0, z). \tag{B.4}$$

Figures B.4(a) and B.4(b) show, respectively, the application of the quadratic process in physical space and its spectral distribution. It can be seen that the response of a non-linear process is completely different to that of a linear one. The interaction (multiplication) between the original wavenumbers leads to the appearance of new ones. Besides, as can be seen in the detailed views of figure B.4(b), energy increases at some wavenumbers while it decreases at others, indicating that, for a non-linear growth process, energy does not grow or decay monotonically with x at all wavenumbers.

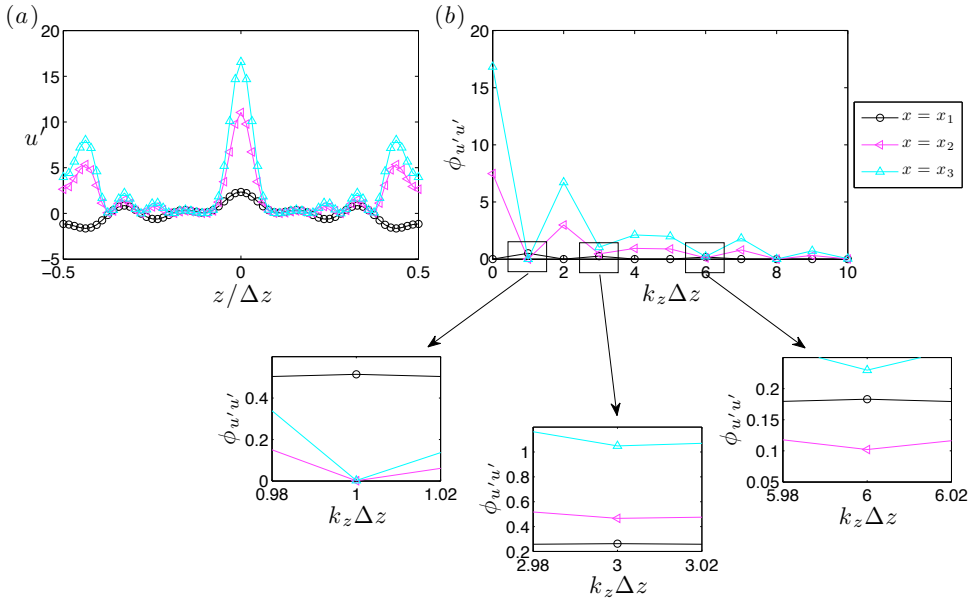


Figure B.4: Quadratic process applied on the wave considered in the example; (a) in physical space, (b) its spectrum distribution and three detailed views.

In fact, as shown in figure B.5, the energy at both the smallest and the largest wavenumber initially decays (despite the fact that $\|G(x_1)\| > 1$) and then grows, while the intermediate wavenumber experiences monotonic growth.

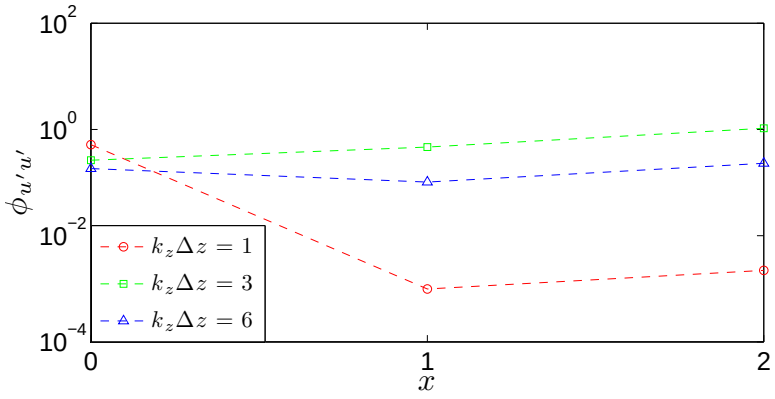


Figure B.5: Streamwise evolution of the constituent wavenumbers of the wave considered in the example.

A second comparison of linear and non-linear processes is also considered. This time the signal u' is extracted from the real LDA data of the present study, but the linear process is still the same as that in the previous example, equations (B.1) and (B.2). The non-linear process, also quadratic, is as follows:

$$u'(x_1, z) = 2.65{u'}^2(x_0, z), \tag{B.5}$$

$$u'(x_2, z) = 3{u'}^2(x_0, z). \tag{B.6}$$

The data are taken from the map of $u'(y, z)$ at $x = 225$ mm, figure 3.27(e), and at the wall-normal location where u'_{rms} peaks, figure 3.33(a). Hence, in this example x_0 corresponds to $x = 225$ mm in the experiments, and x_1 and x_2 are two fictitious downstream stations. Figures B.6(a), B.6(b) and B.6(c) show, respectively, the streamwise evolution of the linear amplification in physical space, the corresponding spectra, and the energy calculated using expression (3.11).

Analogously, figures B.7(a), B.7(b) and B.7(c) show respectively, the streamwise evolution of the non-linear (quadratic) process given by equations (B.5) and (B.6), in physical space, the corresponding spectra, and the associated energy.

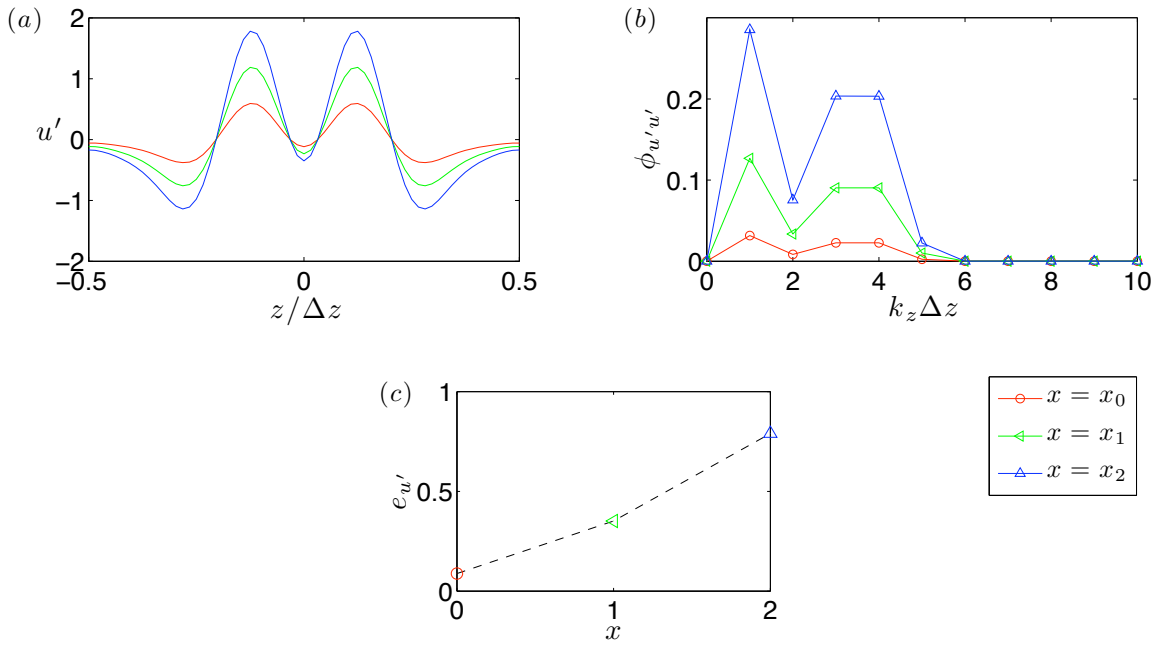


Figure B.6: Linear process applied on a wave from the LDA data; (*a*) in physical space, (*b*) spectra, (*c*) energy associated.

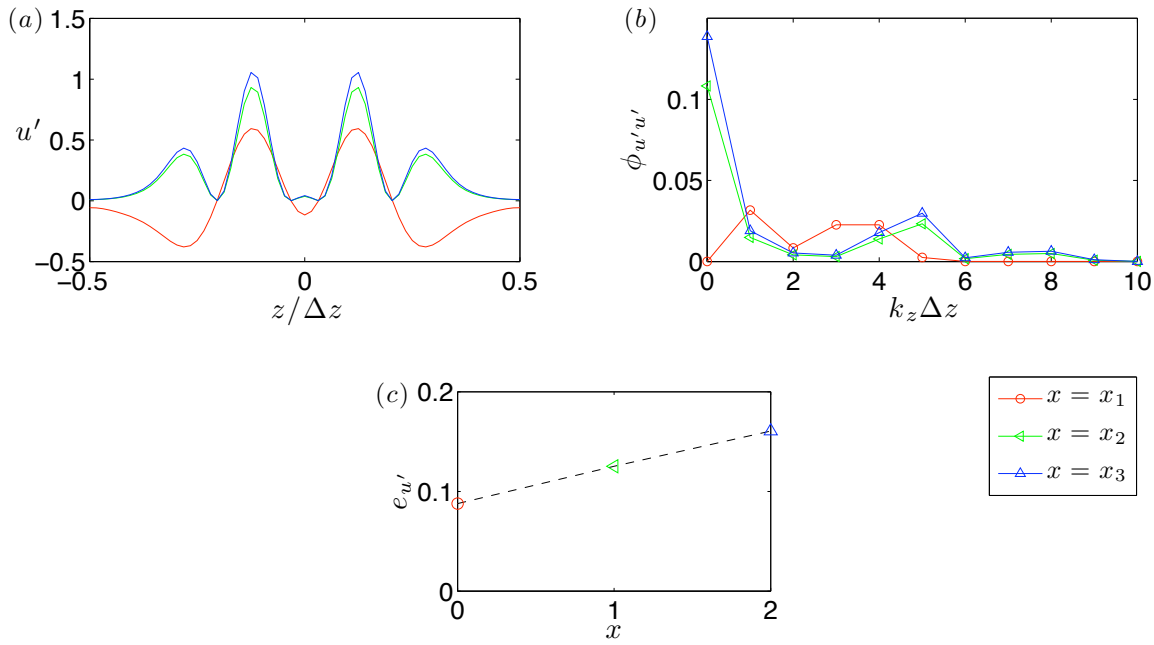


Figure B.7: Quadratic process applied on a wave from the LDA data; (*a*) in physical space, (*b*) spectra, (*c*) energy associated.

It can be seen that, while in the case of a linear growth process the power spectrum increases monotonically at all wavenumbers, in the case of non-linear growth it does not. In fact, $\phi_{u'u'}$ increases for some wavenumbers and decreases for others when going from

one streamwise station to another. Looking only at the streamwise evolution of the energy associated, figure B.7(c), may lead to misleading conclusions because, although the energy appears to grow linearly with x, the fact is that the process is intrinsically non-linear. The same phenomenon seems to occur in the flow of the present study: the energy of some modes grows while that of others decay (see for example figure 3.37), in spite of the fact that the total energy seems to exhibit linear growth with x. Hence, it can be concluded that there exists an underlying non-linear process in the algebraic transient growth of disturbances triggered by roughness element arrays.

Appendix C

Skewness and Kurtosis Analysis of the Roughness-Induced Perturbation

Skewness and kurtosis were calculated from the times series of the u and v velocities at a XZ-plane at $y/k = 1$ covering four wavelengths and $x \in [201.25, 325]$ mm, that is, from just downstream of the roughness element array to the beginning of the u'-energy decay region.

C.1 Definitions

C.1.1 Skewness

The skewness of a quantity u is given by

$$\gamma_u = \frac{E(u - \bar{u})^3}{\sigma^3}, \tag{C.1}$$

where $E(u)$ is the expected value of u, $\bar{u}$ is the mean value of u and σ its standard deviation. In the case that u consists of a finite population of samples:

$$\gamma_u = \frac{\frac{1}{N}\sum_{i=1}^{N}(u_i - \bar{u})^3}{\left(\frac{1}{N}\sum_{i=1}^{N}(u_i - \bar{u})^2\right)^{3/2}}, \tag{C.2}$$

where N is the number of samples of the population.

C.1.2 Kurtosis

The kurtosis of a quantity u is given by

$$\kappa_u = \frac{E(u - \bar{u})^4}{\sigma^4}, \tag{C.3}$$

and it is a measure of the flatness of the probability density function of u. If u follows a normal probability density function, then its kurtosis is 3. In the case that u consists of a finite population of samples, the kurtosis of the population is

$$\kappa_u = \frac{\frac{1}{N}\sum_{i=1}^{N}(u_i - \bar{u})^4}{\left(\frac{1}{N}\sum_{i=1}^{N}(u_i - \bar{u})^2\right)^2}. \tag{C.4}$$

C.2 Results

It is important to note that the size of the population of a reading considerably affects the values of both skewness and kurtosis. Figures C.1 and C.2 show, respectively, an example of the dependence of skewness and kurtosis on number of samples. In the example, pseudorandom number discrete series with normal probability density functions and various series lengths are created. This is repeated five times and, for every repetition, skewness and kurtosis are calculated for every different series length. As the series length is increased, skewness and kurtosis converge to their respective theoretical values of 0 and 3 for a continuous Gaussian series.

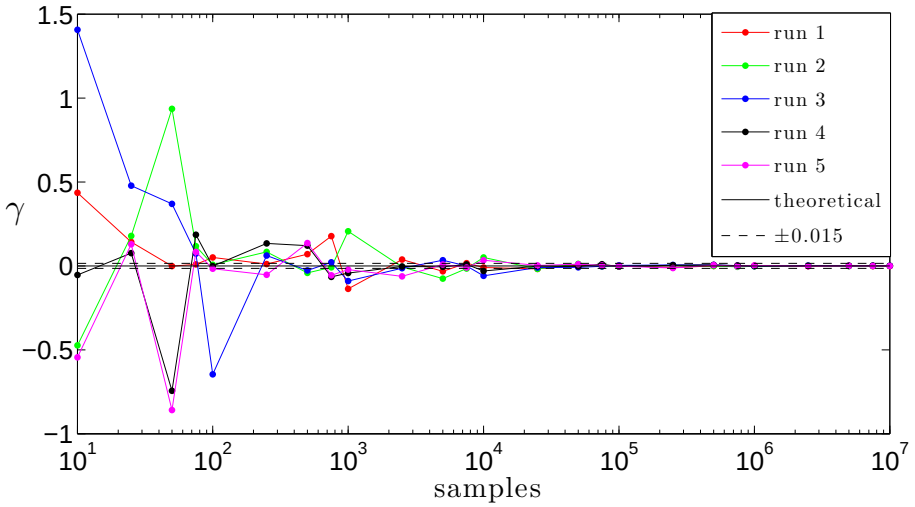


Figure C.1: Dependance of the skewness of five normally distributed pseudorandom number realisations on the number of samples per realisation.

Figure C.3 shows the number of samples per reading at each location of the plane where skewness and kurtosis of u and v are calculated. In the data acquisition stage, a strategy of acquiring 50000 samples per reading in the vicinity of the roughness element and 25000

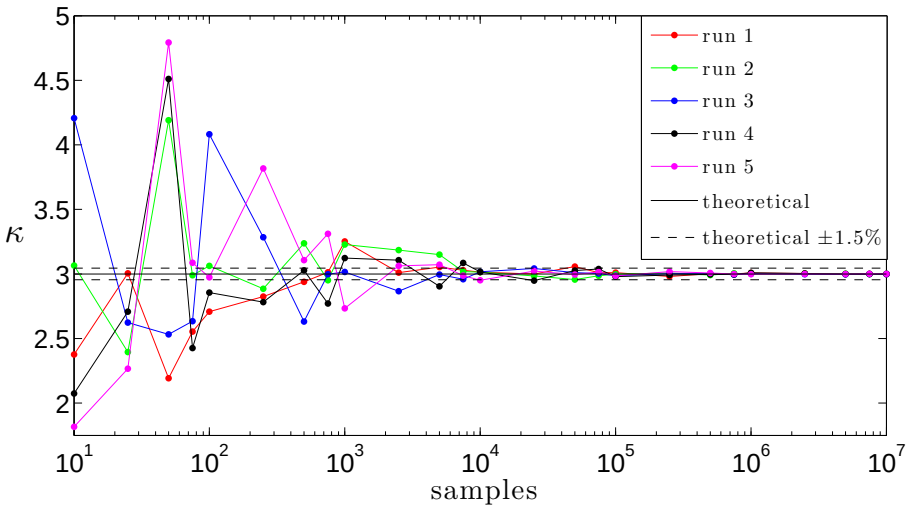


Figure C.2: Dependance of the kurtosis of five normally distributed pseudorandom number realisations on the number of samples per realisation.

further downstream was adopted. According to figures C.1 and C.2, those acquisition targets can provide skewness and kurtosis values within the region of convergence, given by a deviation of ±1.5% from the theoretical values. It can be seen in figure C.3 that those acquisition targets were achieved in the vast majority of the acquisition plane. However, as can also be seen, there were some regions where those acquisition targets could not be achieved, in particular immediately downstream of each roughness element (the minimum number of samples per readings was 15, taking place immediately downstream of the roughness element at $z/\Delta z = 1$).

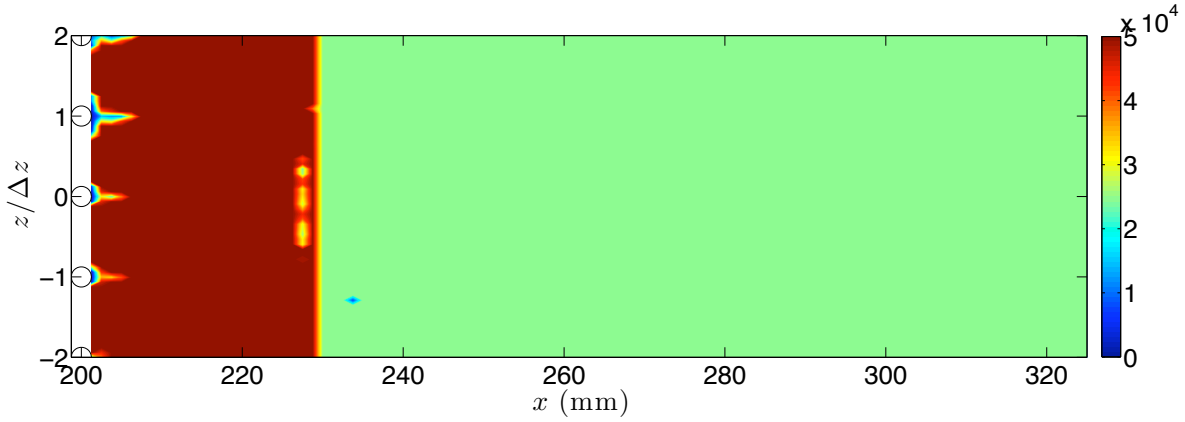


Figure C.3: Iso-contours of number of samples per reading at each location of the plane where skewness and kurtosis of u and v are calculated.

Figures C.4(a) and C.4(b) show, respectively, iso-contours of ensemble-averaged γ_u and γ_v. Different patterns can clearly be seen for each velocity component. With respect to u, a streak of positive skewness is aligned with the centre of the roughness element, with streaks of negative skewness on each side of it. These streaks seem to grow, reach a maximum and then die out with x. Between roughness elements the skewness seems to be near zero. In addition, it is interesting to note the presence of localised regions all across the span of the domain of intense positive skewness at $x \simeq 212.5$ mm, precisely near where the u'-energy starts to grow, and at $x \simeq 290$ mm, that is, near the end of the u'-energy growth region.

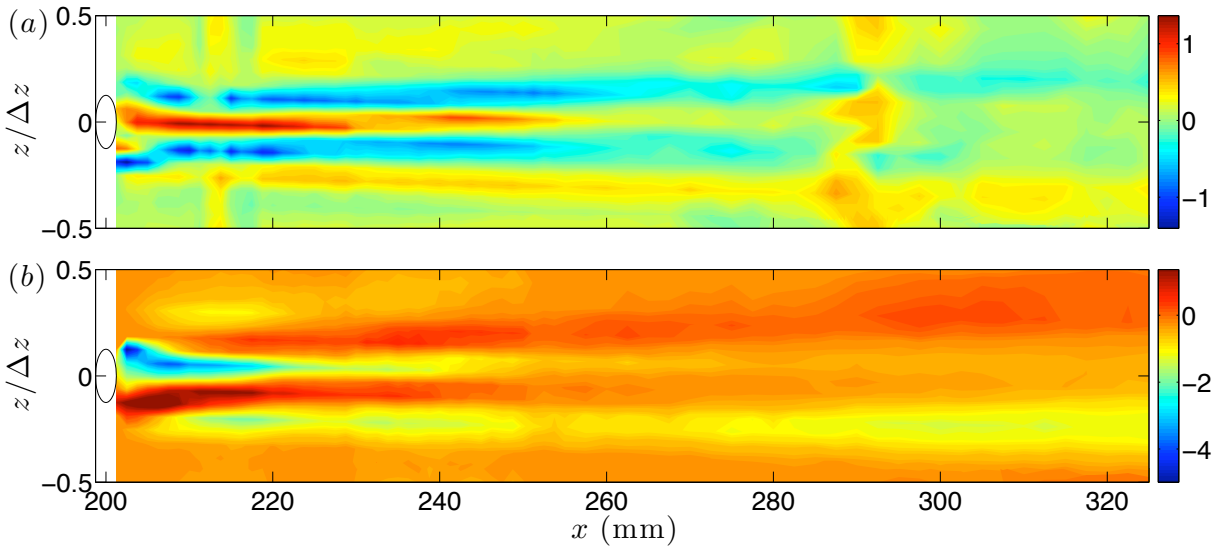


Figure C.4: Iso-contours of spanwise ensemble-averaged skewness; (a) γ_u, (b) γ_v.

Regarding v, a clearly different skewness pattern can be seen. Streaks of both positive and negative skewness are also apparent side-by-side and confined within a span of approximately two roughness diameters. Like γ_u, γ_v is near zero between roughness elements. Unlike γ_u, there is no sign of local variation in γ_v at $x \simeq 212.5$ and $x \simeq 290$ mm. The streamwise evolution seems to be similar to that of γ_u, with its absolute value showing a rapid increase just downstream of the roughness elements, reaching a maximum and then followed by a maintained decay.

Figure C.5 shows ensemble-averaged γ_u and γ_v versus x at $z/\Delta z = 0$. As mentioned, both γ_u and γ_v rapidly increase (in absolute value terms) just downstream of the roughness array, with the rate of growth of γ_v being larger. γ_u reaches its maximum where the

u'-energy starts to grow ($x \simeq 212.5$ mm). Then γ_v tends to zero faster than γ_u. At $x \simeq 250$ mm, γ_u and γ_v seem to have similar gradients. From $x \simeq 240$ mm onwards γ_v tends to negative values at a constant rate, whereas γ_u seems to stabilise around zero. However, as previously noted, at $x \simeq 290$ mm there seems to be a bump of positive γ_u.

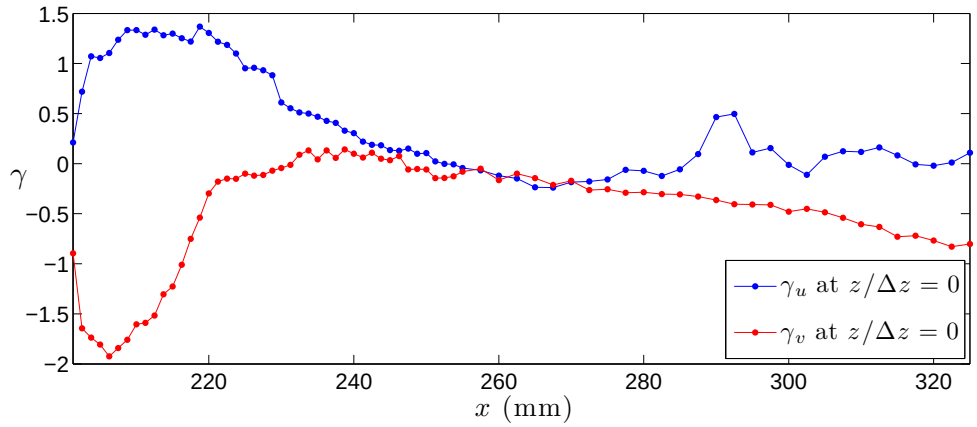


Figure C.5: Streamwise evolution of the ensemble-averaged γ_u and γ_v at $z/\Delta z = 0$.

Figure C.6 shows ensemble-averaged γ_u and γ_v versus x at $z/\Delta z = \pm 0.125$ (at the perimeter of the roughness element). Again, the trends are of opposite sign. As in the case at $z/\Delta = 0$, γ_v varies more rapidly than γ_u in the vicinity of the roughness element. Despite the fact that in the vicinity of the roughness element both γ_u and γ_v have opposite sings compared to their values at $z/\Delta = 0$, further downstream γ_u tends to zero and γ_v to a small negative value. It is worth noting that, while γ_u presents a similar behaviour throughout x at each side of the roughness element, γ_v shows a strong antisymmetric character, particularly in the wake region, characterised by a distinctive peak value. This peak is approximately twice higher on one side than on the other.

Figures C.7(a) and C.7(b) show iso-contours of ensemble-averaged κ_u and κ_v, respectively. The first aspect worth noticing is that both κ_u and κ_v follow similar patterns to those of γ_u and γ_v (in terms of absolute value), respectively. Therefore, at the edges of the roughness element ($z/\Delta z = \pm 0.125$) values of both κ_u and κ_v are large; its centreline ($z/\Delta z = 0$) seems to be sources of large κ_u only; and the u'-energy growth end ($x \simeq 300$ mm) is preceded by a spanwise zone of large κ_u. It is also interesting to note that, at these locations, κ_v is about six times larger than κ_u. This is in contrast with the levels of skewness, in which γ_u and γ_v are approximately of similar magnitude.

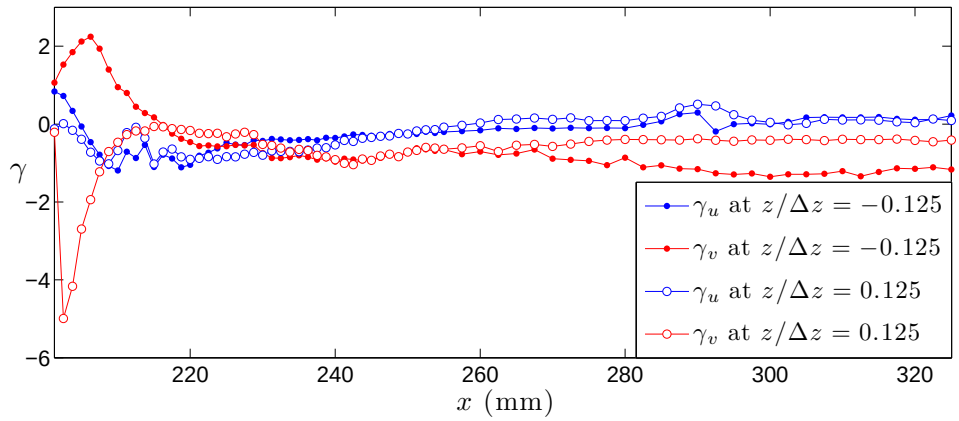


Figure C.6: Streamwise evolution of the ensemble averaged γ_u and γ_v at $z/\Delta z = \pm 0.125$.

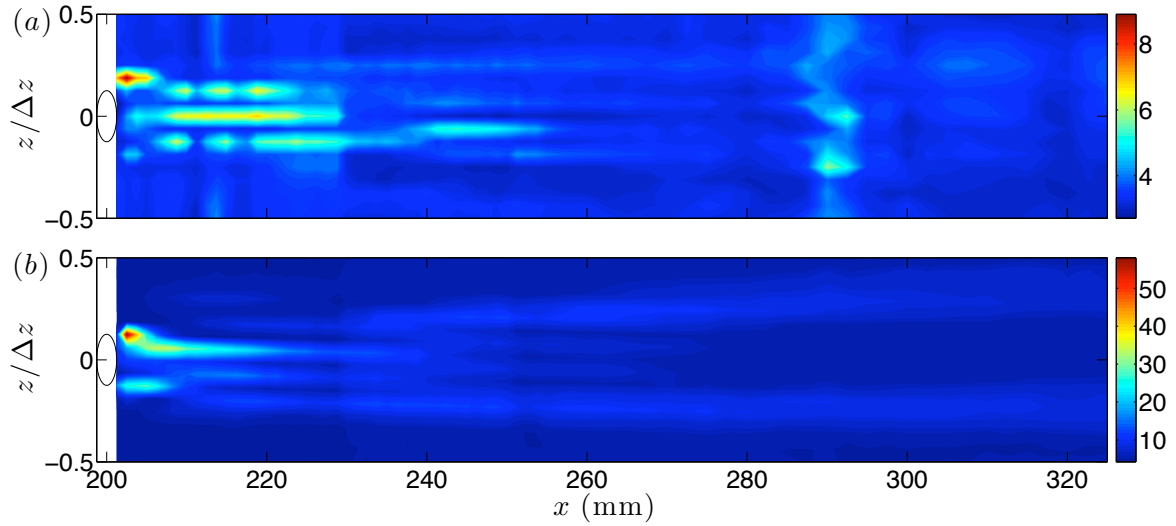


Figure C.7: Iso-contours of spanwise ensemble-average kurtosis; (a) κ_u, (b) κ_v.

Figures C.8(a) and C.8(b) show histograms of the distributions of values of κ_u and κ_v from figures C.7(a) and C.7(b), respectively. It can be seen that, despite the large difference between high levels of κ_u and κ_v, the majority of the values of κ_u is concentrated approximately between 3 and 4 (with 3.4 occurring the most, at 130 locations out of 1224), while the majority of the values of κ_v is concentrated approximately between 4.5 and 15 (with 5.9 occurring the most, at 259 locations out of 1224).

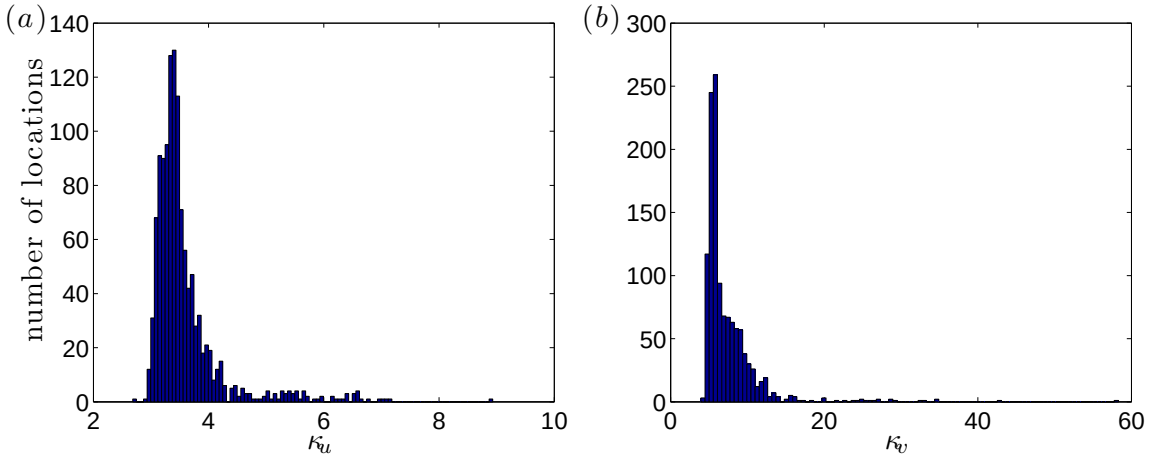


Figure C.8: Distribution of kurtosis occurrences from figure C.7; (*a*) κ_u, (*b*) κ_v.

In summary, this analysis of skewness and kurtosis on time series of both u and v at a plane parallel to the wall at $y/k = 1$ reveals streak-like patterns. Large skewness (for both u and v) in the wake region indicate the possibility of existence of intermittent, hence unsteady, processes. The regions of large (in absolute value) skewness form elongated streak-like patterns aligned with the roughness elements, and with a spanwise dimension of approximately two roughness diameters. Everywhere else the skewness is approximately zero. Inside the region of finite skewness, there is a sudden growth in skewness just downstream of the roughness elements, followed by a progressive decay with x. However, in the case of u only, there is a local increase in skewness at $x \simeq 290$ mm, just before the end of the u'-energy growth region (although without reaching similar levels to those in the wake region). Interestingly, this local increase also occurs in the case of the kurtosis of u. Like the skewness, the kurtosis of both u and v follow similar streak-like patterns to those of the skewness, with high levels aligned with the roughness elements and in a spanwise extent of two roughness diameters. Within these streaks, the levels of kurtosis of v are generally much higher than those of u. Everywhere else, the dominant level of kurtosis of u is approximately 3.4 (near 3, the value for a Gaussian probability distribution), whereas in the case of v the dominant level is approximately 5.9.

Appendix D

Finite Difference Simulations

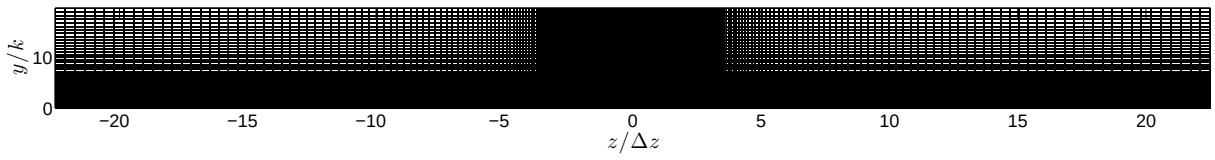


Figure D.1: Grid of the computational domain.

D.1 Purpose

Since this project is conceived in a flow control research group, a code to carry out 2-D time-marching numerical simulations is developed with the purpose of developing actuators and control strategies to suppress $\partial v'/\partial z$. The code serves as a cost-effective workbench to test different actuator configurations, in terms of the types of actuation, the relative location of the actuators, and their amplitudes and frequencies.

D.2 Characterisation of the Active Surface

The actuation was conducted by means of an active surface, formed by a spanwise array of discrete actuators flush with the wall. The span of the active surface was equal to that of the roughness element array used in the experiments. The parameters considered for the characterisation of the active surface were:

1. types of actuator
2. spanwise location of the actuators relative to the roughness elements
3. spacing between actuators
4. frequency and amplitude of actuation.

D.2.1 Types of Actuator

Two types of actuators, "A" and "B", were considered, inspired by Gouder (2010). They essentially consist of a pre-streched sheet of polymer (yellow layers in figure D.2) sandwiched between two (for type-A) or four (for type-B) compliant electrodes (grey/black layers in figure D.2). When a voltage across them is applied, the device acts as a compliant capacitor, in which the electrodes squeeze/release the incompressible polymer in the direction normal to it and, hence, making in-plane expansions or contractions, see figure D.2. Electroactive polymer (EAP) materials have been used successfully for surface-based actuation (Dearing *et al.*, 2007, 2010; Gouder, 2010; Potter *et al.*, 2011; Gouder *et al.*, 2012).

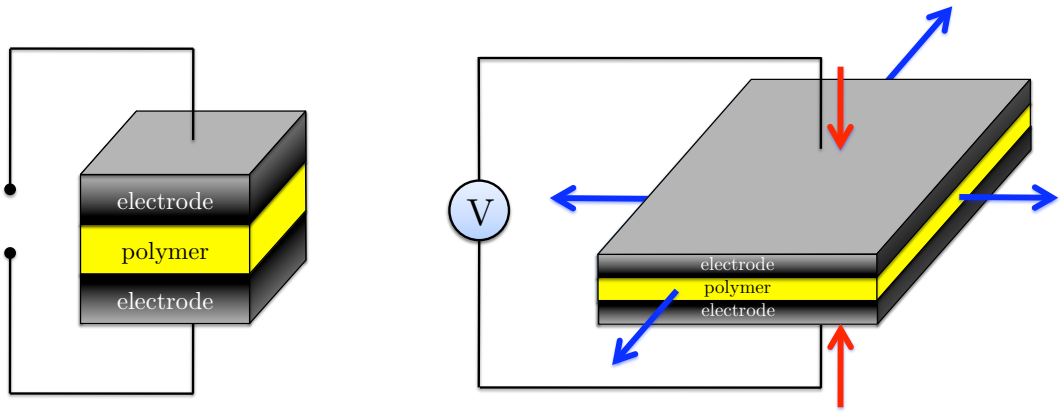


Figure D.2: Simplified schematic of the fundamentals of actuators based on polymer sheets sandwiched by two electrodes.

Both type-A and B actuators are constrained in the streamwise direction so that the deflection of the polymer sheet takes place only in the spanwise direction. In essence, the way that these actuators were thought to work was by performing in-plane spanwise harmonic expansions/contractions (type-A) or oscillations (type-B). Therefore, in terms of the numerical simulations, they provide a boundary condition of imposed spanwise velocity parallel to the boundary and variable with time. If moving harmonically, the actuators will induce a constant flux of secondary motion, with common flow towards the line of symmetry between the two electrodes (Schlichting, 2000). This phenomenon is known as "streaming".

Type A

This type of actuator, shown in figure D.3, consists of a polymer sheet in which two electrode strips (top and bottom) are situated at the centre. The electrode width does not cover the entire span of the actuator so that there is room for spanwise deflections. Owing to the symmetrical configuration with respect to the centre-line of the actuator, the deflection of the polymer sheet is in form of expansions and contractions, which are zero along the centre-line and side edges of the actuator frame, and a maximum at the edges of the electrodes.

The actuator deflection, $A(z)$, taken as the displacement of a point in the actuator with respect to its rest position, varies across the span of the actuator. It is zero at the

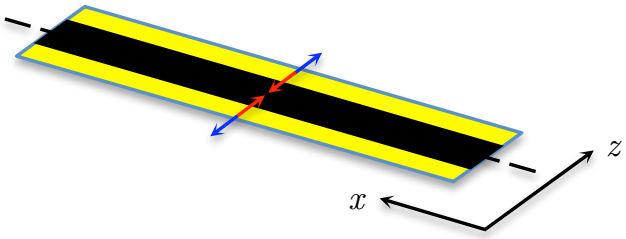


Figure D.3: Schematic of a type-A actuator.

centre-line and at the frame of the actuator, and maximum at the edges of the electrodes. To simulate $A(z)$, a linear model was considered as a first approximation (figure D.4).

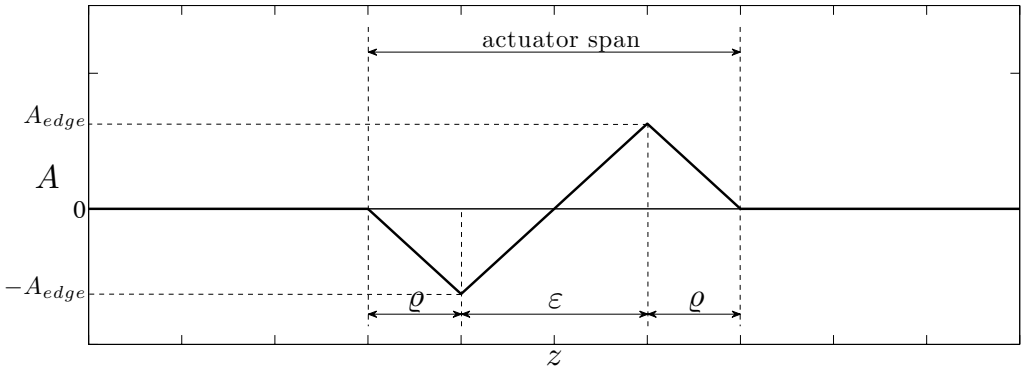


Figure D.4: Spanwise distribution of the deflection amplitude for type-A actuators at a given time.

Taking the origin of z at the centre of the actuator, $A(z)$ can be formulated as:

$$A(z) = \begin{cases} A_{edge}\left[-\frac{1}{\varrho}\left(\frac{\varepsilon}{2}+z\right)-1\right] & z \in [-\frac{\varepsilon}{2}-\varrho, -\frac{\varepsilon}{2}], \\ \frac{A_{edge}}{\varepsilon/2} z & z \in [-\frac{\varepsilon}{2}, \frac{\varepsilon}{2}], \\ A_{edge}\left[\frac{1}{\varrho}\left(\frac{\varepsilon}{2}-z\right)+1\right] & z \in [\frac{\varepsilon}{2}, \frac{\varepsilon}{2}+\varrho], \\ 0 & z \ni (-\frac{\varepsilon}{2}-\varrho, \frac{\varepsilon}{2}+\varrho), \end{cases} \tag{D.1}$$

where A_{edge} is the prescribed value of the maximum deflection amplitude which takes place on the edges of the electrodes, ε the electrode span and ϱ the distance between the electrode edges and the actuator edges. Negative values of $A(z)$ indicate that the deflection is in the negative z direction. Since the applied voltage and deflections are harmonic, $A(z)$ is multiplied by a sine wave to give the spatial/temporal distribution of

deflections, $\hat{d}(z,t)$. Hence:

$$\hat{d}(z,t) = A(z)|\sin(\omega t)|, \tag{D.2}$$

where $\omega = 2\pi f$, with f the frequency of the imposed wall velocity signal. The absolute value applied to the sine function is adopted because the sign of $\hat{d}$ is given by the sign of $A(z)$.

Figure D.5 shows the active surface with the actuators aligned with the roughness elements and at (a) rest state, and (b) maximum deflection state, for a particular case in which $\varepsilon = 2\varrho = d$ (the roughness element diameter), and a value for A_{edge} of $d/4$ (meaning that the electrode area can expand a maximum of $d/2$, half each side).

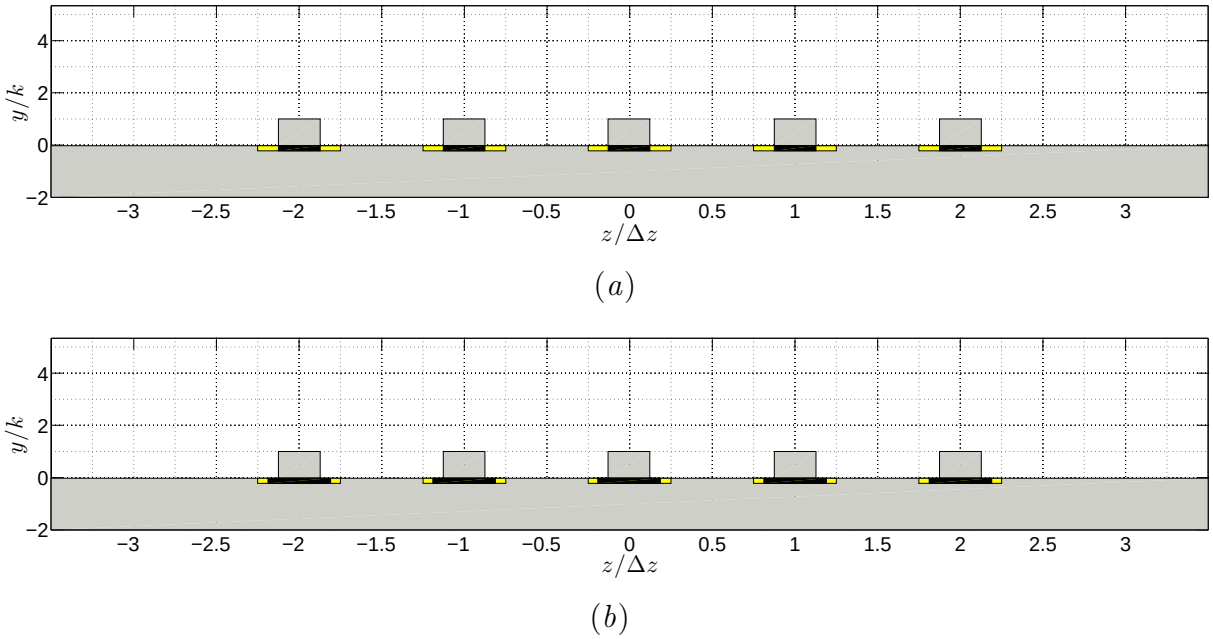


Figure D.5: Active surface with type-A actuators; (a) actuators at rest, (b) actuators at maximum deflection.

The imposed wall velocity for the boundary condition in the numerical simulations given by this type of actuator is obtained simply by differentiating $\hat{d}(z,t)$ with respect to time, hence

$$w_{wall}(z,t) = W(z)\cos(\omega t + \varphi), \tag{D.3}$$

with

$$W(z) = A(z)\omega. \tag{D.4}$$

The phase shift φ is intentionally introduced and prescribed as $-\pi/2$ such that the velocity is zero both at the rest state and at maximum deflection state. Figure D.6 shows a comparison of the driving voltage signal input and the resulting wall deflection and wall velocity signals (at an arbitrary location $z = z^*$ on the right-hand side of an actuator centred at $z = 0$). In a real implementation, the driving voltage signal has to have a rectifying stage which conducts the absolute value of the signal and hence provides the actuator always with a voltage $\geqslant 0$. The frequency of the driving voltage has to be half of that of both the wall velocity forcing and the polymer sheet deflection Gouder (2010) discusses more realistic transfer functions for this type of actuator.

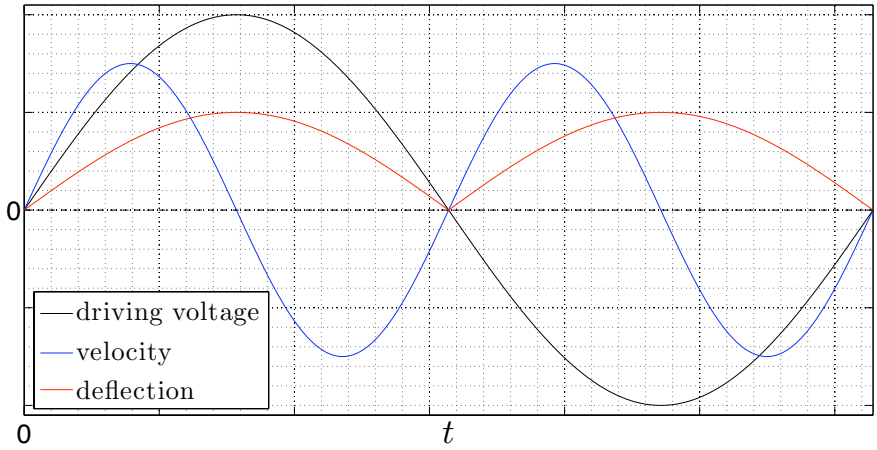


Figure D.6: Comparison of driving voltage, wall deflection and wall velocity signals (arbitrary scales) for a type-A actuator.

Type B

For this type of actuator, the electrode strips are located towards the sides of the polymer sheet, as shown in figure D.7. In this configuration, owing to the constraint at the two free edges, the electrodes perform only half expansions/contractions. Thus, if the electrodes are alternately activated (i.e. in half a driving cycle one electrode is activated and the other deactivated and vice versa), the net combination of the two motions yields harmonic oscillations.

As in the case of type-A actuators, the distribution of the deflection amplitude across the actuator was simulated by a first-order model. In comparison to the behaviour of the electrodes of type-A actuators, the amplitude increases across the span of the activated

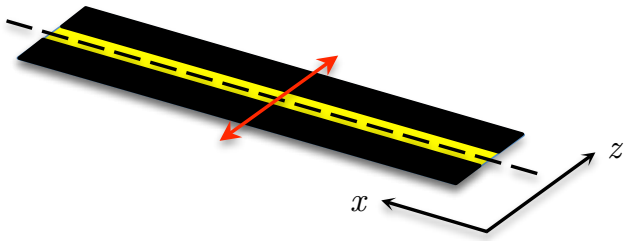


Figure D.7: Schematic of a type-B actuator.

electrode, reaching its maximum at the free edge and then decaying up to the opposite edge of the actuator, as shown in figure D.8. For a clear mathematical formulation, two deflection amplitude distributions are considered: $A_{left}(z)$, when the electrodes of the left-hand side of the actuator are activated, and $A_{right}(z)$ when the right electrodes are activated.

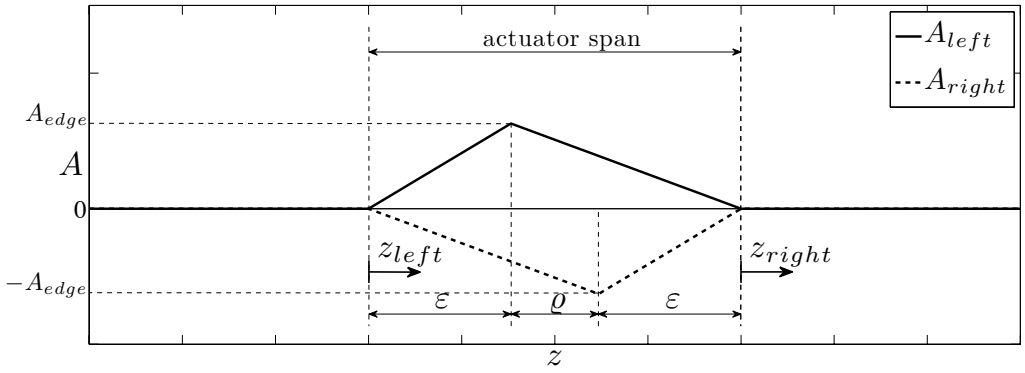


Figure D.8: Spanwise distribution of the deflection amplitude for type-B actuators.

Deflection amplitudes $A_{left}(z)$ and $A_{right}(z)$ are formulated, for origins z_{left} and z_{right} respectively (located at each side of the actuator as shown in figure D.8), as:

$$A_{left}(z_{left}) = \begin{cases} \frac{A_{edge}}{\varepsilon} z_{left} & z_{left} \in [0, \varepsilon], \\ -\frac{A_{edge}}{\varrho} \left(z_{left} - \varrho - \varepsilon\right) & z_{left} \in [\varepsilon, \varrho + \varepsilon], \\ 0 & z_{left} \ni (0, \varrho + \varepsilon), \end{cases} \tag{D.5}$$

and

$$A_{right}(z_{right}) = \begin{cases} -\frac{A_{edge}}{\varrho}\left(z_{right} + \varepsilon + \varrho\right) & z_{right} \in [-(\varepsilon+\varrho), -\varepsilon], \\ \frac{A_{edge}}{\varepsilon} z_{right} & z_{right} \in [-\varepsilon, 0], \\ 0 & z_{right} \ni (-\varepsilon - \varrho, 0), \end{cases} \tag{D.6}$$

where A_{edge}, ε and ϱ mean the same as in the case of type-A actuators. Negative values of deflection indicate that it is opposite to the positive direction of z.

Then, the complete description of the deflections is given by multiplying the deflection amplitude distributions by the absolute value of a sine wave, That is,

$$\hat{d}_{left}(z_{left}, t) = A_{left}(z_{left})|\sin(\omega t)| \tag{D.7}$$

and

$$\hat{d}_{right}(z_{right}, t) = A_{right}(z_{right})|\sin(\omega t)|. \tag{D.8}$$

Figure D.9 shows a similar configuration of active surface to that shown in figure D.5 but with type-B actuators placed between roughness elements. The figure represents D.9(a) left electrodes are activated and at rest state, (b) left electrodes are activated and at maximum deflection state, (c) right electrodes are activated and at rest state, and (d) right electrodes are activated and at maximum deflection state. For a particular case with the actuator span and electrode span are, respectively, twice and 3/8 of the roughness element diameter, and a value for A_{edge} of $d/2$.

The corresponding imposed wall velocity for the boundary condition in the numerical simulations given by this type of actuator is obtained as carried out for type-A actuators, thus

$$w_{wall}(z, t) = W(z)\cos(\omega t + \varphi), \tag{D.9}$$

with $W(z)$ either $A_{left}(z)\omega$ or $A_{right}(z)\omega$ depending on whether left or right electrodes are activated. The phase shift φ is intentionally introduced and prescribed as $-\pi/2$ for the same reason as in the case of type-A actuators.

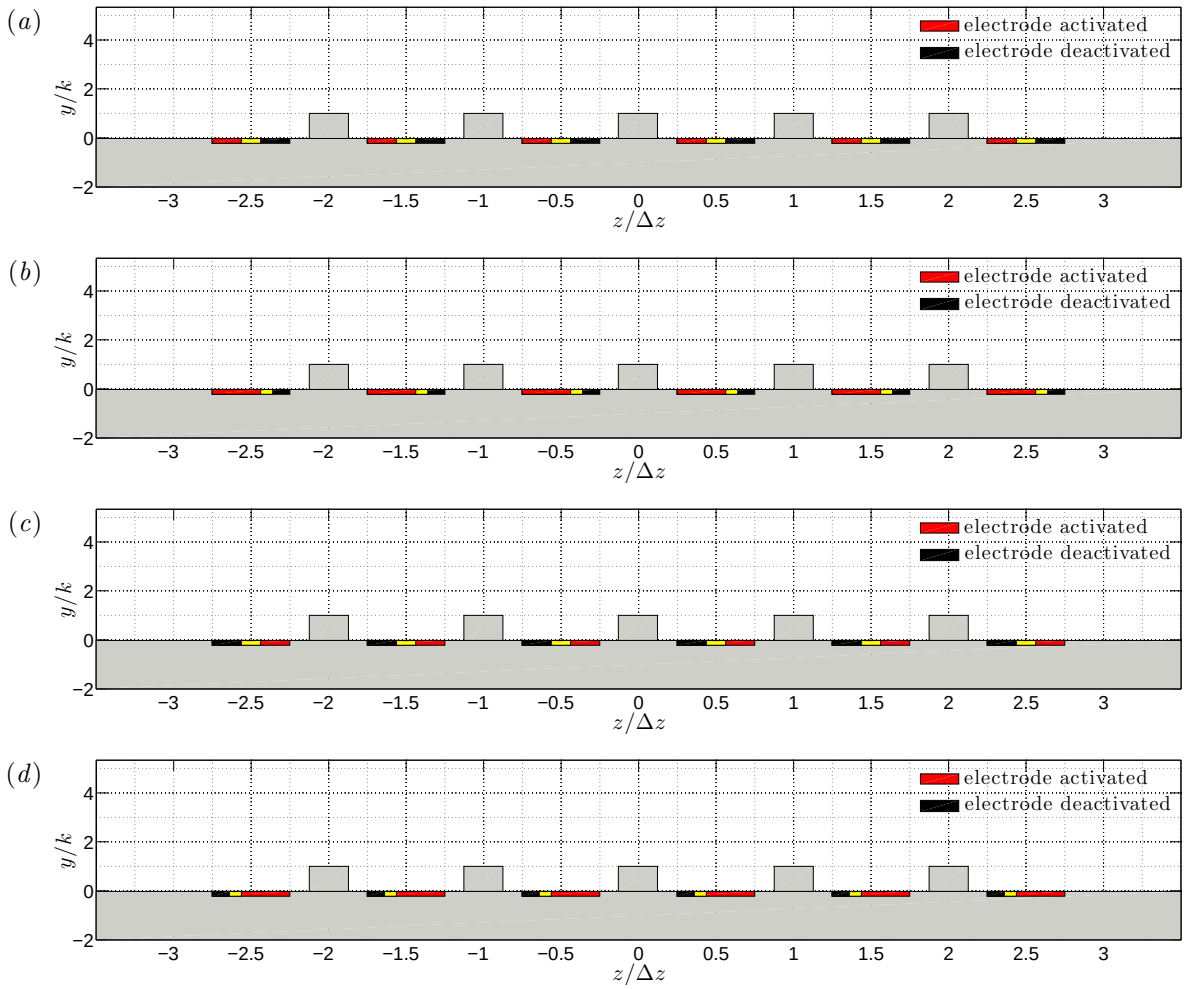


Figure D.9: Active surface with type-B actuators; (a) left electrodes activated and at rest; (b) left electrodes activated and at maximum deflection; (c) right electrodes activated and at rest; (d) right electrodes activated and at maximum deflection.

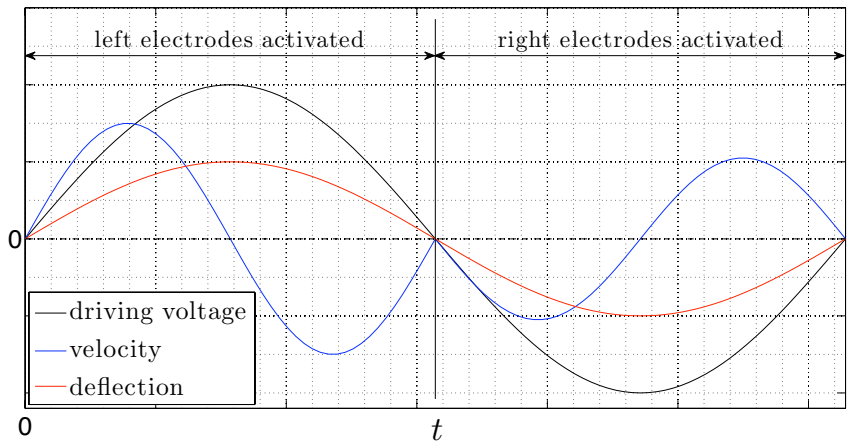


Figure D.10: Comparison of driving voltage, wall deflection and wall velocity signals (arbitrary scales) for a type-B actuator.

D.3 Formulation

Th 3-D unsteady Navier-Stokes equations for incompressible flow are given by

$$\nabla \cdot \vec{u} = 0, \tag{D.10}$$

$$\frac{D\vec{u}}{Dt} = -\frac{1}{\rho}\nabla p + \nu\nabla^2\vec{u}, \tag{D.11}$$

where $\vec{u}$ is the velocity vector field, p the pressure scalar field, ν is the viscosity of the fluid and no body forces were considered.

In order to formulate the problem in 2-D, the actuators are considered to be infinitely long in the streamwise direction and working in stagnant flow (i.e. zero free stream), and therefore the existing flow is produced only by the actuators. With these assumptions, the streamwise velocity component, u, and all the streamwise derivatives, $\partial/\partial x$, are zero. The equations (D.11) can be then re-written in terms of the components of the 2-D velocity field (v, wall-normal; and w, spanwise) as follows:

$$v: \qquad \frac{\partial v}{\partial t} + v\frac{\partial v}{\partial y} + w\frac{\partial v}{\partial z} = -\frac{1}{\rho}\frac{\partial p}{\partial y} + \nu\left(\frac{\partial^2 v}{\partial y^2} + \frac{\partial^2 v}{\partial z^2}\right), \tag{D.12}$$

$$w: \qquad \frac{\partial w}{\partial t} + v\frac{\partial w}{\partial y} + w\frac{\partial w}{\partial z} = -\frac{1}{\rho}\frac{\partial p}{\partial z} + \nu\left(\frac{\partial^2 w}{\partial y^2} + \frac{\partial^2 w}{\partial z^2}\right). \tag{D.13}$$

The terms crossed out were neglected in the formulation of the code, as streamwise variations of the magnitudes are not considered. These simplifications proved to play a major role in the inability to accurately replicate the flow analysed in the experiments. Nevertheless, important conclusions to understand the physical mechanisms that govern the actual flow with surface actuation can still be drawn.

Equations (D.12) and (D.13) were solved using the Stream Function - Vorticity (SFV) formulation, which is suitable for 2-D flows and commonly used, as pointed out by Ortega-Casanova & Fernandez-Feria (2002). In the SFV formulation, the three primitive variables (w, v and p) are replaced by the stream function, ψ, and the component of

the vorticity field $\vec{\omega} = \nabla \wedge \vec{u}$ normal to the computational domain, in this case, ω_x. The pressure field disappears from the equation system since $\nabla \wedge \nabla p \equiv 0$.

The equation for ω_x is derived by subtracting (D.13) differentiated with respect to y from (D.12) differentiated with respect to z, and is expressed in terms of ζ, where $\zeta = -\omega_x$. The continuity equation is identically satisfied in terms of ψ.

The definitions adopted for ψ and ζ are thus:

$$v = \frac{\partial \psi}{\partial z}; \quad w = -\frac{\partial \psi}{\partial y}; \tag{D.14}$$

$$\zeta \equiv -\omega_x = \frac{\partial v}{\partial z} - \frac{\partial w}{\partial y}. \tag{D.15}$$

Finally, the equation system to solve is:

$$\frac{\partial \zeta}{\partial t} = -\left(\frac{\partial \psi}{\partial z}\frac{\partial \zeta}{\partial y} - \frac{\partial \psi}{\partial y}\frac{\partial \zeta}{\partial z}\right) + \nu\left(\frac{\partial^2 \zeta}{\partial y^2} + \frac{\partial^2 \zeta}{\partial z^2}\right), \tag{D.16}$$

$$\zeta = \frac{\partial^2 \psi}{\partial y^2} + \frac{\partial^2 \psi}{\partial z^2}, \tag{D.17}$$

$$\frac{\partial u}{\partial t} = -\left(\frac{\partial \psi}{\partial z}\frac{\partial u}{\partial y} - \frac{\partial \psi}{\partial y}\frac{\partial u}{\partial z}\right) + \nu\left(\frac{\partial^2 u}{\partial y^2} + \frac{\partial^2 u}{\partial z^2}\right). \tag{D.18}$$

Expression (D.16) is the vorticity transport equation, is non-linear and parabolic in time. Note that, once ψ is calculated, u is completely determined.

When simulating the effects of surface actuation under stagnant-flow conditions, only (D.16) and (D.17) were employed, as (D.18) is identically zero due to the absence of streamwise flow.

D.4 Time-Marching Method

The method is a predictor-corrector method based on calculating the solution at the next time step (t^{n+1}) considering the solution at the current time step (t^n) and at a ficticious time step (t^*) between t^n and t^{n+1}.

As its name indicates, this method consists of two stages, one of predicting the solution at t^* computed using the solution at t^n, and the second a correction where the solution at t^{n+1} is computed as a correction based on the solution at both t^n and t^*.

If a first-order approximation to discretise $\partial/\partial t$ is considered:

$$\frac{\partial \zeta}{\partial t} \simeq \frac{\zeta^{n+1} - \zeta^n}{\delta t}, \tag{D.19}$$

and, to simplfy notation, the whole right-hand side term of expression (D.16) at t^n is expressed as a function $F(\psi^n, \zeta^n)$, then (D.16) can be re-written as:

$$\zeta^{n+1} = \zeta^n + \delta t\, F(\psi^n, \zeta^n). \tag{D.20}$$

Based on expression (D.20), the two stages of the predictor-corrector method are written as:

$$\textbf{Prediction:} \qquad \zeta^* = \zeta^n + \frac{\delta t}{2} F(\psi^n, \zeta^n), \tag{D.21}$$

$$\textbf{Correction:} \qquad \zeta^{n+1} = \zeta^n + \delta t\, F(\psi^*, \zeta^*), \tag{D.22}$$

where ψ^* is computed between both stages by inverting (D.17). The time-step size δt was chosen to be constant for all the simulations.

As can be seen, this is a single-step, explicit method. The latter feature makes it easy to be coded, which was the main reason for choosing this method. However, the disadvantage of this method is that it is not unconditionally stable for any δt. Therefore, a stability analysis has to be conducted in order to establish a proper value for δt, which is related to the spatial discretisation of the computational domain through a condition derived from an stability analysis conducted (explained in section D.6).

D.5 Discretisation

D.5.1 Derivative Approximations - Finite Differences

A four-node (3^{rd} order) "hybrid" central-difference scheme for the second-derivative "adaptive" approximations was used. The term "hybrid" is used because, since the number of nodes used for the approximations is even, more nodes are used on one side of the node where the derivative is evaluated than on the other. Besides, at the boundaries and near them, either full forward or backward differences or non-centred central differences were used. For the first-derivative approximations, a three-node (2^{nd} order) "hybrid" central-difference "adaptive" scheme was used. In this case, the term "hybrid" refers just to the fact that, at the boundaries, either full forward or backward differences were used. The term "adaptive" is given because the derivatives were computed on a grid with non-uniform spacing in both z and y.

For simplicity of notation, the explanation of the discretisation scheme for the derivatives is shown for y, because the scheme is identical in z (by just substituting the terms 'bottom/top' for 'left/right' and index 'i' for 'j'). Figures D.11 and D.12 illustrate the combination of nodes used to compute both the first- and second-derivative approximations, respectively. Black nodes are those at which the derivative approximation is calculated, grey nodes are the other nodes contributing to the calculation, and unused nodes are those in white. Note that, depending on whether the node at which the derivative approximation is calculated belongs to the bottom boundary, or is an interior node, or is a top-boundary neighbour node (for second derivatives only) or belongs to the top boundary, the finite-difference scheme has to change.

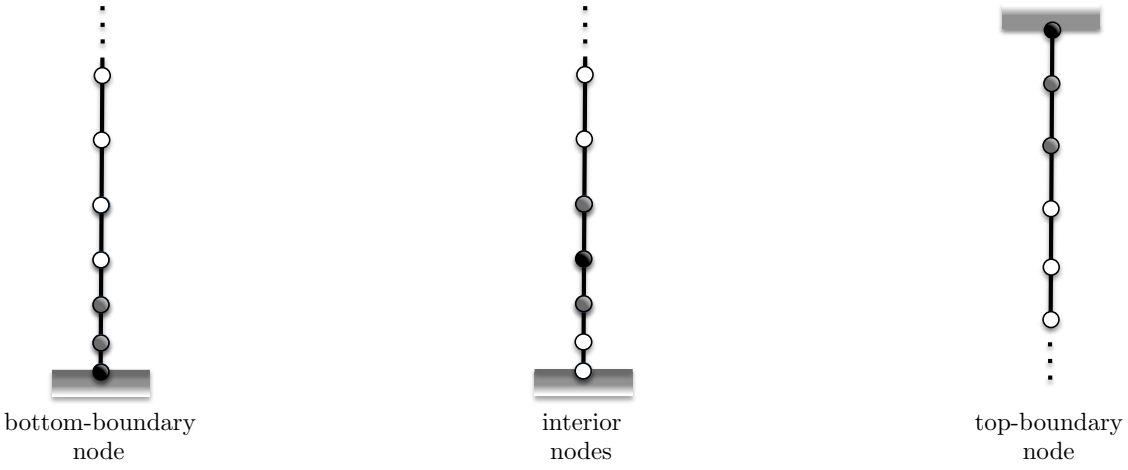


Figure D.11: First-derivative approximations. Black nodes are those at which the derivatives are evaluated, grey nodes are those involved in the calculation and white nodes are unused.

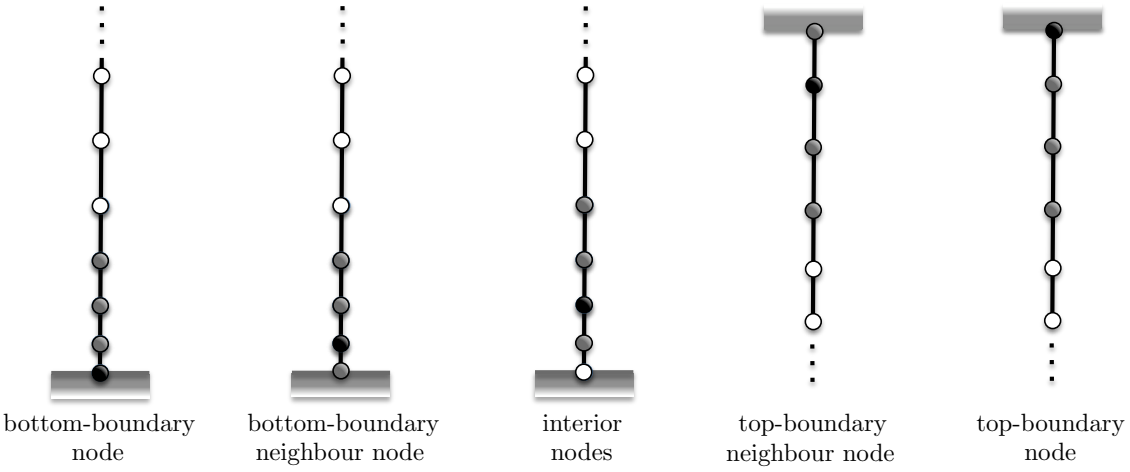


Figure D.12: Second-derivative approximations. Black nodes are those at which the derivatives are evaluated, grey nodes are those involved in the calculation and white nodes are unused.

Before showing the expressions of the employed finite-difference schemes, a simplifying notation is given:

$$h_{i+3} \equiv y_{i+3} - y_i,$$
$$h_{i+2} \equiv y_{i+2} - y_i,$$
$$h_{i+1} \equiv y_{i+1} - y_i,$$
$$h_{i-1} \equiv y_{i-1} - y_i,$$
$$h_{i-2} \equiv y_{i-2} - y_i,$$
$$h_{i-3} \equiv y_{i-3} - y_i,$$

where the index 'i' indicates the node at which the derivative approximation is evaluated.

Then, given the definition shown in figure D.11, the formulae for the first-derivative approximations evaluated at y_i for a generic quantity Φ are:

- **bottom boundary:**

$$\frac{\partial \Phi}{\partial y}\Big|_{y=y_i} \simeq B_i \Phi_i \; + \; B_{i+1}\Phi_{i+1} \; + \; B_{i+2}\Phi_{i+2}, \tag{D.23}$$

  where:

$$B_i = \frac{-(h_{i+1} + h_{i+2})}{h_{i+1}h_{i+2}}, \tag{D.24}$$

$$B_{i+1} = \frac{-h_{i+2}}{h_{i+1}(h_{i+1} - h_{i+2})}, \tag{D.25}$$

$$B_{i+2} = \frac{h_{i+1}}{h_{i+2}(h_{i+1} - h_{i+2})}. \tag{D.26}$$

- **interior:**

$$\frac{\partial \Phi}{\partial y}\Big|_{y=y_i} \simeq B_{i-1}\Phi_{i-1} \; + \; B_i \Phi_i \; + \; B_{i+1}\Phi_{i+1}, \tag{D.27}$$

  where:

$$B_{i-1} = \frac{-h_{i+1}}{h_{i-1}(h_{i-1} - h_{i+1})}, \tag{D.28}$$

$$B_i = \frac{-(h_{i-1} + h_{i+1})}{h_{i-1}h_{i+1}}, \tag{D.29}$$

$$B_{i+1} = \frac{h_{i-1}}{h_{i+1}(h_{i-1} - h_{i+1})}. \tag{D.30}$$

- **top boundary:**

$$\frac{\partial \Phi}{\partial y}\Big|_{y=y_i} \simeq B_{i-2}\Phi_{i-2} \; + \; B_{i-1}\Phi_{i-1} \; + \; B_i \Phi_i. \tag{D.31}$$

  where:

$$B_{i-2} = \frac{1}{h_{i-2}h_{i-1}(-h_{i-2} + h_{i-1})}, \tag{D.32}$$

$$B_{i-1} = \frac{-h_{i-2}}{h_{i-1}(-h_{i-2} + h_{i-1})}, \tag{D.33}$$

$$B_i = \frac{-(h_{i-2} + h_{i-1})}{h_{i-2}h_{i-1}}. \tag{D.34}$$

The formulae for the second-derivative approximations of Φ evaluated at y_i shown in figure D.12, are:

- **bottom boundary:**

$$\left.\frac{\partial^2\Phi}{\partial y^2}\right|_{y=y_i} \simeq C_i\Phi_i \ + \ C_{i+1}\Phi_{i+1} \ + \ C_{i+2}\Phi_{i+2} \ + \ C_{i+3}\Phi_{i+3}, \tag{D.35}$$

where:

$$C_{i+1} = -2\frac{h_{i+2}+h_{i+3}}{h_{i+1}(-h_{i+2}h_{i+1}+h_{i+2}h_{i+3}+h_{i+1}^2-h_{i+3}h_{i+1})}, \tag{D.36}$$

$$C_{i+2} = 2\frac{h_{i+1}+h_{i+3}}{h_{i+2}(-h_{i+3}h_{i+1}+h_{i+2}h_{i+1}-h_{i+2}^2+h_{i+2}h_{i+3})}, \tag{D.37}$$

$$C_{i+3} = -2\frac{h_{i+1}+h_{i+2}}{h_{i+3}(-h_{i+3}h_{i+1}+h_{i+2}h_{i+1}+h_{i+3}^2-h_{i+2}h_{i+3})}, \tag{D.38}$$

$$C_i = -(C_{i+1}+C_{i+2}+C_{i+3}). \tag{D.39}$$

- **interior:**

$$\left.\frac{\partial^2\Phi}{\partial y^2}\right|_{y=y_i} \simeq C_{i-1}\Phi_{i-1} \ + \ C_i\Phi_i \ + \ C_{i+1}\Phi_{i+1} \ + \ C_{i+2}\Phi_{i+2}, \tag{D.40}$$

where:

$$C_{i-1} = -2\frac{h_{i+1}+h_{i+2}}{h_{i-1}(-h_{i-1}h_{i+1}+h_{i+2}h_{i+1}+h_{i-1}h_{i-1}-h_{i-1}h_{i+2})}, \tag{D.41}$$

$$C_i = 2\frac{h_{i-1}+h_{i+1}+h_{i+2}}{h_{i-1}h_{i+1}h_{i+2}}, \tag{D.42}$$

$$C_{i+1} = 2\frac{h_{i-1}+h_{i+2}}{h_{i+1}(-h_{i-1}h_{i+2}+h_{i+1}h_{i-1}-h_{i+1}h_{i+1}+h_{i+1}h_{i+2})}, \tag{D.43}$$

$$C_{i+2} = -2\frac{h_{i-1}+h_{i+1}}{h_{i+2}(-h_{i-1}h_{i+2}+h_{i+1}h_{i-1}+h_{i+2}h_{i+2}-h_{i+1}c)}. \tag{D.44}$$

- **top-boundary neighbour:**

$$\left.\frac{\partial^2\Phi}{\partial y^2}\right|_{y=y_i} \simeq C_{i-2}\Phi_{i-2} \ + \ C_{i-1}\Phi_{i-1} \ + \ C_i\Phi_i \ + \ C_{i+1}\Phi_{i+1}, \tag{D.45}$$

where:

$$C_{i-2} = -2\frac{h_{i+1} + h_{i-1}}{h_{i-2}(-h_{i+1}h_{i-2} + h_{i-1}h_{i+1} + h_{i-2}^2 - h_{i-1}h_{i-2})}, \tag{D.46}$$

$$C_{i-1} = 2\frac{h_{i+1} + h_{i-2}}{h_{i-1}(-ah_{i-2} + h_{i-1}h_{i+1} - h_{i-1}^2 + h_{i-1}h_{i-2})}, \tag{D.47}$$

$$C_i = 2\frac{h_{i+1} + h_{i-1} + h_{i-2}}{h_{i+1}h_{i-1}h_{i-2}}, \tag{D.48}$$

$$C_{i+1} = -2\frac{h_{i-1} + h_{i-2}}{h_{i+1}(-h_{i+1}h_{i-1} + h_{i-2}h_{i-1} + h_{i+1}^2 - h_{i+1}h_{i-2})}. \tag{D.49}$$

- **top boundary:**

$$\frac{\partial^2\Phi}{\partial y^2}\Big|_{y=y_i} \simeq C_{i-3}\Phi_{i-3} + C_{i-2}\Phi_{i-2} + C_{i-1}\Phi_{i-1} + C_i\Phi_i, \tag{D.50}$$

where:

$$C_{i-3} = -2\frac{h_{i-1} + h_{i-2}}{h_{i-3}(-h_{i-3}h_{i-1} + h_{i-2}h_{i-1} + h_{i-3}^2 - h_{i-2}h_{i-3})}, \tag{D.51}$$

$$C_{i-2} = 2\frac{h_{i-1} + h_{i-3}}{h_{i-2}(-h_{i-3}h_{i-1} + h_{i-2}h_{i-1} - h_{i-2}^2 + h_{i-2}h_{i-3})}, \tag{D.52}$$

$$C_{i-1} = -2\frac{h_{i-2} + h_{i-3}}{h_{i-1}(-h_{i-2}h_{i-1} + h_{i-2}h_{i-3} + h_{i-1}^2 - h_{i-3}h_{i-1})}, \tag{D.53}$$

$$C_i = -(C_{i-3} + C_{i-2} + C_{i-1}). \tag{D.54}$$

Derivation of the Coefficients C_k

The derivation of the expressions of the coefficients C_k (for $k = i-3, ..., i+3$) is shown as follows. The derivation of B_k (for $k = i-2, ..., i+2$) is not shown because it is identical to that for C_k and is even simpler due to the use of a lower-order approximation for the first-derivative.

For simplicity, only the derivation in the case of the second-derivative at inner nodes is shown, since that for boundary and boundary-neighbour nodes is analogous.

The second-derivative of a function Φ evaluated at a node i can be expressed as a linear combination of Φ evaluated at the neighbour nodes, that is,[1]

$$\left.\frac{\partial^2\Phi}{\partial y^2}\right|_{y=y_i} \simeq C_{i-1}\Phi_{i-1} \; + \; C_i\Phi_i \; + \; C_{i+1}\Phi_{i+1} \; + \; C_{i+2}\Phi_{i+2}. \tag{D.55}$$

Expanding every term of the right-hand side of the expression above (except that at which the derivative is evaluated) as a Taylor series up to an order of approximation one higher than the number of nodes employed:

$$\Phi_{i-1} = \Phi_i \; + \; \frac{h_{i-1}}{1!}\frac{\partial\Phi_i}{\partial y} \; + \; \frac{h_{i-1}^2}{2!}\frac{\partial^2\Phi_i}{\partial y^2} \; + \; \frac{h_{i-1}^3}{3!}\frac{\partial^3\Phi_i}{\partial y^3} \; + \; \frac{h_{i-1}^4}{4!}\frac{\partial^4\Phi_i}{\partial y^4} \; + \; \mathcal{O}(h_{i-1}^5), \tag{D.56}$$

$$\Phi_{i+1} = \Phi_i \; + \; \frac{h_{i+1}}{1!}\frac{\partial\Phi_i}{\partial y} \; + \; \frac{h_{i+1}^2}{2!}\frac{\partial^2\Phi_i}{\partial y^2} \; + \; \frac{h_{i+1}^3}{3!}\frac{\partial^3\Phi_i}{\partial y^3} \; + \; \frac{h_{i+1}^4}{4!}\frac{\partial^4\Phi_i}{\partial y^4} \; + \; \mathcal{O}(h_{i+1}^5), \tag{D.57}$$

$$\Phi_{i+2} = \Phi_i \; + \; \frac{h_{i+2}}{1!}\frac{\partial\Phi_i}{\partial y} \; + \; \frac{h_{i+2}^2}{2!}\frac{\partial^2\Phi_i}{\partial y^2} \; + \; \frac{h_{i+2}^3}{3!}\frac{\partial^3\Phi_i}{\partial y^3} \; + \; \frac{h_{i+2}^4}{4!}\frac{\partial^4\Phi_i}{\partial y^4} \; + \; \mathcal{O}(h_{i+2}^5), \tag{D.58}$$

where the h_k (for $k = i-1, ..., i+2$) notation is that used in section D.5.1, and substituting them in expression (D.55) gives:

$$\begin{aligned}
\left.\frac{\partial^2\Phi}{\partial y^2}\right|_{y=y_i} \simeq\; & C_{i-1}\left[\Phi_i \; + \; \frac{h_{i-1}}{1!}\frac{\partial\Phi_i}{\partial y} \; + \; \frac{h_{i-1}^2}{2!}\frac{\partial^2\Phi_i}{\partial y^2} \; + \; \frac{h_{i-1}^3}{3!}\frac{\partial^3\Phi_i}{\partial y^3} \; + \; \frac{h_{i-1}^4}{4!}\frac{\partial^4\Phi_i}{\partial y^4}\right] \; + \\
& C_i\left[\Phi_i \qquad\qquad\qquad\

which can be rearranged as:

$$\begin{aligned}\left.\frac{\partial^2\Phi}{\partial y^2}\right|_{y=y_i} \simeq \quad & \Phi_i\left[C_{i-1}+C_i+C_{i+1}+C_{i+2}\right] \; + \\ & \frac{\partial\Phi_i}{\partial y}\left[\frac{h_{i-1}}{1!}C_{i-1}+0C_i+\frac{h_{i+1}}{1!}C_{i+1}+\frac{h_{i+2}}{1!}C_{i+2}\right] \; + \\ & \frac{\partial^2\Phi_i}{\partial y^2}\left[\frac{h_{i-1}^2}{2!}C_{i-1}+0C_i+\frac{h_{i+1}^2}{2!}C_{i+1}+\frac{h_{i+2}^2}{2!}C_{i+2}\right] \; + \\ & \frac{\partial^3\Phi_i}{\partial y^3}\left[\frac{h_{i-1}^3}{3!}C_{i-1}+0C_i+\frac{h_{i+1}^3}{3!}C_{i+1}+\frac{h_{i+2}^3}{3!}C_{i+2}\right] \; + \\ & \frac{\partial^4\Phi_i}{\partial y^4}\left[\frac{h_{i-1}^4}{4!}C_{i-1}+0C_i+\frac{h_{i+1}^4}{4!}C_{i+1}+\frac{h_{i+4}^4}{2!}C_{i+2}\right].\end{aligned} \tag{D.60}$$

Besides, the term $\partial^2\Phi/\partial y^2|_{y=y_i}$ can be written as:

$$\left.\frac{\partial^2\Phi}{\partial y^2}\right|_{y=y_i} = 0\Phi_i + 0\left.\frac{\partial\Phi}{\partial y}\right|_{y=y_i} + 1\left.\frac{\partial^2\Phi}{\partial y^2}\right|_{y=y_i} + 0\left.\frac{\partial^3\Phi}{\partial y^3}\right|_{y=y_i} + 0\left.\frac{\partial^4\Phi}{\partial y^4}\right|_{y=y_i}, \tag{D.61}$$

hence, by term-by-term identification between expressions (D.61) and (D.60) the following equation system, shown in matrix form, is obtained:

$$\begin{bmatrix} 1 & 1 & 1 & 1 \\ \frac{h_{i-1}}{1!} & 0 & \frac{h_{i+1}}{1!} & \frac{h_{i+2}}{1!} \\ \frac{h_{i-1}^2}{2!} & 0 & \frac{h_{i+1}^2}{2!} & \frac{h_{i+2}^2}{2!} \\ \frac{h_{i-1}^3}{3!} & 0 & \frac{h_{i+1}^3}{3!} & \frac{h_{i+2}^3}{3!} \\ \frac{h_{i-1}^4}{4!} & 0 & \frac{h_{i+1}^4}{4!} & \frac{h_{i+2}^4}{4!} \end{bmatrix} \begin{bmatrix} C_{i-1} \\ C_i \\ C_{i+1} \\ C_{i+2} \end{bmatrix} = \begin{bmatrix} 0 \\ 0 \\ 1 \\ 0 \end{bmatrix}. \tag{D.62}$$

Note that the 5×4 Van der Monde matrix on the left-hand side of expression (D.62) is not square, therefore it cannot be inverted. In order to obtain the solution of the system (the coefficients C_{i-1}, C_i, C_{i+1} and C_{i+2}), shown in section D.5.1, the bottom row is removed.

D.5.2 Boundary Conditions

For all the boundaries, the stream function was set to be zero. In the case of vorticity, for those boundaries considered as irrotational (top and lateral boundaries), the vorticity was also set to be zero. For the bottom boundary, which comprises the active surface (non-porous, no-slip condition, in-plane moving wall) and the rest (non-porous, no-slip condition, stationary wall), the following second-order approximation (Ortega-Casanova & Fernandez-Feria, 2002) was employed:

$$\zeta_{i,j=1} = \frac{-7\psi_{i,j=1} + 8\psi_{i,j=2} - \psi_{i,j=3} - 6\delta y^2 W_{wall}}{2\delta y^2} + \mathcal{O}(\delta y^2), \tag{D.63}$$

where W_{wall} is the imposed in-plane velocity of the wall for the active surface portion, which is otherwise zero.

D.5.3 Mesh

The grid adopted is that shown in figures D.1 and D.13. The dimensions of the computational domain were $L_y = 20k$ and $L_z = 43\Delta z$, with $k = 1.5$ mm, and the spacing between roughness element centres $\Delta z = 10$ mm. This means a domain of 30 mm $\times$ 430 mm (height and span, respectively). The grid was structured and the cells were non-skewed rectangles.

In order to have sufficient spatial resolution in the region where high gradients are likely, and at the same time, reduce the penalty in computational cost by having a low number of nodes where the magnitudes are not expected to change considerably, the node spacing in both directions was non-uniform. Therefore, following this philosophy, in the z-direction, a high density of nodes was concentrated across the span of the roughness element array. In fact, in this region, the spacing was decided to be constant (and, obviously, with minimum size), and then increase outwards up to the lateral boundaries. In y-direction, a high density of nodes was concentrated near the floor (bottom boundary), increasing the spacing progressively up to the top boundary. Figure D.13 shows a close-up view of the grid.

One important aspect when creating a non-uniform spacing grid is to ensure that there is no sudden changes or discontinuities in the variation of the spacing. A

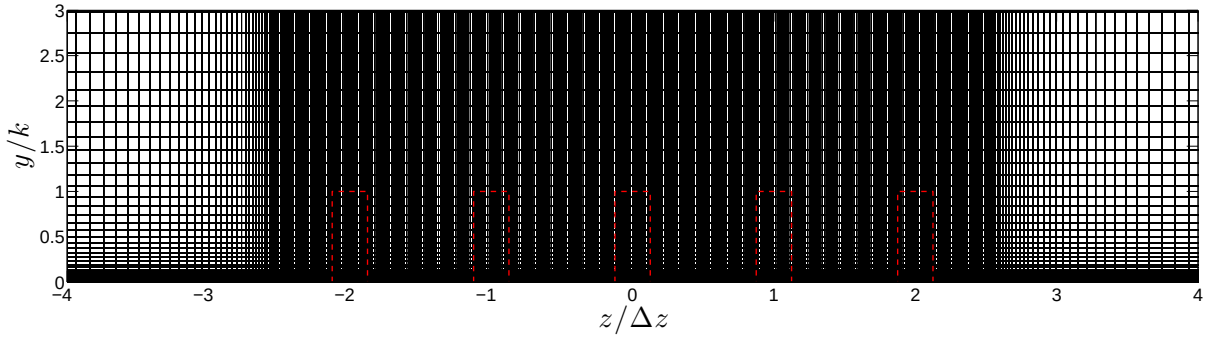


Figure D.13: Close-up view of the grid and the roughness element array (red dashed lines) superimposed.

common technique (Prof. S. Chernyshenko personal communication) is to apply analytical functions with a continuous second derivative on a uniform spacing grid. To safely satisfy this requirement, sine functions (which have an infinite number of continuous derivatives) were used as the analytical functions.

The strategy followed to create the non-uniform spacing grids for both y and z directions was to fix a minimum spacing δy_{min} and δz_{min} for the proper grid, and the number of nodes N_q for the uniform spacing grid q (*base grid*), which therefore defines the spacing size, δq. Then, in order to meet those requirements as well as L_y and L_z, the sine functions were constrained by means of their coefficients. As a result, the values and the sine functions used were:

- ***y*-direction**
  - $\delta y_{min} = k/150 = 0.01$ mm;
  - $q_y \in [0, 1]$, $N_{q_y} = 150$, $\delta q_y = 1/149$;
  - the L_y used for the grid generation was $133.3k$, but then cropped down to $20k$ for the simulations, resulting in a grid of 70 nodes;
  - the grid-generator sine function was:

$$y(q_y) = L_y \left[q_y + b_y \sin(\pi q_y) \right], \tag{D.64}$$

    with

$$b_y = \frac{\frac{\delta y_{min}}{L_y} - \delta q_y}{\sin(\pi \delta q_y)}. \tag{D.65}$$

Figures D.14 shows, (a) y versus q_y, and (b) y versus δy.

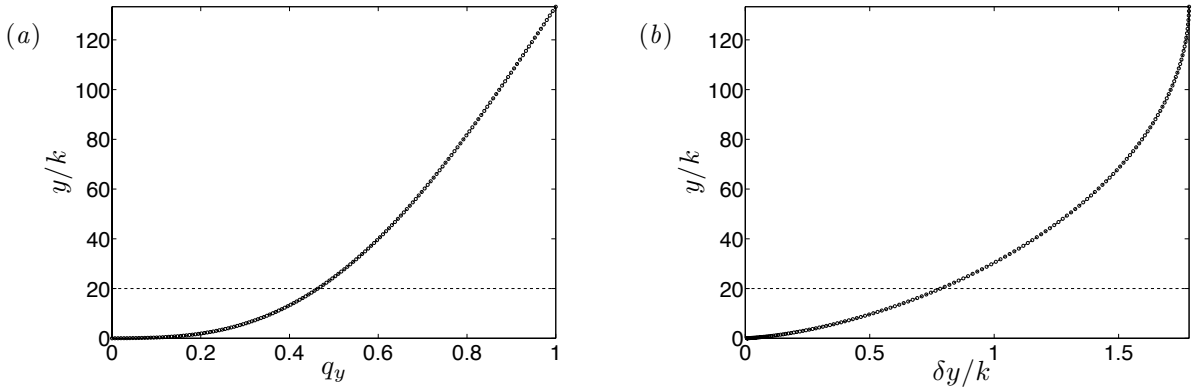


Figure D.14: Evolution of the grid in y-direction; (a) with respect to the number of nodes of an uniform-spacing base grid, and (b) the evolution of the spacing size with respect to its y-location. The dashed lines show the level at which the grid was cropped for the simulations.

- ***z*-direction**

  - $\delta z_{min} = \Delta z/66 = 0.15$ mm;
  - $q_z \in [-1, 1]$, $N_{q_z} = 201$, $\delta q_z = 1/100$;
  - the grid-generator sine function was:

$$z(q_z) = \frac{Lz}{2}\left[1 + q_z + b_z \sin(\pi q_z)\right], \tag{D.66}$$

with

$$b_z = \left(2\frac{\delta z_{min}}{\delta q_z L_z} - 1\right)\left[\frac{1}{\pi \cos\left(\pi q_z\big|_0\right)}\right], \tag{D.67}$$

where $q_z\big|_0$ is the value of q_z evaluated at the node $[(N_{q_z} - 1)/2] + 1$, which corresponded to the central node.

Figures D.15 shows, (a) z versus q_z, and (b) δz versus z, which is essentially a quarter of a sine wave mirrored with respect to the centre of the domain.

However, this was not the final grid used in the z-direction for the simulations: the zone comprising the roughness element array span ($5\Delta z$) was set to have a constant spacing of size δz_{min}. The actual grid was produced by "inserting" 165 nodes equally spaced on either side of the central node ($5\Delta z/2$ each side), so that, outside this constant-spacing region, the sine wave remained unaltered. Figure D.16 shows the resulting "widened" δz distribution versus z.

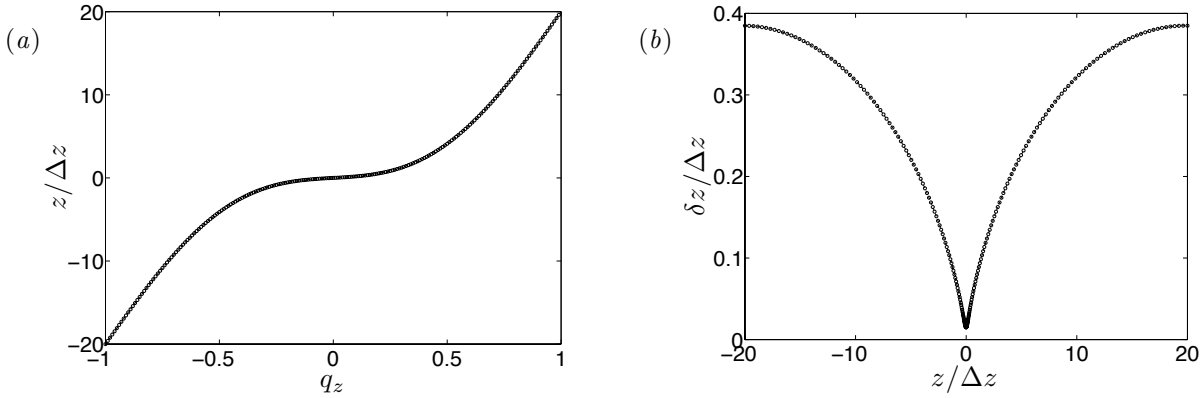


Figure D.15: Evolution of the grid in z-direction; (a) with respect to the number of nodes of an uniform-spacing base grid, and (b) the evolution of the spacing size with respect to its z-location.

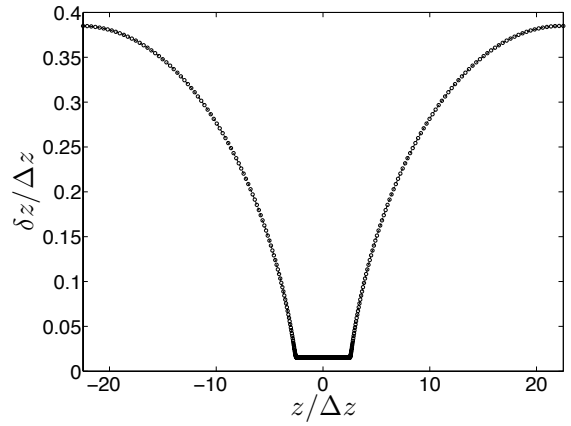


Figure D.16: Final (widened) evolution of the spacing size with respect to its z-location.

D.6 Stability Analysis

Since the discretisation of the derivatives followed an explicit scheme for both time and space, the code was not unconditionally stable and a stability analysis was therefore necessary. Two stability conditions were considered, one for the convective terms and the other for the diffusive terms.

The condition for the convective terms is:

$$\delta t \leq \frac{(\delta y)^2(\delta z)^2}{\frac{1}{2\nu}\left[(\delta y)^2+(\delta z)^2\right]+\delta y\delta z\left(u_{max}\delta y+v_{max}\delta z\right)}, \tag{D.68}$$

and that for the diffusive terms:

$$\delta t \leq \frac{1}{2\nu}\left[\frac{(\delta y)^2(\delta z)^2}{(\delta y)^2+(\delta z)^2}\right]. \tag{D.69}$$

Details of the derivation of these formulae are given by Ames (1992). In equation (D.68), u_{max} and v_{max} were used to provide a global stability condition.

Both expressions (D.68) and (D.69) offer a relationship between the time step and the spatial grid to ensure numerical stability. This was implemented by choosing a spatial grid and using expressions (D.68) and (D.69) with the minimum δz and δy to determine δt_{max}, the upper limit value for the time step. Computing δt from each expression, the minimum was chosen. Since u_{max} and v_{max} could vary from one time step to the next, expression (D.68) was updated at every time step. Therefore, when the δt from expression (D.68) was the most restrictive, it could lead to a variable time-step solution of the problem.

Since (D.68) and (D.69) were derived assuming a uniform grid, the value of δt_{max} that (D.68) and (D.69) provide does not guarantee stability. Furthermore, as noted by Ames (1992), those expressions have to be interpreted as a general guide in the numerical experimentation, since sometimes they are too restrictive and at other times not restrictive enough. In this study $\delta t = 0.5\delta t_{max}$, which worked for all cases.

D.7 Code Validation

Two well-known cases were considered to validate the code: Stokes' 2$^{\text{nd}}$ problem and the lid-driven cavity problem. The reasons for considering two different problems were:

- Stokes' 2$^{\text{nd}}$ problem, to check the behaviour of the code when dealing with a boundary of oscillatory nature.
- Lid-driven cavity problem, to check the behaviour of the code to capture gradients in both directions.

D.7.1 Stokes' 2$^{\text{nd}}$ Problem

The Stokes 2$^{\text{nd}}$ problem refers to the one-dimensional flow about an infinite flat wall that oscillates parallel to itself (Schlichting, 2000). The statement of the problem is

$$\frac{\partial u}{\partial t} = \nu \frac{\partial^2 u}{\partial y^2}, \tag{D.70}$$

where u notes the fluid velocity and y the direction normal to the wall. The boundary condition is:

$$y = 0 : \qquad u(0,t) = U_0 \cos(\omega t), \tag{D.71}$$

with ω the frequency of oscillation. The exact solution is

$$u(y,t) = U_0 e^{-\eta} \cos(\omega t - \eta), \tag{D.72}$$

where η, the non-dimensional wall-normal coordinate, is

$$\eta = \sqrt{\frac{\omega}{2\nu}} y. \tag{D.73}$$

The case for the comparison between theory and numerical simulations was chosen to be in air ($\nu = 1.5 \times 10^{-5}$ m^2/s) and have a driving oscillating wall with parameters:

- angular frequency: $\omega = 100\pi$ rad/s
- amplitude: $U_0 = 2\pi/10$ m/s.

Regarding the set-up of the numerical simulation code to solve this problem, the bottom boundary condition was that given by expression (D.71), the conditions for the two side boundaries as well as the top boundary were those given by the exact solution at every time step. The grid employed was specified by parameters (based on the "depth of penetration" or also called "Stokes layer": $\eta_s = 2\pi\sqrt{2\nu/\omega}$) were:

- domain dimensions: $L_x = 214\eta_s \times L_y = 103\eta_s$
- number of nodes: 301 in x × 150 in y
- smallest spacings: $\delta x = \eta_s/13$, $\delta y = \eta_s/194$
- time-step size: $\delta t = T/12050$ seconds, where T is the period of the driving wave.

Figure D.17 shows one cycle of wall-normal profiles of velocity for several phases from both the theory and the numerical simulations (in the latter, the data were collected at the centre-line of the domain in the wall-normal direction). It can be seen that they overlap well.

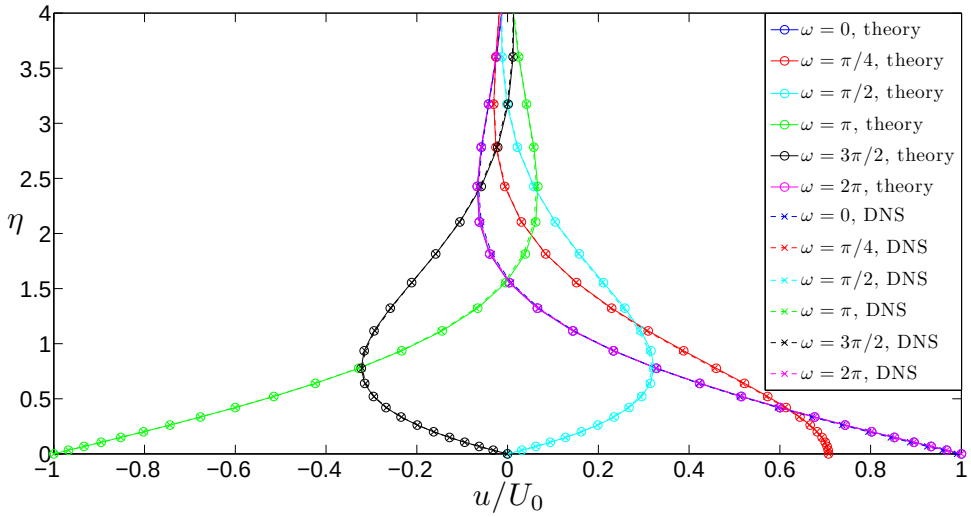


Figure D.17: One cycle of wall-normal profiles of velocity for the Stokes 2$^{\text{nd}}$ problem; theoretical and numerical data.

D.7.2 Lid-Driven Cavity

Further validation to check two-dimensionality was considered, since Stokes' 2$^{\text{nd}}$ problem is one-dimensional. The classic problem of the two-dimensional lid-driven cavity was set up and the results were compared to those from Bruneau *et al.* (2006). The lid-driven cavity consists of three boundaries which are non-porous, no-slip walls, and a fourth one which is considered to be a free stream. The fluid in the cavity first goes through an unsteady regime and then reaches a steady state.

In this study, with all magnitudes being considered non-dimensional, the parameters of the problem were:

- cavity dimensions: $L_x = 1 \times L_y = 1$
- Reynolds number based on the imposed free-stream and a cavity side: $Re = 1000$.

Several grids, all them of constant spacing in both directions, were considered, in order to achieve mesh-independent solutions. The grids were of 101×101, 201×201, 301×301 and 351×351 nodes. The time-step size was set for each case according the stability analysis described in section D.6. Figure D.18 shows the time evolution of the horizontal component of the velocity placed at $x = 1/2$ and $y = 3/4$. It can be seen that the difference between using the 301×301 mesh and the 351×351 is negligible.

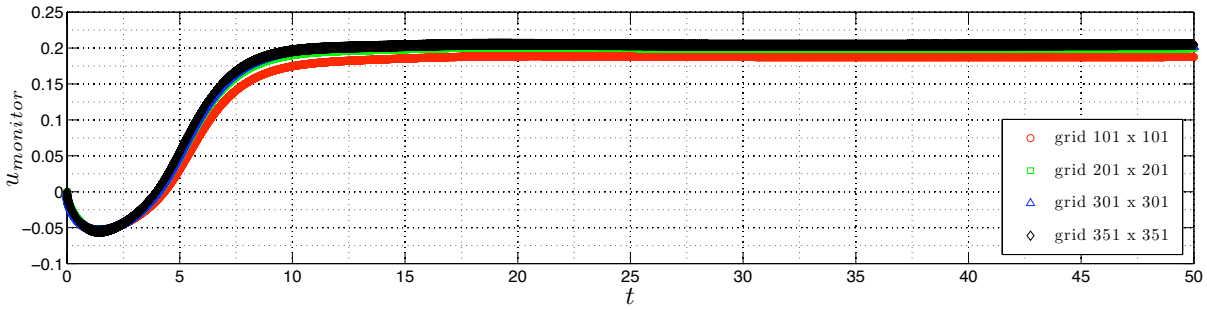


Figure D.18: Driven cavity. Horizontal velocity component time monitor placed at $x = 1/2$ and $y = 3/4$ ($Re = 1000$).

Figure D.19 shows streamlines once steady state is reached for the case considered. The free-stream is imposed at the top boundary, going from left to right. In agreement with the literature, a main clockwise vortex covering the majority of the domain is formed and two secondary counter-clockwise vortices appear on the two bottom corners.

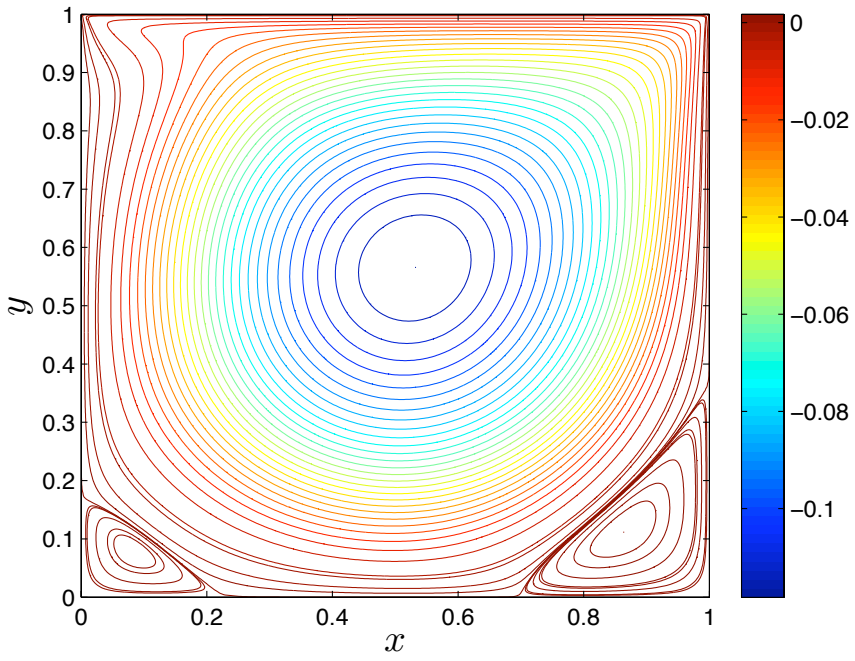


Figure D.19: Streamlines in a 1×1 lid-driven cavity at $Re = 1000$.

The minimum value of stream function given by the numerical simulation code presented in this study for the 351×351 grid is $\psi_{min} = -0.11826$, lying within the range of -0.11503 and -0.11892 given by Bruneau *et al.* (2006). The maximum value of

stream function is $\psi_{max} = 1.7173 \times 10^{-3}$, which is well within the range of 1.7003×10^{-3} and 1.7689×10^{-3} given by Bruneau *et al.* (2006).

D.7.3 Case Set

Type-A Actuators in Stagnant Flow

The only parameter varied when performing simulations with type-A actuators was the driving frequency. Two values were considered, 10 Hz and 100 Hz. The driving signal was sinusoidal and the maximum deflection of the actuator was set at $A_{edge} = d/4$ on each direction ($d/2$ of total width). The active surface configuration, taken as the area comprising a spanwise distribution of actuators, is that shown in figure D.5, that is, actuator centre-lines aligned with roughness element centres, with Δz spacing between actutator centre-lines, $2d$ actuator span and d electrode width at rest state, widening up to $d + d/2$ at the state of maximum deflection.

The reason for aligning the actuators with the roughness element centres was because type-A actuators create a net upwash region, aligned with their centre-line, through wall-normal streaming (an induced steady finite velocity), see figure D.20(a). As seen in the experiments, the disturbance created by the roughness elements adopted the form of a spanwise distribution of streamwise streaks. The high-speed streak (or, in other words, downwash motion) regions have their axes aligned with the roughness element centres (recall figure 3.24). Hence, by locating likewise aligned type-A actuators, it can be hypothesised that, with a proper tuning of the actuator characteristics, the actuator-induced streaming will suppress the downwash of the disturbance.

Type-B Actuators in Stagnant Flow

As in the case of type-A actuators, the only parameter varied when performing simulations with type-B actuators was the driving frequency, that is, 10 Hz and 100 Hz. The active surface configuration was set with an actuator spacing of Δz (see figure D.9). The actuator span was set at the same as that considered for the active surface with type-A actuators, i.e. $2d$, the driving signal was also sinusoidal, the electrode width at rest set at $(3/8)d$, and a maximum deflection of $d/2$.

As shown in the next section, type-B actuators, as with type-A actuators, generate wall-normal streaming. In this case, a net downwash region in the vicinity of the actuator centre-line is generated, see figure D.20(b). Hence it can be hypothesised that, by placing type-B actuators underneath low-speed streaks of the perturbation (i.e. between roughness elements), and with a proper tuning of the actuator characteristics, the downwash streaming may suppress the upwash regions of the disturbance. As a result, an active surface configuration like that shown in figure D.9 (with the actuator centre-lines located with a $\pi/2$ phase-shift with respect to the roughness element centres, or in other words, with an offset of $\Delta z/2$), could be a possible solution.

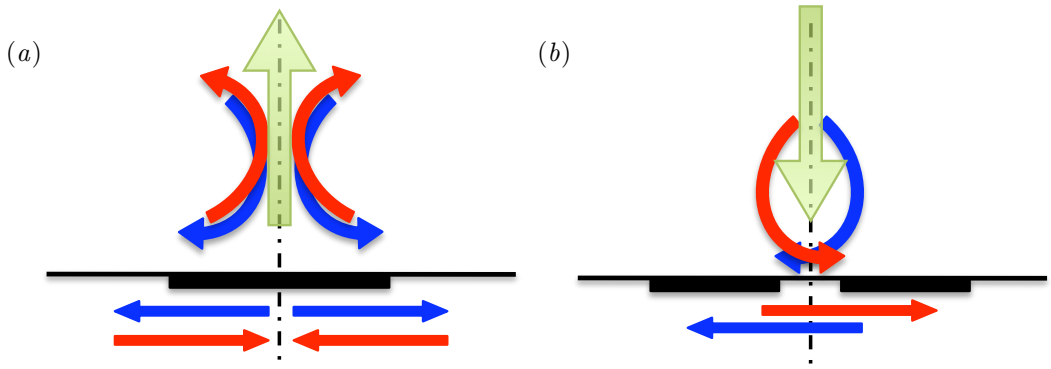


Figure D.20: Schematic of finite net wall-normal velocity (streaming), represented as a light green arrow, induced by (a) type-A actuators, (b) type-B actuators. In (a), blue arrows denote electrode expansion, and red ones denote contraction. In (b), blue arrows denote right-electrode expansion (left-electrode contraction), and red ones vice versa.

D.7.4 Results

Type-A Actuators

Figure D.21 shows a sequence of the velocity vector fields created by the operation of type-A actuators, focusing on the region around the centre of the actuator. The dashed lines represent the silhouette of a roughness element (for illustrative purposes only).

It can be seen that, for each actuator, a pair of counter-rotating streamwise vortices forms, with each vortex at either edge of the electrodes. The sign of the circulation of the vortices changes every half a cycle, that is, when the electrodes expand the vortices push fluid down to the centre of the actuator, and when the electrodes contract, the vortices push fluid away from the centre of the actuator.

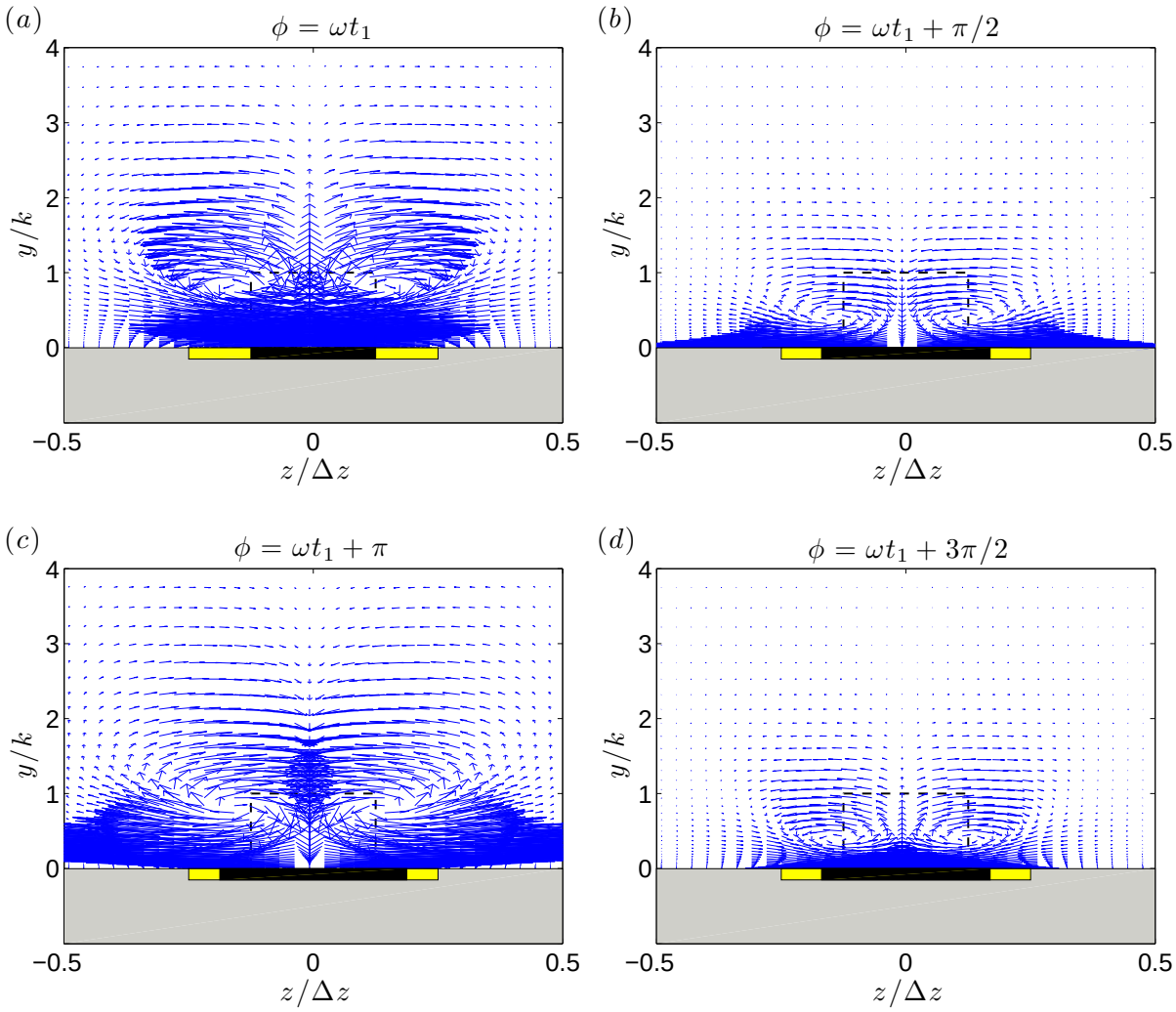


Figure D.21: Sequence at four different instants of the velocity vector field created by a type-A actuator with wall velocity signal at $f = 10$ Hz (driving forcing at 5 Hz) at, (a) $\phi = \omega t_1$; (b) $\phi = \omega t_1 + \pi/2$; (c) $\phi = \omega t_1 + \pi$; and (d) $\phi = \omega t_1 + 3\pi/2$.

Figure D.22 shows the time series of v at $(z/\Delta z,\ y/k) = (0,\ 0.5)$ for two type-A actuators with driving frequency set at $f = 10$ Hz and $f = 100$ Hz. Figure D.23 shows the same but with v normalised by the imposed wall velocity and t normalised by the forcing frequency. From this figure it can be clearly seen that the higher the forcing frequency, the smaller the velocity for the same location or, in other words, the smaller the penetration depth.

A more important feature of this type of actuator is the creation of streaming, that is, the integral under the curve of a sinusoidal velocity time series captured by a probe

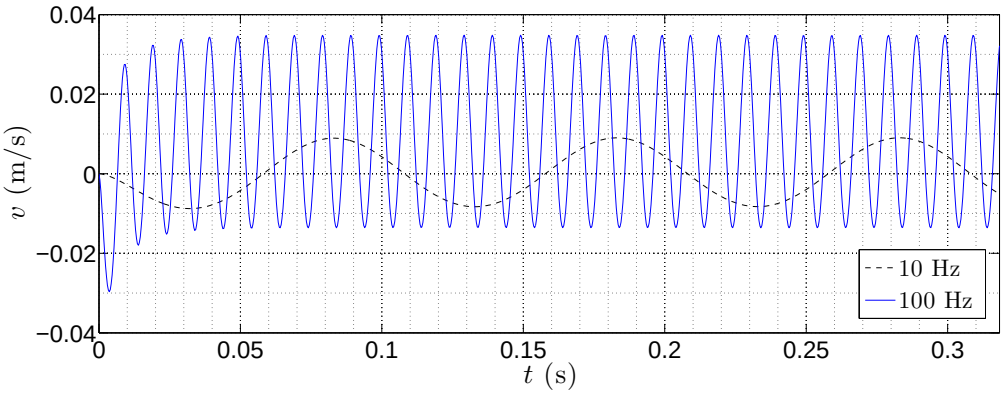


Figure D.22: Dimensional time series of v at ($z/\Delta z = 0$, $y/k = 0.5$) for type-A actuators with wall velocity signal at $f = 10$ Hz (- -) and $f = 100$ Hz (–).

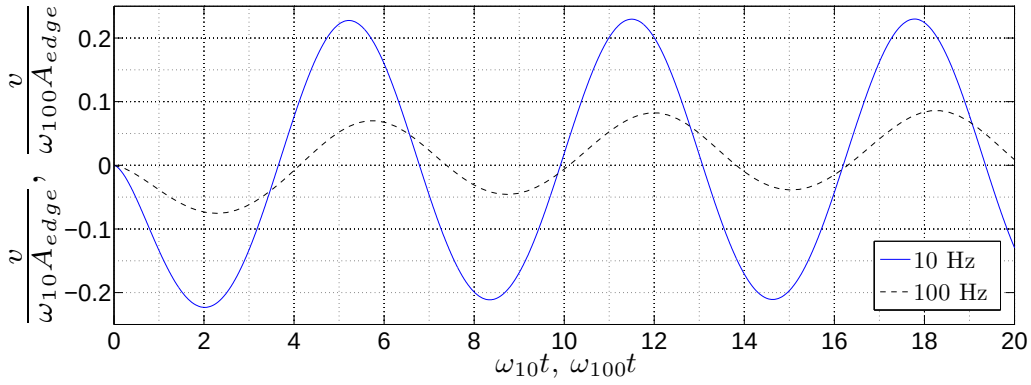


Figure D.23: Non-dimensional time series of v at ($z/\Delta z = 0$, $y/k = 0.5$) for type-A actuators with wall velocity signal at $f = 10$ Hz (- -) and $f = 100$ Hz (–).

placed in the fluid domain is non-zero over a complete cycle. As can be seen from figure D.22, after a transient, the time-averaged wall-normal velocity component at the location of study has a net positive value. The streaming is stronger as the forcing frequency increases (for the same forcing amplitude). This is an important finding, because it means that actuators of this type can be placed where the incoming flow presents regions of negative wall-normal velocity component and tuned so that the streaming generated by the actuator cancels the incoming natural negative wall-normal velocity.

Figure D.24 shows iso-contours of the time-averaged wall-normal velocity component created by a type-A actuator with wall velocity set at $f = 100$ Hz.

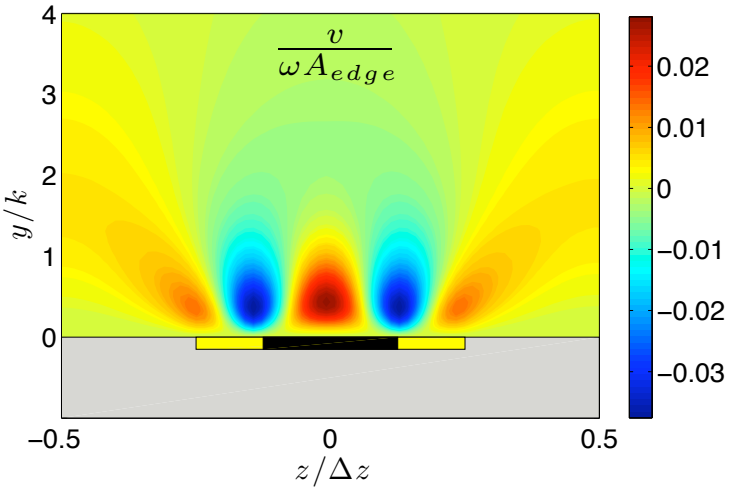


Figure D.24: Iso-contours of time-averaged wall-normal velocity created by a type-A actuator with forcing at $f = 100$ Hz.

It can be seen that the streaming flow field created by type-A actuators results in a central upwash region aligned with the actuator centre-line with two downwash regions at each side of the former. This flow field is precisely opposite to that behind a cylindrical roughness element. Therefore, by placing type-A actuators downstream of, and aligned with, roughness elements, and with a proper tuning of frequency and deflection amplitude, the incoming perturbation may be directly cancelled.

Type-B Actuators

Figure D.25 shows a sequence of the velocity vector field in the vicinity of one actuator and created by the operation of type-B actuators. It can be seen that, conversely to type-A actuators, type-B creates a single vortex which changes direction every half a cycle and whose centroid is aligned with the actuator centre-line.

Figures D.26 and D.27 show the time series of w in the same way as for v presented in the previous section, at $(z/\Delta z, y/k) = (0, 0.5)$, for two type-B actuators with wall velocity set at $f = 10$ Hz and $f = 100$ Hz. Figure D.27 clearly shows that, as in the case of type-A actuators, the higher the forcing frequency, the smaller the penetration depth. In relation to this, the phase shift shown is a consequence of the size of the vortex generated. For the 10-Hz case, the vortex centre is located above the selected probe location, whereas for the 100-Hz case the vortex centre is underneath.

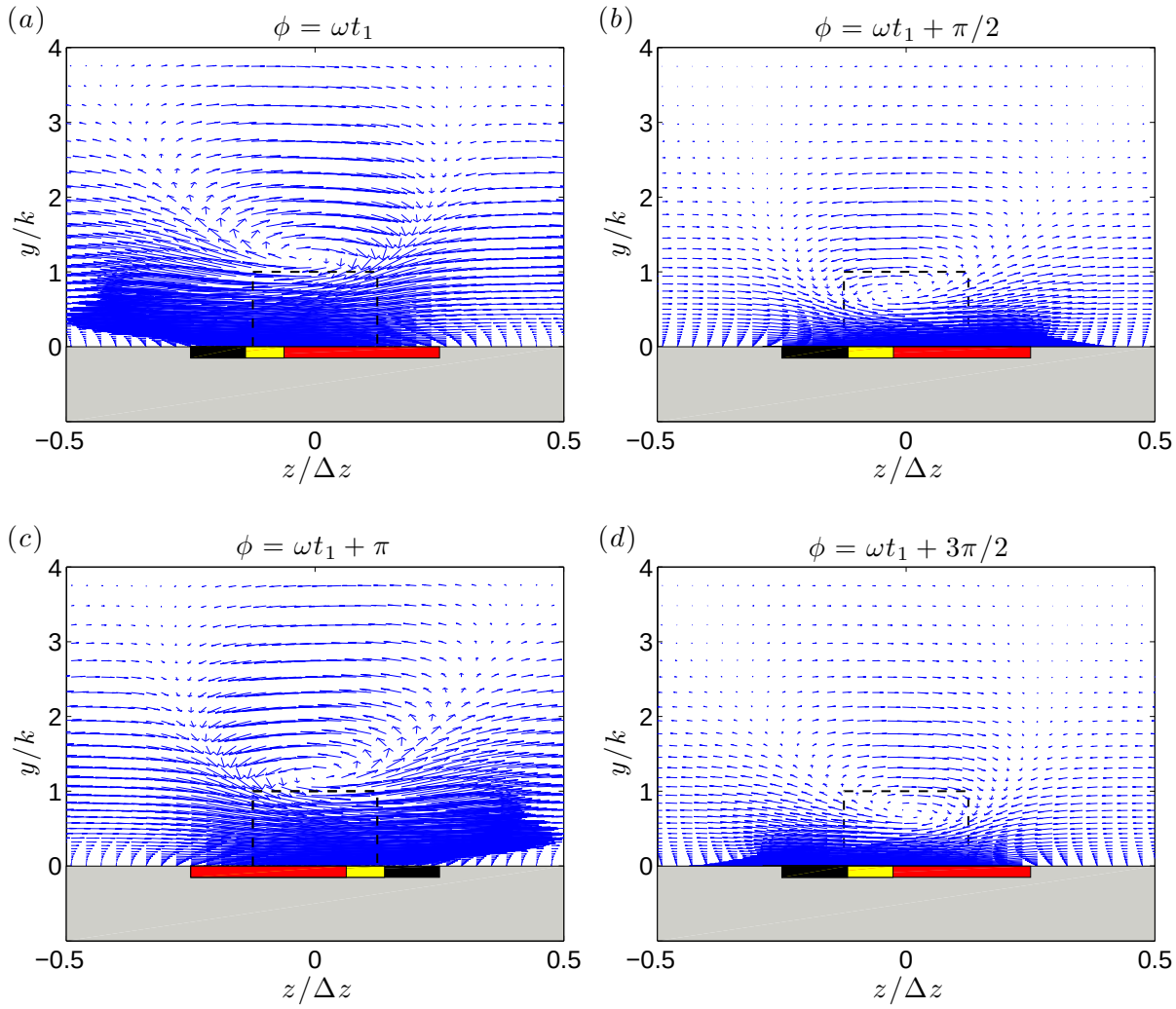


Figure D.25: Sequence at four different instants of the velocity vector field created by a type-B actuator with wall velocity signal at $f = 10$ Hz (driving forcing at 5 Hz), (a) $\phi = \omega t_1$; (b) $\phi = \omega t_1 + \pi/2$; (c) $\phi = \omega t_1 + \pi$; and (d) $\phi = \omega t_1 + 3\pi/2$.

As can be seen from figure D.26, this type of actuator also develops streaming. After a transient, the time-averaged wall-normal velocity component at the location of study has a negative positive value. The streaming becomes stronger as the forcing frequency increases for the same forcing amplitude, as in the case of type-A actuators.

Comparing figure D.26 with figure D.22, it can be seen that, for the same forcing frequency (for instance at 100 Hz), type-B actuators take approximately twice as long as type-A ones to reach a steady state (~ 0.1 s versus ~ 0.05 s, respectively). Furthermore, for a same probe location, the streaming created by type-B actuators is opposite in sign to that

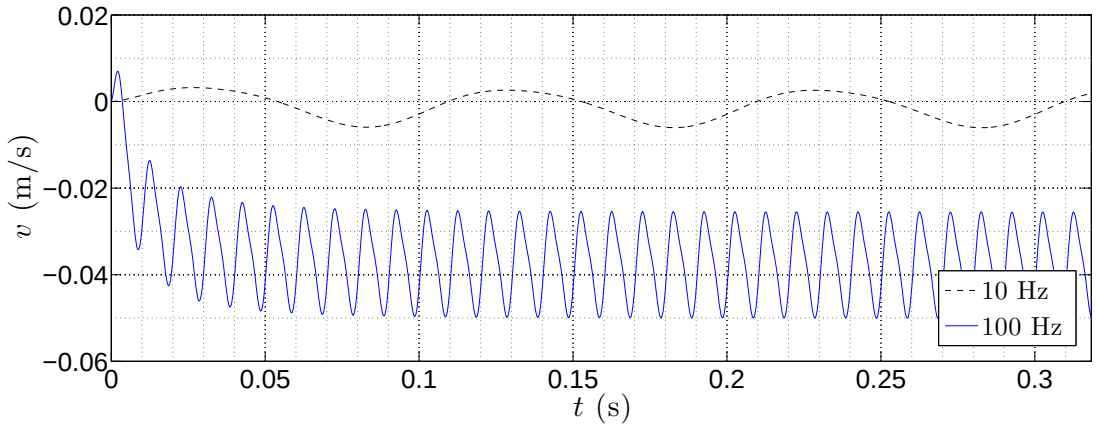


Figure D.26: Dimensional time series of v at ($z/\Delta z = 0$, $y/k = 0.5$) for type-B actuators with wall velocity signal at $f = 10$ Hz (- -) and $f = 100$ Hz (–).

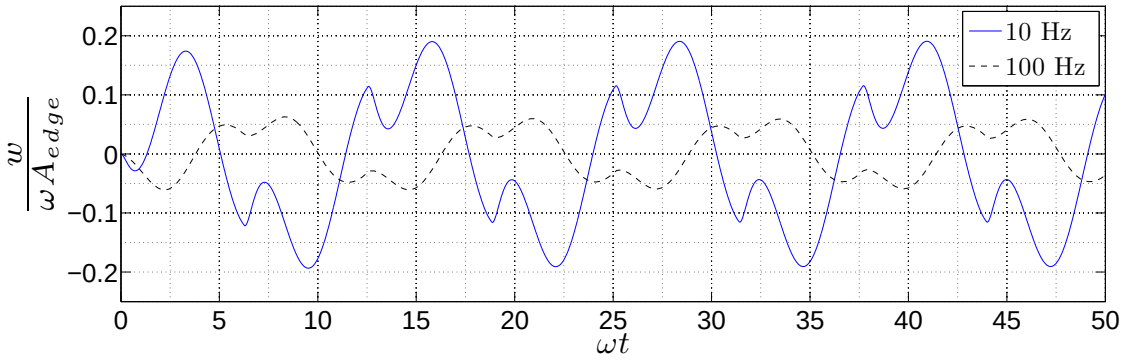


Figure D.27: Non-dimensional time series of v at ($z/\Delta z = 0$, $y/k = 0.5$) for type-A actuators with wall velocity signal at $f = 10$ Hz (- -) and $f = 100$ Hz (–).

created by type-A ones. It is also interesting to note that, for the same prescribed values of ω and A_{edge} for both types of actuators, the streaming created by type-B actuators is stronger than that created by type-A ones.

Figure D.28 shows iso-contours of the time-averaged wall-normal velocity component created by a type-B actuator with the same forcing values (ω and A_{edge}) as the iso-contours shown in figure D.24 for a type-A actuator. It can be seen that there is a well-defined central region, aligned with the actuator centre-line, of downwash surrounded by upwash regions at each side. The structure is similar to that created by type-A actuators but with opposite sign. The maximum value of the upwash regions for both type-B and type-A actuators is similar ($v/(\omega A_{edge}) = 2.96\times10^{-2}$ versus 2.81×10^{-2}, respectively), whereas the

downwash for type-B actuators is slightly stronger than that for type-A ones (a minimum value of $v/(\omega A_{edge}) = -5.02 \times 10^{-2}$ versus -3.76×10^{-2}, respectively).

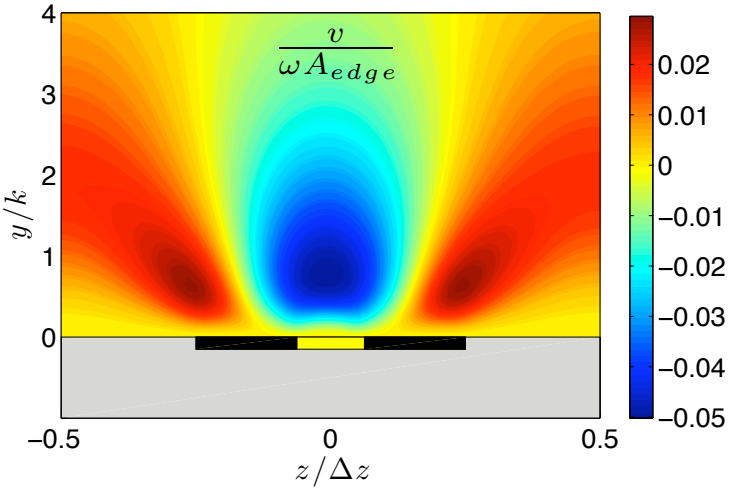


Figure D.28: Iso-contours of time-averaged wall-normal velocity created by a type-B actuator with forcing at $f = 100$ Hz.

As in the case of type-A actuators, the generation of streaming by type-B actuators is a remarkably useful finding. This is because actuators of this type could be placed where the incoming flow presents regions of positive wall-normal velocity component. Accordingly tuned, the streaming that they generate could cancel the incoming natural positive v-component. For instance, for purposes of cancellation of the transient growth of disturbances generated by an array of cylindrical roughness elements, a combined distribution of type-A and type-B actuators may be employed. Type-A actuators can be placed aligned with the roughness elements, so that their streaming central upwash can cancel the downwash created by the counter-rotating vortices of the incoming perturbance. And type-B actuators can be placed in between roughness elements, so that their streaming central downwash can cancel the upwash related to the incoming low-speed streaks of the perturbation.

Appendix E

Finite Volume Simulations

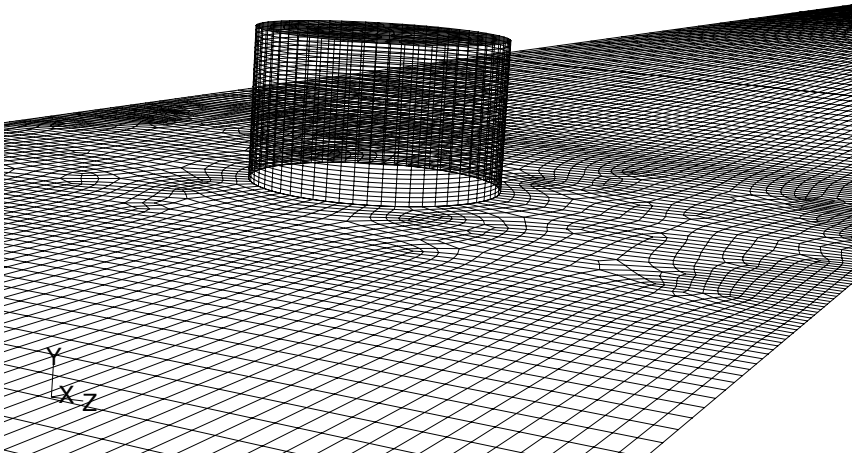


Figure E.1: Detail of the grid on the considered computational domain.

E.1 Purpose

As indicated in Chapter D, since the DNS was conceived as a test bed for different actuation configurations, a reliable initial condition was needed in order to replicate as accurately as possible what actually happens. Ideally, this initial condition might have come from the experiments. However, this was not feasible. Besides, given the two-dimensional nature of the DNS code, simulating the flow field around a three-dimensional object, as a roughness element is, was beyond the purpose of this study. Therefore, as a low-cost and easily implementable alternative, simulations employing a Finite Volume Simulation (FVS) commercial package were conducted. The choices were GAMBIT©, as the mesh generator, and FLUENT©, as the FVS solver.

E.2 Problem Statement

The statement of the problem was three-dimensional, but instead of recreating the entire roughness element array, a domain with one single roughness element and with periodic side boundaries was implemented, in order to minimise the computational cost. The election of this type of boundary condition seemed to be realistic since, as shown by the experimental results, the flow field within the boundary layer is spanwise-periodic.

E.3 Boundary Conditions

The rest of boundary conditions (figure E.2) was set as follows:

- Inlet plane: "velocity inlet" (all the nodes of that cross-section with an imposed constant value of velocity equal to the free-stream considered).
- Outlet plane: "outflow" (no reverse-flow imposed).
- Roughness element and lower boundary: "fixed wall" (non-porous and with no-slip condition).
- Top boundary: "moving wall" (non-porous and with zero shear-stress, to simulate a free-stream iso-surface with an imposed velocity equal to the free stream).

E.4 Computational Domain Dimensions

The dimensions of the roughness elements were the same as those used in the experiments, that is, diameter d of 2.5 mm and and height k of 1.5 mm. The boundary-layer origin coincided with the inlet plane, hence the streamwise location of the roughness element was $x_k/k = 133.33$ (200 mm), as in the experiments. The dimensions of the computational domain are:

- **streamwise length:** $L_x/k = 533.33$ (800 mm) – long enough to ensure that there is no reverse flow at the outlet plane and the perturbation created by the roughness elements has fully developed.

- **spanwise length:** $L_z/k = 6.67$ (10 mm), being the value of the spacing Δz between roughness elements.

- **wall-normal length:** $L_z/k = 20$ (30 mm), long enough to guarantee that the top boundary was well above the boundary layer edge over the full streamwise length.

Figure E.2 shows a schematic of the computational domain with the boundary conditions considered.

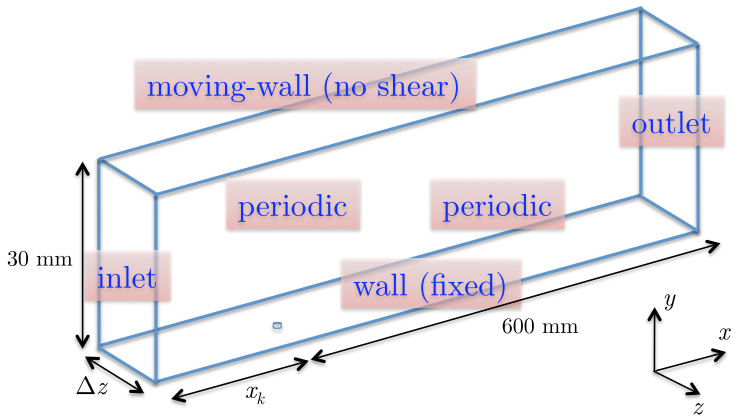


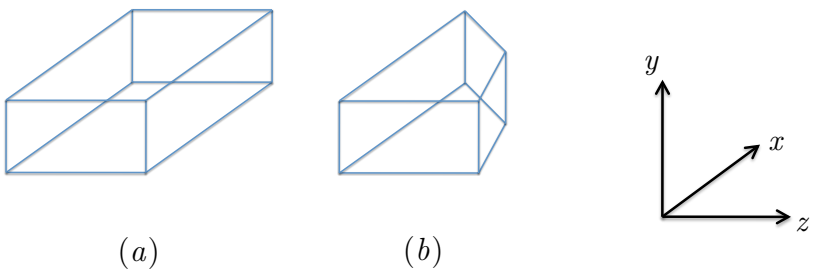
Figure E.2: Schematic of the computational domain showing the boundary conditions used.

E.5 Spatial Grid

The resolution of the final grid was shown to provide full resolution by comparison to the experimental results. The strategy followed to distribute the nodes was to have a high density of nodes near the lower boundary and around the roughness element, in order to capture as accurately as possible the boundary layer as well the formation and development of the disturbance. Then, in order to save computational cost, the node spacing was gradually increased away from both the wall and the roughness element. Figure E.1 shows a detail of the mesh on the wall and the faces of the roughness elements.

The computational domain was divided into a number of sub-volumes, in order to control the variation of node spacing independently between different regions of the domain. The mesh was set to be structured, which gives better results than unstructured meshes for the same number of nodes (Fluent, 2004).

A cuboid topology was chosen for all of the cells. For those sub-volumes not containing nor being affected by the presence of the roughness element, the cuboids were rectangular, as shown in figure E.3(a); whereas for those sub-volumes either containing or being affected by the presence of the roughness element, their faces perpendicular to the lower boundary had non-othogonal faces, as shown in figure E.3(b). Figure E.1 shows the region of the latter type of cells.



(a) (b)

Figure E.3: Two generic examples of both types of cells employed in the mesh.

The grid which was eventually used had 1316055 cells. The volume of the smallest cell was $V_s \simeq V_k/40000$ ($= 1.95 \times 10^{-4}$ mm^3) and the volume of the largest $V_l \simeq V_k/2$ (=3.92 mm^3), where V_k is the volume of the roughness element ($k\pi d^2/4$). In non-dimensional

terms, provided the Blasius length scale, $\delta = \sqrt{\nu x_k / U_\infty}$, at the streamwise position of the roughness element x_k, ${V_s}^{1/3}/\delta \simeq 0.75$ and ${V_l}^{1/3}/\delta \simeq 20.4$.

E.6 Physical Model

Since the study was focused only on the laminar region of the boundary layer and the perturbation created by the roughness element array was considered to be steady, the steady viscous laminar solver in FLUENT was selected.

E.7 Method

The numerical methods implemented in FLUENT solve systems of linear algebraic equations, resulting from discretising, integrating and linearising the set of governing equations (mass and momentum conservation) on every grid cell (Fluent, 2006). This approach is the "finite-volume" method.

A segregated pressure-based solver was employed to solve the set of mass and momentum conservation equations. The term "segregated" comes from the fact that the solver is based on an algorithm that solves the equations in a segregated manner, that is, one after another and de-coupled from other equations. The choice of a segregated solver (between segregated or coupled) was made based on better economy of memory, as suggested in Fluent (2006). The term "pressure-based" is given because mass conservation is achieved by solving a "pressure-correction" equation. The *SIMPLE* algorithm was chosen as the pressure-velocity coupling procedure.[1] The pressure equation is derived from the combination of the continuity and momentum equations and, as result, the velocity field corrected by the pressure satisfies continuity. The choice between pressure-based and density-based approaches was based on the fact that the pressure-based approach is suitable for low-speed incompressible flows (Fluent, 2006).

A second-order upwind approximation (to balance between reasonable accuracy and computational time) was adopted for the discretisation of the equations and these were

[1] *SIMPLE* stands for Semi-Implicit Method for Pressure Linked Equations

linearised using implicit formulation inherent to the pressure-based solver.

Further details of the formulations of the methods, algorithms and approaches can be found in Fluent (2006).

E.8 Convergence

Convergence criteria have to be set in order to determine when the solution is considered converged. In this study, the iterations of the following quantities were used as the indicators to determine convergence:

- the residuals of the continuity equation and the three velocity components from the momentum equations;
- the streamwise velocity component at two locations, downstream from the roughness element within the boundary layer and in the free stream;
- the mass flux through both inlet and outlet;

were the indicators to determine convergence.

Convergence was accepted when, simultaneously, the residuals decreased by three orders of magnitude, the variation of the streamwise velocity component was within 1% and the discrepancy of mass flux rate between inlet and outlet was within 1%.

E.9 Validation

The suitability of the problem statement, the adopted numerical method and the computational grid was validated against experimental data: single hot-wire data from Lavoie *et al.* (2008).

The comparison was based on the wall-normal profile of the rms of the perturbed streamwise velocity field u by the presence of the roughness elements with respect to its spanwise average, $\langle u \rangle_z$, at the streamwise location $x/k = 200$ (300 mm downstream from the leading edge of the flat plate, that is, 100 mm downstream from the roughness element

array). The free stream $U_\infty = 5$ m/s was set to be the same, as were roughness element array parameters: spacing $\Delta z = 10$ mm, diameter $d = 2.5$ mm and height $k = 1.5$ mm.

The perturbation velocity, $u' = u - \langle u \rangle_z$, could be interpreted as the isolated contribution to the base (unperturbed) flow, hence the rms of u was defined as:

$$u'_{rms} = \sqrt{\frac{1}{Np} \sum_{p=1}^{Np} u'^2}, \tag{E.1}$$

where Np is the number of boundary layer profiles considered in the spanwise direction.

Figure E.4 shows the u'_{rms} profiles normalised by the free-stream velocity for both hot-wire measurements and FVS results. It can be seen that the agreement is quite good, with a discrepancy of the prediction of the u'_{rms} peak of 2.5% with respect to the hot-wire data, and a discrepancy regarding the location of the peak.

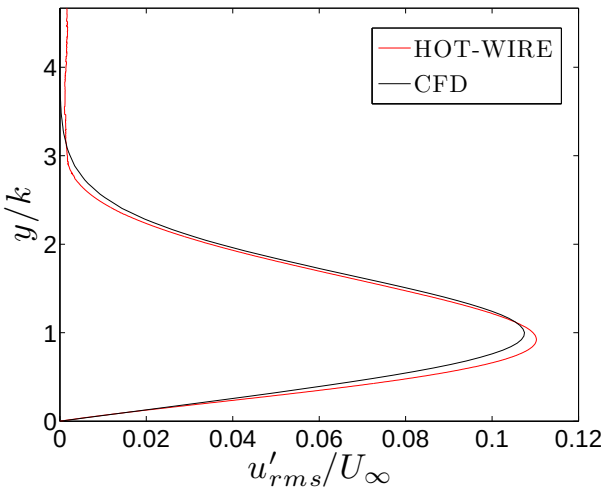


Figure E.4: Wall-normal profiles of u'_{rms} from both single hot-wire data from Lavoie *et al.* (2008) and FVS data.

Figure E.5 shows a comparison of profiles of u'_{rms}, at the same streamwise location as figure E.4, for two versions of grid: one, the eventually used, and the other, doubling the number of nodes in both z and y directions, while all other parameters remain unchanged. The results confirm that the grid used was sufficiently good to give results that are independent of the grid resolution.

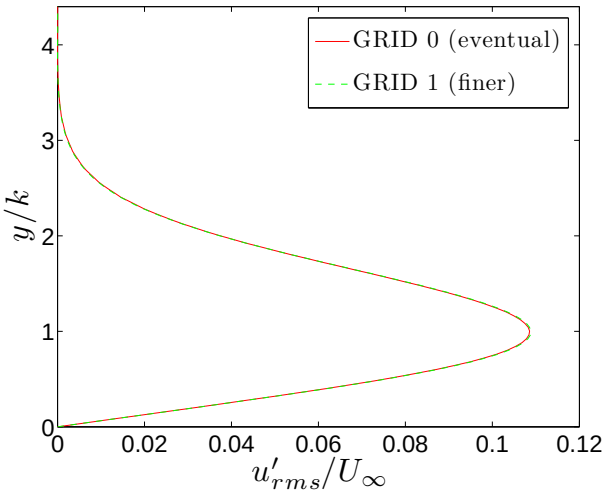


Figure E.5: Wall-normal profiles of u'_{rms} from the FVS data with the eventual grid employed (red) and another twice as fine in z and y directions (dashed blue).

Despite the good agreement of u' shown in figure E.4, the results regarding the v' component reveal some anomalies. Figure E.6 shows wall-normal profiles of v'_{rms} again at $x = 300$ mm for several grid cases: the grid used ("GRID 0"), a grid twice as fine in the z and y directions ("GRID 1"), and a grid ("GRID 2") twice as long in the y direction as GRID 0 (increasing the number of nodes only in that direction to conserve the same growth rate of the node spacing). It can be clearly seen that, despite the fact that the profiles for GRID 0 and GRID 1 are on top of each other, the FVS results are not grid-independent outside the boundary layer ($y/k \gtrsim 3.14$). Instead of having a sharp decay of v'_{rms} moving away from the wall, it decays linearly up to the top boundary. This is clearly non-physical for all the grids, and appears to be the result of the free-stream boundary condition.

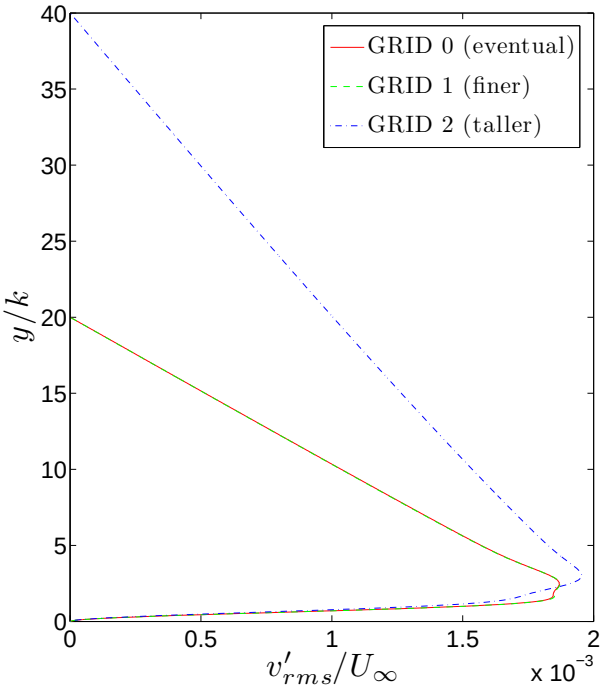


Figure E.6: Wall-normal profiles of v'_{rms} from the FVS data with the eventual grid employed (red), the same grid but twice as fine in z and y directions (dashed green), and the same grid as that eventual but twice as tall (dashed-doted blue). Note that GRID 0 and GRID 1 are precisely onto one another.